The Impacts of Star Formation on Galaxy Evolution since the End of Cosmic Reionization

Harry Michael Owen Stephenson

Physics

Department of Physics

Lancaster University

May 20, 2026

A thesis submitted to Lancaster University for the degree of Doctor of Philosophy in the Faculty of Science and Technology

Supervised by

Dr. John Stott

Abstract

Star-forming galaxies at different epochs of the Universe, and those residing in a range of environments, exhibit significant variations in their physical properties and scaling relations, both among themselves and relative to quiescent galaxy populations. Connecting the evolutionary pathways followed by these populations is therefore crucial to understanding galaxy formation and evolution as a whole. In this thesis, we present an analysis of star-forming galaxies across ~ 11 billion years of cosmic history ($0.2 \lesssim z \lesssim 6.1$), spanning both field and galaxy cluster environments. We probe a wide range of galaxy properties and scaling relations using both space- and ground-based facilities, and a variety of observational techniques including slitless grism spectroscopy, wide-field broad-band imaging, and narrow-band emission-line selection.

We begin by analysing the chemical evolution of star-forming field galaxies at Cosmic Noon ($1.99 < z < 2.32$), the epoch during which the cosmic star formation rate density was at its peak. Using strong emission-line calibrations applied to *Hubble Space Telescope* grism spectroscopy, we determine the gas-phase metallicities of galaxies in the Quasar Sightline and Galaxy Evolution (QSAGE) survey. This analysis allowed us to determine the scaling relations between gas-phase metallicity, galaxy stellar mass and star formation rate to probe the chemical evolution of Cosmic Noon galaxies relative to those in the local Universe.

In Chapter 3, we study the spatial distribution of star-forming galaxies in massive clusters at $0.206 < z < 0.494$ in the Cluster Lensing And Supernova survey with Hubble (CLASH). Utilising the wide-field

imaging capabilities of the Subaru Prime Focus Camera, we investigated the phenomenon known as "anisotropic quenching" (also referred to as "angular conformity" or "angular segregation"), which describes angular dependence of satellite galaxy colour and passive fraction with respect to the major axis of the brightest cluster galaxy. This analysis was conducted to assess the impact of large-scale cosmic web structure on satellite populations in galaxy clusters.

In the final science chapter, we analyse the multi-wavelength sizes of star-forming galaxies toward the end of the Epoch of Reionization ($z = 6.1$) using data from the *JWST* Emission Line Survey (JELS), the first survey to perform narrow-band rest-optical emission-line selection at this epoch. We use these narrow- and broad-band size measurements to determine the size–mass relation of star-forming galaxies at $z = 6.1$. The novel narrow-band imaging from JELS enables a direct comparison between the spatial extent of active star formation and that of established stellar populations, providing new insights into galaxy assembly during the first major epoch of galaxy formation. Since both in-situ star formation and mergers play key roles in galaxy growth, we additionally perform a close-pair analysis to estimate the merger fraction at this epoch.

This thesis is dedicated to my parents for always letting me forge my own path.

Acknowledgements

There are many people I want to acknowledge by name in this thesis.

First and foremost, I want to say a huge thank you to my supervisor John Stott. Ever since my MPhys project, it was abundantly clear that we were as compatible a pairing as you could hope for between student and supervisor. I could not have asked for a better mentor during this PhD. I thank him for his advice, endless list of contacts, good humour, and for always putting up with me waltzing into his office unannounced!

It would be remiss of me to not acknowledge the teacher who reignited my love of astrophysics: Mr Ian Barnes. My interest in physics had drifted for a time, and it was not until he invited me on a "Physics Masterclass" to Lancaster University when I was in Year 10 — the only Year 10 student on a trip intended for Sixth Formers — that I realised researching astrophysics was what I wanted to do in my future career. He saw something in me other teachers did not, and his compassion through my later school years has stuck with me to this day.

To the staff and post-docs in the Observational Astrophysics group over the years: Isobel Hook, Brooke Simmons, Julie Wardlow, Sam Oates, Mat Smith, Young-Lo Kim, Chris Duffy, Georgios Dimitriadis, Lydia Makrygianni, Sonny Bailey, and, of course, John. I thank you for creating an incredible social and working environment for all students. In my future career, wherever that may be, I will hope to follow your lead in making the workspace somewhere people enjoy doing research!

To my friends from C45: Heather Wade, Tom Cornish, David O'Ryan, Matthew Thorne, Andrew Milligan, Izzy Garland, Rahul Rana, Nick Amos, Amy Hewitt, Jamie Dumayne, Fergus Henstridge, Melzie Ghendrih, Jason Shingirai Makechemu, Sam Shilling, Pascale Desmet, Alice

Mead, Miranda Andersen, Libby Roxby and Charlie Hamilton. You made the office a special place to work in on a daily basis. I particularly want to pay credit to Heather and Tom who took me under their wing early on and made me feel part of the group so quickly, and to David for our conference adventures which I hope will continue! I wish you all the very best in your future careers!

The end of my PhD marks my eighth year in Lancaster, and during my Masters I met some of the most amazing people in my life who will be friends for the rest of it: Charlie Wells, Amaia Imaz Blanco, Ben Frondigoun, Eloise Page, Scott Henderson, Georgia Lowes, Elliot Howatson, Louise Frankland, Alex Smith, Jason Poon, Tom Fell, Lizzie Pollard and Lizzy Morritt. It is because of you and your continued friendship that I was able to make it to a PhD in the first place. I want to specifically acknowledge Charlie and Scott, along with Jakub Waniek, for being brilliant housemates for the majority of the PhD, as well as Luke Fairley for the Luke Days which provided weekly escapism, world-class beers and the occasional Settlers of Catan win!

To my boys from home: Matthew Wilson, Dan Jones, Jack Humble, Alex "Basher" Birkett, Alex Fisher, Archie Gannon, Ebony Townley, Ethan Vaughan, Hannah Reed, Izzy Price, Jack Bates, Joe & Josh Hayes, Lizzie Pickering, Ollie Dawson, Remi Benson, Robbie Swift and Sam Frank. From the Division 1 titles with It Runs Deep & Fat Heads Argyle, to the Matty Holiday Stories and all the many, *many* beers in between, you guys are simply the best. You have kept me going all these years with your humbling humour. Long may our friendship continue!

Finally, and most importantly, to my family: Mum, Dad, Abz and Dave The Dog. Whilst the content of my degree has given you some of the best sleep in years, I could not have done any of this without you. Your support in every aspect means the world to me and always has. I love you all so much.

Declaration

This thesis is my own work and no portion of the work referred to in this thesis has been submitted in support of an application for another degree or qualification at this or any other institute of learning.

"The only stupid question is the one you don't ask."

— N. Withington, Homebase, Kendal, 30th August 2016

Rotund Drinker: "Pint of lager, please Mary."
Mary Porter: "Right you are my love."

— *Hot Fuzz* (2007)
Screenplay by Edgar Wright & Simon Pegg
Directed by Edgar Wright

"Is it my imagination,
Or have I finally found something worth living for?"

— *Cigarettes and Alcohol* (1994)
Written by Noel Gallagher
Performed by Oasis

Arbiter: "Were it so easy."

— *Halo 3* (2007)
Written by Joseph Staten, Robt McLees, & Luke Smith
Voiced by Keith David

Contents

List of Figures

List of Tables

Relevant Publications by the Author

Chapter 2

- "Quasar Sightline and Galaxy Evolution (QSAGE) – III. The mass–metallicity and fundamental metallicity relation of $z \approx 2.2$ galaxies"; **Stephenson H. M. O.**, Stott J. P., Cullen F., Bielby R. M., Amos N., Dutta R., Fumagalli M., Tejos N., Burchett J. N., Crain R. A., Prochaska J. X., **2024, MNRAS, 527, 7891**

Chapter 3

- "Evidence that pre-processing in filaments drives the anisotropic quenching of satellite galaxies in massive clusters"; **Stephenson H. M. O.**, Stott J. P., Butler J., Webster M., Head J., **2025a, MNRAS, 537, 1542**

Chapter 4

- "The *JWST* Emission Line Survey (JELS): The sizes and merger fraction of star-forming galaxies during the Epoch of Reionization"; **Stephenson H. M. O.**, Stott J. P., Pirie C. A., Duncan K. J., McLeod D. J., Best P. N., Brinch M., Clausen M., Cochrane R. K., Dunlop J. S., Flury S. R., Geach J. E., Hale C. L., Ibar E., Kondapally R., Zefeng Li, Matthee J., McLure R. J., Ossa-Fuentes L., Patrick A. L., Sobral D., Swinbank A. M., **2025b, MNRAS, 544, 1412**

Co-Author Papers

- "The *JWST* Emission Line Survey (JELS): Extending rest-optical narrow-band emission line selection into the Epoch of Reionization"; Duncan K. J., McLeod D. J., Best P. N., Pirie C. A., Clausen M., Cochrane R. K., Dunlop J. S., Flury S. R., Geach J. E., Grogin N. A., Hale C. L., Ibar E., Kondapally R., Zefeng Li, Matthee J., McLure R. J., Ossa-Fuentes L., Patrick A. L., Smail Ian, Sobral D., **Stephenson H. M. O.**, Stott J. P., Swinbank A. M., **2025, MNRAS, 541, 1329**

- "The *JWST* Emission Line Survey (JELS): An untargeted search for Hα emission line galaxies at $z > 6$ and their physical properties"; Pirie C. A., Best P. N., Duncan K. J., McLeod D. J., Cochrane R. K., Clausen M., Dunlop J. S., Flury S. R., Geach J. E., Hale C. L., Ibar E., Kondapally R., Zefeng Li, Matthee J., McLure R. J., Ossa-Fuentes L., Patrick A. L., Smail Ian, Sobral D., **Stephenson H. M. O.**, Stott J. P., Swinbank A. M., **2025, MNRAS, 541, 1348**

Chapter 1

Introduction

When the first Hubble Deep Field image was released in January 1996, following over 100 hours of *Hubble Space Telescope* (*HST*) imaging (Williams et al. 1996), it revealed to astronomers that the Universe is populated by more galaxies than anticipated (Madau et al. 1996). Subsequent Deep Field observations, not least the 2004 Hubble Ultra Deep Field image (Beckwith et al. 2006), provided unprecedented views of galaxies as far back as ≈ 600 Myr after the Big Bang, and cemented galaxies as fundamental building blocks of large-scale structure (LSS) in the Universe.

1.1 Background Cosmology

Cosmological models describe the nature of the Universe and how its early and subsequent evolution resulted in the structure and distribution of matter at later times. The currently accepted cosmological model is the 'Lambda Cold Dark Matter' model (ΛCDM; Blumenthal et al. 1984; Dunkley et al. 2009). Observational evidence suggests that there exist three distinct components to our Universe: baryonic matter, Dark Matter (DM) and Dark Energy. Baryonic matter consists of the particles that make up all the observable structure that interact with light, from atoms to whole galaxies. The two 'dark' components make up ≈ 95 per cent

of the energy density of the Universe (Frieman et al. 2008), and do not interact with the electromagnetic force, making their detection difficult.

DM has been inferred from observations of galaxies. The first observed effects of some 'missing mass' were identified by Swiss astronomer Fritz Zwicky in 1933 when studying the Coma Cluster (Zwicky 1933). He measured the velocity dispersion of member galaxies and found a value exceeding $\sigma \gtrsim 1000\,\mathrm{km\,s^{-1}}$. Applying the virial theorem, Zwicky found that the cluster mass inferred from the velocity dispersion of its members was over two orders of magnitude larger than the mass calculated from the visible matter (Zwicky 1937). He concluded that there must be some invisible matter that is keeping these galaxies gravitationally bound to the cluster, which he referred to as "dunkle Materie" (Zwicky 1933). Further evidence for DM came from Vera C. Rubin who observed nearly flat rotation curves in the outer regions of local spiral galaxies (Rubin & Ford 1970; Rubin et al. 1980). The stars and gas (see Bosma 1978) in these outer regions were orbiting the galactic centre faster than expected based on the observed mass of these central regions, implying that there is more mass in these galaxies than can be directly observed.

The Λ in ΛCDM is what we colloquially refer to as Dark Energy. It is thought to be a form of energy that permeates the Universe and acts as a negative pressure, increasing the rate of expansion of the Universe. This expansion, first predicted by Georges Lemaître in 1927 (Lemaître 1927), was subsequently supported observationally by Edwin Hubble's demonstration that more distant galaxies recede more rapidly (Hubble 1929; Hubble & Humason 1931). Hubble estimated galaxy distances from Cepheid variables and other distance indicators and combined these with recessional velocities drawn largely from measurements by Vesto Slipher (Slipher 1917). Lemaître later proposed the "primeval atom" hypothesis (Lemaître 1931), an early formulation of what we now call the Big Bang. However, observations of Type Ia supernovae (SNe Ia; see Chapter 1.4.4) in distant galaxies in the late 1990s indicated that this expansion is accelerating. These SNe have a remarkably consistent peak luminosity, making them effective 'standard candles' for measuring distances to their host galaxies. In particular, SNe Ia at $0.1 \lesssim z \lesssim 0.8$ were found to be fainter than expected for a constant or slowing expansion rate — implying that they were more distant than expected —

and thus providing evidence for an *increasing* expansion rate (Riess et al. 1998; Perlmutter et al. 1998, 1999). Further evidence from observations of the Cosmic Microwave Background (CMB; Penzias & Wilson 1965; Dicke et al. 1965) supports this conclusion (Planck Collaboration et al. 2020a).

1.2 Galaxies Background

1.2.1 Galaxies and their Formation

This thesis focuses on the observational properties of galaxies across different cosmic epochs of the Universe. As discussed in Chapter 1.1, galaxies play a key role in cosmological models; their rotation curves provide evidence for DM, and their spatial distribution provides insights into the growth of overdense regions.

Galaxies are gravitationally bound systems of stars, gas, and dust. They are surrounded by DM haloes, which dominate their overall mass content (Navarro et al. 1996). Most galaxies host a supermassive black hole (SMBH) residing at their centre, with only a few notable exceptions, including Messier 33 (M33) in the Local Group (Gebhardt et al. 2001). Surrounding the SMBH, the baryonic matter of a galaxy often flattens into a rotationally supported disk, provided it is not significantly disturbed by interactions with other galaxies or feedback processes. In the event of such disturbances, the disk can be heated, perturbing stellar orbits and often leading to the formation of a central bulge. As will be discussed in Chapter 1.4, galaxy shapes fall into a range of morphological classifications that are influenced by their environment (see Chapter 1.2.2), merger history, and internal processes.

Within ΛCDM, structure in the Universe is predicted to build up hierarchically, as first proposed by White & Rees (1978). According to accepted theories, quantum fluctuations in the scalar field during inflation (Guth 1981; Bardeen et al. 1983) expanded rapidly to macroscopic scales, producing heterogeneities in the matter distribution across the Universe. The temperature fluctuations measured in the CMB have repeatedly supported the existence of this non-uniform build-up of matter (Bennett et al. 1996; Jarosik et al. 2011; Planck Collaboration

et al. 2020a,b). These perturbations then began to overcome the cosmic expansion and collapse under gravity, starting with cold DM on small scales prior to recombination (see Chapter 1.3.3). These DM haloes grew in size and, when the first atoms formed, baryonic matter fell into them to form the first stars in what are called proto-galaxies. These first stars are theorised to be Population III stars, forming from the collapse of metal-free gas from the primordial Universe as it cools (Kashlinsky & Rees 1983; McDowell 1986; see Bromm 2013 and Klessen & Glover 2023 for reviews of these first stars). These Population III stars are yet to be observed, as they are thought to form predominantly at extremely high redshifts ($z \gtrsim 20$), although simulations suggest that pockets of pristine or near-pristine gas may allow low-level Population III star formation to continue at later epochs ($z \sim 3 - 6$; e.g. Scannapieco et al. 2003; Tornatore et al. 2007; Trenti et al. 2009). They are also expected to have a top-heavy initial mass function (IMF; e.g. Larson 1998; Marks et al. 2012). The IMF describes the mass distribution of stellar populations that arises from the non-uniform collapse of gas (e.g. Salpeter 1955; Kroupa 2001; Chabrier 2003). In the case of Population III stars, the number density distribution is skewed towards higher-mass stars (100–1000 $\mathrm{M}_{\odot}$), which can live for $\lesssim 10$ Myr, meaning that they mostly exist at these high redshifts.

Many early simulations explored the formation of galactic structures within DM haloes in which Population III stars are thought to have formed. In general, infalling gas into a DM halo undergoes collisions and cools, and conservation of angular momentum causes the rotation of this gas to speed up, transforming an initial spheroid into a disk. Fall & Efstathiou (1980) developed one of the most influential early analytical frameworks describing disk formation in DM haloes, where they focused on tidal torque forces imparting initial angular momentum in a spherically symmetric DM halo, which then collapses into a disk following the aforementioned collisions. The seminal work by White & Frenk (1991) pioneered the use of semi-analytic models to model galaxy formation, incorporating feedback from star formation and the chemical enrichment of circumgalactic gas. The first hydrodynamical simulations in three dimensions shortly followed, with Navarro & Benz (1991) first investigating how galaxies form from hierarchical clustering (see also Katz & Gunn 1991; Katz 1992; Navarro & White 1994).

These studies provided important insights into the non-linear evolution of DM haloes and the formation of structure within them. Despite these models, galaxies come in a variety of shapes that arise from mechanisms beyond simple hierarchical growth, which will be explored in Chapter 1.4.2.

1.2.2 Galaxy Environments

Galaxies reside in a variety of environments which can be broadly described by three categories: the field, groups and clusters.

Field galaxies are isolated, with few, if any, neighbouring systems appreciably close. They are typically disk galaxies that have not undergone significant mergers or tidal interactions. Since there are few external mechanisms to prevent star formation, these galaxies are often actively star-forming (SF) and will only cease forming stars when their surrounding gas reservoirs are exhausted. Whilst described as being 'alone', field galaxies are commonly found embedded in the large-scale cosmic structure known as the 'Cosmic Web' (Bond et al. 1996). The Cosmic Web is a network of filaments composed of matter that connect to nodes occupied by high-density galaxy clusters. Field galaxies may reside along these filaments, or they may be embedded in the walls that surround cosmic voids (gaps in the filamentary structure; Gregory & Thompson 1978; Jôeveer et al. 1978). Galaxies do reside in voids, but these are usually referred to separately as "void galaxies" and only make up $\sim 7\%$ of the galaxy population (Pan et al. 2012).

Systems with multiple galaxies are known as galaxy groups. These are gravitationally bound systems, typically containing up to 40–60 galaxies (depending on the adopted luminosity or stellar-mass limit), and residing within DM haloes of characteristic mass $M_h \sim 10^{13}$–$10^{14}\,\mathrm{M}_\odot$ (e.g. Eke et al. 2004; Yang et al. 2007; Tully 2015), though the exact threshold is not strictly defined. At halo masses more massive than this, groups are typically classified as a cluster (e.g. Kravtsov & Borgani 2012). The Local Group, housing our own Milky Way, is an example of a galaxy group, containing at least 50 confirmed members and upwards of 30 unconfirmed dwarf galaxies (McConnachie 2012). As a result of the increased number density, interactions between galaxies in groups are much more common,

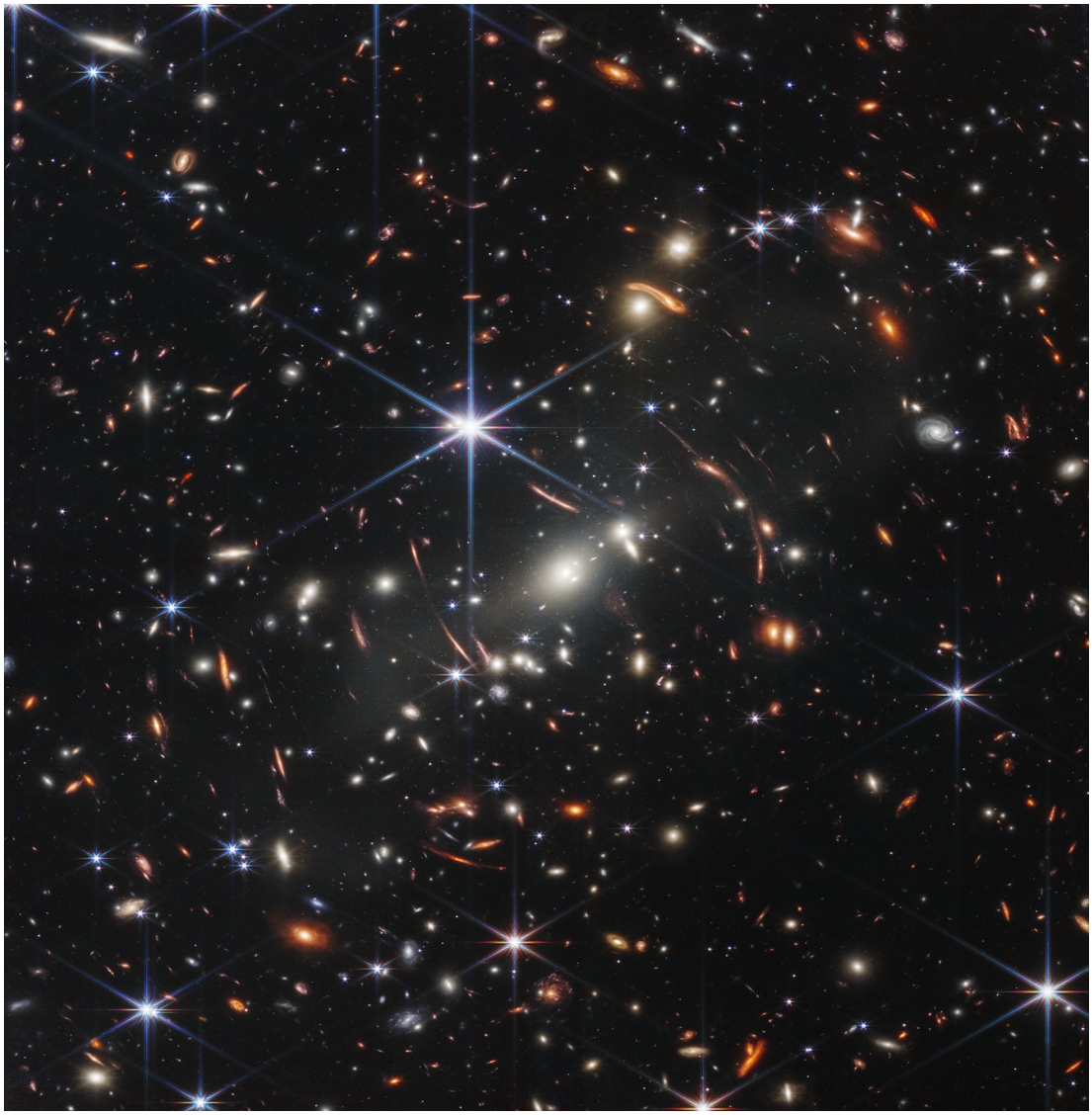

Figure 1.1: Multi-wavelength *JWST* image of the SMACS 0723 galaxy cluster ($z = 0.39$; Coe et al. 2019), better known as "Webb's First Deep Field" — the first full-colour operational image taken by *JWST*. The image is composed of observations taken in the F090W, F150W, F200W, F277W, F356W and F444W *JWST*/NIRCam filters on 7 June 2022. Image credit: NASA, ESA, CSA, STScI.

leading to 'harassment' (Moore et al. 1996), which can have a dramatic impact on galaxy properties. Groups are commonly found within the Cosmic Web, where multiple galaxies form in regions of higher DM density. These groups then travel along filaments of gas, galaxies, and other groups that compose the Cosmic Web, migrating toward the dense nodes where clusters reside.

Galaxy clusters are the largest gravitationally bound structures in the Universe. They can host up to thousands of galaxies and permeating throughout is a hot intracluster medium (ICM) of gas that emits strongly in the X-ray. Clusters form within the most massive DM haloes in the Universe, whose total mass distribution can be inferred through several methods, including the velocity dispersion of member galaxies, the X-ray temperature of the ICM, and gravitational lensing of background sources (see Kravtsov & Borgani 2012 for a review). For example, the Virgo Cluster — the nearest cluster to the Milky Way — has a DM halo mass of $\approx 6.5 \times 10^{14}\,\mathrm{M}_{\odot}$ (Kashibadze et al. 2020). Such massive haloes are found at the nodes of the Cosmic Web, where the infall of galaxies leads to the high number densities observed in clusters. Figure 1.1 shows an example of a galaxy cluster, SMACS 0723, which was identified as part of the Southern MAssive Cluster Survey (SMACS; see Ebeling et al. 2001; Repp & Ebeling 2018). The image was taken with the *JWST* Near-Infrared Camera (NIRCam) and released as its first full-colour operational image, known as "Webb's First Deep Field". In Figure 1.1, clear examples of gravitationally lensed systems are visible surrounding the elliptical brightest cluster galaxy (BCG) at the centre of the image. Clusters have a diffuse, but luminous, light associated with them known as the intracluster light (ICL) that comes from stars gravitationally bound to the cluster potential but not to any individual galaxy. Cluster environments are not suited to star formation, with prevalent environmental mechanisms preventing, or actively shutting down, star formation in cluster members (Butcher & Oemler 1978, 1984; Peng et al. 2010b).

Figure 1.2: Image of the Andromeda galaxy (Messier 31) observed using equipment from the Physics Department, Lancaster University. Also pictured are the dwarf galaxies Messier 110 (below Andromeda) and Messier 32 (also known as Le Gentil; above Andromeda). All three galaxies are members of the Local Group. Image credit: Orlando Prügel-Bennett, Lancaster University Astronomy Society.

1.3 The Frontiers of Galaxy Astronomy

1.3.1 Local Universe

In the history of galaxy observations, there have been three key frontiers that have been advanced with the advent of new technology and observational techniques. The first of these frontiers is the local Universe. Though the exact definition of "local" is loosely defined in the literature, it can either refer to galaxies in the Local Group or, more broadly, to galaxies in the nearby Universe.

As previously discussed, there are $\approx$ 80 galaxies in the Local Group — a number which may rise with further detections of faint dwarf galaxies. Its three

largest members are the Milky Way, the Andromeda Galaxy (M31), and the Triangulum Galaxy (M33). Andromeda and Triangulum are catalogued as Messier objects, named after the 18th-century astronomer Charles Messier, who compiled a list of "nebulae" and star clusters (Messier 1781). Andromeda, the largest member by radius, was first recorded as a "small cloud" in Persian astronomical texts around the 10th century, long before Edwin Hubble suggested that it is another galaxy external to the Milky Way (Hubble 1925). Figure 1.2 shows an image of Andromeda, as well as dwarf galaxies M110 and M32 (also known as Le Gentil, named after the French astronomer Guillaume Le Gentil who first discovered it), taken by Orlando Prügel-Bennett using equipment supplied by the Physics Department at Lancaster University. Triangulum, the third-largest member, was identified in the 17th century before similarly being confirmed as an external galaxy by Hubble. There are also two well-known dwarf galaxies orbiting the Milky Way: the Large and Small Magellanic Clouds. These are irregular dwarf satellites visible to the naked eye in the Southern Hemisphere. Together, these galaxies and their satellites form the nearest environment for detailed studies of galaxy formation and evolution.

We have known about other galaxies beyond our own group for nearly a century now, and the broader definition of the "local" frontier is likely better described by the nearby LSS. For example, M83 was first discovered in the 1700s and is now known to be $\approx 4.5\,\mathrm{Mpc}$ from the Milky Way as part of a different galaxy group (Tully et al. 2016). The first galaxy cluster discovered was the Virgo cluster, and whilst galaxies in the cluster were actually first observed as early as the 1700s (Messier 1781), it was only in the late 1920s and early 1930s that it was recognised as a cluster of galaxies (see Shapley & Ames 1926; Hubble & Humason 1931; Smith 1936). Thanks to the advent of wide-field sky surveys, such as the Sloan Digital Sky Survey (SDSS; York et al. 2000), we have been able to map the local LSS of cosmic filaments, which extends out to ≈ 200–$300\,\mathrm{Mpc}$. In the future, new facilities, most notably the Vera C. Rubin Observatory's Legacy Survey of Space and Time (LSST; Ivezić et al. 2019), are set to deepen our knowledge of the local Universe to even fainter systems. Overall, the local Universe is now more accurately defined as being at $z \lesssim 0.05$.

1.3.2 Cosmic Noon

The cosmic star formation rate (SFR) density peaked approximately 2–4 Gyr after the Big Bang ($1 \lesssim z \lesssim 3$; Madau & Dickinson 2014; see Figure 1.3). This epoch followed reionisation (see Section 1.3.3) and was fueled by the abundance of readily available metal-poor gas reservoirs that accreted efficiently onto galaxies, resulting in molecular gas fractions several times higher than those observed in the local Universe (Daddi et al. 2010; Tacconi et al. 2013; Aravena et al. 2016; Tacconi et al. 2018). By contrast, the SFR density of the present-day Universe is only $\sim 10\%$ of its $z \sim 2$ peak value (Madau & Dickinson 2014). The decline in SFR toward low redshift is attributed to a combination of diminishing cold gas supply, increasing gas depletion times, and the growing influence of regulatory processes such as stellar and active galactic nucleus (AGN) feedback. Consequently, this epoch corresponds not only to the peak of cosmic star formation activity, but also to the period of most rapid stellar mass (M_*) assembly (e.g. Ilbert et al. 2010, 2013).

Cosmic Noon became a new frontier in extragalactic observations because detecting galaxies at $2 \lesssim z \lesssim 3$ required both deeper surveys and instruments capable of detecting in the infrared (IR), as much of the rest-frame optical light of these galaxies is redshifted beyond the visible spectrum. Key emission lines (e.g. Hα, [O II]$\lambda\lambda 3727, 3729$, [O III]$\lambda\lambda 4959, 5007$) remain accessible in the near-IR (NIR) out to Cosmic Noon, and it was largely thanks to the capabilities of *HST* that this frontier was pushed back. *HST* achieved unprecedented depth and spatial resolution in the ultraviolet (UV) and optical, while its NIR capabilities, particularly following the installation of the Wide Field Camera 3 (WFC3; MacKenty et al. 2008, 2010), enabled access to emission lines that had previously been inaccessible from space-based facilities.

Cosmic Noon therefore represents a crucial epoch for studying galaxy evolution, capturing not only the peak in star formation activity, but also the rapid assembly of stellar mass, peak in SMBH feeding (Madau & Dickinson 2014) and the emergence of ordered galaxy structures (Schreiber & Wuyts 2020).

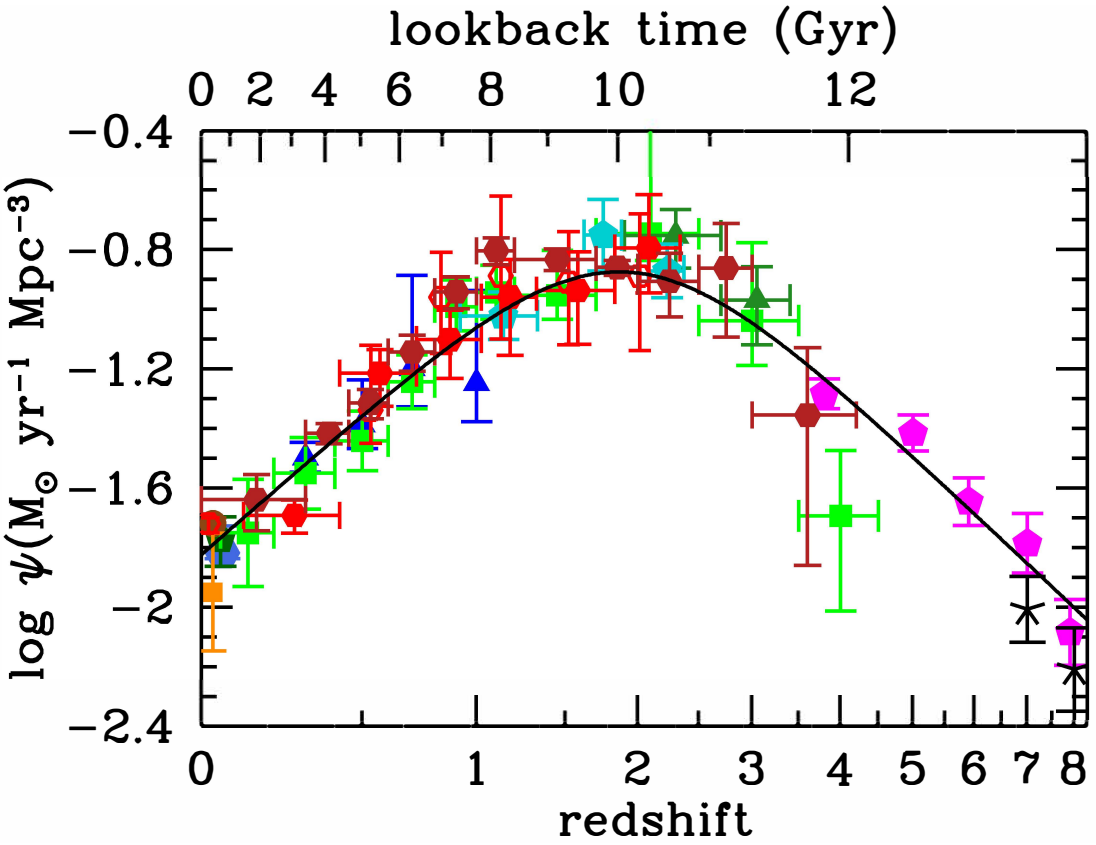

Figure 1.3: The evolution of the cosmic SFR density as a function of redshift determined from both rest-frame IR and UV measurements. The solid black curve represents the best-fit SFR density, with the peak at $1 < z < 3$ corresponding to the epoch known as Cosmic Noon. Figure from Madau & Dickinson (2014).

1.3.3 The Epoch of Reionization

The final major frontier of galaxy observations is the Epoch of Reionization (EoR). To understand the significance of this epoch, it is necessary to consider how the Universe came to be *re*ionised. The early phases of the Universe were briefly discussed in Chapter 1.2.1 in the context of DM buildup, but here the focus is on the key periods prior to the EoR, assuming a ΛCDM cosmology. Following inflation in the first $\sim 10^{-32}$ s of its lifetime, the Universe existed as a hot plasma of free protons and electrons, with photons undergoing continuous Thomson scattering and leaving the Universe opaque. Only after $\approx 380\,000$ yr ($z \approx 1100$) did recombination occur, once the Universe had expanded and cooled to ~ 3000 K. This allowed the first neutral atoms to form. These atoms were predominantly hydrogen and helium, with measurements of the CMB indicating a primordial helium nucleon fraction from Big Bang nucleosynthesis of $Y_{\rm P}^{\rm BBN} = 0.2437$ (Planck Collaboration et al. 2020a; see also Aver et al. 2015; Peimbert et al. 2016). In other words, $\approx 24.4\%$ of all baryonic nucleons were locked into helium, while the remainder — primarily protons — existed as neutral hydrogen, with only trace amounts forming deuterium, lithium, and other light nuclei. At this stage, the reduced free-electron fraction dramatically lowered the opacity of the primordial plasma, allowing photons to decouple from matter and propagate freely. This radiation is observed today as the CMB.

What followed was a period known as the "Dark Ages", during which no luminous sources had yet formed. During this epoch, the first DM haloes assembled, gravitationally attracting pristine primordial gas into their potential wells. This process laid the foundations for the formation of the first stars and galaxies, and ultimately for the emergence of the LSS observed in the local Universe.

The first stars in the Universe are thought to have formed at $z \approx 30$ (Barkana & Loeb 2001; Klessen & Glover 2023). These stars emitted energetic photons with energies well above the 13.6 eV threshold required to ionise neutral hydrogen. As a result, regions of ionised hydrogen surrounding these first stars began to form, known as H II regions. As star formation became more widespread within the centres of DM haloes by $z \approx 15$, larger H II regions developed in environments

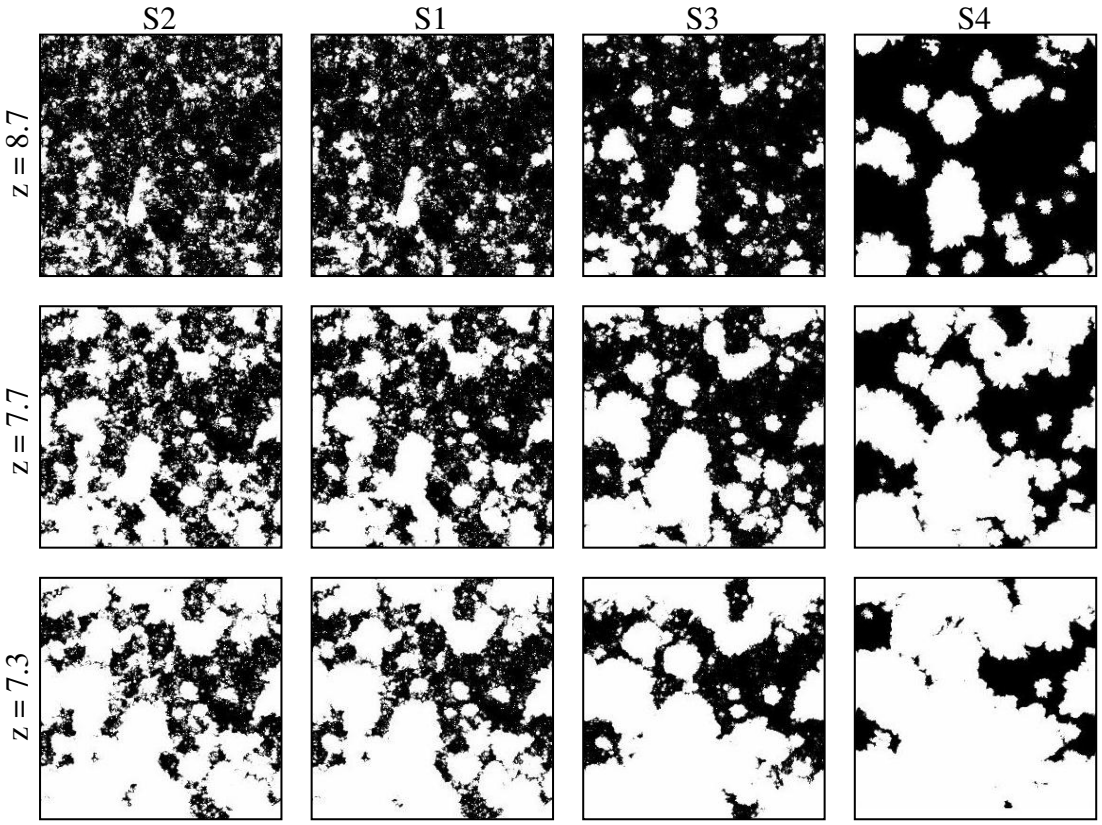

Figure 1.4: The evolution of ionised (white) and neutral (black) regions of four different radiative transfer simulations (S1–4) post-processed on the same density field. Each row highlights the ionising regions at three different redshifts during the EoR. Each panel represents a 94 Mpc (comoving) wide cutout. Figure from McQuinn et al. (2007).

where neutral hydrogen was abundant. These 'bubbles' of ionised hydrogen expanded around early galaxies as radiation from their constituent stars escaped into the surrounding intergalactic medium (IGM). The Universe is thought to have been completely ionised (defined as when these H II regions entirely overlap) by $z \approx 6$ (Fan et al. 2006b). Figure 1.4 shows an example of reionisation based on a suite of post-processed radiative transfer simulations from McQuinn et al. (2007), using four different source prescriptions (see their paper), where white regions indicate ionised gas and black regions indicate neutral gas.

1.4 Galaxy Properties and their Evolution

This thesis focuses on several key properties of SF galaxies across different epochs. In this chapter, we briefly outline some of the most widely studied: star formation, colour, morphology, light profiles, and gas-phase metallicity. Each of these properties provides insight into the evolution of galaxies and establishes the context for the detailed analysis in later chapters.

1.4.1 Star Formation and Colour

SF galaxies are, by definition, systems in which active star formation is taking place. Stars form from collapsing clouds of molecular gas, composed primarily of H_2 and CO (McKee & Ostriker 2007). These molecules are important in star formation as they enable the gas to cool to temperatures that prevent pressure from overcoming gravitational collapse. In the early Universe, when metals had not yet formed, H_2 dominated the cooling of the interstellar gas (Bromm et al. 2002; Bromm 2013). In contrast, CO is the primary coolant in metal-rich environments, as its rotational transitions are more easily excited at low temperatures (Goldsmith & Langer 1978). Population III stars formed from pristine primordial gas, while subsequent generations (Population II and I) formed with an increasing amount of metals locked inside them as a result of enrichment from SNe and stellar mergers.

Stars form across a range of masses, from $\gtrsim 0.15\,M_\odot$ to $\lesssim 100\,M_\odot$. Their fundamental properties, including temperature (colour), luminosity and lifetime, vary strongly with mass. The majority of stars spend most of their lifetimes on the main sequence, which describes the evolutionary phase during which hydrogen fusion occurs in the stellar core. For main-sequence stars, these properties correlate closely with stellar surface temperature, which forms the basis of the stellar classification system. This classification applies most directly to main-sequence stars, and the broader discussion here does not consider later evolutionary stages such as white dwarfs, red giants and neutron stars, as well as Population III stars, which have a significantly different chemical composition. Cooler stars (e.g. M-type dwarfs) are low-mass, faint, and red in colour, while the hottest stars (e.g.

O-type stars) are blue, extremely massive, and highly luminous. Lifetimes also vary dramatically, with O-type stars surviving for only $\sim 10\,\mathrm{Myr}$, whereas low-mass dwarf stars can continue burning for trillions of years.

The relationship between colour and lifespan in stellar populations is critical in observational studies of galaxies, particularly when distinguishing between SF and quiescent systems. SF galaxies host populations of massive, short-lived blue stars that dominate the emitted light, causing these galaxies to appear blue. In contrast, galaxies that have been quiescent for extended periods have lost their massive stars, leaving behind older, redder stellar populations. This has led to quiescent galaxies being colloquially described as "red and dead" (Romeo et al. 2008; Brammer et al. 2009). The resulting colour–SFR connection produces a pronounced bimodality in galaxy populations that has been observed extensively in galaxy surveys (Strateva et al. 2001; Bell et al. 2004; Baldry et al. 2004, 2006; Wetzel et al. 2012; Taylor et al. 2015) and simulations (Nelson et al. 2018; Cui et al. 2021).

Among SF galaxies, observations have revealed a strong correlation between stellar mass and SFR, extending at least to the EoR (Brinchmann et al. 2004; Speagle et al. 2014; Schreiber et al. 2015; Popesso et al. 2023). This relation, known as the SF "main sequence" of galaxies (not to be confused with the stellar main sequence), describes how more massive galaxies typically exhibit higher SFRs than less massive systems at fixed redshift. The SF main sequence remains relatively tight over a wide range of stellar masses (Daddi et al. 2007; Whitaker et al. 2012; Leja et al. 2022), although it flattens at high masses ($\sim 10^{10}\,\mathrm{M}_{\odot}$; Ilbert et al. 2015; Lee et al. 2015; Schreiber et al. 2016). As a result of its small intrinsic scatter, the SF main sequence is often used to classify galaxies based on their offset from the relation at fixed stellar mass. Quiescent galaxies typically lie well below the sequence, while systems significantly above it exhibit elevated SFRs and are often interpreted as undergoing a starburst phase during which gas reservoirs are rapidly depleted.

The process by which galaxies transition from actively SF to passively evolving systems is known as "quenching", with quiescent systems commonly referred to as quenched galaxies. Quenching can occur through a variety of mechanisms that are broadly divided into "mass quenching" and "environmental quenching",

following Peng et al. (2010b; see also Peng et al. 2012, 2014; Zhang et al. 2021). Mass quenching refers to mechanisms that originate internal to the galaxy, typically associated with stellar mass growth or the presence of an AGN. Conversely, environmental quenching mechanisms originate from interactions with the surrounding environment, particularly in overdense regions such as galaxy groups and clusters.

Examples of mass quenching include feedback from AGN (Fabian 2012; Harrison 2017) or SNe (Larson 1974; Dekel & Silk 1986; Stinson et al. 2006), which can heat gas sufficiently to suppress collapse or drive powerful winds that eject gas from the galaxy. Morphological quenching (Martig et al. 2009, 2013; Cano-Díaz et al. 2019) occurs when a pressure-supported spheroid (e.g. a central bulge or an elliptical galaxy; see Chapter 1.4.2) stabilises the gas against fragmentation, thereby inhibiting the formation of SF clumps relative to a disk-dominated system. Bar quenching (Gavazzi et al. 2015; Khoperskov et al. 2018; Géron et al. 2021) describes scenarios in which the formation of a central bar funnels gas towards the centre or generates turbulence in the disk that prevents star formation.

Environmental quenching mechanisms include ram pressure stripping (RPS; Gunn & Gott 1972; Fujita & Nagashima 1999; Quilis et al. 2000), whereby galaxies infalling into dense environments containing hot gas (e.g. an ICM) have their interstellar medium (ISM) stripped; strangulation (Larson et al. 1980; Balogh et al. 2000; Peng et al. 2015), which halts the accretion of cold gas and leaves galaxies to exhaust their existing reservoirs; and tidal stripping (Richstone 1975, 1976; Farouki & Shapiro 1981), in which close interactions with more massive systems remove gas as a result of strong tidal forces (also referred to as "harassment" in the case of repeated interactions; Moore et al. 1996). Galaxy mergers, particularly major mergers in which the interacting systems are comparable in mass, can also quench galaxies by funnelling gas into central regions, triggering intense starbursts that rapidly deplete gas reservoirs, or fuelling an AGN that generates strong feedback (Mihos & Hernquist 1994a,b, 1996; Hopkins et al. 2008). However, in high-density environments such as clusters, mergers are relatively rare owing to the high velocity dispersions of orbiting satellites ($\sigma \sim 1000\,\mathrm{km\,s^{-1}}$; e.g. Struble & Rood 1999). The increasing prevalence of environmental quenching mechanisms at $z \lesssim 1$ is widely thought to contribute to the rapid decline in the

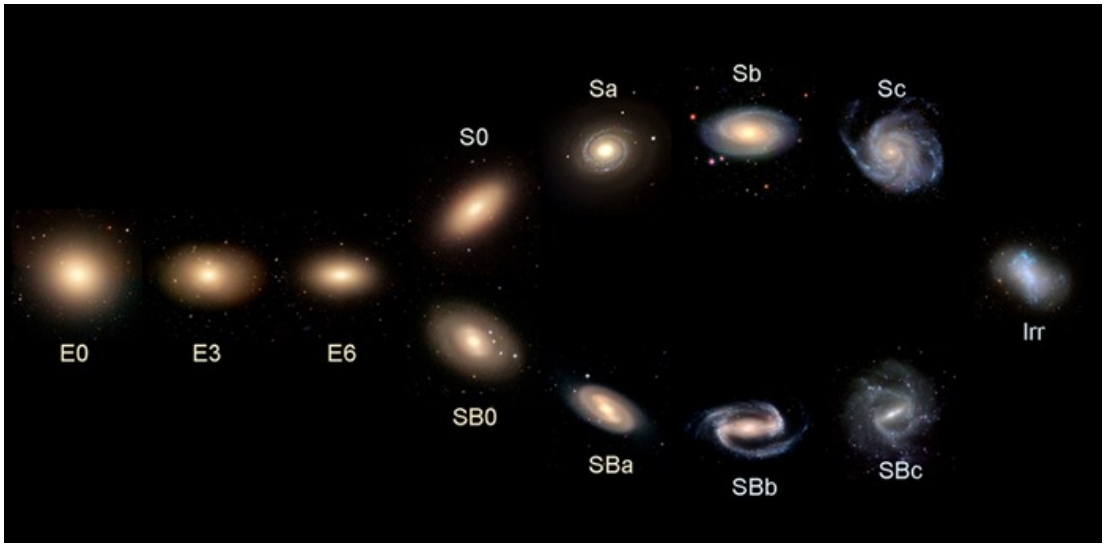

Figure 1.5: Diagram of the Hubble tuning fork illustrating galaxy morphologies based on the Hubble (1936) classifications. Each morphological class is represented by an example galaxy image. Figure from Cui et al. (2014).

cosmic SFR density (Bell et al. 2007; Ilbert et al. 2013; Moustakas et al. 2013; Madau & Dickinson 2014).

1.4.2 Morphologies

Galaxy morphology is a fundamental property that reflects the wide variety of shapes exhibited by galaxies. In addition to establishing the extragalactic nature of so-called nebulae, Edwin Hubble introduced one of the earliest galaxy classification schemes based on visual morphology. In his initial work, galaxies were divided into ellipticals and spirals (Hubble 1926), before the later development of what is now known as the "Hubble tuning fork" diagram (Hubble 1936; see Figure 1.5). The tuning fork introduced additional categories, including lenticular galaxies, barred and unbarred spirals, and irregulars. It is a system that is still widely used to describe galaxy morphology today.

In the tuning fork system, elliptical galaxies are denoted by 'E'. They are ellipsoidal and smooth in appearance, owing to the absence of stellar clumps or actively SF regions. Their classification ranges from E0 (nearly spherical) to E7 (highly elongated). They are generally thought to form through major mergers of

spiral galaxies (Toomre & Toomre 1972; De Lucia et al. 2006), which disrupt the ordered motion of stars and funnel both stars and gas toward the centre of the newly formed gravitational potential, resulting in a dense central concentration of mass (Conselice 2003). Elliptical galaxies are often referred to as "early-type galaxies" (ETGs), a term originating from Hubble's description of their smooth and featureless appearance, analogous to the relatively featureless appearance of the spectra of early-type stars (O-, B- and A-type). Despite the terminology, this classification does not imply a temporal evolutionary sequence, although the convention has persisted. ETGs are typically quenched systems, dominated by older stellar populations and have significantly lower gas fractions than spiral galaxies.

Lenticular galaxies, denoted 'S0', represent another class of ETGs and act as a bridge between ellipticals and spirals in the tuning fork diagram. Unlike ellipticals, S0 galaxies contain both a prominent central bulge and an extended disk component, although their disks lack spiral arms. In the absence of resolved spectra, distinguishing S0 galaxies from ellipticals is difficult, particularly when light from the central bulge dominates or the disk component is faint (Cappellari et al. 2011). Inclination further complicates their classification, as disks are difficult to visually identify in face-on systems, while the absence of spiral arms can be ambiguous in edge-on orientations (Bamford et al. 2009).

Spiral galaxies are classified as "late-type galaxies" (LTGs). In contrast to ETGs, their morphologies are more complex, with features such as prominent spiral arms, a central bulge, H II regions, and, in many cases, a stellar bar. The terminology again originates from an analogy with late-type stars (e.g. K- and M-dwarfs), whose cooler temperatures produce spectra rich in molecular absorption features and thus appear more complex. Spiral galaxies are characterised by large, rotationally supported disks with prominent spiral arms and are subdivided into barred (denoted 'SB', e.g. SBa, SBb, SBc) and unbarred ('S', e.g. Sa, Sb, Sc) systems. Barred spirals host a stellar bar passing through the central bulge, while unbarred systems lack this structure. The sub-classes 'a', 'b' and 'c' describe both the tightness of the spiral arms and the relative size of the bulge, with 'a' spirals exhibiting tightly wound arms and a large bulge, and 'c' spirals having loosely wound arms and smaller bulges. The disks of spiral galaxies typically host

ongoing star formation, giving them a bluer appearance than ellipticals. Spiral galaxies are also more commonly found residing in low-density environments, where environmental quenching mechanisms are less prevalent.

The final galaxy type in Hubble's original classification are irregular galaxies. They do not lie along the main branches of the tuning fork and are therefore considered a separate morphological category. As their name suggests, these galaxies lack a well-defined structure and span a wide range of shapes, leading to their classification as LTGs. Irregular galaxies are typically SF, as they are rich in neutral hydrogen, although their resulting star formation is often clumpy due to lower gas surface densities compared to spiral disks (Conselice 2003, 2014; see Hunter et al. 2024 for a recent review of dwarf irregulars).

1.4.3 Sérsic Light Profiles

The Hubble tuning fork system is based on the visual morphologies of galaxies observed in images. While this provides a useful descriptive framework of galaxy shapes, a more quantitative approach to galaxy classification comes from measuring how light is distributed across a galaxy, known as its surface brightness profile. This profile describes how the intensity of a galaxy's light varies as a function of galactocentric radius. Early studies of galaxy light profiles focused primarily on elliptical galaxies and the steep decline in their surface brightness at large radii (e.g. Reynolds 1913; Hubble 1930). The most influential of these early works was de Vaucouleurs (1948), who showed that the light profiles of ellipticals follow $I(r) \propto \exp(-kr^{1/4})$, where $I(r)$ is the intensity at galactocentric radius r and k is a scale constant. This relation is now known as the de Vaucouleurs profile.

Early analyses of the light profiles of disk galaxies were also carried out (e.g. Patterson 1940), with the most widely recognised being the seminal work of Freeman (1970). This study formalised the concept that spiral galaxies are well described by an "exponential disk" light profile in the form $I(r) \propto \exp(-r/h)$, where $I(r)$ is the intensity at galactocentric radius r and h is the disk scale length.

José Luis Sérsic developed a major generalisation of galaxy light profiles in his influential work Sérsic (1963), which he fully developed in Sérsic (1968). This

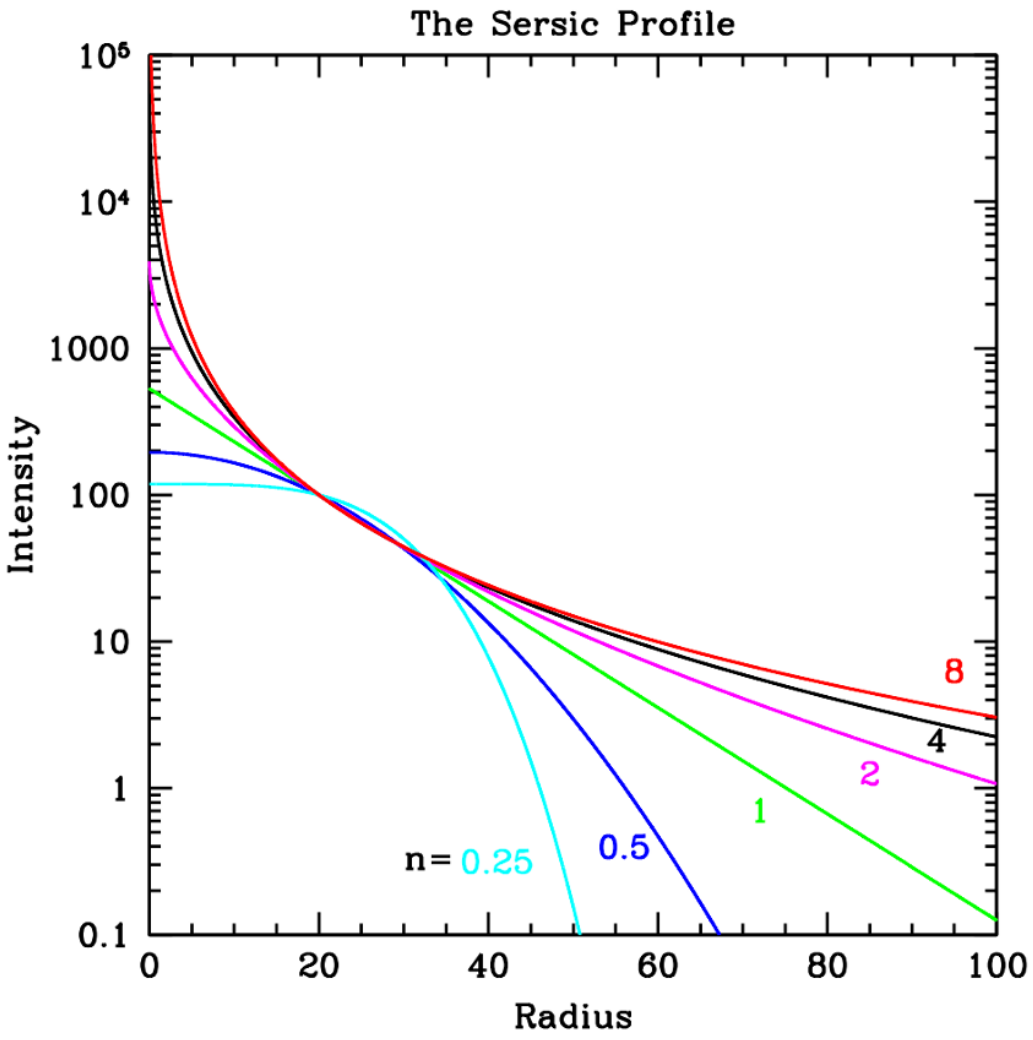

Figure 1.6: Illustration of Sérsic surface brightness profiles for a range Sérsic indices, n. This highlights how increasing n produces more centrally concentrated light distributions and more extended outer wings. Figure from Peng et al. (2010a).

"Sérsic light profile" unifies the previously described light profiles of both ellipticals and spirals, and is expressed as

$$I(r) = I_e \exp\left\{-b_n \left[\left(\frac{r}{r_e}\right)^{1/n} - 1\right]\right\}, \tag{1.1}$$

where $I(r)$ is the intensity at a radius r from the centre of the galaxy, r_e is the effective (half-light) radius, b_n is a dimensionless scale factor that depends on the Sérsic index n, and I_e is the intensity at r_e. The Sérsic index governs the overall shape of the light profile and is therefore commonly quoted as a structural classification parameter for galaxies. For example, a Sérsic index of $n = 1$ reduces the model to a purely exponential disk, which provides a good description of spiral galaxies, with $n \lesssim 2.5$ generally being used to characterise LTGs. By contrast, a Sérsic index of $n = 4$ reproduces the classical de Vaucouleurs (1948) profile typically associated with elliptical galaxies, with $n \gtrsim 2.5$ generally applying to ETGs, as they have steeper inner light profiles. Figure 1.6 illustrates Sérsic surface brightness profiles for a range of n values. As discussed in Chapter 1.4.2, it is common for galaxies to have multiple components, each of which may be better described by different Sérsic indices. For instance, spiral galaxies commonly host a SF disk characterised by an $n \sim 1$ profile alongside a bulge component with a light profile closer to $n \sim 4$. In such cases, multi-component Sérsic fitting is required to accurately model the overall light distribution.

Following Sérsic's generalisation, a complementary quantitative approach to classifying galaxy morphology emerged to accompany the qualitative one pioneered by Hubble (see Graham 2013 for a historical review).

1.4.4 Gas-phase Metallicity

Earlier in this chapter, we discussed the properties that distinguish SF galaxies from quiescent populations in terms of colour, morphology, and surface brightness profile. I also briefly introduced metals in the context of early star formation and their absence in Population III stars. The metal content of galaxies is another fundamental property in the study of galaxy evolution.

The abundance of metals in a galaxy, referred to as its metallicity, is defined as the relative abundance of elements heavier than helium compared to hydrogen. Relevant for this thesis is "gas-phase" metallicity, which is a measure of the abundance of heavy elements within a galaxy's ISM. Gas-phase metallicity is most commonly measured as the oxygen abundance relative to hydrogen and is expressed as $12 + \log(\mathrm{O/H})$. Oxygen is used as a metallicity tracer because it is the most abundant metal in the Universe (Tinsley 1979; Nomoto et al. 2013) and produces strong emission lines that are more readily observable than those of other key metals. For reference, the solar oxygen abundance has been measured to be $12 + \log(\mathrm{O/H}) \approx 8.69$ (Asplund et al. 2009).

As explained in Chapter 1.3.3, $\approx 24.4\%$ of nuclei produced during Big Bang nucleosynthesis were helium, with $\approx 75\%$ being hydrogen and only trace amounts of lithium and beryllium. Nearly all heavier elements were subsequently produced through either *stellar* nucleosynthesis or explosive stellar events, such as SNe and neutron star mergers. For example, key tracers of chemical enrichment, such as carbon, oxygen, neon, magnesium, and silicon, are primarily released during core-collapse (Type II) SNe. These elements are synthesised in the cores of massive stars ($\gtrsim 8\,\mathrm{M}_\odot$) through nuclear fusion, accumulate over the star's lifetime, and are then expelled during the supernova (SN) explosion along with other heavy elements formed during core collapse. Iron is also produced in Type II SNe, as it forms during the final evolutionary stages of massive stars. Perhaps more significantly for iron production are Type Ia SNe. These are thought to arise from the thermonuclear explosion of white dwarfs accreting material from a companion star, occurring as the white dwarf approaches a mass of $\approx 1.44\,\mathrm{M}_\odot$ (the Chandrasekhar limit; Chandrasekhar 1931). This process leads to the rapid synthesis of intermediate-mass and iron-peak elements, including silicon, calcium, sulfur, and predominantly nickel-56, a radioactive isotope that subsequently decays into iron.

As with other galaxy properties, gas-phase metallicity differs between SF and quiescent galaxies at fixed stellar mass, with SF systems typically exhibiting lower metallicities. This arises because sustained star formation requires a continuous inflow of cold, relatively *metal-poor* gas to replenish the ISM. Such inflows di-

lute the metal content of the ISM, resulting in systematically lower gas-phase metallicities in SF galaxies.

Quiescent galaxies, on the other hand, are quenched primarily because they *lack* an ongoing supply of cold gas, either having exhausted their reservoirs through star formation or lost them via environmental processes (see Chapter 1.4.1). Consequently, the dominant sources of gas within their ISM come from internal stellar processes, including SNe, stellar mergers, and winds from evolved stars. These processes progressively enrich the remaining gas in the ISM, leading to higher gas-phase metallicities in quiescent systems.

At higher redshifts, SF galaxies are generally expected to have lower gas-phase metallicities at fixed stellar mass than those in the local Universe. This reflects the fact that they are observed at an earlier stage of chemical enrichment, when their stellar populations have had less time to process gas into metals, and when high gas fractions, accretion of metal-poor gas, and feedback-driven outflows play a more significant role in regulating the metal content of the ISM.

Chapter 2

The Mass–Metallicity and Fundamental Metallicity Relation of $z \approx 2.2$ Galaxies

Abstract

We present an analysis of the mass–metallicity relation (MZR) for a sample of 67 [O III]-selected SF galaxies at a redshift range of $1.99 < z < 2.32$ ($z_{\rm median} = 2.16$) using *HST*/WFC3 grism spectroscopy from the Quasar Sightline and Galaxy Evolution (QSAGE) survey. Metallicities were determined using empirical gas-phase metallicity calibrations based on the strong emission lines [O II]3727, 3729, [O III]4959, 5007, and Hβ. SF galaxies were identified, and distinguished from AGN, via Mass–Excitation diagrams. Using $z \sim 0$ metallicity calibrations, we observe a negative offset in the $z = 2.2$ MZR of ≈ -0.51 dex in metallicity when compared to locally derived relationships, in agreement with previous literature analyses. A similar offset of ≈ -0.46 dex in metallicity is found when using empirical metallicity calibrations that are suitable out to $z \sim 5$, though our $z = 2.2$ MZR, in this case, has a shallower slope. We find agreement between our MZR and those predicted from various galaxy evolution models and simulations. Addi-

tionally, we explore the extended fundamental metallicity relation (FMR), which includes an additional dependence on SFR. Our results consistently support the existence of the FMR, as well as revealing an offset of 0.28 ± 0.04 dex in metallicity compared to locally derived relationships, consistent with previous studies at similar redshifts. We interpret the negative correlation with SFR at fixed mass, inferred from the existence of an FMR for our sample, as being caused by the efficient accretion of metal-poor gas fuelling star formation at Cosmic Noon.

2.1 Introduction

Analysis of the relationship between a galaxy's stellar mass and its gas-phase metallicity (the mass–metallicity relation, MZR) is a key diagnostic of galaxy evolution, reflecting the complicated interplay between the formation and enrichment of stars and the inflow and outflow of gas in galaxies. The MZR shows that as stellar mass increases, galaxies have enhanced metallicities, with some studies finding the relation flattening at higher masses (e.g. Tremonti et al. 2004; Stott et al. 2013b; Zahid et al. 2014; Curti et al. 2020a). The MZR has been studied in the literature for decades. A similar relation to the MZR, showing a correlation between the magnitude of a galaxy and its gas-phase metallicity, was first observed in the 1970s (Lequeux et al. 1979; Garnett & Shields 1987). Magnitude was used as a substitute for stellar mass in these early works because of the difficulty in obtaining accurate mass values. Following influential works on stellar population synthesis (e.g. Charlot & Longhetti 2001; Bruzual & Charlot 2003) and stellar mass determination (e.g. Kauffmann et al. 2003; Chabrier 2003), the MZR has now been fully established in later studies up to at least $z \sim 3.5$ (e.g. Tremonti et al. 2004; Erb et al. 2006a; Mannucci et al. 2010; Stott et al. 2013b; Zahid et al. 2014; Ly et al. 2016; Wuyts et al. 2016; Brown et al. 2018; Torrey et al. 2019; Sanders et al. 2021; Suzuki et al. 2021; Wang et al. 2022; Sextl et al. 2023; Langan et al. 2023), as well as the stellar mass–stellar metallicity relation (Cullen et al. 2019, 2021; Kashino et al. 2022). See Maiolino & Mannucci (2019) and references therein for a comprehensive review of the MZR.

The MZR has been extended to include a dependence on SFR. This three dimensional relationship has been called the fundamental metallicity relation (FMR) and was initially discussed by Ellison et al. (2008), before being expanded upon and fully proposed by Mannucci et al. (2010; see also Lara-López et al. 2010). The FMR suggested by Mannucci et al. (2010) defines a tight relationship that shows gas-phase metallicity strongly decreasing with increasing SFR for low-mass galaxies, but no SFR-dependence on metallicity for high-mass galaxies. Unlike the MZR, there is more debate surrounding the form, and even the existence of, the FMR in galaxies. Sánchez et al. (2013) studied the MZR and FMR using the Calar Alto Legacy Integral Field Area (CALIFA) survey (Sánchez et al. 2012) and found that their results contradicted those of Mannucci et al. (2010; see also Sánchez et al. 2017). Additionally, Barrera-Ballesteros et al. (2017) found no strong relationship between the MZR with SFR (or specific SFR; sSFR) from the Mapping Nearby Galaxies at APO (MaNGA) survey (Bundy et al. 2015; Wake et al. 2017), particularly at low SFRs. However, many other studies have observed a form of the FMR in SF galaxies at higher redshifts, with suggestions of a redshift evolution compared to local SDSS (York et al. 2000; Adelman-McCarthy et al. 2006; Abazajian et al. 2009) galaxies. As well as finding a strong relationship in SDSS galaxies, Mannucci et al. (2010) analysed the FMR in higher z galaxies from the literature. From their results, they suggest that the FMR exists, but does not evolve, out to $z \sim 2.5$ for galaxies of any stellar mass and SFR, but a large offset from the trend was found for a sample of $z \sim 3.3$ galaxies from Maiolino et al. (2008) and Mannucci et al. (2009). Mannucci et al. (2011) built upon the work done by Mannucci et al. (2010) and found a new form of the FMR that extends smoothly down to lower mass SDSS galaxies ($10^{8.3}\,\mathrm{M}_{\odot}$, down from a previous minimum of $\approx 10^{9.2}\,\mathrm{M}_{\odot}$) by studying the properties of long gamma-ray burst hosts. Utilising the grism technology of *HST* in the 3D–HST survey (Brammer et al. 2012), Cullen et al. (2014) found the FMR in their $z \sim 2.16$ galaxies but they were offset from the Mannucci et al. (2010) FMR by 0.3 dex, suggesting that an evolution in the ionisation conditions between the redshifts of the samples affected the metallicity calibrations, and that the choice of metallicity indicator may affect measured values of gas-phase metallicity (see also Teklu et al. 2020 for the latter conclusion). More recently, Li

et al. (2023) used the capabilities of *JWST* to study the MZR in dwarf galaxies between $2 < z < 3$ and found the FMR exists for a mass range 10^6–$10^{10}\,M_\odot$ in a marginally different form than observed by Mannucci et al. (2010), but one that is in close agreement with other studies at this redshift (e.g. Sanders et al. 2021). Evidence is increasing that the MZR does have a secondary dependence with SFR (e.g. Yates et al. 2012; Andrews & Martini 2013; Stott et al. 2013b; Salim et al. 2014, 2015; Cresci et al. 2019; Curti et al. 2020a; Baker et al. 2022; Schaefer et al. 2022). The FMR provides a more complete picture of the processes that regulate galaxy evolution, as it accounts for the fact that there is a relationship between SFR and gas-phase metallicity at a fixed stellar mass. Further investigation of the FMR is paramount for understanding the complex mechanisms that link star formation and chemical evolution in galaxies.

The origins of the MZR and FMR are still not fully understood, and several models have been proposed to explain their existence. These include inflows and outflows of both metal-enriched (Edmunds 1990; Spitoni et al. 2010, 2017; Saracco et al. 2023) and metal-poor, potentially pristine, gas (Finlator & Davé 2008; Davé et al. 2010; Jimmy et al. 2015), as well as feedback from SNe (Sakstein et al. 2011; Collacchioni et al. 2018) and AGN (Torrey et al. 2019; van Loon et al. 2021; Yang et al. 2022). Additionally, recent observations and simulations have suggested that the MZR also has a secondary dependence on gas mass (Brown et al. 2018; De Lucia et al. 2020), with some claiming that it is the more fundamental property linked to mass and gas-phase metallicity, and that SFR is simply a tracer for gas mass in the FMR (Scholte & Saintonge 2022). In particular, studies have suggested that the secondary dependence is with H I mass or neutral gas fraction, as the relationship between gas-phase metallicity and SFR could be a by-product of the dependence on gas density via the Kennicutt–Schmidt relation (Bothwell et al. 2013; Lagos et al. 2016; De Rossi et al. 2017). Recently, however, Baker & Maiolino (2023) conclude that it is in fact stellar mass that is the primary property that drives the gas-phase metallicity in galaxies, ahead of any other galaxy property including SFR, velocity dispersion and dynamical mass. Furthermore, they find that not only does gas-phase metallicity have no other significant dependence when stellar mass is included, it potentially has

an anti-correlation with dynamical mass at fixed stellar mass once the primary dependence has been accounted for.

The evolution of the MZR and FMR with redshift is an active area of research, as it can provide insights into the formation and evolution of galaxies during certain epochs of the Universe's lifetime. Several studies have investigated this and the results are mixed. Both Savaglio et al. (2005) and Erb et al. (2006a) found offsets from the MZR in $1 < z < 2$ galaxies compared to the local $z \sim 0.1$ MZR suggested by Tremonti et al. (2004). Similar offsets from local calibrations have been reported in many later studies (e.g. Maiolino et al. 2008; Curti et al. 2022). Given the proposed existence of the FMR (see above), Baker & Maiolino (2023) suggest that any offset likely arises from the fact that the MZR is tracing the SFR evolution with redshift (Madau & Dickinson 2014). However, as previously mentioned, Mannucci et al. (2010) found no redshift evolution in the FMR out to $z \sim 2.5$ but a large offset for their $z > 3$ sample, whereas Cullen et al. (2014) did find an offset at $z \sim 2.16$. Results from other studies have shown that there is no evolution in the FMR out to $2.0 \lesssim z \lesssim 2.5$ (e.g. Henry et al. 2013; Barrera-Ballesteros et al. 2017), and others find only a mild evolution with redshift (e.g. Baker et al. 2022).

Some studies suggest any perceived evolution in the FMR toward higher redshifts is a result of the choice of metallicity calibration, specifically those developed using samples of low-z galaxies that may not be applicable for sources at high-z. Many of these calibrations use emission line diagnostics (Maiolino et al. 2008; Dopita et al. 2016; Bian et al. 2018). In their review on the use of emission lines to study galaxy evolution, Kewley et al. (2019) emphasise the need for reliable emission line diagnostics to accurately determine fundamental properties of galaxies, including their metallicities. Some of the challenges they discuss include the limited number of emission lines available to some studies, the changing ionisation structure of H II regions and the ISM, and contamination from shock excitation (see Kewley et al. 2019 for a detailed review). Some studies have sought to develop metallicity calibrations that are independent of these problems, such as Dopita et al. (2016) who developed a calibration that relies only on [N II]6585, [S II]6717, 6732 and Hα emission lines which relieves the issues caused by ISM pressure and ionisation parameter. Cullen et al. (2014) concluded

that offsets from the FMR of their sample mentioned above are likely down to the empirical Maiolino et al. (2008) metallicity calibrations — derived from local SDSS galaxies — not being applicable for their $z \gtrsim 2$ sample, as they do not account for changes in ionisation conditions in SF galaxies. Recently, Garg et al. (2024) used the SIMBA hydrodynamical cosmological galaxy formation simulations (Davé et al. 2019) and photoionisation modelling (Ferland et al. 2017; Garg et al. 2022) to analyse the redshift evolution of a number of emission line ratios used as metallicity indicators. They found that all of the emission lines they study, which are typically calibrated on $z = 0$ populations of galaxies, do have some evolution with redshift, suggesting that as the galactic properties they use in their models evolve with redshift, they have a discernible impact on the line ratios. Further studies have found that metallicities of high-z SF galaxies derived using locally calibrated strong-line diagnostics are offset from the tight sequence defined in the Baldwin–Phillips–Terlevich (BPT; Baldwin et al. 1981) diagram of galaxies at the same redshift. This suggests a systematic discrepancy arising from the choice of calibration (Steidel et al. 2014; Shapley et al. 2015; Bian et al. 2018).

The work in this chapter aims to contribute to our understanding of the MZR and FMR by exploring them in a sample of SF galaxies at $1.99 < z < 2.32$ ($z_{\rm median} = 2.16$) using NIR *HST* grism data from the Quasar Sightline and Galaxy Evolution (QSAGE) survey (Bielby et al. 2019). The QSAGE survey was designed to obtain hundreds of galaxy redshifts by centering *HST*/WFC3 on 12 known quasars, all of which had pre-existing *HST* UV spectra. Focussing on quasar sightline-selected fields allows the circumgalactic medium (CGM) of galaxies that are not subject to any selection effects to be studied in detail (Bielby et al. 2019). These data can be used to further develop models of galaxy feedback and fuelling mechanisms associated with the CGM (see e.g. Bielby et al. 2017) and investigate the effect of galaxy environments on the CGM (see e.g. Dutta et al. 2021). However, in this chapter, we study galaxies that are generally at higher z than the quasars.

This chapter is arranged as follows. In Chapter 2.2, the QSAGE survey is described and the sample used for this work, including how the data was reduced, is explained in detail. The methods for determining galaxy properties, namely

stellar mass values (Chapter 2.2.3.1) and SFRs (Chapter 2.2.3.2), can be found in Chapter 2.2.3. Chapter 2.3 provides an overview of the Mass–Excitation diagram, which was used to distinguish between AGN and SF galaxy populations. Details on the metallicity calibrations used for our sample of galaxies, namely those from Maiolino et al. (2008) and Bian et al. (2018), are found in Chapter 2.4.1 and 2.4.2 respectively. The results are outlined in Chapter 2.5. Discussion and conclusions are summarised in Chapter 2.6.

A standard ΛCDM cosmology model is assumed with values $\Omega_\Lambda = 0.7$, $\Omega_m = 0.3$, $H_0 = 70\,\mathrm{km\,s^{-1}\,Mpc^{-1}}$. Any magnitudes stated are presented using the AB system. All results and models in this chapter assume a Chabrier (2003) IMF throughout and any comparison results that use a different IMF (i.e. Salpeter 1955; Kroupa 2001) are converted accordingly.

2.2 Sample and Data

2.2.1 QSAGE

The data used for the analysis in this chapter are from the QSAGE survey (*HST* Cycle 24 Large Program 14594; PIs: R. Bielby, J. P. Stott; see Bielby et al. 2019 and Stott et al. 2020). The QSAGE survey's main science goal was to obtain redshifts for galaxies along the lines-of-sight to quasars with pre-existing UV spectra in a redshift range $1.2 < z < 2.4$, with the main aim of analysing the galaxies' CGM. The survey utilised the capabilities of *HST*/WFC3, particularly the IR G141 grism, which provides useful spectra in the range of $\lambda = 10\,750$–$17\,000\,\text{Å}$, and also imaging from the F140W and F160W filters with spectral ranges of $\lambda = 11\,854$–$16\,129\,\text{Å}$ and $\lambda = 13\,854$–$16\,999\,\text{Å}$ respectively. Each target quasar field was observed with 16 grism exposures lasting approximately 1000 seconds, as well as eight $\approx 250\,\text{s}$ exposures in both the F140W and F160W filters, across a total of eight *HST* orbits. The G141 grism observations are the primary focus of the survey, as they provide spectroscopic data for potentially hundreds of objects simultaneously, allowing for analysis of both foreground and background galaxies around the target quasar. Imaging data, mainly from the

Table 2.1: The QSAGE sample. Field Name is the name of the central quasar of each observation but here refers to the target field for the SF galaxies. The right ascension (R.A.) and declination (Dec.) of the target quasar are derived by Stott et al. (2020). The number of $z \sim 2.2$ SF galaxies in each field (No. SF Galaxies) refers to the number of objects within the completeness limits of the sample that are deemed to satisfy the definition of SF via the Coil et al. (2015) Mass–Excitation diagram diagnostic (see Chapter 2.3).

Field Name	R.A.	Dec.	No. SF Galaxies	SF Galaxies z Range
QSO-J1130-1449	11:30:07.1	-14:49:27.4	3	2.29–2.32
LBQS-1435-0134	14:37:48.3	-01:47:10.8	8	2.00–2.23
QSO-B1521+1009	15:24:24.5	+09:58:29.1	11	2.03–2.28
QSO-B1634+7037	16:34:29.0	+70:31:32.4	3	2.16–2.17
PKS-0232-04	02:35:07.3	-04:02:05.3	5	2.18–2.32
QSO-B1630+3744	16:32:01.1	+37:37:50.0	4	2.06–2.21
PG0117+213	01:20:17.3	+21:33:46.2	3	2.12–2.13
QSO-B0810+2554	08:13:31.3	+25:45:03.1	5	2.15–2.30
HE0515-4414	05:17:07.6	-44:10:55.6	5	1.99–2.30
2QSO-B0747+4259	07:50:54.6	+42:52:19.3	3	2.02–2.26
QSO-J1019+2745	10:19:56.6	+27:44:01.7	12	2.02–2.24
QSO-B1122-168	11:24:42.9	-17:05:17.4	5	2.03–2.16

F140W filter which has a similar spectral range to G141, is used to provide source coordinates for extracting the object spectra. As grism spectra will inevitably include contamination from nearby sources, the survey includes four separate *HST* roll angles for the grism observations as well as a quantitative estimate of the contamination for each source using GRIZLI[1] (Brammer 2023). Table 2.1 includes the location of the quasar fields in the QSAGE survey and an upper limit on the number of $z \sim 2.2$ SF galaxies found in the images of each (see Chapter 2.3 for explanations of "upper limit" and what defines an SF galaxy in this work).

2.2.2 Sample Selection

In order to select only those $z \sim 2.2$ objects relevant to the analysis in this work, the following criteria must be met:

1. The objects are primarily selected based on their [O III]5007 emission flux. This was chosen as the primary selection criterion because this line is much stronger compared to other lines at the target redshift of this chapter (namely

[1] https://github.com/gbrammer/grizli

[O II]3727 and Hβ). Therefore the objects must have a clean spectrum with [O III]5007 coverage. Given the need for multiple emission lines to determine gas-phase metallicity and distinguish ionisation processes, objects must also have a spectroscopic [O III]5007 redshift that puts [O II]3727 and Hβ within the wavelength range of the G141 grism. The definition of "clean spectrum" is explained by Stott et al. (2020) as being galaxies with a "quality flag" of 3 or 4. As defined in Stott et al. (2020), "3" is a good quality spectrum with at least one spectral line having signal-to-noise ratio (SNR) > 3, and "4" is a spectrum with lines that have SNR > 10. This cut was necessary in order to make sure that any emission line of an object could be reliably used when calibrating its gas-phase metallicity and used in ionisation mechanism diagnostics (see Chapter 2.3).

2. Additionally, objects must have an [O III]5007 emission line flux with a SNR ≥ 3. SNR here is defined as the [O III]5007 flux value over the flux error.

These selection criteria cut the original sample of 1953 objects down to 153. It was clear, however, that this new sample was incomplete for lower valued bins in both [O III]5007 flux and stellar mass, so an additional completeness limit was then applied to this sample of 153 objects. In this case, that was any object with $\log_{10}(f([\mathrm{O\,III}]5007)\,\mathrm{erg\,s^{-1}\,cm^{-2}}) \gtrsim -16.2$ and $\log_{10}(M_*/M_\odot) \gtrsim 9.4$, which are the lower values of the most occupied bin in each property (see Figures 2.1 and 2.2). The stellar mass and [O III]5007 flux distributions of this sample of selected objects, as well as the completeness limits, can be seen in Figures 2.1 and 2.2 respectively. Statistical analysis found that both the stellar mass and [O III]5007 flux cuts represent a $\sim 95\%$ completeness limit of the original sample. After applying these, there were 92 objects in total for analysis within a redshift range of $1.99 \lesssim z \lesssim 2.32$.

2.2.3 Galaxy Properties

2.2.3.1 Galaxy Stellar Mass Calibration

The QSAGE masses are inferred using an approximation based on their apparent magnitude in the IR. For this study, the calibrations from Stott et al. (2020) are

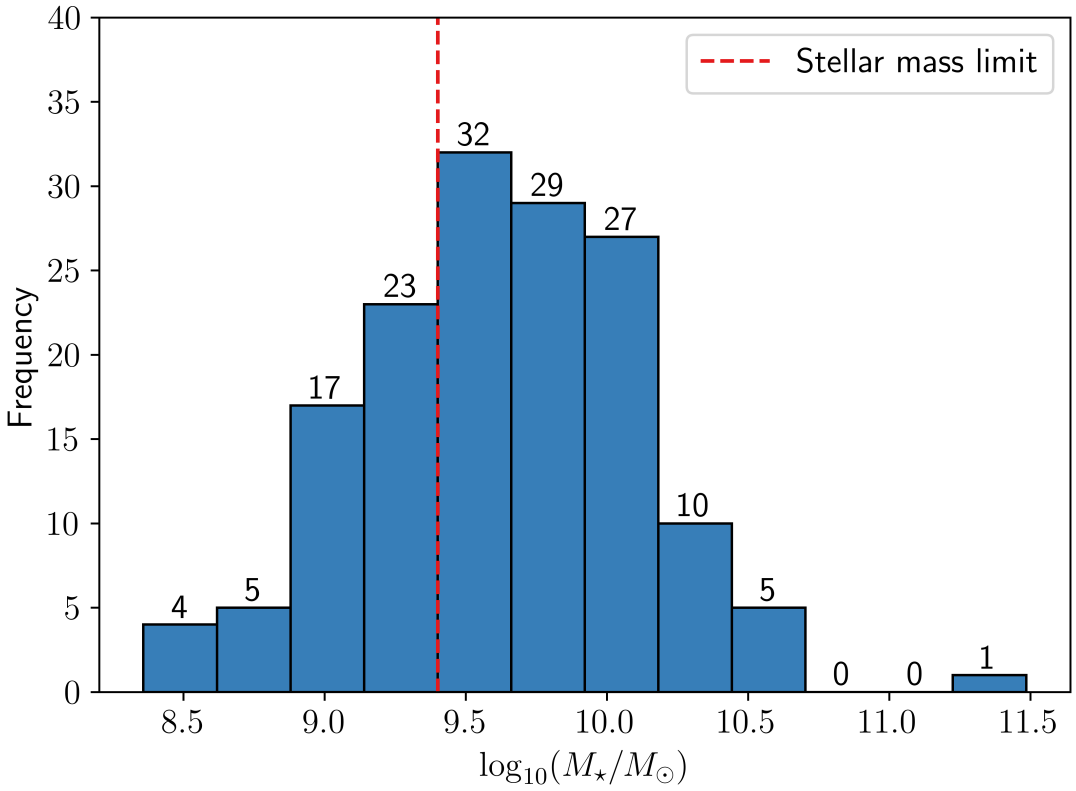

Figure 2.1: The stellar mass distribution of the objects that met the selection criteria in Chapter 2.2.2, where the red dashed line indicates the approximate mass-complete limit of the sample ($\sim 10^{9.4}\,\mathrm{M}_\odot$). The numbers above each bin indicate the number of objects that occupy that bin.

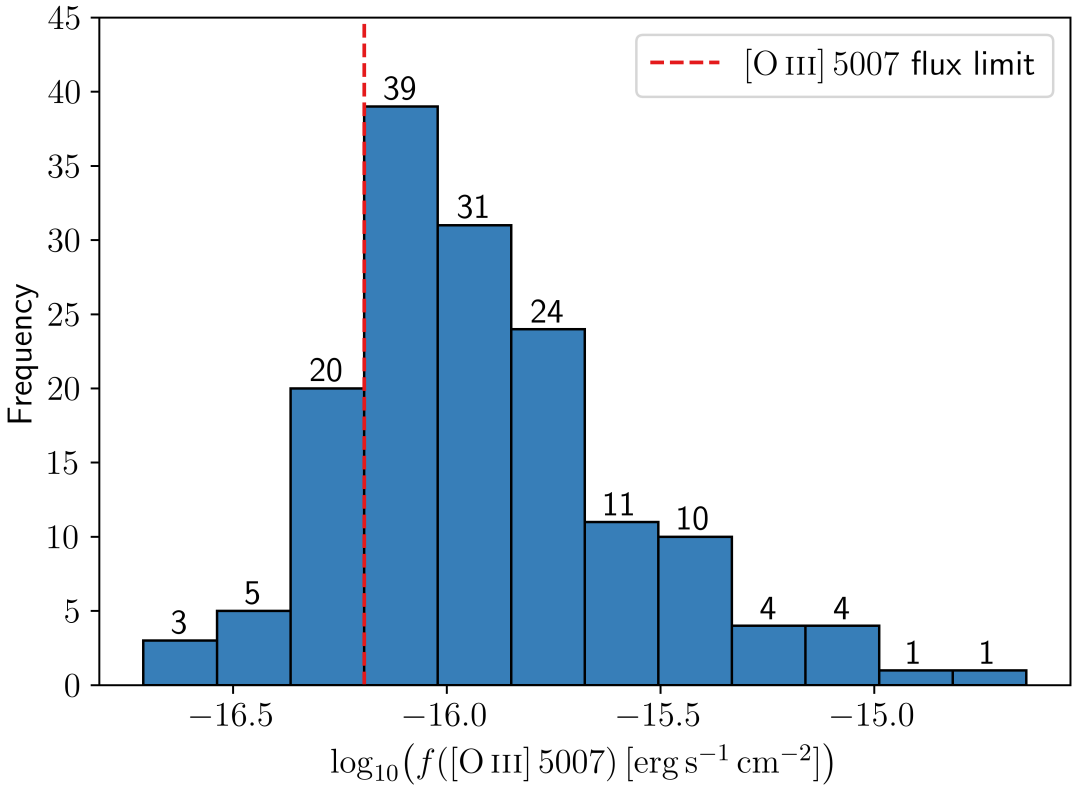

Figure 2.2: The [O III]5007 flux distribution of the objects that met the selection criteria in Chapter 2.2.2, where the red dashed line indicates the flux-complete limit of the sample ($\sim 10^{-16.2}\,\mathrm{erg\,s^{-1}\,cm^{-2}}$). The numbers above each bin indicate the number of objects that occupy that bin.

used. They found linear relationships between stellar mass and F160W magnitude at different redshifts based on galaxies from the Cosmic Assembly Near-infrared Deep Extragalactic Legacy Survey (CANDELS; Barro et al. 2019). They derive the relationships in individual redshift bins of $\Delta z = 0.1$. The parameters they use can be found in Table A1 of their paper. Of the 92 objects in our complete sample, two do not have F160W coverage (both found in the QSO-J1130-1449 field). The F160W magnitudes for these two objects were estimated based on a linear fit between the F140W and F160W magnitudes of all the $z \sim 2.2$ objects with spectra flagged as "good".

As described above, Stott et al. (2020) demonstrate a strong correlation between F160W and full spectral energy distribution (SED) stellar mass for SF galaxies in the CANDELS survey. In the absence of deep homogeneous data across all 12 of the QSAGE fields, we chose to use this F160W magnitude calibration (corresponding to rest-V-band). This is redward of the 4000 Å break and is therefore less affected by ongoing SF than shorter wavelengths. The primary samples we use to analyse the MZR and FMR are all SF galaxies, which means they will all have similar mass-to-light ratios. We fully account for the scatter in the Stott et al. (2020) relationship in our stellar mass errors (the typical error on stellar mass can be seen in the lower right corner of Figure 2.5).

2.2.3.2 Determining SFRs

The FMR describes the dependence of gas-phase metallicity on both stellar mass and SFR (Ellison et al. 2008; Mannucci et al. 2010). In order to analyse the FMR using the samples in this work, the SFRs of each galaxy are required. The SFRs were calculated using the Kennicutt (1998) calibrations, with conversion from a Salpeter (1955) to a Chabrier (2003) IMF by dividing the resulting SFRs by a conversion factor of 1.59 (Madau & Dickinson 2014). SFRs were calculated using the Hβ line luminosity, with the commonly adopted conversion factor of Hα/Hβ = 2.86 (Gaskell & Ferland 1984; Osterbrock & Ferland 2006) used to estimate the corresponding Hα luminosity. The theoretical value of the Balmer decrement, Hα/Hβ = 2.86, is used because the spectra in our sample do not have Hα coverage at these redshifts. The emission line luminosity was extinction

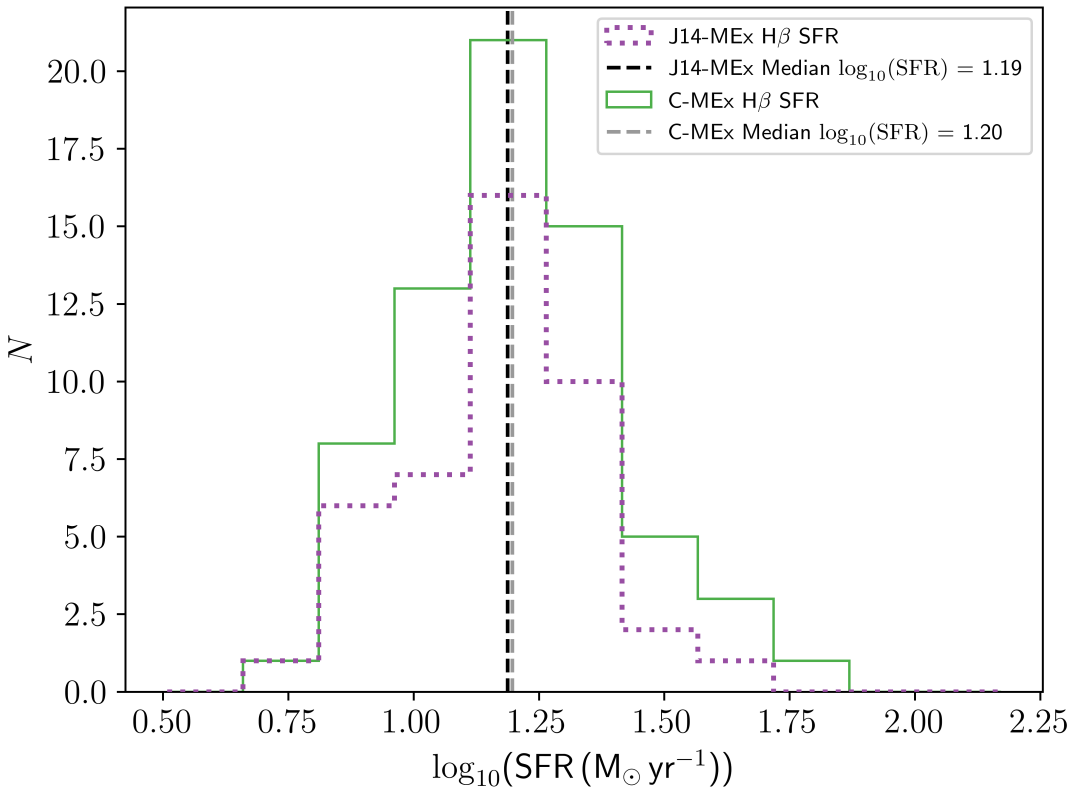

Figure 2.3: The SFR distribution of our complete J14–MEx (purple dotted histogram) and C–MEx (solid green histogram) SF galaxy samples. The dashed black line indicates the median SFR of our J14–MEx sample, and the grey dashed line shows the median SFR of the C–MEx sample. The SFR distributions were derived using the Hβ emission line flux (Kennicutt 1998).

corrected assuming $A_V = 1$, which, based on the properties of our sample, was most appropriate following the extinction relationships of Sobral et al. (2012). This single attenuation correction is a simplification, since A_V is expected to vary between galaxies and may correlate with properties such as stellar mass and SFR (e.g. Garn & Best 2010; Zahid et al. 2013). This assumption enters not only the dust correction applied to the Hβ-based SFRs, but also, where relevant, any metallicity diagnostics involving ratios of emission lines separated significantly in wavelength. While adopting a single A_V value is necessary given the available wavelength coverage, which prohibits direct Balmer decrement measurements for individual galaxies, it may introduce additional systematic uncertainty into the inferred SFRs and metallicities, and therefore into the derived scaling relations. In order to correct for underlying stellar absorption, Hβ flux values were boosted by 3%, in line with other studies into the FMR (Henry et al. 2013; Cullen et al. 2021; Sanders et al. 2021; Curti et al. 2022). These SFRs, calculated using the Hα calibration from Kennicutt (1998), will be referred to as Hβ SFR hereafter. The SFR distribution of our sample can be found in Figure 2.3.

Figure 2.4 shows the correlation between SFR and stellar mass for individual SF galaxies in our sample. The grey dashed line shows the "UV+IR/IR SFRs" SF main sequence from Speagle et al. (2014) evaluated at the median redshift of our sample ($z_{\mathrm{median}} = 2.16$), with the grey shaded region indicating the scatter based on the errors on their relationship. From Figure 2.4, our sample is consistent with the main sequence from Speagle et al. (2014).

2.3 Mass–Excitation Diagram

The selection criteria listed in Chapter 2.2.2 do not distinguish between object spectra that belong to an AGN or those that belong to SF galaxies — the primary target of the analysis in this chapter. Therefore, diagnostics to differentiate the two populations must be employed so as to not contaminate the sample. Traditionally, researchers have used BPT diagrams (Baldwin et al. 1981) to distinguish between AGN and SF galaxies. These diagrams use different emission line ratios to distinguish the ionisation mechanism of gas in the ISM. However, as previously

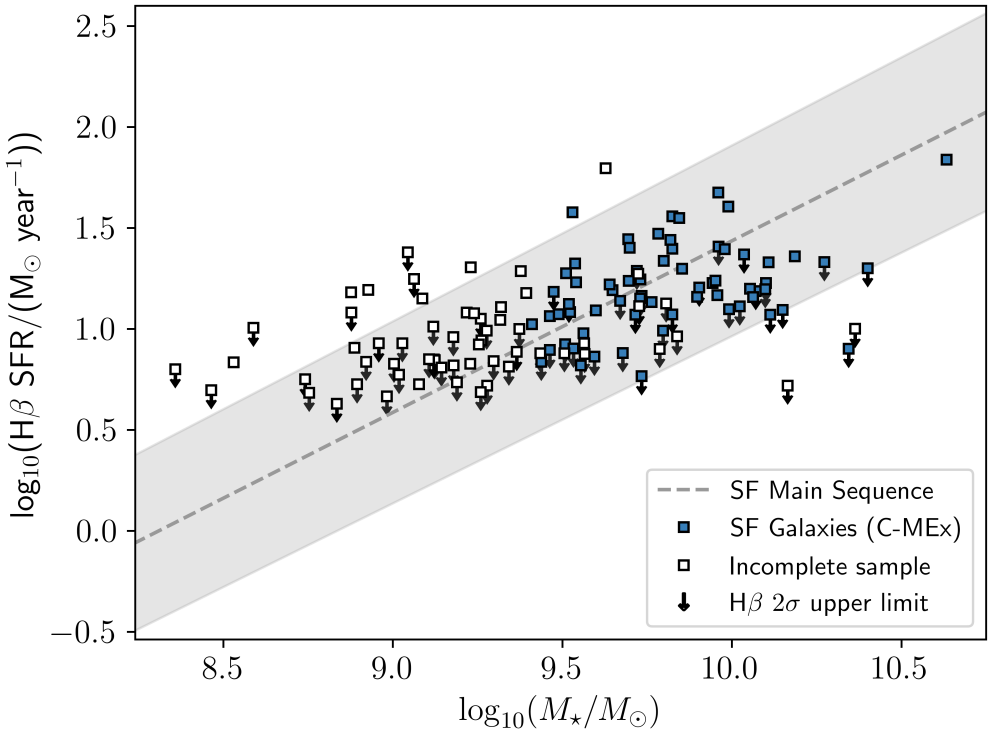

Figure 2.4: The relationship between stellar mass and SFR for the SF galaxies in our C–MEx sample. The grey dashed line shows the "UV+IR/IR" SF main sequence from Speagle et al. (2014) evaluated at the median redshift of our sample ($z_{\mathrm{median}} = 2.16$), with the grey shaded region indicating the scatter around the fit based on the errors of their equation. The blue squares show the individual galaxies in the mass and flux complete sample of our work, with white squares showing SF galaxies in the incomplete sample.

discussed, the emission lines used in our analysis are [O III]4959, 5007, [O II]3727 and Hβ and therefore no form of BPT diagram can be used to categorise these populations.

Juneau et al. (2011) showed that comparing the line ratio [O III]5007/Hβ (hereafter O3) against the total stellar mass of a galaxy successfully distinguishes between ionisation from AGN and that from active star formation. They termed this the Mass–Excitation (hereafter MEx) diagram, and demonstrated that BPT–SF and BPT–AGN classifications are well separated in this plane. They further showed that BPT–composites (populations that have some combination of SF and AGN contributions) are reasonably well-defined in a central region known as "MEx-intermediates". The distinct classes in the MEx diagram come from two empirical curves that maximise this separation. However, Juneau et al. (2011) notes that this diagnostic was only applied at intermediate redshifts ($0.3 < z < 1$) and may not be accurate for higher redshift samples. Studies have found that the Juneau et al. (2011) MEx diagram (hereafter J11–MEx) does hold up to $z \lesssim 1.6$ (e.g. Juneau et al. 2013; Trump et al. 2013), but it generally fails at accurately distinguishing SF galaxies from AGN at $z \sim 2$ (e.g. Newman et al. 2013; Henry et al. 2013).

While Juneau et al. (2011) used a SNR criterion that applied to the individual emission lines (requiring SNR > 3 on all the lines), Juneau et al. (2014) developed a new MEx diagram (hereafter J14–MEx) which instead requires all *line ratios* to have a SNR $> 3/\sqrt{2} \approx 2.12$ (equivalent to an average 3σ detection at the lower limit for the individual lines in the ratio), resulting in a 20% larger sample. Additionally, Juneau et al. (2014) make use of SDSS DR7 (Abazajian et al. 2009) for their low redshift sample, rather than SDSS DR4 (Adelman-McCarthy et al. 2006) used for the original J11–MEx. However, the most important update to the J14–MEx is its application to higher redshift samples ($z \gtrsim 2$) by taking into account the evolution of galaxy populations, in particular the fading of the luminosity function of emission-line galaxies toward lower redshifts (e.g. Colbert et al. 2013; Khostovan et al. 2015; Hayashi et al. 2020). They find that as the cut-off line luminosity is raised, the split between AGN and SF galaxies occurs at higher masses and so they employ a mass-offset as a function of the threshold line luminosity of a sample following the form

$$\Delta \log_{10}(M_*/M_\odot) = a_0 + a_1 \arctan\Big[\Big(\log_{10}(L_{\rm threshold}) - a_2\Big)a_3\Big]\,,$$

with coefficients {0.28988, 0.28256, 40.479, 0.82960}. Using the line flux limit of the QSAGE survey ($f > 2{\times}10^{-17}\,\mathrm{erg\,s^{-1}\,cm^{-2}}$; Bielby et al. 2019) and the median redshift of our complete sample ($z \sim 2.16$), the mass offset on the J14–MEx for this sample is $\Delta \log_{10}(M_*/M_\odot) \approx 0.25$ which agrees with offsets calculated by other studies with similar flux limits and redshifts (e.g. Coil et al. 2015).

This mass shift of 0.25 dex may be insufficient to clearly separate high-z AGN and SF galaxies, despite the prescriptions in Juneau et al. (2014). Coil et al. (2015) also found a shift of 0.25 dex to the MEx diagram for their sample but found that this shift still leaves many known SF galaxies in the AGN region (see their Figure 5). Instead, Coil et al. (2015) found that a shift of $\Delta \log_{10}(M_*/M_\odot) = 0.75$ is needed and results in all ten of their X-ray and IR-selected AGN being consistent with occupying the AGN region of the J14–MEx diagram. They note that other studies with samples at a similar redshift (e.g. Newman et al. 2013; Price et al. 2014) found that a similarly substantial shift of 0.75 dex is needed for the original J11–MEx, suggesting the prescriptions in Juneau et al. (2014) are generally insufficient for samples at $z \gtrsim 2$. For completeness, the analysis of the MZR and FMR in this study will look at samples of SF galaxies determined using both a 0.25 dex and 0.75 dex shift to the Juneau et al. (2014) prescriptions (43 and 67 SF galaxies respectively), with the primary focus being on the Coil et al. (2015) 0.75 dex shift (hereafter the C–MEx sample). Figure 2.5 shows the MEx diagram for the sample of objects in this chapter with both the shifted Juneau et al. (2014) and Coil et al. (2015) curves discussed in this chapter highlighted. For the purposes of this chapter, an object was considered a SF galaxy if it was below the upper solid line of the empirical curves, including those that would otherwise be considered as MEx-intermediates. We used a 2σ upper limit on the value of Hβ here (lower limit on O3) where the SNR < 2, which means the number of SF galaxies determined via this method is also an upper limit.

The stellar mass range of our J14–MEx sample of 43 SF galaxies is $\mathrm{M_*} = 10^{9.41}$–$10^{10.19}\,\mathrm{M_\odot}$ (median stellar mass $\mathrm{M_*} = 10^{9.70}\,\mathrm{M_\odot}$), and the range for our C–MEx sample of 67 SF galaxies is $\mathrm{M_*} = 10^{9.41}$–$10^{10.63}\,\mathrm{M_\odot}$ (median stellar mass $\mathrm{M_*}$

$= 10^{9.80}\,M_\odot$). The SFR range of our J14–MEx sample is 5.8–37.7 $M_\odot\,yr^{-1}$ (median SFR of 15.4 $M_\odot\,yr^{-1}$), and the range for our C–MEx sample is 5.8–68.9 $M_\odot\,yr^{-1}$ (median SFR of 15.7 $M_\odot\,yr^{-1}$).

2.4 Determining Gas-phase Metallicity

Gas-phase metallicity at high redshifts ($z > 1$) could only be properly determined using strong-line metallicity diagnostics, as measurements of the electron temperature (T_e, often used to directly measure metallicities in local galaxies) become difficult due to the faintness of temperature sensitive emission lines (Sanders et al. 2020). However, the resolution and spectroscopic capabilities of *JWST* are now making this possible (e.g. Curti et al. 2022; Sanders et al. 2024), meaning studies using it will not necessarily have to rely on strong-line calibrations to measure the metallicity of these high-z galaxies. Strong-line diagnostics follow the relationship between optical emission line ratios and the abundance of heavy elements in a galaxy. It is important to note that analysis into the MZR (or other metallicity relations) is strongly dependent on the choice of calibration as it can result in significantly different curve shapes and intercepts (see Kewley & Ellison 2008 for a detailed review). It is therefore crucial to use the same metallicity calibration as those comparison studies. Here, two key calibrations are adopted for analysing the MZR and FMR. They are the calibration curves from Maiolino et al. (2008), who developed strong-line relations from a combination of metallicities measured using the T_e method in Nagao et al. (2006) and photoionisation models on SDSS DR4 galaxies (Adelman-McCarthy et al. 2006), and those from Bian et al. (2018) who developed empirical calibrations from local galaxies with properties analogous to galaxies at $z \sim 2$.

2.4.1 Maiolino et al. (2008) Calibrations

The Maiolino et al. (2008) calibrations were needed in order to compare the MZR and FMR determined for our sample to those by Mannucci et al. (2010) and Cullen et al. (2014). As described above, Maiolino et al. (2008) used a

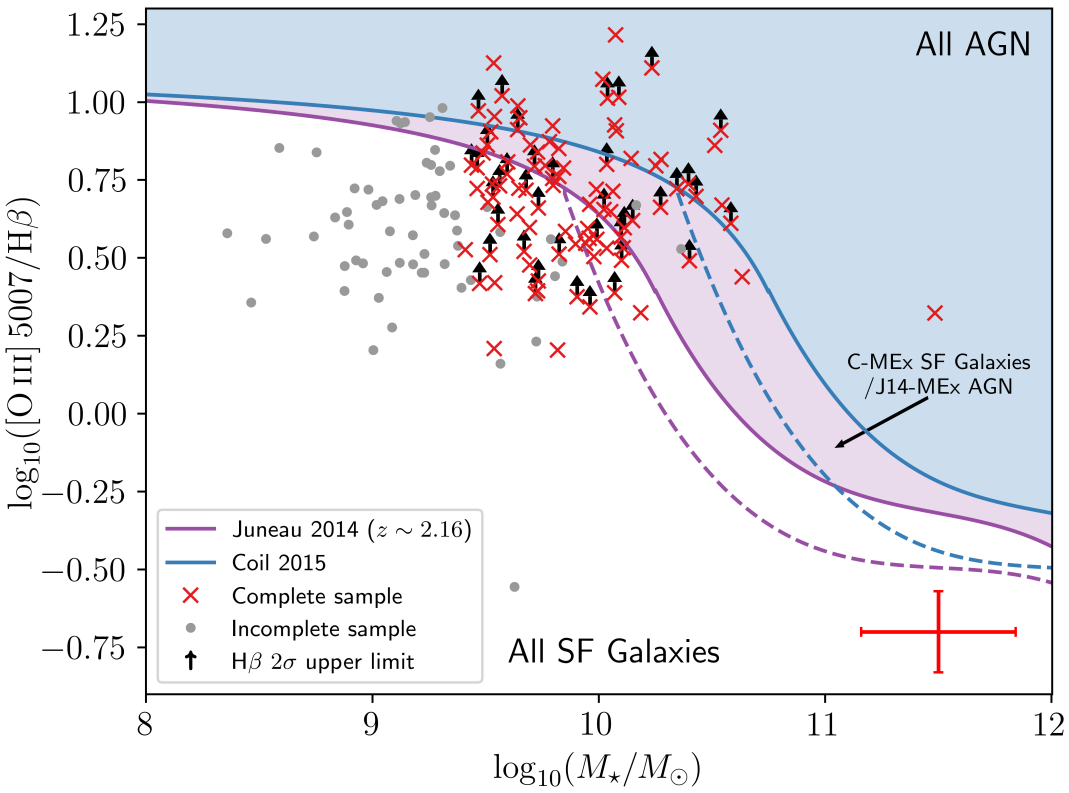

Figure 2.5: The Mass–Excitation diagram used to distinguish between ionisation from AGN and that from star formation. The red crosses are objects that lie within the completeness limits of both stellar mass and [O III]5007 flux, while grey points lie outside of one or both limits. Black arrows indicate objects in our complete sample that have an Hβ upper limit (lower limit on O3). Both of the curves show the MEx prescriptions used to distinguish ionisation processes for our sample, namely the mass-shifted (0.25 dex) Juneau et al. (2014) curve that is more applicable to higher redshifts (purple), and the Coil et al. (2015) curve (blue) that shifted the Juneau et al. (2014) curve further (0.75 dex). The area in between the dashed and solid curves indicates a population of "MEx-intermediates" where there is some combination of SF and AGN activity (analogous to BPT-composites which are reasonably well-defined in this region). For our samples, we considered these MEx-intermediates to be SF galaxies. Objects occupying the unshaded region below the solid Juneau et al. (2014) MEx curve are always considered SF galaxies, and objects occupying the blue shaded region above the solid Coil et al. (2015) MEx curve are always considered AGN. In the purple shaded region between the two curves, objects are considered to be SF galaxies for the C–MEx diagnostic (because they lie below the solid blue curve), but are considered to be AGN for the shifted J14–MEx (because they lie above the solid purple line). The red error bars in the bottom-right corner show the typical errors of the objects.

combination of directly measured metallicities via the T_e method and photoionisation models. However, it is well documented that the T_e method fails at high metallicities (reliable for $12 + \log_{10}(\mathrm{O/H}) \lesssim 8.3$, see Stasińska 2005; Bresolin 2007) as a result of temperature fluctuations. Photoionisation models are also prone to systematic effects as well as high uncertainties and often do not reliably reproduce expected trends at low metallicities (e.g. Dopita et al. 2006; Dors Jr et al. 2011). Therefore, Maiolino et al. (2008) combines a low-metallicity sample from Nagao et al. (2006) that used direct gas-phase metallicity measurements via T_e, and a high-metallicity sample using galaxies from SDSS DR4 (Adelman-McCarthy et al. 2006) with the photoionisation models described in Kewley & Dopita (2002). They then fitted polynomial curves to various strong-line ratio relationships against gas-phase metallicity after binning the galaxies in $\sim 0.1\,\mathrm{dex}$ metallicity bins. The key relationships for our sample were those using $R_{23} = ([\mathrm{O\,III}]5007 + [\mathrm{O\,III}]4959 + [\mathrm{O\,II}]3727)/\mathrm{H}\beta$, $[\mathrm{O\,III}]5007/[\mathrm{O\,II}]3727$ (herein O32), $[\mathrm{O\,II}]3727/\mathrm{H}\beta$ (herein O2) and O3. For the $[\mathrm{O\,III}]4959, 5007$ doublet, the QSAGE team fitted a triple Gaussian to determine the line flux. However, due to the grism's spectral resolution constraints, the peaks are only marginally resolved in most spectra and so a fixed flux ratio of $[\mathrm{O\,III}]5007/[\mathrm{O\,III}]4959 = 2.98$ was assumed (Storey & Zeippen 2000). This fit also included Hβ ($\lambda = 4861\,\text{Å}$) since its close proximity may have led to some blending (Stott et al. 2020). The general form of the polynomials fitted by Maiolino et al. (2008) is

$$\log_{10}(R) = c_0 + c_1 x + c_2 x^2 + c_3 x^3 + c_4 x^4, \tag{2.1}$$

where R is the strong-line ratio, $x = 12 + \log_{10}(\mathrm{O/H}) - 8.69$ and c_n are coefficients that depend on the chosen ratio (see Table 4 in Maiolino et al. 2008).

We calibrated metallicities by following a χ^2 minimisation approach adopted by Sanders et al. (2021; see also Cullen et al. 2021; Curti et al. 2024). This method involves minimising the χ^2 of multiple line ratios simultaneously using the formula

$$\chi^2(x) = \sum_i \frac{\left(R_{\mathrm{obs},i} - R_{\mathrm{cal},i}(x)\right)^2}{\sigma^2_{\mathrm{obs},i} + \sigma^2_{\mathrm{cal},i}} \tag{2.2}$$

where the sum over i represents the set of line ratios used for the gas-phase

metallicity determination, $x = 12 + \log_{10}(\mathrm{O/H})$, $R_{\mathrm{obs},i}$ is the logarithm of the ith observed line ratio, $R_{\mathrm{cal},i}(x)$ is the predicted logarithmic value of R_i at x from the Maiolino et al. (2008) calibrations, $\sigma_{\mathrm{obs},i}$ is the uncertainty in the ith observed line ratio, and $\sigma_{\mathrm{cal},i}$ is the uncertainty of the ith line ratio at a fixed x of the Maiolino et al. (2008) calibrations. For $\sigma_{\mathrm{cal},i}$, we used the values from Table 2 of Sanders et al. (2021) which are the average values for multiple calibrations (including Maiolino et al. 2008), but they note that all of them have similar scatter for each of the line ratios used. Metallicities were calculated by selecting the value that minimised Equation 2.2. To determine the uncertainty of the gas-phase metallicity, we followed the method of Cullen et al. (2021); the observed line ratios were perturbed by their uncertainty values using a Gaussian distribution and the metallicity that minimised Equation 2.2 was recalculated 500 times. The 1σ uncertainty on the calculated metallicity was then derived from the 68th percentile width of the resulting distribution of perturbed metallicities.

Since [O II]3727 and Hβ may be undetected in the QSAGE sample (SNR < 2), the strong-line ratios used to calibrate the gas-phase metallicity must be carefully chosen. The reader should be reminded that [O III]5007 is detected to SNR > 3 in all cases (see Chapter 2.2.2). The selection process for the ratio(s) used in Equation 2.2 is as follows:

i) If [O II]3727 and Hβ are both detected with SNR ≥ 2, then all of R_{23}, O3, O2 and O32 are used in Equation 2.2 (applies to 28/67 C–MEx SF galaxies; circles in Figures 2.6 and 2.7).

ii) If [O II]3727 is poorly detected (SNR < 2), but Hβ is well detected (SNR ≥ 2) then only O3 is used (9/67 C–MEx SF galaxies; pentagons in Figures 2.6 and 2.7).

iii) If Hβ is poorly detected (SNR < 2), but [O II]3727 is well detected (SNR ≥ 2) then only O32 is used (26/67 C–MEx SF galaxies; squares in Figures 2.6 and 2.7).

iv) In the event that both Hβ *and* [O II]3727 are poorly detected (SNR < 2), then the χ^2 minimisation method is not followed. Instead, we solve Equation 2.1 using O32 with an upper limit on [O II]3727 (4/67 C–MEx SF

galaxies; diamonds in Figures 2.6 and 2.7). The upper limit was applied as follows: if [O II]3727 flux was poorly detected (i.e. $0 < \mathrm{SNR} < 2$), then the flux was corrected to double the value of the uncertainty on the measurement i.e. a 2σ upper limit. If no [O II]3727 was detected, then the [O II]3727 flux value was set to be double the value of the corresponding [O III]5007 flux error for that object; if the [O II]3727 upper limit results in an O32 value that is on the curve described by Equation 2.1, then this metallicity was selected (upper limit on metallicity). Should an object have an O32 value that is above the curve, then the metallicity corresponding to the maximum strong-line ratio on the curve would have been selected (and these were noted with extreme caution as having a lower metallicity limit), but there were no such cases in this sample.

Since some of the curves defined by Equation 2.1 have multiple solutions, O32 was used to discriminate between them since the shape of the O32 curve in the metallicity range $7 \lesssim 12 + \log_{10}(\mathrm{O/H}) \lesssim 9.5$ has a single solution.

2.4.2 Bian et al. (2018) Calibrations

To compare our MZR and FMR results to higher redshift studies, we need to adopt the higher redshift metallicity calibrations that these studies used. We primarily look at the FMR of Li et al. (2023) who recently analysed the gas-phase metallicity of galaxies at $2 < z < 3$ using *JWST* (and also their MZR, see Chapter 2.5.1). In order to compare to Li et al. (2023), the metallicity calibrations from Bian et al. (2018) must be used. Bian et al. (2018) selected a sample of local galaxies from the Max Planck Institute for Astrophysics (MPA) and Johns Hopkins University (JHU) value-added catalogues (hereafter MPA–JHU) of SDSS DR7[1] (Abazajian et al. 2009) that are analogous to $z \sim 2$ SF galaxies on the O3 versus [N II]6584/Hα BPT diagram, making these calibrations more applicable to high redshift samples. Bian et al. (2018) used definitions of SF on the BPT diagram as defined in Kewley et al. (2013) for the local reference sample and Steidel et al. (2014) for the high-z analogue sample (using Kewley et al. 2006

[1]https://wwwmpa.mpa-garching.mpg.de/SDSS/DR7/

criterion to remove AGN and shock contamination to the emission line flux). The Bian et al. (2018) calibrations used for our sample are

$$m = 8.54 - (0.59 \times \mathrm{O32_B}), \tag{2.3}$$

$$\mathrm{O3_B} = 43.9836 - 21.6211m + 3.4277m^2 - 0.1747m^3, \tag{2.4}$$

$$\mathrm{R_{23}} = 138.0430 - 54.8284m + 7.2954m^2 - 0.32293m^3, \tag{2.5}$$

where $\mathrm{O32_B} = \log_{10}\left(\frac{[\mathrm{O\,III}]\,4959,5007}{[\mathrm{O\,II}]\,3727,3729}\right)$, $\mathrm{O3_B} = \log_{10}\left(\frac{[\mathrm{O\,III}]\,4959,5007}{\mathrm{H}\beta}\right)$, and $m = 12 + \log_{10}(\mathrm{O/H})$. We will refer to the [O II]3727, 3729 doublet as [O II]3727 herein, with [O II]3727 flux referring to the summed flux of the doublet. We determined gas-phase metallicity values following the χ^2 minimisation method explained in Chapter 2.4.1, including the same selection process for when [O II]3727 and/or Hβ are poorly detected (an upper limit on [O II]3727 is used in Equation 2.3 in the case of both [O II]3727 and Hβ being poorly detected, resulting in an upper limit on metallicity in all four cases where this was used). The solution to Equation 2.3 was used to discriminate between any multiple solutions. Equation 2.3 is suitable for $0.3 < \mathrm{O32} < 1.2$ (Bian et al. 2018) but here, following the method of Li et al. (2023), we extrapolated the relationship linearly.

2.5 Results

2.5.1 Mass–Metallicity Relation

Figures 2.6 and 2.7 show the MZR of our complete sample compared with other observational works. The Figure 2.6 shows the MZR for J14–MEx sample of SF galaxies, and Figure 2.7 shows the same but for our C–MEx sample. The MZR was determined by measuring the best fit to the median stellar mass and gas-phase metallicity values in approximately equal-sized mass bins for both of our samples (8–9 SF galaxies per bin for the J14–MEx sample, and 12 SF galaxies per bin for the C–MEx sample). The error bars on these bins are the width of the bin in

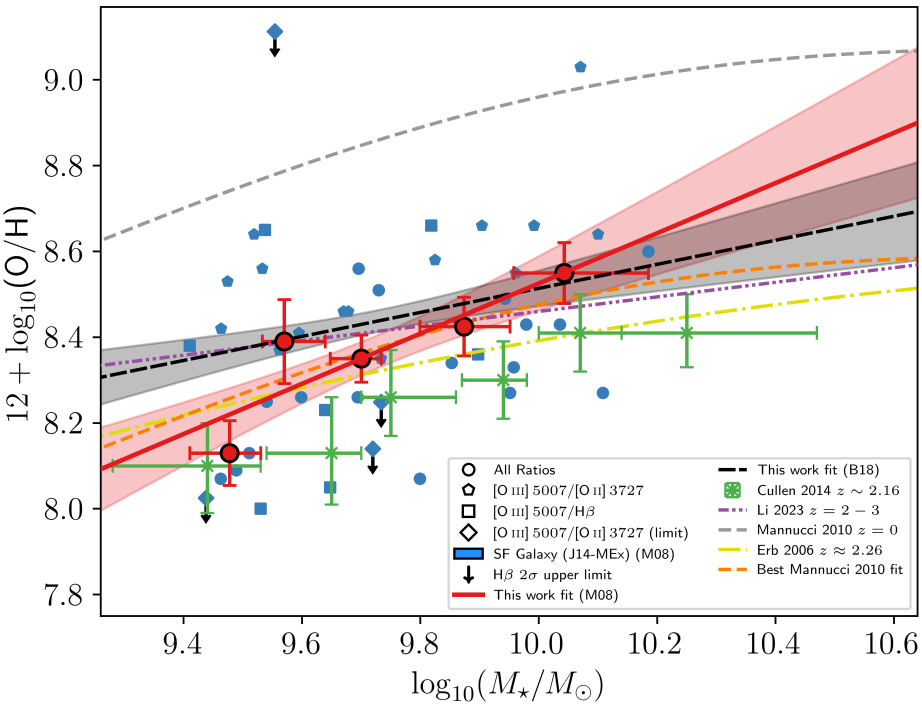

Figure 2.6: The MZR for our sample using the J14–MEx diagnostic to identify SF galaxies. The shape of the blue points (individual SF galaxies calibrated from the Maiolino et al. 2008 calibrations) is selected based on the strong-line ratio(s) used to determine the galaxy's gas-phase metallicity. Black arrows indicate limits on metallicity. The red circles are the binned averages of the SF galaxies within the completeness limit of the J14–MEx sample, with the error on $\log_{10}(M_*/M_\odot)$ representing the width of the bin, and the error on metallicity being the standard error within that bin. The solid red line shows the fit of the binned averages of our Maiolino et al. (2008) sample. The green crosses show the Cullen et al. (2014) MZR data. The grey dashed line shows the $z = 0$ MZR from Mannucci et al. (2010), and the orange dashed line shows the offset version of their MZR to our sample. The yellow dash-dot line shows the MZR from Erb et al. (2006a). The purple dash-double dot line shows the linear MZR from Li et al. (2023). Erb et al. (2006a) and Li et al. (2023) used different metallicity calibrations to those of our sample and direct comparisons should be noted with caution. The black dashed line shows our MZR fit to median bins using the Bian et al. (2018) metallicity calibrations, which are more applicable to high-z. We do not plot the individual or binned data points of SF galaxies from the Bian et al. (2018) calibrations to avoid confusion for the reader. As with the Erb et al. (2006a) and Li et al. (2023) lines, this fit should be noted with caution. The shaded regions indicate the 1σ scatter of both fits.

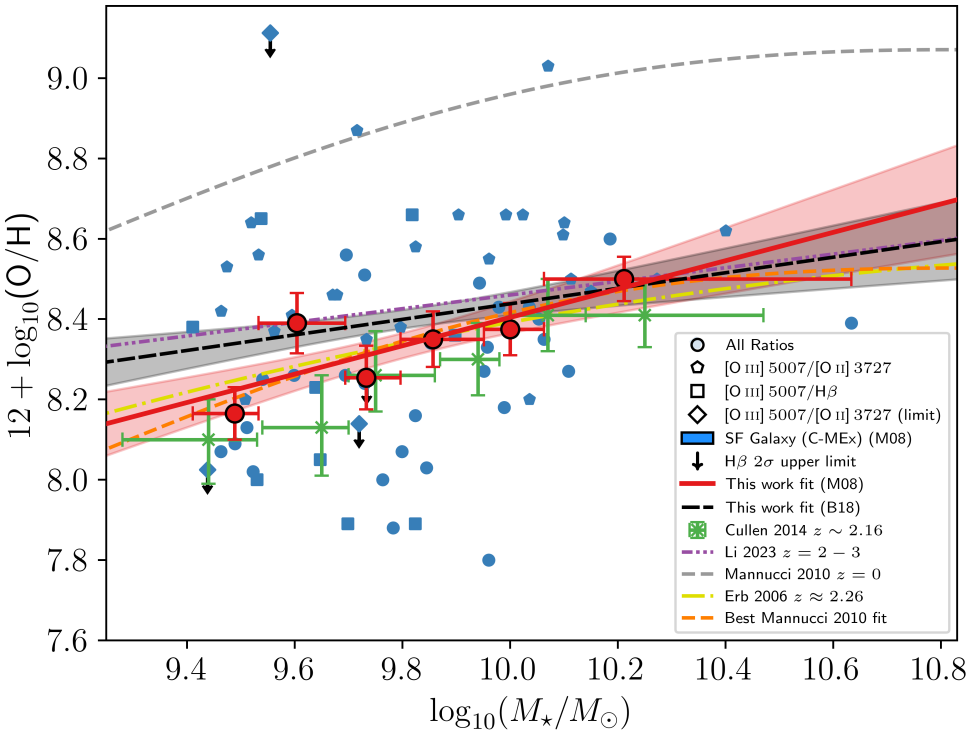

Figure 2.7: As in Figure 2.6, but using the C–MEx diagnostic for identifying SF galaxies.

Table 2.2: MZR fits for the binned data in Figure 2.6 and Figure 2.7 in the form $12 + \log_{10}(\mathrm{O/H}) = a \cdot \log_{10}(M_*/M_\odot) + b$.

Maiolino et al. (2008) Calibration	a	b
J14–MEx	0.59 ± 0.20	2.67 ± 1.80
C–MEx	0.35 ± 0.10	4.87 ± 1.30
Bian et al. (2018) Calibration	a	b
J14–MEx	0.28 ± 0.10	5.71 ± 1.00
C–MEx	0.19 ± 0.10	6.50 ± 0.90

mass and the standard error for the median metallicity. These fits are compared with other works. The best fit was found to be linear in the form $a \cdot x + b$, where $x = \log_{10}(M_*/M_\odot)$, a is the slope of the fit and b is the intercept. The fit to our sample is shown by the dashed red line in both Figure 2.6 and Figure 2.7, with the red shaded region representing the 1σ scatter. The properties of these fits to both our J14–MEx and C–MEx samples can be found in Table 2.2. From both figures, it can be seen that there is a correlation between gas-phase metallicity and stellar mass for the galaxies in our complete sample. The binned medians of our sample in the mass range of Cullen et al. (2014; $\log_{10}(M_*/M_\odot) = 9.44$–$10.25$) follow the same general trend, but their points are offset by -0.08 ± 0.05 dex in metallicity in the same mass range for our C–MEx sample (-0.17 ± 0.06 dex for our J14–MEx sample).

In order to compare our MZR to those of other studies, different forms of the MZR found by these works are fit to our data by allowing their intercept to vary but keeping higher order coefficients fixed. Doing this gives a clearer perspective on how the MZR found in this chapter is different from those found in the literature. From the Mannucci et al. (2010) MZR, the best fit of their curve to our sample is offset from the original ($z = 0$ relation) by -0.51 ± 0.03 dex in metallicity. This is a similar offset that is suggested by Erb et al. (2006a) of -0.56 dex from the local Tremonti et al. (2004) MZR. This large offset is likely due to the fact that the MZR in Mannucci et al. (2010) is based on a sample of local galaxies from SDSS which do not reflect the SF population of $z \sim 2.2$ galaxies from our sample. It should be noted that comparisons between Mannucci et al. (2010) and Erb et al. (2006a) should be made with caution because Erb

et al. (2006a) use the Pettini & Pagel (2004) metallicity calibrations whereas Mannucci et al. (2010) use those from Maiolino et al. (2008).

There is better agreement between the Li et al. (2023) MZR and our data, with just a small average offset from their MZR to ours of ≈ -0.04 dex in metallicity for our C–MEx sample (≈ -0.08 dex offset for the J14–MEx sample). This consistency should be noted with caution as Li et al. (2023) use metallicity calibrations from Bian et al. (2018) whereas the comparisons above are using results calibrated using Maiolino et al. (2008). In order to make a more accurate comparison to Li et al. (2023), we have overlaid the MZR derived from the Bian et al. (2018) calibrations for the same samples of galaxies (black dashed line in Figures 2.6 and 2.7). We find the MZR exists at $z \sim 2.2$ with these higher redshift calibrations, albeit with a shallower slope for both the J14–MEx and C–MEx sample (see Table 2.2). The difference from the Li et al. (2023) MZR is just ≈ -0.03 dex in metallicity for the C–MEx sample (≈ 0.04 dex offset for the J14–MEx sample). These offsets are similar and the slopes are much more consistent; the Li et al. (2023) MZR occupies the 1σ scatter of our fit for almost the entire mass range of our C–MEx sample.

In Figure 2.8, we compare the MZR of our C–MEx sample using both the Maiolino et al. (2008; dashed red line) and Bian et al. (2018; dashed black line) calibrations to results from simulations in the literature at comparable redshifts. These simulations are the $z = 2.07$ binned median MZR from L-Galaxies[1] in Yates et al. (2023), which is a cosmological semi-analytic galaxy evolution simulation (Springel et al. 2005; Henriques et al. 2020); the $z = 2$ MZR found by Torrey et al. (2019), derived from the IllustrisTNG TNG100 cosmological hydrodynamical simulation (Marinacci et al. 2018); the $z = 2.4$ MZR determined by De Rossi et al. (2017) using the Evolution and Assembly of GaLaxies and their Environments (EAGLE) suite of cosmological hydrodynamical simulations; the $z = 2.25$ MZR from analysis by Fontanot et al. (2021) using the GAEA semi-analytic model of galaxy formation (Hirschmann et al. 2016); and the $z = 2.3$ MZR from Davé et al. (2019) found using the SIMBA cosmological hydrodynamical simulations. For the Fontanot et al. (2021) line, we chose to use their MZR that is shifted by -0.1 dex in metallicity from their intrinsic model predictions.

[1] https://lgalaxiespublicrelease.github.io

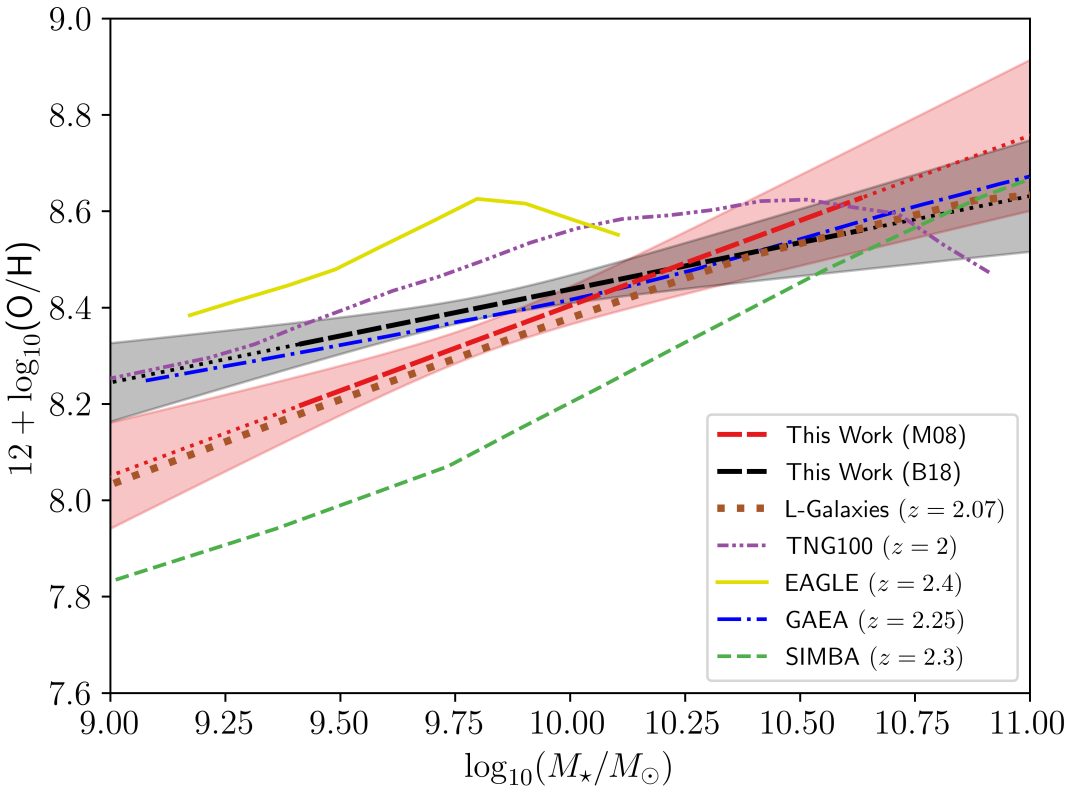

Figure 2.8: The MZR for our sample compared to MZRs generated from simulations of galaxy evolution. The dashed red line shows the fit of the binned averages of our C–MEx sample using metallicity calibrations from Maiolino et al. (2008; the red shaded region indicates the 1σ error of the fit). The dashed black line shows the fit of the binned averages of our C–MEx sample using metallicity calibrations from Bian et al. (2018; the black shaded region indicates the 1σ error of the fit). The brown dotted line indicates the $z = 2.07$ binned median MZR relationship of the cosmological semi-analytic galaxy evolution simulation, L-Galaxies from Yates et al. (2023). The dash-dotted purple line shows the $z = 2$ MZR derived from the IllustrisTNG TNG100 cosmological hydrodynamical simulation in Torrey et al. (2019). The solid yellow line shows the $z = 2.4$ MZR determined by De Rossi et al. (2017) using the EAGLE suite of cosmological hydrodynamical simulations. The blue dash-dot line shows the shifted $z = 2.25$ MZR from analysis by Fontanot et al. (2021) using the GAEA semi-analytical model of galaxy formation. The green dashed line indicates the Davé et al. (2019) $z = 2.3$ MZR using the SIMBA cosmological hydrodynamical simulations.

We selected this instead of the direct model because, as Fontanot et al. (2021) explain, this shift is acceptable given the uncertainty in the normalisation of the MZR from the metallicity indicators, and this offset finds much better agreement with the $z \sim 0$ observations they compare to, whilst maintaining agreement with observations at all other redshifts they analyse (see their Section 4.1). From Figure 2.8, the MZR of our C–MEx galaxies for both calibrations generally agrees with those measured in simulations at these redshifts, especially at higher masses ($\sim 10^{10.25}$–$10^{10.75}\,\mathrm{M}_\odot$), although the EAGLE simulations from De Rossi et al. (2017) only go up to $\sim 10^{10.1}\,\mathrm{M}_\odot$. The MZR from L-Galaxies (Yates et al. 2023), which is the median binned relationship of their simulated galaxies, agrees remarkably well with our Maiolino et al. (2008) calibrated relationship at low stellar masses ($\sim 10^{9}$–$10^{10}\,\mathrm{M}_\odot$), but then strongly agrees with our Bian et al. (2018) calibrated relationship at higher stellar masses ($\sim 10^{10.25}$–$10^{11}\,\mathrm{M}_\odot$) following a flattening of their relationship. Additionally, there is strong agreement between the semi-analytic model from Fontanot et al. (2021) and our Bian et al. (2018) calibrated sample for the entire mass range of Figure 2.8, with their MZR not falling outside the 1σ scatter of our relationship.

2.5.2 The Fundamental Metallicity Relation

Mannucci et al. (2010) introduced a way to project the 3D relationship between SFR, stellar mass and gas-phase metallicity onto a 2D plane by combining stellar mass and SFR into a single axis. They describe this as showing a more accurate correlation with gas-phase metallicity because, for a given stellar mass, galaxies with a higher SFR have reduced metallicities and exhibit properties of lower mass galaxies. As a result, while direct relationships between SFR and gas-phase metallicity may show that they are directly correlated properties, they may be masking over more complicated trends when stellar mass is considered as well. This FMR projection is in the form

$$\mu_\alpha = \log_{10}(M_*/M_\odot) - \alpha \log_{10}\left(\frac{\mathrm{SFR}}{\mathrm{M}_\odot\,\mathrm{yr}^{-1}}\right), \tag{2.6}$$

where α is a free parameter determined by finding the minimum gas-phase metallicity dispersion in this plane. Using this minimisation method to project into 2D, galaxies with limiting values were not weighted or treated differently from the rest of the sample. The majority of these limits arise from galaxies with Hβ detected at SNR < 2, for which the Hβ-based SFR is therefore treated as an upper limit, and correspondingly have lower limits on μ_α for $\alpha > 0$ (from Equation 2.6). In addition, four galaxies have gas-phase metallicity upper limits because both [O II]3727 and Hβ are poorly detected and the χ^2 metallicity-minimisation method was not applied (see Chapter 2.4.1). These were likewise included using their quoted limiting values, so the resulting α values should be interpreted with this caveat. This method was adopted to produce a directly comparable FMR projection across both samples, and to the literature. Since the limiting values primarily arise from the same Hβ measurements used to derive the Hβ-based SFRs, excluding these galaxies would preferentially remove objects with weak Hβ emission and could bias the dynamic range in SFR. Treating the limiting values identically to the rest of the sample therefore avoids introducing additional selection effects, though the reader should still note any comparisons with caution.

For their data, Mannucci et al. (2010) found $\alpha = 0.32$. For our samples, using the higher redshift metallicity calibrations from Bian et al. (2018), the scatter around metallicity was minimised for $\alpha = 0.48$ when using the J14–MEx, and $\alpha = 0.65$ for the C–MEx sample. The latter value of 0.65 is consistent with α values obtained for galaxies in this redshift range in the literature (e.g. Curti et al. 2020a; Sanders et al. 2021; and Li et al. 2023, see below). Figure 2.9 shows the metallicity dispersion as a function of α for the C–MEx sample. Despite still indicating the existence of an FMR, an α of 0.48 for the J14–MEx sample is somewhat at odds with expected values in this redshift range. Randomly sampling the C–MEx sample to match the size of the J14–MEx sample 10 000 times gives an average $\alpha \approx 0.71 \pm 0.19$, which is consistent with the C–MEx value of $\alpha = 0.65$. This suggests that the smaller sample size resulting from the more restrictive J14–MEx prescriptions is not the primary cause of the lower value. The lower α is instead likely due to the J14–MEx sample not probing as wide a mass and SFR range as the C–MEx sample. Figure 2.10 shows the FMR using these obtained α values for our [O III]5007 flux and stellar mass complete sample.

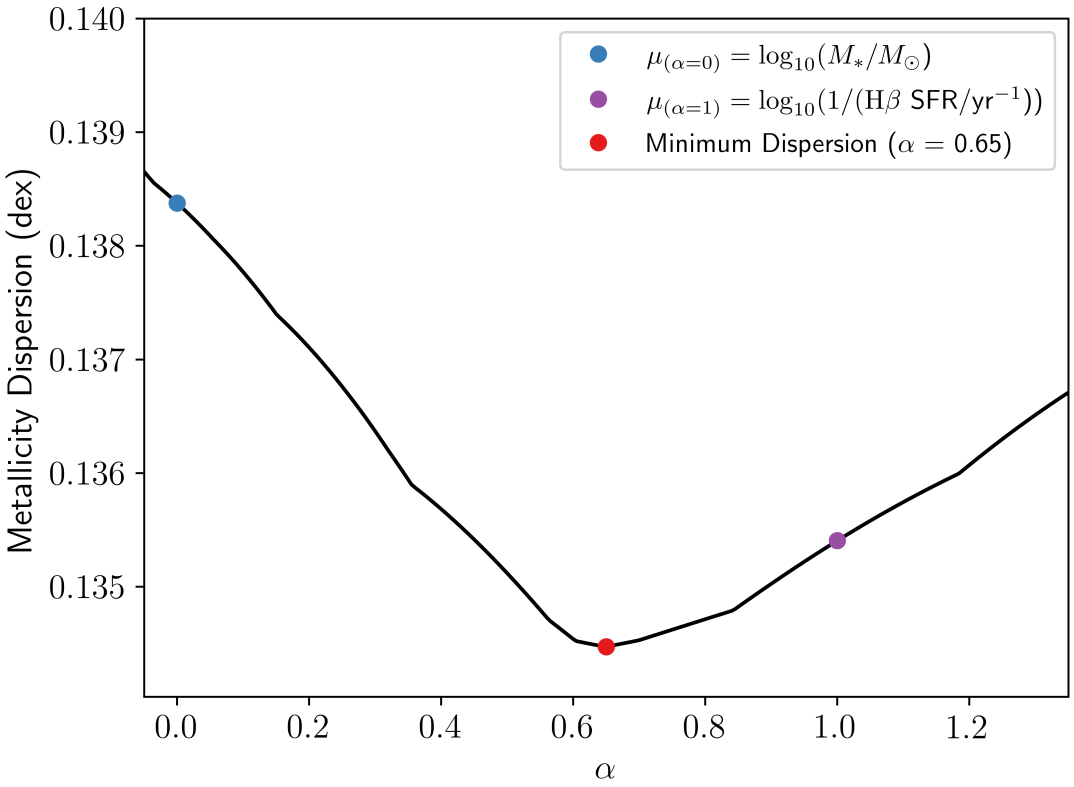

Figure 2.9: Metallicity dispersion of SF galaxies defined using the C–MEx as a function of α (defined in Equation 2.6). Shown are α values corresponding to the minimum dispersion about metallicity ($\alpha = 0.69$; red point), $\alpha = 0$ ($\mu_0 = \log_{10}(M_*/M_\odot)$; blue point) and $\alpha = 1$ ($\mu_1 = \log_{10}(\frac{1}{\mathrm{H}\beta \mathrm{sSFR/yr}^{-1}})$; purple point).

The FMR in the right panel of Figure 2.10, which is for our C–MEx sample, is constructed in the form of

$$12 + \log_{10}(\mathrm{O/H}) = (4.8 \pm 0.9) + (0.4 \pm 0.1)\mu_{0.65}. \tag{2.7}$$

This linear form is fit to equally sized bins of our complete sample showing the median metallicity of the galaxies in each bin. The significance of the slope of this relation is $\sim 4\sigma$, calculated by dividing the slope of the fit by its uncertainty. The shaded region around the red dashed line indicates the 1σ uncertainty about the fit.

Comparisons with the FMRs of other works can be made by using their values

of α, making sure to maintain the same calibrations for metallicity calculations. Figure 2.11 shows our samples on the FMR plane of Mannucci et al. (2010), with the purple fit showing their general form of the FMR for galaxies of any stellar mass, SFR and redshift up to $z \approx 2.5$. We used the metallicity calibrations from Maiolino et al. (2008) for this comparison. The Mannucci et al. (2010) FMR is in the form

$$12 + \log_{10}(\mathrm{O/H}) = \begin{cases} 8.90 + 0.47\,(\mu_{0.32} - 10) & \text{if } \mu_{0.32} < 10.2, \\ 9.07 & \text{if } \mu_{0.32} > 10.5. \end{cases} \tag{2.8}$$

All the galaxies in our sample have $\mu_{0.32} < 10.2$, so for simplicity we will represent this as $12 + \log_{10}(\mathrm{O/H}) = 4.20 + 0.47\mu_{0.32}$. From the right panel of Figure 2.11, using $\alpha = 0.32$ and $x = \mu_{0.32}$, the FMR for our sample of C–MEx SF galaxies is found to be

$$12 + \log_{10}(\mathrm{O/H}) = (3.92 \pm 1.0) + (0.47 \pm 0.10)\mu_{0.32}. \tag{2.9}$$

The slope is in very good agreement with the general linear form found by Mannucci et al. (2010), but is offset by $\sim 0.28 \pm 0.04$ dex in metallicity in the $\mu_{0.32}$ range of our sample. The error on this offset is the median 1σ error about our fit in this range. This offset is in good agreement with Cullen et al. (2014) who found that the FMR of their sample of $z_{\mathrm{median}} \sim 2.16$ SF galaxies, also observed with *HST* grism, was offset by an average of ~ 0.3 dex. They determined that this discrepancy is due to the selection of the metallicity indicator because Maiolino et al. (2008) relies on local SF galaxies to determine their metallicity calibrations, which may not be applicable at high-z, and our result adds evidence to this suggestion.

Figure 2.12 shows the FMR found by Li et al. (2023) for $2 < z < 3$ dwarf galaxies (brown dash-double dot line). Using their value of $\alpha = 0.6$ for the galaxies in our C–MEx sample, and using the Bian et al. (2018) metallicity calibrations as they do, yields an FMR in the form

$$12 + \log_{10}(\mathrm{O/H}) = (4.76 \pm 0.9) + (0.40 \pm 0.1)\mu_{0.60}. \tag{2.10}$$

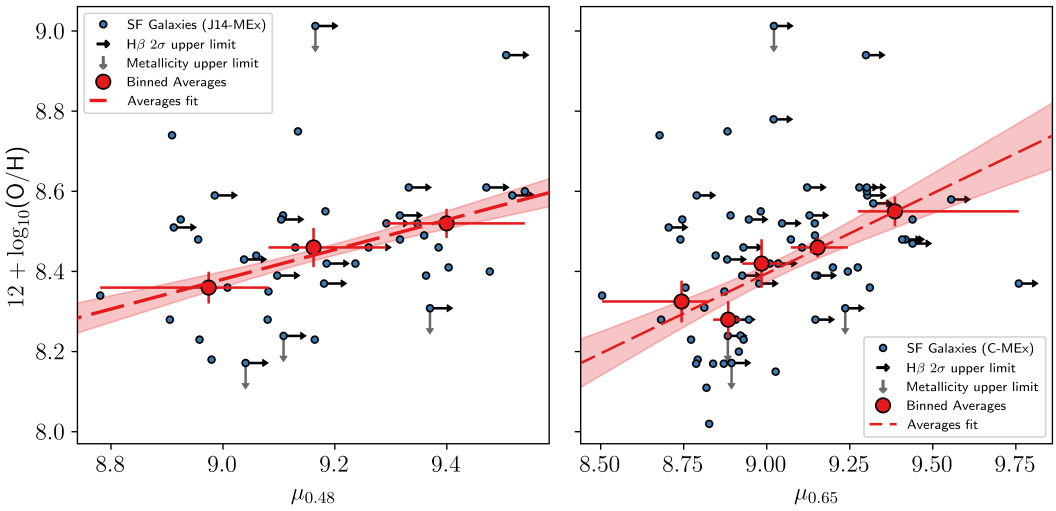

Figure 2.10: The 2D projection of the fundamental metallicity relation using the form $\mu_\alpha = \log_{10}(M_*) - \alpha \log_{10}(\mathrm{SFR})$ as introduced in Mannucci et al. (2010). The α values in both panels are those calculated when the scatter about gas-phase metallicity is minimised. *Top* - The 2D-projected FMR using SF galaxies as defined by the shifted J14–MEx curve, where $\alpha = 0.48$. *Bottom* - The 2D-projected FMR using SF galaxies as defined by the C–MEx, where $\alpha = 0.65$. In both panels, the blue points show the individual SF galaxies in our complete sample. The red points show the median values for our complete sample in approximately equal sized μ_α bins, with the red dashed line showing the best fit to these points (the red shaded regions indicate the 1σ scatter about the fit).

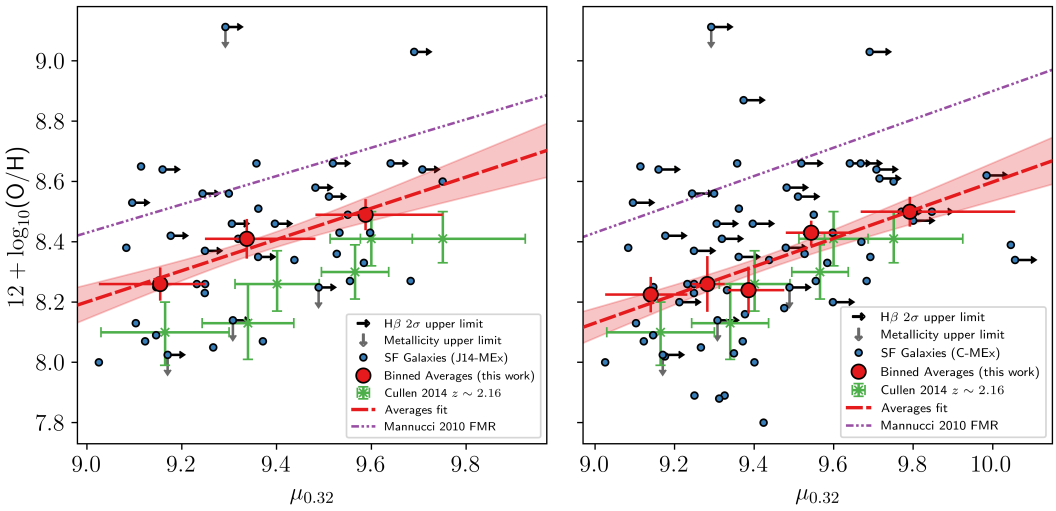

Figure 2.11: The 2D projection of the fundamental metallicity relation using the form $\mu_{0.32} = \log_{10}(M_*) - 0.32\log_{10}(\mathrm{SFR}) - 10$ as used by Mannucci et al. (2010). $\alpha = 0.32$ was found to minimise the scatter on gas-phase metallicity of local SDSS galaxies by Mannucci et al. (2010). *Left* - The 2D-projected FMR using SF galaxies from our sample as defined by the shifted J14–MEx. *Right* - The 2D-projected FMR using SF galaxies from our sample as defined by the C–MEx. In both panels, the purple dash-double-dot line shows the exact form found by Mannucci et al. (2010) for galaxies of all stellar mass, SFR and at any redshift when $\mu_{0.32} < 10.2$. The blue points show the individual SF galaxies within our complete sample. The red points show the median values for SF galaxies in our complete sample in equal-sized $\mu_{0.32} - 10$ bins, with the red dashed line showing the best fit to these points (the red shaded region indicates the 1σ scatter about the fit). The green crosses show the data from Cullen et al. (2014) in this plane.

This form is a much steeper slope than the trend found by Li et al. (2023) of $(0.17 \pm 0.02)\mu_{0.60}$. This could be caused by the contributions of their lower mass bins ($\approx 10^{6.5}$–$10^{7.6}\,M_{\odot}$) which extend beyond the lower limit of masses in this work. Instead, a more appropriate comparison would be to the $z \sim 2.3$ Sanders et al. (2021) sample (pink triangles) in Figure 2.12 as they all fall within the $\mu_{0.60}$ range of this work (red points) and were also used for comparison in Li et al. (2023). Sanders et al. (2021) investigated the redshift evolution of the MZR by analysing samples of galaxies at $z \sim 2.3$ and $z \sim 3.3$ from the Multi-Object Spectrometer For Infra-Red Exploration (MOSFIRE) Deep Evolution Field (MOSDEF) Survey (see Kriek et al. 2015). Comparisons are made to their $z \sim 2.3$ sample as it is a similar redshift to the galaxies in our complete sample and they use the metallicity calibrations from Bian et al. (2018). A fit to their sample in the same form as the FMR from Li et al. (2023) yields

$$12 + \log_{10}(\mathrm{O/H}) = (4.39 \pm 0.4) + (0.45 \pm 0.04)\mu_{0.60}, \tag{2.11}$$

which is in good agreement with our work. This is more evidence that the FMR exists for SF galaxies at this redshift.

Li et al. (2023) discuss the possible reasons why their slope of the MZR is shallower than that of Sanders et al. (2021). They suggest that the evolution of the MZR slope may be determined by different feedback mechanisms and wind models, both of which regulate the fraction of gas ejected from a galaxy (Wang et al. 2022) and determine the MZR in individual galaxies. If low-mass galaxies are dominated by different feedback mechanisms compared to high-mass galaxies, then an evolution in the MZR will be visible. They comment that the results of their study are consistent with that of a momentum-driven wind model (see Finlator & Davé 2008; Guo et al. 2016) but at odds with other studies that analyse the MZR at low mass (e.g. Torrey et al. 2019). Given our FMR results agree with Sanders et al. (2021) for an overlapping $\mu_{0.60}$ range, but see a steepening of the slope compared to the lower range of Li et al. (2023), it seems to suggest that there is a turnover in these relationships from low to high mass at $z \sim 2.2$. However, while the reasons above for a steepening of the slope in the MZR could apply to a change in slope in the FMR toward higher μ_{α} values, Li

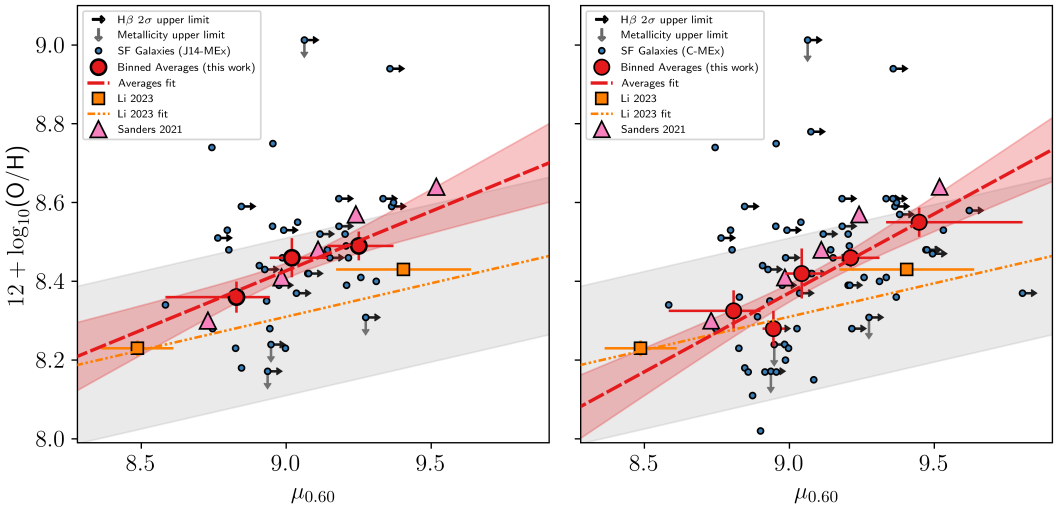

Figure 2.12: The 2D projection of the fundamental metallicity relation using the form $\mu_{0.60} = \log_{10}(M_*) - 0.60\log_{10}(\mathrm{SFR})$ as used by Li et al. (2023). $\alpha = 0.60$ was found to minimise the scatter on gas-phase metallicity of the $2 < z < 3$ galaxies in Li et al. (2023). *Left* - The 2D-projected FMR using SF galaxies from our sample as defined by the shifted J14–MEx. *Right* - The 2D-projected FMR using SF galaxies from our sample as defined by the C–MEx. In both panels, the orange squares show the median values from Li et al. (2023) as defined in their paper, with the orange dash-double-dot line showing their fit (grey shaded region indicates the 1σ scatter about their fit). The pink triangles show the median values of data from Sanders et al. (2021) in this plane. The blue points show the individual SF galaxies in our complete sample. The red points show the median values in equal-sized $\mu_{0.60}$ bins for our complete sample, with the red dashed line showing the best fit to these points (the red shaded region indicates the 1σ scatter about our fit).

et al. (2023) highlight the need for further analysis of the MZR in dwarf galaxies at these redshifts before making any firm conclusions. Additionally, the fact our Bian et al. (2018) MZR slopes agree with Li et al. (2023) indicates that the above explanations regarding different wind models should not be confidently applied to the FMR.

2.6 Discussion & Conclusions

This work analyses the relationship between gas-phase metallicity, stellar mass and SFR in $1.99 < z < 2.32$ SF galaxies from QSAGE. We used the commonly utilised [O II]3727, 3729, [O III]4958, 5007 and Hβ strong-emission lines in order to calibrate metallicities (Maiolino et al. 2008; Bian et al. 2018) as they lie in the wavelength range of *HST* grism spectra at these redshifts. Since many strong-emission lines that are used to generate BPT diagrams (Baldwin et al. 1981) are unavailable in the wavelength range of our grism spectra, MEx diagrams from Juneau et al. (2014) and Coil et al. (2015) were used to differentiate SF galaxies from AGN. These MEx diagrams use the O3 strong-emission line ratio. As a result of the nature of the observations, [O III]5007 flux and stellar mass limits were applied in order to negate selection effects that arise from incomplete bins in these two properties. SF galaxies were binned in equal-sized mass bins and an MZR was constructed and compared to previous works in the literature, including MZRs constructed using $z \sim 0$ galaxies. In the analysis of the FMR, SF galaxies are binned in equal sized μ_α bins (see Equation 2.6), where α varies depending on the scatter in gas-phase metallicity. The conclusions of this work are as follows:

i) Using the metallicity calibrations from Maiolino et al. (2008) — making use of four different strong-emission line ratios in our available wavelength range — an MZR can be seen for SF galaxies at the redshift range of our sample. MZRs were built using both of the two MEx diagnostics from Juneau et al. (2014) and Coil et al. (2015) using measured values and upper limits for Hβ flux in the MEx plane. For both the J14–MEx (Figure 2.6) and C–MEx (Figure 2.7), our MZR is consistent with those in the literature for similar redshift ranges (Erb et al. 2006a; Cullen et al. 2014).

ii) We compared the MZR of our C–MEx sample to a variety of cosmological hydrodynamical simulations and semi-analytic models at comparable redshifts ($z = 2 - 2.4$), using both the Maiolino et al. (2008) and Bian et al. (2018) metallicity calibrations. We find that, in general, these simulations are consistent with our MZR, particularly at higher stellar masses of $\approx 10^{10.25}$–$10^{10.75}\,\mathrm{M}_\odot$.

iii) The FMR was investigated using a 2D projection that combines stellar mass and SFR (see Mannucci et al. 2010). Analysis using $\alpha = 0.65$, a value which minimises the dispersion about gas-phase metallicity for C–MEx galaxies, yields a $\sim 4\sigma$ slope for the best fit in this FMR plane. This value of α agrees broadly with recent values in the literature at this redshift. Using the J14–MEx, the value for α which minimises dispersion around gas-phase metallicity comes to $\alpha = 0.48$. Despite not agreeing with α values at this redshift in the literature, this fit is still consistent with an FMR being present in our sample. The lower value of α could be due to the J14–MEx not probing as wide a stellar mass and SFR range.

iv) In the Mannucci et al. (2010) FMR plane, where $\alpha = 0.32$, our results show that the FMR exists for both J14–MEx and C–MEx diagnostics (Figure 2.11). Using the C–MEx, the slope for our sample came to 0.47 ± 0.10, a value that is in excellent agreement for the SDSS sample in Mannucci et al. (2010). The FMR is offset by 0.28 ± 0.04 dex in metallicity, which is consistent with the offset found by Cullen et al. (2014). According to Mannucci et al. (2010), this FMR should be consistent for all masses, SFRs, and redshifts so this offset could be a result of the choice of metallicity calibration at this redshift, a conclusion Cullen et al. (2014; who similarly used the Maiolino et al. 2008 calibrations) came to.

v) Using $\alpha = 0.6$ as was used by Li et al. (2023), the FMR is again found for both J14–MEx and C–MEx SF galaxies. For C–MEx galaxies, the slope of the FMR is found to be 0.40 ± 0.1. This is similar to the slope in the Mannucci et al. (2010) plane but much steeper than the slope found by Li et al. (2023). This is likely due to the fact that their stellar mass range extends down by an additional ~ 3 dex compared to our sample. The slope is in very good agreement with a fitted slope to the Sanders et al. (2021) data in the same plane (0.45 ± 0.04), who had a $\mu_{0.60}$ range that overlapped completely with that of this work. The FMR being visible in all three planes analysed in this work strongly suggests that it exists in SF galaxies at this redshift.

Regarding the FMR, we believe the negative correlation with SFR at fixed mass is due to the accretion of metal-poor gas fuelling SFR at Cosmic Noon (e.g. Kereš et al. 2005; Dekel et al. 2009). There is mounting evidence in the literature that metallicity gradients of higher sSFR galaxies are flat or even positive (i.e. lower metallicity in the central region and increasing with radius; Stott et al. 2014. See also Wang et al. 2017; Gillman et al. 2020, 2022). It is believed these positive metallicity gradients are caused by this metal-poor gas accretion being focussed on the centre of the galaxy (Sharda et al. 2021) which can be triggered by either efficient accretion (Stott et al. 2014) or merger events (Rupke et al. 2010). Accretion of low-metallicity gas like this results in a dilution of the chemical abundance. Recently, Heintz et al. (2023) used public *JWST* Near Infrared Spectrograph (NIRSpec) datasets to analyse $z > 7$ galaxies, and suggested that the drop in gas-phase metallicity they see in these very high redshift galaxies is a result of dilution caused by accretion. Funnelled accretion then drives high sSFR in the centre of galaxies and is thought to be the cause of a relationship between sSFR and metallicity gradient (Wuyts et al. 2016; Curti et al. 2020b). In this context, metal-poor gas being efficiently accreted into the central cores of the galaxies greatly enhances the SFR whilst simultaneously reducing the overall average gas-phase metallicity of a galaxy on short timescales, which drives the negative correlation between SFR and gas-phase metallicity for fixed stellar mass we see in the FMR (see also Troncoso et al. 2014; Kashino et al. 2017; Wang et al. 2019; Simons et al. 2021). Results from simulations of galaxy evolution lend support to this. From analysis of galaxies in the EAGLE simulations, De Rossi et al. (2017) found that for lower mass galaxies ($M_* < 10^{10.3}\,M_\odot$), their results indicate higher fractions of metal-poor gas drive higher sSFRs and reduce gas-phase metallicity values, and that this is regulated by metal-poor inflows, with a particular focus on satellite galaxies. It is worth noting that for their higher mass systems ($M_* \gtrsim 10^{10.3}\,M_\odot$), the impact of AGN feedback becomes much more significant to the point where it causes an inversion in the MZR plane for fixed stellar mass; metallicity starts increasing with sSFR for fixed stellar masses at $\gtrsim 10^{10.3}\,M_\odot$, but at lower masses it is an anti-correlation at fixed stellar mass (they also found a similar inversion at fixed stellar mass for the gas fraction of

the SF component of gas). Torrey et al. (2019) found that accretion plays a significant role shaping the FMR in SF galaxies in TNG100, and that, additionally, the MZR is a consequence of the accretion (and enrichment) history of galaxies.

Chapter 3

Evidence that Pre-processing in Filaments Drives the Anisotropic Quenching of Satellite Galaxies in Massive Clusters

Abstract

We use a sample of 11 $0.2 \lesssim z \lesssim 0.5$ ($z_{\rm median} = 0.36$) galaxy clusters from the Cluster Lensing And Supernovae survey with Hubble (CLASH) to analyse the angular dependence of satellite galaxy colour ($B-R$) and passive galaxy fraction ($f_{\rm pass.}$) with respect to the major axis of the BCG. This phenomenon has been dubbed "anisotropic quenching", "angular conformity" or "angular segregation", and it describes how satellite galaxies along the major axis of the BCG are more likely to be quenched than those along the minor axis. A highly significant anisotropic quenching signal is found for satellites, with a peak in $(B-R)$ and $f_{\rm pass.}$ along the major axis. We are the first to measure anisotropic quenching out to cluster-centric radii of $2R_{200}$ ($R_{200,\rm median} \approx 1900\,$kpc). We find that the signal is significant out to at least $1.5R_{200}$, and the amplitude of the signal peaks

at $\approx 0.75R_{200}$. This is the first time a radial peak of the anisotropic quenching signal has been measured directly. We suggest that this peak could be caused by a build-up of backsplash galaxies at this radius. Finally, we find that $f_{\text{pass.}}$ is significantly higher along the major axis for fixed values of local surface density. The density drops less rapidly along the major axis and so satellites spend more time being pre-processed here than along the minor axis. We therefore conclude that pre-processing in LSS and not AGN outflows is the cause of the anisotropic quenching signal in massive galaxy clusters, although this may not be the cause in lower mass halos.

3.1 Introduction

Galaxy clusters are the densest and most massive virialized structures in the Universe, often hosting thousands of galaxies. They form from the collapse of large, gravitationally-bound overdensities in the initial density field of the Universe and follow a hierarchical sequence of DM halo mergers (Kravtsov & Borgani 2012), resulting in masses of $M_h \gtrsim 10^{14}\,\mathrm{M}_\odot$ (Overzier 2016). Permeating between cluster galaxies is hot, dense gas known as the ICM, which can be used to parametrize clusters since the X-ray luminosity and temperature of the gas scale with the overall mass of the system. These dense environments, combined with the hot ICM, lead to the quenching of star formation within their galaxies, resulting in cluster galaxies being typically redder (Butcher & Oemler 1984; De Lucia et al. 2006), less SF (Chartab et al. 2020) and more elliptical (Dressler 1980; Postman et al. 2005) than those found in the field.

Many different quenching mechanisms can lead to the suppression of star formation. Peng et al. (2010b) found that the effects of a galaxy's stellar mass and its surrounding environment can be cleanly separated into different mechanisms known as mass quenching and environmental quenching, respectively. In galaxy clusters, it is environmental quenching mechanisms that dominate the suppression of star formation in satellite galaxies as they orbit within the cluster potential. This is due to the density of the ICM, the proximity of galaxies to other satellites and the massive DM halo. RPS is an environmental quenching mechanism which

occurs when a galaxy falls into a cluster and its cold ISM is shocked and removed by the much hotter ICM (Gunn & Gott 1972; Boselli et al. 2014). This strips away the fuel for star formation, leaving the galaxy to quench on a relatively quick timescale of $\sim$ 1–2 Gyr (Roberts et al. 2019; Akins et al. 2021). RPS may also cause significantly higher SFRs at the shock front for a brief period, which causes the galaxy to burn through fuel quickly, again leading to quenching. Satellite galaxies can also have their gas stripped away as a result of tidal interactions with other galaxies (Richstone 1975, 1976). This will happen if a galaxy experiences a close encounter with a more massive galaxy, such as the central BCG. Similarly, a satellite is likely to experience several encounters with other satellite galaxies due to their high number density, leading to the repeated loss of cold gas in a process that is more commonly known as galaxy harassment (Moore et al. 1996). These interactions can also funnel gas towards the centre of satellites which results in a burst of star formation that quickly spends all the cold gas available, leading to a period of quiescence (Barnes & Hernquist 1996; Barnes 2004; Hopkins 2013). These tidal effects are not just limited to direct interactions between the galaxies themselves, but could also be the result of the potential of the cluster disturbing the thin disk of gas and triggering bursts of star formation (Byrd & Valtonen 1990; Moore et al. 1999). Mergers of galaxies can also lead to the quenching of star formation (Mihos & Hernquist 1994a; Hopkins et al. 2008; Poggianti et al. 2017), but this is relatively rare in clusters due to the high-velocity dispersions of $\sigma \sim 1000\,\mathrm{km\,s^{-1}}$ (Struble & Rood 1999).

Satellite galaxies replenish cold gas that is used up in the process of forming stars by accreting it from reservoirs of gas in the galactic halo (see Putman et al. 2012 for a review). If this supply is cut off from the galaxy, either via heating from the ICM (e.g. Dekel & Birnboim 2006) or removed from the galaxy's DM halo (e.g. Vaughan et al. 2020), then any gas in the ISM is used up over time with no replenishment and the galaxy will become quiescent on timescales of up to 4 Gyr (Roberts et al. 2019) in a process known as "starvation" or "strangulation" (Larson et al. 1980).

In clusters, the distribution of satellite galaxies around the central cluster galaxy (typically the BCG) is anisotropic such that there exists a relative over-density of galaxies along the BCG major axis compared to its minor axis. This is

known as BCG–cluster alignment (Sastry 1968; Brainerd 2005). This signal has been observed in both observations (e.g. Carter & Metcalfe 1980; Wang et al. 2008; Huang et al. 2016) and simulations (e.g. Kang et al. 2007; Ragone-Figueroa et al. 2020; Gu et al. 2022), and is thought to arise from a combination of the preferential infall of satellite galaxies along cosmic filaments that align with the BCG (e.g. Libeskind et al. 2011, 2013; Welker et al. 2018; Smith et al. 2023), primordial alignment during the formation of the BCG (e.g. West 1994) and satellite galaxies gradually aligning with the local tidal field as a result of gravitational torques (e.g. Catelan & Theuns 1996). These distributions could be linked to the anisotropic shape of the overall DM halo which tends to be triaxial, as seen in both cosmological simulations (Frenk et al. 1988; Vega-Ferrero et al. 2017) and observations (Sereno et al. 2013; Gonzalez et al. 2021). DM haloes have been found to become more ellipsoidal with increasing cluster mass as well (Despali et al. 2017; Okabe et al. 2020). The mass of a cluster may also directly influence the satellite distribution around the BCG (Paz et al. 2006, 2011). See Kirk et al. (2015) for a more detailed review of these galaxy alignments in observations, and Kiessling et al. (2015) for a review in simulations.

Within the aforementioned anisotropic distribution of satellites is a clearer alignment of red satellites along the major axis of the central galaxy. Yang et al. (2006) found an excess of satellites along the major axes of galaxy groups in SDSS. They find that the signal is strongest when they only consider those groups with red central galaxies and red satellites, a result that was soon repeated by Azzaro et al. (2007) for isolated hosts using SDSS DR4 (Adelman-McCarthy et al. 2006). Huang et al. (2016) used the redMaPPer cluster catalogue (Rykoff et al. 2014) to analyse the satellite distribution in galaxy clusters, and they too found that red satellites are more likely to reside along the major axis of the central cluster galaxy, concluding that it is colour that is the strongest predictor of what they call “angular segregation”. This stronger alignment of red satellites has also been seen in simulations (e.g. Dong et al. 2014). This preferential alignment of red satellites could suggest that there are quenching mechanisms that seem to favour the major axis of the central galaxy. This has recently been dubbed “anisotropic quenching” or “angular conformity” (Martín-Navarro et al. 2021).

Martín-Navarro et al. (2021) analysed 124 000 $z \approx 0.08$ satellite galaxies from SDSS DR10 (Ahn et al. 2014) using galaxy group/cluster catalogues built by Tempel et al. (2014). They found that satellites positioned along the minor axis of the central galaxy were less quenched compared to those along the major axis, measured using a change in the quiescent fraction of galaxies. The authors attributed this anisotropic quenching to minor axis outflows from the AGN activity of the central galaxy, creating bubbles of low-density gas in the CGM. The efficiency of RPS within these bubbles is greatly reduced, which leads to a lower fraction of quenched galaxies along this axis. Martín-Navarro et al. (2021) solidify these observations by reproducing the signal in the IllustrisTNG cosmological hydrodynamical simulations (Nelson et al. 2019), and by also observing a stronger signal in SDSS for satellites orbiting central galaxies with more massive supermassive black holes. These results were later supported by Zhang & Zaritsky (2022) who found a drop in the emission line flux of [O III] and Hβ from the major to the minor axis which indicates a drop in the density of the CGM, which they link to AGN activity (though their results are statistically marginal and are only qualitatively consistent with those of Martín-Navarro et al. 2021).

Stott (2022) found the same result as Martín-Navarro et al. (2021) but extended the observation out to $z \sim 0.5$ using the Cluster Lensing And Supernova Survey with Hubble (CLASH; Postman et al. 2012). He found a significant anisotropic quenching signal for his sample of $0.391 < z < 0.545$ clusters but was limited by the narrow field-of-view (FOV) of *HST*/WFC3 (MacKenty et al. 2008, 2010) for his lower redshift sample. He found an anisotropic quenching signal in both average galaxy colour and quenched fraction, noting that galaxies bluer than the red sequence were less common in a region $\pm 45°$ from the major axis of the BCG. Stott (2022) offered an alternative suggestion to Martín-Navarro et al. (2021) for the observed signal: since the shape and major axis of both the cluster and BCG typically align with each other (e.g. Binggeli 1982; West 1994), the ICM density at a fixed radius from the BCG would be higher along the major axis. Conversely, along the minor axis, the lower density leads to a reduction in the efficiency of environmental quenching mechanisms in the minor axis plane of the BCG. Therefore, an anisotropic quenching signal may arise from the fact that these ellipsoidal effects are studied within a circular cluster-centric radius that

does not take into account the non-circular distribution of the ICM. However, he notes that the CLASH clusters are not highly elliptical (average ellipticity $\bar{\epsilon} = 0.19$; Postman et al. 2012). On a related point, he suggests it may be due to the increased galaxy density on the major axis that increases galaxy interactions.

Going out to $z \sim 1$, Ando et al. (2023) detected anisotropic quenching in $0.25 < z < 1$ CAMIRA (Oguri 2014) clusters using the Hyper Suprime-Cam Subaru Strategic Program S20A data (HSC–SSP; Aihara et al. 2018, 2022; see Oguri et al. 2018 for information on the S20A data). However, Ando et al. (2023) found no evidence of a signal at $z > 1$. They observed that quiescent fractions along the major axis are consistently higher within R_{200}, but found the fractions are similar along both axes at larger radii, which implies physical mechanisms that only operate within the DM halo of the cluster are responsible for anisotropic quenching. They go further by ruling out the cause of the anisotropic signal being differences in the local density of satellite galaxies along both axes because the quiescent fraction remains higher along the major axis when this parameter is fixed. Additionally, they find that the excess in the quiescent fraction along the major axis compared to the minor axis is independent of stellar mass. Given low-mass galaxies are more susceptible to RPS (Gunn & Gott 1972; Steyrleithner et al. 2020), this suggests a different quenching process may be responsible instead, contradicting the theory proposed by Martín-Navarro et al. (2021). However, Ando et al. (2023) note that their stellar mass cut may be too high to definitively conclude this.

In this chapter, we aim to further probe anisotropic quenching in galaxy clusters by analysing Subaru observations of the CLASH clusters at $0.206 < z < 0.494$ (Postman et al. 2012; Umetsu et al. 2014). We measure both the colour and the quiescent fraction of satellite galaxies as a function of the orientation angle from the BCG major axis. One of the main aims of this work is to extend the analysis of anisotropic quenching out to larger cluster-centric radii than was possible for Stott (2022) — who also analysed the CLASH clusters — by utilising the much larger FOV of the Subaru Telescope compared to *HST*/WFC3. This allows us to probe out to $2R_{200}$ ($\approx$ 3000–4300 kpc) for the clusters in our sample. We also perform a test to see if any detected signal is dependent on the local density of satellite galaxies along both axes, by measuring the overall number density of

satellites as well as the average number density within the average area out to the 4th- and 5th-nearest neighbours of each satellite.

This chapter is arranged as follows. In Chapter 3.2, the CLASH survey is described and the sample used for this work is explained in detail. The results are outlined in Chapter 3.3. A discussion of the results can be found in Chapter 3.4. Our conclusions are summarised in Chapter 3.5.

A standard ΛCDM cosmology model is assumed with values $\Omega_\Lambda = 0.7$, $\Omega_m = 0.3$, $H_0 = 70\,\mathrm{km\,s^{-1}\,Mpc^{-1}}$. Any magnitudes stated are presented using the AB system. All results and models in this chapter assume a Chabrier (2003) IMF throughout. The clusters will be referred to using abbreviations of their full name: Abell clusters will still be referred to as Abellxxxx (e.g. Abell611); the MAssive Cluster Survey[1] (MACS) clusters (see Ebeling et al. 2001) will be referred to as MACSxxxx (e.g. MACS1206.2-0847 will be MACS1206); and RXJ2129+0005, RXJ1532.9+3021 & RXJ1347-1145 will be abbreviated to RXJxxxx.

3.2 Sample and Data

Our work focuses on observations of galaxy clusters from CLASH (*HST* Cycle 18 Multi-Cycle Treasury Program GO-12065; PI: M. Postman; see Postman et al. 2012). CLASH imaged 25 massive galaxy clusters at intermediate redshifts ($0.187 < z < 0.890$) from 524 *HST* orbits in order to establish their mass and DM concentrations via gravitational lensing (Postman et al. 2012; Umetsu et al. 2012). Of these 25 clusters, 5 were selected based on their gravitational lensing properties (to increase the probability of discovering $z > 7$ galaxies) and 20 were X-ray selected to limit the effect of lensing biases in their overall sample (Postman et al. 2012).

The data for our work are from observations using the Subaru Prime Focus Camera (Suprime-Cam; Miyazaki et al. 2012) mounted on the wide-field prime focus of the Subaru Telescope. Suprime-Cam is an 80-mega pixel ($10\,240 \times 8192$) mosaic CCD camera and is built for extremely wide-field images. The camera covers a FOV of $34' \times 27'$ with a resolution of 0.202" per pixel (Miyazaki et al.

[1] https://home.ifa.hawaii.edu/users/ebeling/clusters/MACS.html

Table 3.1: Our sample of CLASH clusters. The R.A. and declination Dec. of the BCG are derived from the Subaru observations performed by Umetsu et al. (2014). The M_{200}, Scale Radius (r_s) and R_{200} Concentration Parameter ($c_{R_{200}}$) data are taken from Tables 6 and 7 in Merten et al. (2015). The R_{200} data are calculated by $R_{200} = c_{R_{200}} \cdot r_s$.

Cluster	z_s	BCG R.A.	BCG Dec.	M_{200} ($10^{14}\,M_\odot$)	r_s (kpc)	$c_{R_{200}}$	R_{200} (kpc)	Filters
Abell209	0.206	01:31:52.56	-13:36:40.32	13.57 ± 1.0	657 ± 100	3.3 ± 0.9	2169 ± 677	B_J, V_J, R_C, i', z'
RXJ2129	0.234	21:29:39.96	00:05:20.70	8.71 ± 0.86	429 ± 71	4.3 ± 1.4	1843 ± 674	B_J, V_J, R_C, i', z'
Abell611	0.288	08:00:57.02	36:03:28.30	12.14 ± 0.71	586 ± 86	3.4 ± 0.9	1991 ± 602	$B_J, V_J, R_C, I_C, i', z'$
MACS2137	0.313	21:40:15.10	-23:39:38.63	14.86 ± 0.86	686 ± 71	3.1 ± 0.6	2126 ± 467	B_J, V_J, R_C, I_C, z'
RXJ1532	0.345	15:32:53.76	30:21:00.43	7.57 ± 1.14	557 ± 14	3.0 ± 1.4	1671 ± 890	B_J, V_J, R_C, I_C, z'
MACS1931	0.352	19:31:49.61	-26:34:34.43	9.86 ± 0.71	586 ± 100	3.2 ± 0.9	1874 ± 617	B_J, V_J, R_C, I_C, z'
MACS1115	0.352	11:15:51.89	01:29:57.69	12.86 ± 1.29	886 ± 157	2.3 ± 0.7	2037 ± 718	B_J, V_J, R_C, I_C, z'
MACS1720	0.391	17:20:16.92	35:36:26.50	10.71 ± 1.14	443 ± 86	4.3 ± 1.4	1904 ± 721	B_J, V_J, R_C, I_C, z'
MACS1206	0.440	12:06:12.10	-08:48:05.24	12.29 ± 1.57	443 ± 86	4.3 ± 1.5	1904 ± 760	B_J, V_J, R_C, I_C, z'
MACS0329	0.450	03:29:41.55	-02:11:44.13	10.43 ± 1.43	471 ± 114	3.8 ± 1.6	1791 ± 870	B_J, V_J, R_C, I_C, z'
MACS1311	0.494	13:11:01.78	-03:10:37.49	6.57 ± 0.43	343 ± 43	4.4 ± 1.0	1508 ± 391	$B_{842}, V_{843}, R_C, z'_{\mathrm{IMACS}}$ [a]

[a] - For the equivalent B- and V-band in MACS1311 observations, Umetsu et al. (2014) make use of data from the Wide-Field Imager on the European Southern Observatory's MPG/ESO telescope (Baade et al. 1999; B_{842} and V_{843} respectively). For the equivalent z'-band, observations from the Magellan–Baade telescope's Inamori–Magellan Areal Camera and Spectrograph (IMACS; Dressler et al. 2011) are used (z'_{IMACS}).

2002). The Suprime-Cam data was primarily analysed by Umetsu et al. (2014) for their investigation into the joint shear-and-magnification weak-lensing of 20 CLASH clusters between $0.187 < z < 0.690$, and are publicly available on the CLASH website[1]. Each of the clusters was observed in at least three optical bands and up to six total bands for some clusters, with exposure times between 1000–10 000 s per passband. The six broad-band (BB) filters used for these observations were $B_{\rm J}$ and $V_{\rm J}$ from the Johnson–Morgan system (Johnson & Morgan 1953), $R_{\rm C}$ and $I_{\rm C}$ from the Cousins system (Cousins 1978) and the i' and z' filters from the SDSS system (Fukugita et al. 1996). These six filters cover a total spectral range of $\sim$ 3600–10 700 Å (with the exception of MACS1311 which only had R_C data available from Subaru; see Table 3.1). Umetsu et al. (2014) present most of their results in $R_{\rm C}$, and describe the typical limiting magnitudes as $\sim$ 26–26.5 mag in this band for a 3σ detection. Further independent analysis of these clusters as part of the '*Weighing the Giants*' project, for which a substantial fraction of this data was taken, can be found in the series of papers cataloguing their results (Von Der Linden et al. 2014; Kelly et al. 2014; Applegate et al. 2014; Mantz et al. 2015, 2016).

We used the CLASH catalogue generated by Molino et al. (2017) to acquire the position angles of the BCG in order to analyse the angular dependence of galaxy colour and passive galaxy fraction ($f_{\rm pass.}$). The data from Molino et al. (2017) are also available on the CLASH website. We determine the BCG from visual inspection of the Subaru images, selecting the brightest galaxy at the same redshift as the cluster, typically with a cD halo, and close to the X-ray centroid of the observations (excluding clusters with ambiguous BCGs, see below). The photo-z estimates for the Subaru data are derived by Umetsu et al. (2014) who ran the Bayesian photometric redshift estimation code (Benítez 2000) and corrected for Galactic extinction following the dust maps of Schlegel et al. (1998).

Of the 25 original CLASH clusters, we determined that 11 were suitable for analysis in this work. Primarily, we wanted to focus on curating a sample that uses a consistent colour index that would correlate well with SFR. This colour index should therefore have magnitudes from filters that are on either side of the rest-frame 4000 Å break, i.e. an approximation of rest-frame $U - V$. The 4000 Å

[1] https://archive.stsci.edu/prepds/clash/

break is often used as a dividing line between young, SF galaxy populations and older, quiescent galaxies as a result of an accumulation of absorption lines from metals and the Balmer series at this wavelength. As stellar populations age and cool, the break becomes larger as they get more opaque, making it easier to determine if a galaxy is actively forming new stars (e.g. Dressler & Shectman 1987; Kauffmann et al. 2003; Kriek et al. 2011). In our case, the best-observed colour index is $B_J - R_C$ (hereafter $B - R$) and, as a result of the evolving position of the break moving beyond the wavelength range of these filters, 7 clusters at $z \gtrsim 0.5$ are excluded. Abell1423 and RXJ2248 were removed because there is no available Subaru data. Abell383 was removed because the maximum fraction of R_{200} that could be probed with Subaru ($\approx 1.5R_{200}$) was deemed to be too restrictive compared to higher redshift clusters ($\geq 2R_{200}$). Following visual inspection, the BCGs in Abell2261 and MACS0416 had multiple identified cores — possibly as a result of a merger — which made it difficult to determine the position angle so they were excluded. Similarly, RXJ1347 has multiple possible BCGs so this was also excluded. Finally, MACS0429 was removed as no B_J data was taken in the Subaru observations. The details of our final cluster sample can be found in Table 3.1. The median M_{200} of our final cluster sample, using the cluster masses determined by Merten et al. (2015), is $M_{200,\mathrm{median}} = (10.71 \pm 2.45) \times 10^{14}\,\mathrm{M}_\odot$ with a median $R_{200,\mathrm{median}} = 1904 \pm 184\,\mathrm{kpc}$.

To determine cluster membership, we applied an evolving photometric redshift restriction on galaxies in the Subaru catalogue. This designation was determined following analysis of the scatter of the photometric redshifts in Umetsu et al. (2014) compared to spectroscopically confirmed redshifts of the same sources. Spectroscopic redshifts are available for cluster members in Abell209 (Annunziatella et al. 2016), MACS1206 (Biviano et al. 2013) and MACS2129 (Monna et al. 2017) following observations by the European Southern Observatory (ESO) CLASH–VLT programme (ESO VLT Large programme 186.A-0798; PI: P. Rosati; see Rosati et al. 2014). Spectroscopic redshifts are available from the Grism Lens-Amplified Survey from Space (GLASS[1]; *HST* Cycle 21 Large Program 13459; PI: T. Treu; see Schmidt et al. 2014; Treu et al. 2015) for cluster members of MACS0717, MACS0744, MACS1149, MACS1423 and RXJ1347. Additional

[1]https://archive.stsci.edu/prepds/glass/

spectroscopic redshifts were acquired for known sources in two of the clusters in our final sample from the literature: for Abell209, spectroscopic redshifts are acquired from the ESO New Technology Telescope (ESO–NTT) observations by Mercurio et al. (2003, 2008); for MACS1149, spectroscopic follow-ups were taken to study the SN "Refsdal" using both the Multi Unit Spectroscopic Explorer (MUSE; ESO prog.ID 294.A-5032; PI: C. Grillo; see Grillo et al. 2016) and MOSFIRE (Brammer et al. 2016) which generated additional redshifts (see Treu et al. 2016 for a summary of the MACS1149 catalogues). Sources with spectroscopic redshifts were then matched to the photo-z catalogues of Umetsu et al. (2014). The standard deviation of the photo-z at each respective cluster's redshift was measured and we fitted a linear relationship in the form of

$$\log_{10}(2 \cdot \sigma_{\mathrm{ph}z}) = (3.26 \pm 1.05) \cdot \log_{10}(1 + z_{\mathrm{cluster}}) - (1.56 \pm 0.19),$$

where z_{cluster} is the spectroscopic redshift of the cluster and $\sigma_{\mathrm{ph}z}$ is the standard deviation of the photo-z measurements at z_{cluster}. We used $2 \cdot \sigma_{\mathrm{ph}z}$ to be confident we are taking into account the uncertainty on the photo-z measurements. Therefore, based on this fit, we designated any galaxy to be a cluster member if they were within $\Delta z = 0.03 \cdot (1 + z_{\mathrm{cluster}})^{3.26}$.

We also chose to apply an R-band completeness limit such that only cluster members with an R-band absolute magnitude $\lesssim -16.8$ mag were included, which corresponds to a stellar mass of $\log_{10}(M_*/\mathrm{M}_\odot) \gtrsim 9.3$. This limit was determined by taking the 95 per cent completeness limit in apparent R-band magnitude of the highest redshift cluster in our final sample, MACS1311 ($z = 0.494$), of ≈ 25.6 mag. Analysis was also performed on a sample with a limit corresponding to $\log_{10}(M_*/\mathrm{M}_\odot) > 10$, or $\lesssim -18.6$ mag in absolute R-band at $z = 0.494$, to test the effects of stellar mass cuts on the anisotropic quenching signal.

3.3 Results

The principal aim of this study was to analyse the effect that a satellite galaxy's position angle from the BCG major axis had on its star formation. We do this in two ways: looking at the angular distribution of the corrected $(B - R)_{\mathrm{corr.}}$ colour

of satellites (Chapter 3.3.1), and the quiescent fraction of satellites in the same angular bins (Chapter 3.3.2).

3.3.1 Colour Relationship

To probe the colour distribution of BCG satellites, we used the colour index $(B-R)_{\text{corr.}}$ (see Chapter 3.2). These clusters cover a redshift range $0.206 < z < 0.494$, meaning the rest-frame magnitudes are affected by k-corrections and possible evolution of the galaxy populations between the upper and lower redshift limits ($\approx 2.2\,\text{Gyr}$). To account for these effects, we apply a k- and evolution-correction to shift the clusters to the median redshift of the sample ($z_{\text{median}} \approx 0.362$) using a simple stellar population (SSP) model from Bruzual & Charlot (2003) with a formation redshift of $z_f = 2$, Chabrier (2003) IMF, and solar metallicity ($Z_\odot = 8.69$; Asplund et al. 2009). This model is appropriate for quiescent cluster galaxies but less appropriate for SF galaxies, though the small redshift range means the corrections are suitable for the majority of cases (see also Stott 2022). For each cluster, this colour correction is defined as

$$\begin{aligned}(B-R)_{\text{corr.}} = (B-R)_{\text{obs.}} &+ [(K_B+E_B)_{z_{\text{median}}} - (K_B+E_B)_z] \\ &- [(K_R+E_R)_{z_{\text{median}}} - (K_R+E_R)_z]\,,\end{aligned} \tag{3.1}$$

where the k-correction, K_{band}, and evolution-correction, E_{band}, terms are taken from the Bruzual & Charlot (2003) SSP model. Across the sample, this method corrects $(B-R)$ by -0.274 to $+0.245\,\text{mag}$ from the highest- to lowest-redshift clusters in our sample respectively, corresponding to a total colour-correction span of $0.519\,\text{mag}$. The model shifts applied to the individual bands span $0.673\,\text{mag}$ in B-band and $0.154\,\text{mag}$ in R-band. The dominance of the B-band correction reflects our sample of cluster satellites being dominated by passive galaxies as, over the cluster redshift range, B-band samples the rest-frame blue-optical/near-ultraviolet (NUV) continuum shortward of the $4000\,\text{Å}$ break, where the SEDs of passive galaxies vary rapidly with wavelength and stellar-population age, whereas R-band samples a smoother, redder continuum.

We plotted $(B-R)_{\text{corr.}}$ against angle from the BCG major axis in degrees and then binned the median colour in bins of ≈ 35–$40°$. This range in the bin widths

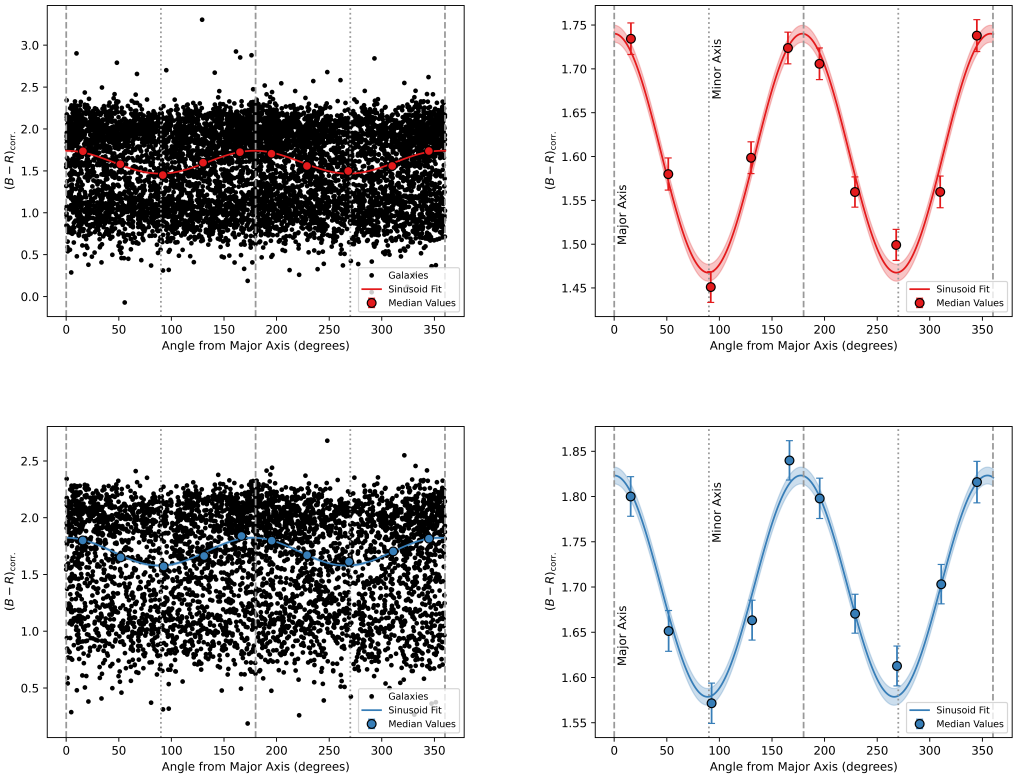

Figure 3.1: Anisotropic quenching signal in colour–angle space for satellite galaxies within $0.75R_{200}$. The left panels show the sinusoidal signal overlaid on the whole population of individual satellites (black points) in this plane, and the right panels just show the binned medians and the sinusoid fits. The red points and fit in the top panels are the anisotropic signal using an absolute R-band completeness limit of -16.8 mag, and the blue points and fit in the bottom panels use a more restrictive limit of -18.6 mag. The $(B-R)_{\text{corr.}}$ errors for both red and blue points represent the standard error within that bin. The shaded regions represent the 1σ error of the fits. The grey dashed lines indicate the angle at which satellites are along the major axis of the BCG, and the grey dotted lines indicate the angle along the minor axis of the BCG.

is a result of keeping the number of galaxies in each bin approximately constant. We did this using both a -16.8 mag completeness limit in absolute R-band and a sample with a more restrictive -18.6 mag magnitude limit (see Chapter 3.2). We then fit a sinusoid to the median colour values in the form

$$y = A \cdot \cos(f \cdot x) + c, \tag{3.2}$$

where y is the median colour of a given angle bin, x is the central angle of the bin from the major axis of the BCG, A is the amplitude of the fit, f is the frequency of the fit, and c is the offset which corresponds to the median colour of the bins.

The top panels in Figure 3.1 show the signal for bins of all satellites within $0.75R_{200}$ for our sample using our R-band completeness limit. Both panels show the same sinusoidal fit, though we include the whole population of satellites for visual reference in the left panel. The red points show the median $(B-R)_{\text{corr.}}$ colour in approximately equal-sized angle bins, with grey dashed (dotted) lines indicating angles along the major (minor) axis. The red shaded region indicates the 1σ error on c from Equation 3.2. From Figure 3.1, there is a clear anisotropic signal, with peaks in colour along the major axis of the BCG and troughs along the minor axis. The fit has a significant amplitude of $A = 0.14 \pm 0.01$ and a period of $1/f = P = (178.9 \pm 1.8)^\circ$. This period is consistent with 180°, demonstrating that our data shows the anisotropic quenching signal first put forward by Martín-Navarro et al. (2021). The bottom panels of Figure 3.1 show the same as the top panels, except this time the satellite galaxies have a more restrictive absolute R-band magnitude limit of -18.6 mag. The fit for this more conservative sample (blue points and line) has an amplitude of $A = 0.12 \pm 0.01$ and a period of $P = (177.5 \pm 1.9)^\circ$, again demonstrating a very significant anisotropic signal that peaks close to the major axis of the BCG.

Figure 3.1 shows the signal for galaxies within a radius of $0.75R_{200}$. However, we also determined the anisotropic signal for all satellites within increasing cluster-centric radii out to $2R_{200}$ at intervals of $0.125R_{200}$. The amplitudes of these fits are shown in Figure 3.2, where each point represents the signal for all galaxies within the corresponding radius. There is no clear radial peak in amplitude for either sample, with the amplitudes for our -16.8 mag limited sample

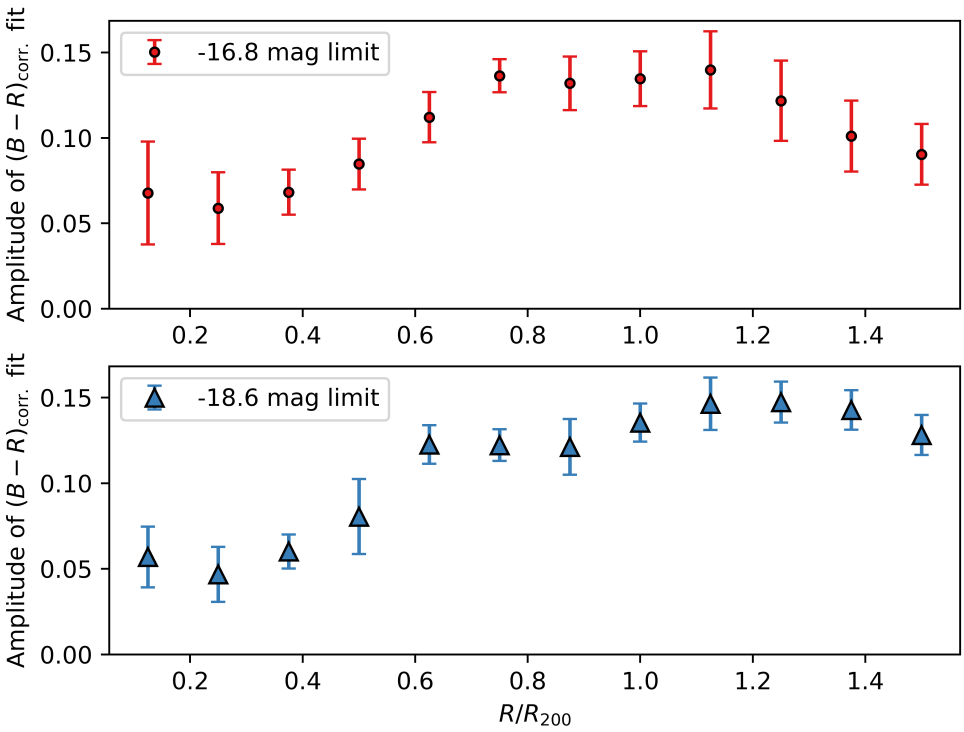

Figure 3.2: The amplitude of the anisotropic quenching signal at different clustercentric radii. The points represent the amplitude of the fit for all satellites within the corresponding R/R_{200} radius. The errors are the uncertainty on the amplitude of the anisotropic quenching signal. The top panel (red points) indicates the radially evolving amplitude for satellites using our -16.8 mag absolute R-band magnitude completeness limit, and the bottom panel (blue triangles) shows this for our -18.6 mag limited sample.

remaining approximately constant from 0.75–1.25R_{200} before steadily dropping. This drop is likely caused by the contribution of increasingly isotropic galaxy populations at large distances from the centre of the clusters. For the -18.6 mag limited sample, there is a similar rise in amplitude with cluster-centric radii, though the peak appears to remain plateaued out to slighty larger radii before similarly declining.

To isolate the signal for galaxies at larger cluster-centric radii, and to get a better understanding of the radius at which anisotropic quenching is most prevalent, it is better to analyse the signal within fixed circular annuli going out from the BCG. Figure 3.3 shows the amplitude of the sinusoid fit to the anisotropic quenching signal in 0.25R_{200}-wide annuli ($\approx$ 475 kpc). The points represent the amplitude of the signal within each annulus, and the corresponding R/R_{200} represents the central R_{200} value of the bins, which are shown by the dashed lines. From Figure 3.3, it can be seen that for a completeness limit of -16.8 mag in R-band there is a peak amplitude at 0.5–0.75R_{200} of 0.13 ± 0.03. For our sample with a brighter magnitude limit, the peak amplitudes are similar in annuli between 0.25–1.0R_{200} ($A \approx 0.14$–0.15) following a significant rise from the innermost regions of the cluster, before a similarly significant decline beyond this.

3.3.2 Passive Galaxy Fraction Relationship

Galaxy quenching describes the process via which a galaxy's star formation is suppressed. Therefore, analysis of any possible anisotropic quenching signal would benefit from using the fraction of passive to total galaxies along the major and minor axes. To do this, we split the galaxy populations based on $(B-R)_{\text{corr.}}$ colour for all the available clusters with B- and R-band data in which $B-R$ is the most applicable colour index for distinguishing SF populations given the location of the 4000 Å break. We then analysed the resulting colour distribution, which included clusters that are not in our final sample due to having an unclear BCG. Figure 3.4 shows the distribution of $(B-R)_{\text{corr.}}$ colours for galaxies in the redshift range $0.187 < z < 0.494$. The purple dashed line represents the middle of the two peaks in the colour distribution and corresponds to $(B-R)_{\text{corr.}} = 1.45$.

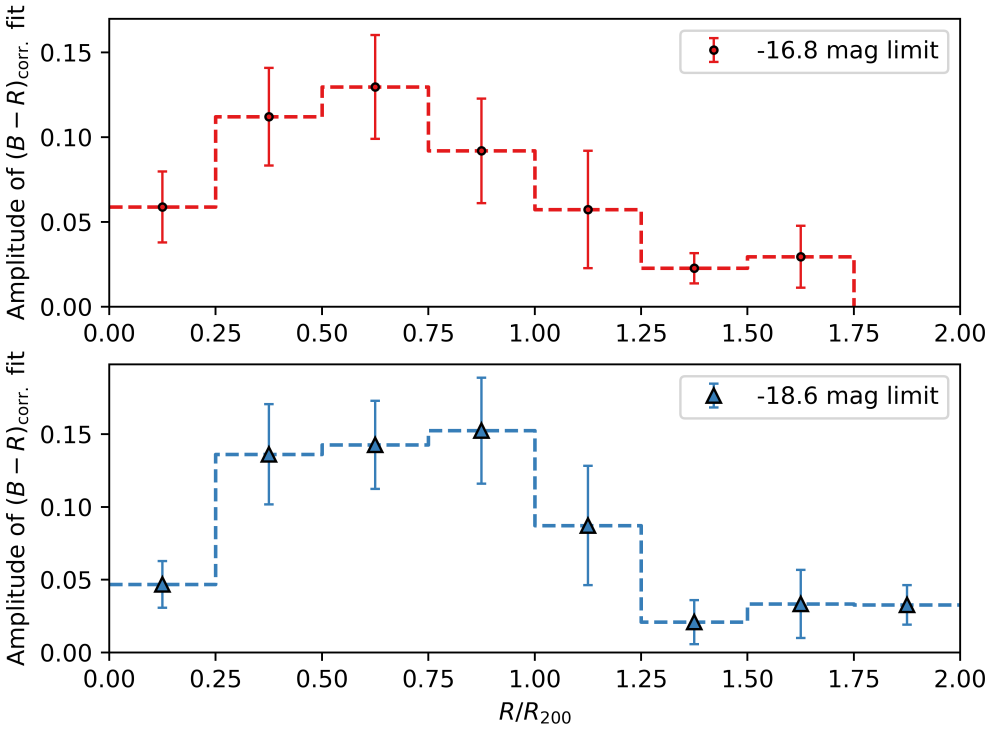

Figure 3.3: The amplitude of the anisotropic quenching signal in colour–angle space within $0.25R_{200}$-wide circular annuli as a function of cluster-centric radius. The points represent the amplitude of the fit within each annulus, and the corresponding R/R_{200} value is the central value of the annulus. The error bars are the uncertainty on the amplitude of the anisotropic quenching signal. The dashed step function represents the range of each circular annulus. The top panel (red points and line) indicates the evolving amplitude for satellites using our -16.8 absolute R-band magnitude completeness limit, and the bottom panel (blue triangles and line) shows the evolution for our -18.6 mag limited sample.

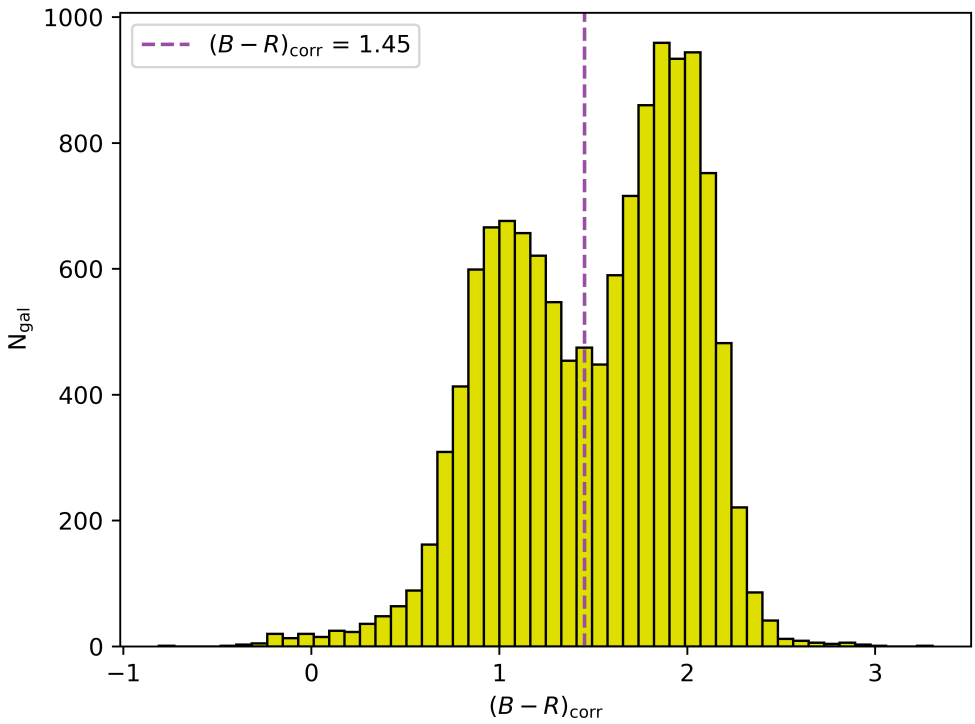

Figure 3.4: The $(B-R)_{\rm corr.}$ colour distribution of all objects in available CLASH clusters from the Subaru observations of Umetsu et al. (2014) in which $B-R$ is the most applicable colour to distinguish SF populations. The purple dashed line indicates the central $(B-R)_{\rm corr.}$ value between the two distinct peaks in the sample distribution, corresponding to $(B-R)_{\rm corr.} \approx 1.45$. This value was used to distinguish SF satellite galaxies and quiescent ones.

As a result, we split the satellite galaxies into two populations: SF galaxies that have a colour $(B-R)_{\rm corr.} < 1.45$ and "passive" galaxies with $(B-R)_{\rm corr.} > 1.45$. We then took the same bins as were used in the colour distributions in Figure 3.1 and divided the number of passive galaxies by the total number of galaxies in each bin to give $f_{\rm pass.}$.

Figure 3.5 shows $f_{\rm pass.}$ against angle from the BCG major axis for satellite galaxies within $0.75R_{200}$ of the cluster centre. As in Figure 3.1, the red (blue) points show the median $f_{\rm pass.}$ in approximately equal-sized angle bins for our $-16.8\,$mag ($-18.6\,$mag) R-band magnitude-limited sample, with the shaded regions indicating the 1σ error on c from Equation 3.2. There is a clear anisotropic signal for $f_{\rm pass.}$, with an amplitude of $A = 0.059 \pm 0.007$ and period of $P = (179.5 \pm 3.0)^\circ$ for the $-16.8\,$mag sample (average passive galaxy fraction of $\overline{f}_{\rm pass.} = 0.57 \pm 0.005$), with $A = 0.064 \pm 0.005$ and period of $P = (176.1 \pm 2.1)^\circ$ for the $-18.6\,$mag sample ($\overline{f}_{\rm pass.} = 0.62 \pm 0.004$). Both of these signals are greater than 5σ and clearly indicate that the SFR of cluster galaxies is lower along the major axis of the BCG.

Martín-Navarro et al. (2021) also studied the angular dependence of passive-galaxy fractions around the BCG in $z \sim 0.08$ SDSS galaxies. They define SF and passive galaxies based on their position on the SF main sequence, fitted in Martín-Navarro et al. (2019) as $\log_{10}({\rm SFR}) = 0.75\log_{10}(M_*) - 7.5$. A passive galaxy is defined in their study as one that is offset below the main sequence by $> 1\,$dex in SFR, and SF if it is within $1\,$dex of the main sequence. They found an anisotropic quenching signal in their sample with an amplitude of 0.025 ± 0.001. This is a significant signal, but one that is under half of the strength of those found in our sample of CLASH clusters. They also found an anisotropic quenching signal in IllustrisTNG100 (Weinberger et al. 2017; Nelson et al. 2019) for SDSS-like galaxies (Rodriguez-Gomez et al. 2019) and found the signal had an amplitude of 0.032 ± 0.004, which is in excess of 3σ, but again smaller than for our sample. Ando et al. (2023) analysed the angular dependence of passive galaxy fraction in galaxy clusters using HSC-SSP in redshift bins out to $z \sim 1.25$. In their $0.25 < z < 0.5$ sample — which overlaps best with the redshift sample of our CLASH clusters — they found an anisotropic quenching signal with an amplitude of 0.0167 ± 0.0032 on a sample with an average passive galaxy fraction of ≈ 0.82.

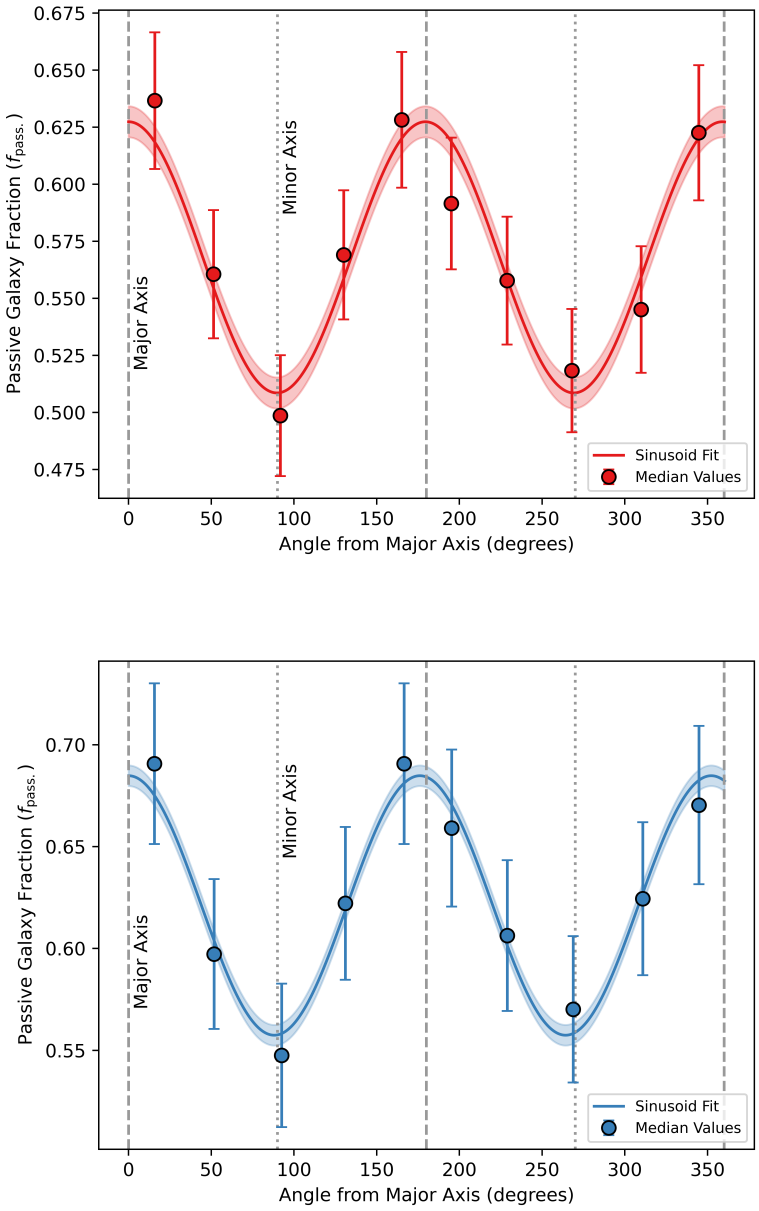

Figure 3.5: Anisotropic quenching signal in $f_{\text{pass.}}$–angle space for satellite galaxies within $0.75R_{200}$ using a -16.8 mag completeness limit in R-band. The red points and fit in the top panel use an absolute completeness limit of -16.8 mag, while the blue points and fit in the bottom panel use a more restrictive limit of -18.6 mag. The $f_{\text{pass.}}$ errors represent Poisson uncertainties. The shaded regions show the 1σ fit uncertainty. Grey dashed (dotted) lines indicate the major (minor) axis of the BCG.

They define a galaxy as being passive if it has a sSFR $< 10^{-11}\,\mathrm{yr}^{-1}$. This is a much lower amplitude than the one found in this work, but is still highly significant. These smaller signals from the literature may relate to different properties of the surveys and samples. Martín-Navarro et al. (2021) analysed systems with DM halo masses between $M_h = 10^{11.7}$–$10^{14.5}\,\mathrm{M}_\odot$ and Ando et al. (2023) studied clusters with halo masses of $M_{200} \approx 10^{13.7}$–$10^{14.7}\,\mathrm{M}_\odot$, whereas our cluster sample covers a cluster mass range of $M_{200} \approx 10^{14.5}$–$10^{14.9}\,\mathrm{M}_\odot$.

As in Chapter 3.3.1, we analysed the strength of the anisotropic signal of average $(B-R)_{\mathrm{corr.}}$ in different annular bins to isolate the distance at which the anisotropic quenching signal peaks. Here we look at how $f_{\mathrm{pass.}}$ changes with angle from the BCG major axis for both magnitude limits out to $2R_{200}$ at intervals of $0.25R_{200}$-wide annuli. Figure 3.6 shows the variation of the amplitude of the signal in these annuli. Similarly to Figure 3.3, the top panel of Figure 3.6 shows that, for our -16.8 mag sample, there is a peak at 0.5–$0.75R_{200}$ of 0.072 ± 0.02 before dropping at larger radii. The peak for our -18.6 mag sample occurs in the same annulus with a peak amplitude of 0.075 ± 0.018, although we note that, similar to the bottom panel of Figure 3.3, the amplitudes over 0.5–$1.0R_{200}$ are similar.

3.3.3 Local Galaxy Number Density

Ando et al. (2023) showed that satellite galaxies are preferentially distributed along the major axis of central cluster galaxies, which would indicate that, along this axis, the number density of satellites is higher (see also Yang et al. 2006; Huang et al. 2016, 2018). It is also well known that galaxies that are found in denser environments have more suppressed SFRs compared to galaxies found in relative isolation (e.g. Peng et al. 2012; Darvish et al. 2016; Crossett et al. 2017; Schaefer et al. 2019). As Stott (2022) suggested, it is therefore possible that the difference in quiescent fractions along both axes could be a consequence of the difference in local densities rather than a preferential quenching mechanism acting along the major axis.

Following a similar method to Ando et al. (2023), we analyse the local number density of each satellite galaxy across our full sample. We adopt an nth-nearest-

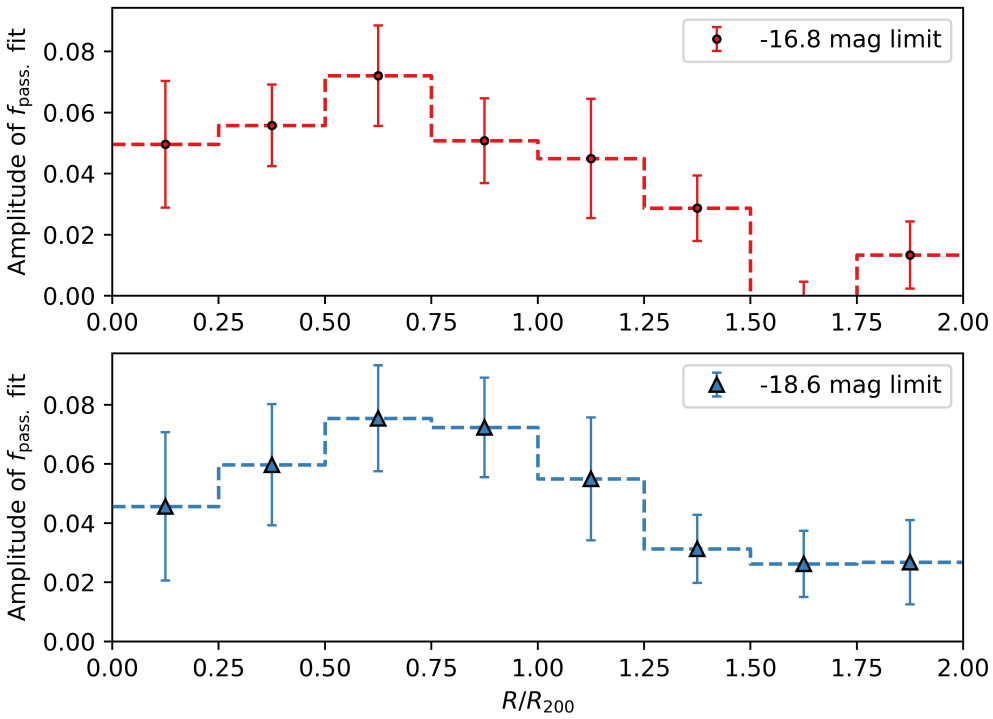

Figure 3.6: The amplitude of the anisotropic quenching signal in $f_{\text{pass.}}$–angle space within $0.25R_{200}$-wide circular annuli as a function of cluster-centric radius. The points represent the amplitude of the fit within each annulus, and the corresponding R/R_{200} value is the central value of the annulus. The errors are the uncertainty on the amplitude of the anisotropic quenching signal. The dashed step function represents the range of each circular annulus. The top panel (red points and line) indicates the radially evolving amplitude for satellites using our -16.8 mag absolute R-band magnitude completeness limit, and the bottom panel (blue triangles and line) shows this for our -18.6 mag limited sample.

neighbour method to measure the local surface density of satellite galaxies as it has been shown to be the best estimate of galaxy number densities in massive haloes (see Cooper et al. 2005 and Muldrew et al. 2012 for reviews on density measurements). For this work, we define surface density using an average between the 4th- and 5th-nearest-neighbour surface density using

$$\log_{10}(\Sigma_{\overline{n=4,5}}) = \frac{1}{2}\log_{10}\left(\frac{4}{\pi d_{n=4}^2}\right) + \frac{1}{2}\log_{10}\left(\frac{5}{\pi d_{n=5}^2}\right), \tag{3.3}$$

where d_n is the distance to the nth-nearest neighbour. We used this averaged surface density approach following other galaxy environment studies (e.g. Bamford et al. 2009; Ellison et al. 2010) and chose $n = 4$ and $n = 5$ as they are common values used in the literature for the nth-nearest neighbour method (e.g. Etherington & Thomas 2015; Wang et al. 2023; Santucci et al. 2023; de Vos et al. 2024). Analysis was also conducted using a basic surface density calculation $\Sigma_n = n/(\pi d_n^2)$ for $n = 4, 5$, but the overall conclusions were the same as using Equation 3.3.

Figures 3.7 and 3.8 shows $(B-R)_{\text{corr.}}$ colour against local surface density calculated from Equation 3.3 for cluster galaxies using a -16.8 mag completeness limit. Figure 3.7 includes the full population of galaxies as well as showing the individual distributions of both local surface densities and galaxy colours, whereas Figure 3.8 just shows the median values for clarity. We define a galaxy as being along the minor or major axis if it is within $\pm 15°$ of that axis. We chose this value to be consistent with the analysis of Ando et al. (2023; though we note that using a range of opening angles from 10° to 60° has no effect on our conclusions). From Figure 3.8, we can see that with increasing surface density, the median colour in both major and minor axes broadly increases. However, we can see that for fixed surface density, median $(B-R)_{\text{corr.}}$ is significantly higher along the major axis for surface density bins $< 10^{-4.0}\,\text{kpc}^{-2}$ before becoming less significant at higher densities. In addition to analysing $(B-R)_{\text{corr.}}$, we also analysed average $f_{\text{pass.}}$ as a function of local surface density in Figure 3.9. This was done by taking the surface density bins of Figure 3.8 and calculating $f_{\text{pass.}}$ within each of them for both axes. In the top panel of Figure 3.9, we see an increase in $f_{\text{pass.}}$ with surface density, which is a reflection of increased local density suppressing star formation

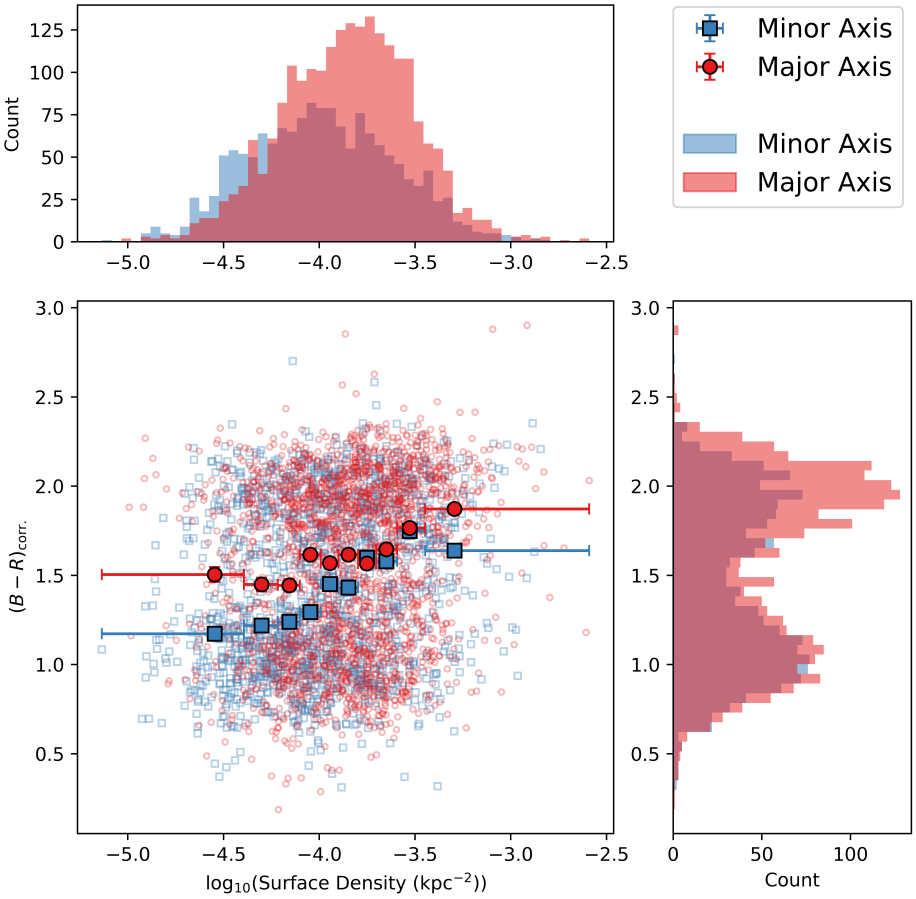

Figure 3.7: The distribution of $(B-R)_{\mathrm{corr.}}$ against local surface density of satellite galaxies that are $\pm 15°$ from either the minor or major axis. In the left panel, the solid red circles and solid blue squares represent the median $(B-R)_{\mathrm{corr.}}$ in surface density bins for galaxies along the major and minor axes respectively. The error on median $(B-R)_{\mathrm{corr.}}$ represents the standard error of the values in each bin, and the error on surface density represents the range of individual values that occupy them. The smaller, empty points represent the individual satellites in this plane. The upper histogram shows the distribution of surface density values, with the red bars indicating satellites along the major axis and the blue bars for those along the minor axis. The right-hand histogram shows the distribution of $(B-R)_{\mathrm{corr.}}$ values along both axes. In the right panel, the points are the same median values as in the left panel, but the individual satellites and surface density errors are removed for additional clarity on the median distribution.

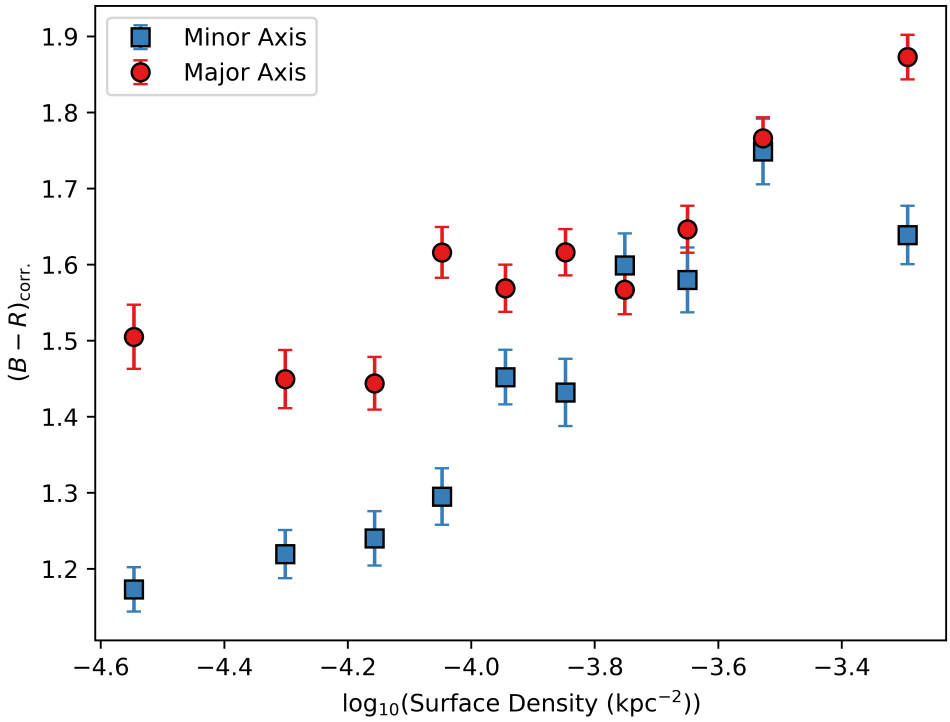

Figure 3.8: As in the main panel of Figure 3.7 without the individual satellite points.

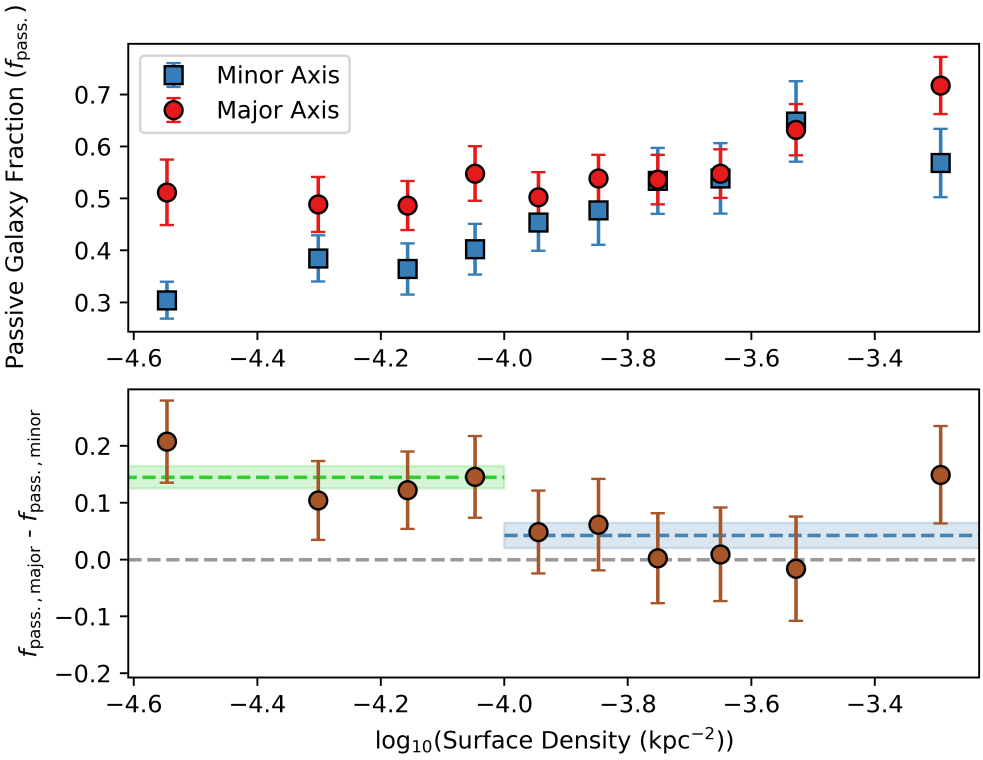

Figure 3.9: The top panel shows the distribution of median $f_{\mathrm{pass.}}$ values in local surface density bins of satellite galaxies that are $\pm 15°$ from either the minor or major axis. The red points (blue squares) indicate the $f_{\mathrm{pass.}}$ values along the major (minor) axis. The error on $f_{\mathrm{pass.}}$ indicates the Poisson error within each bin. The bottom panel shows the difference between the passive galaxy fraction along the major axis ($f_{\mathrm{pass,major}}$) compared to along the minor axis ($f_{\mathrm{pass,minor}}$) in the same bins. The error is the uncertainty on this difference based on the error of the median $f_{\mathrm{pass.}}$ values in the top panel. The green (blue) dotted line indicates the mean value of $f_{\mathrm{pass,major}} - f_{\mathrm{pass,minor}}$ at $\leq 10^{-4.0}\,\mathrm{kpc}^{-2}$ ($> 10^{-4.0}\,\mathrm{kpc}^{-2}$), with the shaded regions indicating the standard error of the mean. The grey dashed line indicates where there would be no difference between the two axes.

more effectively (e.g. Peng et al. 2012; Darvish et al. 2016; Kawinwanichakij et al. 2017).

In Figure 3.9, we see that for fixed local surface densities $\leq 10^{-4.0}\,\mathrm{kpc}^{-2}$, $f_{\mathrm{pass.}}$ is significantly higher along the major axis than the minor axis, with higher densities showing a smaller difference. This is emphasised in the bottom panel of Figure 3.9 which shows the difference between $f_{\mathrm{pass.}}$ along the major axis compared to the minor axis. The dotted lines reflect the average difference between the densities along the two axes, with the green dotted line showing the average for fixed surface densities $\leq 10^{-4.0}\,\mathrm{kpc}^{-2}$ of 0.15 ± 0.02, and the blue line indicating the difference at $> 10^{-4.0}\,\mathrm{kpc}^{-2}$ of 0.04 ± 0.02. The difference at low surface densities is significant and suggests that the anisotropic signal we see is caused by some quenching mechanism(s) that preferentially impacts satellites residing along the major axis rather than being a reflection of the different local environments. However, in Chapter 3.4.2, we argue that it is the comparative length of time spent in higher density environments along the two axes that causes the signal. For galaxies that reside in higher surface densities, the much lower difference is likely reflecting the increasingly dominant effects of environmental quenching which occur in high-density groups of satellites (Peng et al. 2010b).

3.4 Discussion

3.4.1 Impact of AGN Outflows

We see that the amplitude of our anisotropic quenching signal using $(B-R)_{\mathrm{corr.}}$ and $f_{\mathrm{pass.}}$ peaks at 0.5–$0.75R_{200}$ in Figures 3.3 and 3.6 respectively, and we analyse the signal out to $2R_{200}$ ($\approx 3800\,\mathrm{kpc}$). These are the largest cluster-centric radii that anisotropic quenching has been analysed in observations, and also the first time the peaks of individual sinusoidal amplitudes have been measured within fixed circular annuli extending out from the centre of galaxy clusters. This has allowed us to observe a peak in the signal that other studies that measure the radial dependence of anisotropic quenching have not. For example, Ando et al. (2023) analysed the radial dependence of overall quiescent fractions in annuli

along a 30° wedge from both axes, but here we directly analyse the overall signal in $0.25R_{200}$ annuli from the BCG. Other studies have analysed galaxy properties in clusters as a function of cluster-centric radius and linked them to anisotropic quenching, such as green valley fraction and sSFR (Jian et al. 2023). From our results in Chapter 3.3, we have shown that anisotropic quenching is not just an effect in the innermost regions of galaxy clusters, but instead remains significant — and even rises — out to at least $0.75R_{200}$. The cause of the signal dropping beyond $\sim 1R_{200}$ is likely driven, at least in part, by geometric effects associated with our definition of major-axis membership. Since we classify galaxies within $\pm 15°$ of the cluster major axis, the corresponding wedge subtends a progressively larger physical area with increasing cluster-centric radius. At larger radii, this expanding cone therefore encompasses an increasing surface area of the surrounding field population, introducing a growing fraction of isotropically distributed field galaxies not associated with the LSS. This geometric effect dilutes the contrast between major- and minor-axis populations, leading to a decline in the anisotropic signal strength.

When they first noted anisotropic quenching, Martín-Navarro et al. (2021) suggested that feedback from the AGN of the BCG could be responsible. As discussed in Chapter 3.1, if the radio jets of these powerful AGN are aligned with the minor axis of the BCG, then they could reduce ICM density and make RPS less efficient. This follows from the X-ray cavities or "bubbles" (Boehringer et al. 1993; Heckman & Best 2014) that are left in the wake of the powerful radio jets. For this to be a plausible explanation for the results we see in this work, these cavities would need to extend out to large cluster-centric radii. However, evidence in the literature suggests the spatial extent of X-ray cavities is relatively small compared to the radii over which our anisotropic quenching signal remains significant. In their review on AGN feedback, McNamara & Nulsen (2007) used *Chandra* (Weisskopf et al. 2002) data from the cluster sample of Rafferty et al. (2006) and found that the detection rates of X-ray cavities in clusters decline rapidly from a peak at 30 kpc from the core of the host galaxy, with very few detected at > 100 kpc. More recent observations have also confirmed that cavities typically extend to 15–30 kpc from their central host (e.g. Hlavacek-Larrondo et al. 2013; Bîrzan et al. 2020; Timmerman et al. 2022). Simulations have shown that X-ray

cavities can extend to 200–300 kpc from the BCG before being suppressed by gas inflows (e.g. Cielo et al. 2018), and there are rare examples of cavities extending to 200 kpc in observations (e.g. Nulsen et al. 2005; McNamara et al. 2005; Wise et al. 2007). The median cluster size of our sample is $R_{200,\mathrm{median}} = 1904 \pm 184$ kpc. With this in mind, taking the higher estimate of 300 kpc, X-ray cavities would only extend to $\approx 0.2R_{200}$ at most from the BCG of the CLASH clusters. It would require an X-ray cavity to reach ≈ 475 kpc to begin to influence satellites beyond the first annulus of our analysis in Figures 3.3 and 3.6. This does not rule out the influence of AGN feedback in the inner-most regions of our clusters, since we do see an anisotropic quenching signal at $R \leq 0.25R_{200}$, and Martín-Navarro et al. (2021) provide evidence from IllustrisTNG100 (Nelson et al. 2018) that supports their observations which only extend to $\sim 0.75R_{200}$ at most (Stott 2022). However, we note that we have also shown that there is no significant difference in the anisotropic quenching signal between the two magnitude-limited samples. If the reduced efficiency of RPS caused by the AGN was the primary driver, then a larger signal would be expected for the -16.8 mag sample populated by more lower-mass satellites that are less resistant to the stripping of their gas by the ICM.

AGN-fuelled X-ray cavities would also need to be common in clusters of galaxies at this redshift, and last long enough to have a noticeable impact on the efficiency of RPS of orbiting satellites. Hlavacek-Larrondo et al. (2012) studied AGN feedback from the BCG in 76 MACS clusters, including three in our sample (MACS1720, MACS1931 and MACS1115). They find clear cavities in only 13 of the 76 clusters, with a further seven that have possible cavities, giving a detection rate of just $\approx 26\%$ (though we note that they find cavities in all 3 of the aforementioned clusters which we also analyse here). Bîrzan et al. (2020) used data from the International Low-Frequency Array (LOFAR; van Haarlem et al. 2013) Two-metre Sky Survey (LoTSS; Shimwell et al. 2017, 2019) to study 42 systems that host possible X-ray cavities, of which 25 are clusters of galaxies. Whilst their study was used to analyse groups and clusters that already had possible cavities, they found only $\sim 54\%$ of their massive clusters show evidence for significant radio-mode AGN feedback. Other studies have similar cavity detection rates of ~ 30–50% (e.g. Panagoulia et al. 2014; Shin et al. 2016; Olivares et al. 2023). One

would expect that, in order to be a primary driver of the anisotropic quenching signal in a population of galaxy clusters, significant X-ray cavities would need to be present in at least a majority of systems. Furthermore, the X-ray cavities need to have existed long enough to influence the properties of the satellites that may interact with them. Using a simple estimate of the average crossing time for our sample of clusters where $R_{200,\mathrm{median}} \approx 1900\,\mathrm{kpc}$ and a typical cluster velocity dispersion of $\sigma = 1000\,\mathrm{km\,s^{-1}}$ (Struble & Rood 1999) then we get an average cluster crossing time of $t_{\mathrm{cross}} \approx \frac{R_{200,\mathrm{median}}}{\sigma} \approx 1.9\,\mathrm{Gyr}$. However, typical cavity ages are 0.01–0.27 Gyr (e.g. Nulsen et al. 2005; Hlavacek-Larrondo et al. 2012, 2013; Macconi et al. 2022). It is therefore unlikely that a significant number of orbiting satellites will have had time to pass through these cavities since they were formed.

There is also direct evidence from simulations that suggests the impact of AGN outflows on anisotropic quenching is minimal. Karp et al. (2023) analysed results from the TNG100 cosmological hydrodynamical simulations and UniverseMachine, which is an empirical post-processing algorithm (Behroozi et al. 2019). They run these on the Small MultiDark Planck (SMDPL; Rodríguez-Puebla et al. 2016) simulation as part of the MultiDark cosmological DM-only suite (Klypin et al. 2016) to reassess Martín-Navarro et al. (2021)'s conclusions. They find that AGN outflows are not required to explain the anisotropic quenching signal, which is instead fully explained by the hierarchical formation of clusters, which involves the accretion of satellites along cosmic filaments (see Chapter 3.4.2).

3.4.2 Large-scale structure and pre-processing

The anisotropic signal remaining significant beyond R_{200} (to $\sim 2\sigma$) suggests that the cause of the anisotropic quenching signal could be related to LSS. From Figures 3.8 and 3.9, it is clear that the anisotropic quenching signals we see in Figures 3.1 and 3.5 respectively are not a reflection of the change in local environment between the major and minor axes. This is because, for fixed surface density values, $(B-R)_{\mathrm{corr.}}$ and $f_{\mathrm{pass.}}$ are significantly higher along the major axis. As such, to probe the possibility of LSS, we analyse the cluster-centric radial evolution of $f_{\mathrm{pass.}}$ directly, and also how local surface density evolves towards the outskirts of the cluster.

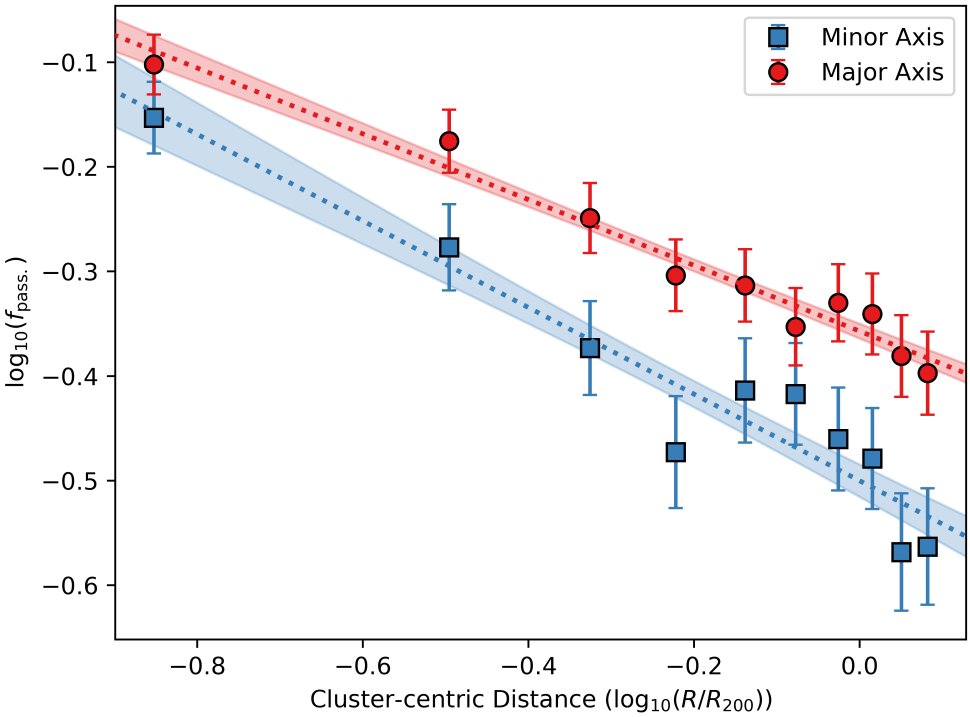

Figure 3.10: The relationship between $\log_{10}(f_{\text{pass.}})$ and distance from the cluster centre in units of $\log_{10}(R/R_{200})$. The red points (blue squares) indicate the median $\log_{10}(f_{\text{pass.}})$ values along the major (minor) axis in cluster-centric distance bins. The error bars represent the Poisson error of the median $f_{\text{pass.}}$ in each bin. The dotted lines represent the best linear fit to the corresponding points, with the shaded region indicating the 1σ error.

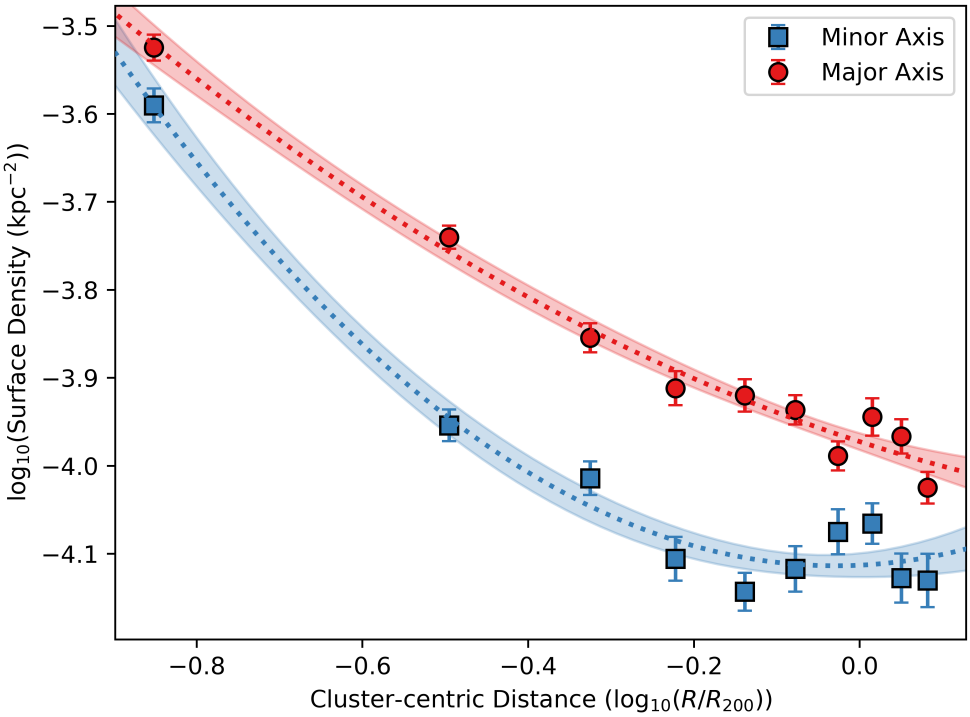

Figure 3.11: The relationship between local surface density and distance from the cluster centre in units of $\log_{10}(R/R_{200})$. The red points (blue squares) indicate the median surface density values along the major (minor) axis in cluster-centric distance bins. The error bars represent the standard error of the median surface density in each bin. The dotted lines represent the best fit in the form $\log_{10}(\Sigma_{\overline{n=4,5}}) = a \cdot \log_{10}(R/R_{200})^2 + b \cdot \log_{10}(R/R_{200}) + c$ to the corresponding points. The shaded region indicates the 1σ error of the fit.

Figure 3.10 shows the relationship between $f_{\text{pass.}}$ and distance from the centre of the cluster. We can see that $f_{\text{pass.}}$ remains higher along the major axis (red points) compared to the minor axis (blue squares) for fixed distances from the BCG. The slope of the minor axis relationship is steeper than that along the major axis, but the two agree within errors. The two linear fits (dotted lines) are

$$\log_{10}(f_{\text{pass.,major}}) = -(0.29 \pm 0.02) \cdot \log_{10}(R/R_{200}) - (0.330 \pm 0.007),$$

$$\log_{10}(f_{\text{pass.,minor}}) = -(0.40 \pm 0.04) \cdot \log_{10}(R/R_{200}) - (0.47 \pm 0.01).$$

We can see that $f_{\text{pass.}}$ is ≈ 0.13 dex higher along the major axis at $1R_{200}$. A similar result is seen in Figures 5 and 6 of Ando et al. (2023) where they also found that passive galaxy fractions are generally higher along the major axis for fixed local overdensity.

Figure 3.11 shows the relationship between median local surface density and distance from the BCG. The fit to both sets of data here is best described by a quadratic in the form

$$\log_{10}(\Sigma_{\overline{n=4,5}}) = a \cdot \log_{10}(R/R_{200})^2 + b \cdot \log_{10}(R/R_{200}) + c,$$

though we note that the best fit to the major axis data points was also well described by a linear fit. From Figure 3.11, we see a decline in the local surface density along both axes out to $1.25R_{200}$. However, we see that the surface densities fall more rapidly along the minor axis before flattening at $\approx 1.3R_{200}$, though they are significantly below the equivalent surface densities along the major axis. This shows the median density to be generally much higher along the major axis, demonstrating that the results seen in Figures 3.8 and 3.9 are mostly driven by galaxies along the major axis having consistently resided in higher density regions than corresponding galaxies along the minor axis. This interpretation assumes that the projected position angle of cluster satellites retains information about

their infall direction. This is a reasonable approximation, particularly for those that reside along the major axis of the BCG, because galaxies and groups are expected to be accreted anisotropically into clusters along filaments, which are often aligned with the cluster or BCG major axis (e.g. Altay et al. 2006; Gouin et al. 2020; Zakharova et al. 2025). Under this interpretation, galaxies observed near the major axis are more likely to have been accreted through denser filamentary environments and therefore to have experienced greater pre-processing before or during cluster infall. However, this should not be interpreted as requiring individual galaxies to remain, nor assuming they do remain, on fixed radial orbits after infall, since orbital mixing, projection effects and virialisation can obscure the original infall direction.

In a hierarchical framework, pre-processing describes the scenario in which satellite galaxies that have previously spent time as part of a group of galaxies before their infall into a larger cluster experience a degree of environmental quenching before interacting with the dense ICM (Zabludoff & Mulchaey 1998; Fujita 2004). Smaller groups, or individual galaxies, may also have their star formation suppressed as they travel along cosmic filaments where other quenching mechanisms may be enhanced compared to the field (e.g. Sarron et al. 2019; Kraljic et al. 2020; Donnan et al. 2022; Hoosain et al. 2024).

There is strong observational evidence for the pre-processing of satellite galaxies in clusters. Cortese et al. (2004) discovered an infalling group belonging to Abell1367 (see also Sakai et al. 2002 and Iglesias-Páramo et al. 2002), and in a follow-up analysis, Cortese et al. (2006) were able to reconstruct the evolutionary history of the group. They discovered that in the process of infalling into Abell1367, tidal interactions within the group resulted in gas stripping and a weakened potential well that made RPS by the ICM more efficient on the outskirts of the cluster. Olave-Rojas et al. (2018) studied two $z \sim 0.4$ CLASH clusters — MACS0416 and MACS1206, the latter of which is part of our cluster sample — to determine the environmental effects in substructures of galaxies in and around them. In the substructures they identified, they found that the fraction of red galaxies (a good proxy for our $f_{\text{pass.}}$ parameter) is higher in substructures on the outskirts of the clusters than the field, which they conclude is a clear sign of pre-processing in action. They go further and find that the quenching efficiency

in groups at cluster-centric radii of $R \geq R_{200}$ is similar to that of the main cluster itself. This supports the idea that pre-processing can lead to already-red galaxies entering larger structures. Estrada et al. (2023) supports the results of Olave-Rojas et al. (2018) by finding three substructures at $\sim 5R_{200}$ from the centre of MACS0416 which have galaxy populations of similar density, luminosity and colour as those in the core of the cluster, suggesting they are already evolved prior to their incorporation. More observational evidence of pre-processing on the outskirts of clusters ($R \gtrsim R_{200}$), and other high-mass haloes, exists in the literature (e.g. Gill et al. 2005; McGee et al. 2009; Dressler et al. 2013; Bianconi et al. 2018; Džudžar et al. 2019; Einasto et al. 2020; Werner et al. 2021), as well as evidence in simulations (e.g. Yi et al. 2013; Joshi et al. 2017; Han et al. 2018; Bakels et al. 2021).

Massive galaxy clusters are found at the nodes of cosmic filaments (Bond et al. 1996), which feed infalling, often pre-processed, galaxies into the cluster (as discussed above; e.g. Ebeling et al. 2004; Martínez et al. 2016; Salerno et al. 2019). As demonstrated in Figure 3.11, there is tentative evidence that the major axis of the BCG is preferentially aligned with the LSS. This was first noted by Argyres et al. (1986), and further confirmed by Lambas et al. (1988), who found a correlation between the BCG major axis and Lick galaxy counts (Seldner et al. 1977) in Abell clusters. Recently, Smith et al. (2023) found that the BCGs in their sample of 211 X-ray-selected clusters are significantly preferentially aligned with the LSS out to as far as $10R_{200}$ from the cluster centre. In a similar result, Paz et al. (2011) found that there was a correlation between the overall shapes of galaxy groups and their surrounding galaxies out to distances of $\approx 30\,\mathrm{Mpc}$. Additionally, some studies have gone further and found that, as well as aligning with cosmic filaments, clusters can also align with other nearby clusters and thereby the filaments that may connect them (see Govoni et al. 2019). van Uitert & Joachimi (2017) found that redMaPPer clusters tend to align with neighbouring clusters, suggesting the systems share what they dub a "common alignment mechanism" (see also Smargon et al. 2012).

Additionally, some studies have found that there exists a significant population of backsplash galaxies that occupy the outer regions of relaxed clusters (Gill et al. 2005; see also Balogh et al. 2000; Mamon et al. 2004; Knebe et al. 2011). For

example, Kuchner et al. (2021) found that as many as 40–60% of satellites at 1–1.5R_{200} of relaxed clusters are backsplash galaxies in The ThreeHundred[1] cosmological zoom-in simulations (Cui et al. 2018). We suggest that the peak anisotropic quenching signal found at 0.5–1R_{200} may be due to a build-up of backsplash galaxies along the major axis.

Our results show that galaxies on the major axis have been in high density regions for longer and therefore have experienced more pre-processing. This reconciles all previous works on anisotropic quenching in massive clusters, as our results suggest it is simply pre-processing in major filaments aligned with the BCG.

3.5 Conclusions

In this work, we have investigated the observed phenomenon dubbed anisotropic quenching (also known as "angular conformity" or "angular segregation") of satellite galaxies in 11 CLASH clusters at $z \sim 0.36$. We analysed galaxy colour $(B-R)_{\text{corr.}}$ and passive galaxy fractions ($f_{\text{pass.}}$) as a function of their orientation angle from the major axis of the BCG. This analysis was done on two samples of galaxies determined by setting different R-band magnitude limits to see if the effects of anisotropic quenching differ between galaxy populations. The SFR of a satellite galaxy is highly dependent on its local environment (Peng et al. 2010b), therefore we also measured $(B-R)_{\text{corr.}}$ and $f_{\text{pass.}}$ as a function of local surface density using an nth-nearest neighbour method (see Equation 3.3) along both axes to determine if the signal was caused by a difference in environment between them. Our results are summarised as follows:

i) From Figure 3.1, we find there is an anisotropic angular distribution of $(B-R)_{\text{corr.}}$ from the BCG major axis in the CLASH clusters. Using a -16.8 mag (-18.6 mag) R-band magnitude limit, we find the signal is well described by a cosine fit (see Equation 3.2), where the amplitude of the signal is $A = 0.14 \pm 0.01$ ($A = 0.12 \pm 0.01$) and peaks along the major

[1] https://www.nottingham.ac.uk/astronomy/The300/index.php

axis. This is a significant amplitude and is among the largest found when analysing the angular evolution of satellite colour from the BCG (e.g. Stott 2022). The period of the signal is $P = 178.9 \pm 1.8°$ ($P = 177.5 \pm 1.9°$).

ii) To analyse anisotropic quenching more directly, it is more appropriate to analyse differences in $f_{\text{pass.}}$ and, from Figure 3.5, we find a clear anisotropic signal. Using Equation 3.2 to fit the signal to our $-16.8\,\text{mag}$ ($-18.6\,\text{mag}$) magnitude-limited sample, we find an amplitude of $A = 0.059 \pm 0.007$ ($A = 0.064 \pm 0.005$) with a period of $P = 179.5 \pm 3.0°$ ($P = 176.1 \pm 2.1°$). The amplitude of this signal is in excess of 5σ with a fitted period consistent with $\approx 180°$, which peaks along the major axis. This is a clear sign that there is anisotropic quenching in our sample of galaxy clusters.

iii) We find little difference in the strength of the anisotropic quenching signal between our two magnitude-limited samples. This indicates that the driver of the signal may not be RPS, as we would expect to see a larger impact on the more complete sample.

iv) We measured the amplitude of the anisotropic quenching signal in $0.25R_{200}$-diameter circular annuli going out from the centre of the cluster up to $2R_{200}$. This is the largest cluster-centric radius in which anisotropic quenching has been observed, and also marks the first time the amplitude of the sinusoidal signal in individual annuli has been measured. We find that the amplitude of the $f_{\text{pass.}}$ fit is significant out to at least $1.25R_{200}$, beyond which the amplitude begins to drop. The peak of the fit occurs at ~ 0.5–$1R_{200}$, with little difference between our two samples.

v) We find that $f_{\text{pass.}}$ increases with increasing local surface density, in line with expectations. However, we find that $f_{\text{pass.}}$ is 0.15 ± 0.02 higher along the major axis of the BCG for surface density values $\lesssim 10^{-4.0}\,\text{kpc}^{-2}$. This is a significant difference which suggests that differences in local density between the major and minor axes are not the primary driver of anisotropic quenching. For surface densities $\gtrsim 10^{-4.0}\,\text{kpc}^{-2}$, the difference in $f_{\text{pass.}}$ drops to 0.04 ± 0.02, suggesting the effects of environmental quenching in these denser groups begin to dominate.

vi) We analysed how surface densities evolve from the centre of the cluster. We find that both $f_{\rm pass.}$ (see Figure 3.10) and local surface densities (see Figure 3.11) are higher along the major axis than along the minor axis. Both parameters drop more quickly along the minor axis than the major axis. We interpret this as galaxies, which are being preferentially fed along the major axis, infall into the cluster in groups that have been pre-processed over a longer time. This reconciles previous works on anisotropic quenching in massive clusters.

A paper from Zakharova et al. (2025) came out during the final review stage of our study for publication, which investigated anisotropic quenching in satellite galaxies of $M_h = 10^{12}$–$10^{14.2}\,\mathrm{M}_\odot$ haloes in the IllustrisTNG simulations, specifically the TNG100-1 magneto-hydrodynamical model. They analysed the anisotropic quenching signal out to $5R_{200}$, separating between young and old populations. They find that satellite galaxies preferentially infall into the haloes along the major axis of the central galaxy through cosmic filaments that themselves tend to align with the major axis. This agrees with our interpretation here based on observations of the CLASH clusters. They conclude that the anisotropic quenching signal emerges at the point young satellites infall into the larger halo and that this signal is significant out to large radii from the centre of the halo ($5R_{200}$). Their findings further agree with our conclusions by showing that AGN feedback cannot explain the signal at these large radii. Whilst based on an analysis with a lower average halo mass than our sample, we believe the remarkable agreement between our conclusions and those of Zakharova et al. (2025) further strengthens the interpretation that anisotropic quenching is a result of LSS.

A logical extension to the anisotropic quenching signal we observe is that galaxies along the major axis may be more elliptical, and those along the minor axis may be more disc-like. Existing observations of the satellites in our sample could confirm if this is the case here, and simulations can be used to test if this is a regular occurrence. If it is, then this may have implications for weak gravitational lensing measurements, with contaminants from the cluster having a different shape depending on their orientation about the BCG (see Kirk et al. 2015 for a review on weak lensing). Additionally, as discussed in Chapter 3.4.2, there

have been simulations that support the idea of pre-processing of infalling cluster galaxies, as well as those that show that the overall shape of clusters aligns with the cosmic filaments that feed them these pre-processed groups. In the future, to probe the ideas presented in this chapter, further simulations of infalling galaxy groups should be explored with an additional focus on whether pre-processed galaxies remain in orbit along the major axis long enough for an anisotropic quenching signal to be readily apparent as a result of their incorporation into the cluster. Future studies should also focus on the impact of backsplash galaxies on this signal.

Chapter 4

The Sizes and Merger Fraction of Star-forming Galaxies During the Epoch of Reionization

Abstract

We used observations from the *JWST* Emission Line Survey (JELS) to measure the half-light radii (r_e) of 23 Hα-emitting SF galaxies at $z = 6.1$ in the PRIMER/COSMOS field. Galaxy sizes were measured in *JWST*/NIRCam observations in rest-frame Hα (tracing recent star formation) with the F466N and F470N narrow-band filters from JELS, and compared against rest-frame R-band, V-band (tracing established stellar populations) and near-UV sizes. We find a size–stellar mass (r_e–M_*) relationship with a slope that is consistent with literature values at lower redshifts, though offset to lower sizes. We observe a large scatter in r_e at low stellar mass ($M_* < 10^{8.4}\,\mathrm{M}_\odot$) which we believe is the result of bursty star formation histories (SFHs) of SF galaxies at the EoR. We find that the stellar and ionised gas components are similar in size at $z = 6.1$. The evidence of already-established stellar components in these Hα emitters (HAEs) indicates previous episodes of star formation have occurred. As such, following

other JELS studies finding our HAEs are undergoing a current burst of star formation, we believe our results indicate that SF galaxies at the end of the EoR have already experienced a bursty SFH. From our r_e–M_* relationship, we find $r_{e,\mathrm{F444W}} = 0.76 \pm 0.46\,\mathrm{kpc}$ for fixed stellar mass $M_* = 10^{9.25}\,\mathrm{M}_\odot$, which is in agreement with other observations and simulations of SF galaxies in the literature. We find a close-pair (major) merger fraction of ($f_{\mathrm{maj.merger}} = 0.44 \pm 0.22$) $f_{\mathrm{merger}} = 0.43 \pm 0.11$ for galaxy separations $d \lesssim 25\,\mathrm{kpc}$, which is in agreement with other $z \approx 6$ studies.

4.1 Introduction

The redshift evolution of the basic physical properties of galaxies, such as their size, stellar mass, luminosity, and morphology provide vital constraints for models of galaxy formation. Additionally, how these properties change with respect to each other can constrain the evolutionary tracks that galaxies follow. One example is the size distribution of galaxies as a function of their stellar mass. Galaxy sizes are often measured in units of "effective" or "half-light" radius (r_e), defined as the radius in which half of a galaxy's light is contained. r_e can range from $\approx 0.1\,\mathrm{kpc}$ (e.g. Ono et al. 2023) to $\gtrsim 10\,\mathrm{kpc}$ (e.g. Kawamata et al. 2015; Dullo et al. 2017). The distribution and evolution of r_e can be used to infer properties of the host DM halo, including its virial radius (Mo et al. 1998; Dutton et al. 2007; Fu et al. 2010), spin or angular momentum (Bullock et al. 2001; Dutton 2009), and merger history (Naab et al. 2009; Ownsworth et al. 2014).

There is strong evidence that galaxy sizes correlate with stellar mass such that higher mass galaxies have a larger r_e (the size–mass relationship; r_e–M_*). In their influential work, Shen et al. (2003) studied the r_e distributions of $\approx$ 140 000 galaxies in SDSS as a function of stellar mass and luminosity and found a clear correlation with both. They also found that both relations are significantly steeper for ETGs than LTGs, the latter of which has a characteristic stellar mass in the local Universe ($M_{*,0} = 10^{10.6}\,\mathrm{M}_\odot$) above which the slope steepens but remains shallower than that of ETGs. van der Wel et al. (2014) extended the analysis of the r_e–M_* relationship out to higher redshifts, covering $0 \lesssim z \lesssim 3$

by making use of *HST* data from the 3D–HST survey (Brammer et al. 2012) and CANDELS (Grogin et al. 2011; Koekemoer et al. 2011). The results of van der Wel et al. (2014) are in qualitative agreement with Shen et al. (2003) such that the slope of the r_e–M_* relation is shallower for LTGs, though they see a flattening in the slope of ETGs at $M_* \lesssim 10^{10}\,\mathrm{M}_\odot$. Many studies have measured r_e–M_* relations at a range of redshifts ($0 < z < 5$; Daddi et al. 2005; Trujillo et al. 2006, 2007; Stott et al. 2011, 2013a; Lange et al. 2015; Paulino-Afonso et al. 2017; Faisst et al. 2017; Mowla et al. 2019a,b). More recently, studies have utilised the high resolution of *JWST* (Gardner et al. 2006; Rigby et al. 2023) in the NIR to study the structural properties of galaxies in the rest-frame optical at $z \gtrsim 3$ including sizes (Suess et al. 2022; Ono et al. 2023; Ormerod et al. 2023; Allen et al. 2025; Martorano et al. 2024; Varadaraj et al. 2024; Ward et al. 2024; Miller et al. 2025; Westcott et al. 2025; Ji et al. 2026), resolved star formation (Ji et al. 2024; Li et al. 2024; Matharu et al. 2024; Morishita et al. 2024) and morphology (Ito et al. 2024; Ono et al. 2024, 2025; Vega-Ferrero et al. 2024).

As mentioned above, there has been a clear redshift evolution of r_e and the r_e–M_* relationship. van der Wel et al. (2014) found that their r_e measurements at $z \sim 0$ are consistent with those of SDSS galaxies in Shen et al. (2003) and Guo et al. (2009; after accounting for systematic differences in their respective methods; see van der Wel et al. 2014), but observed an increasing offset from the local r_e–M_* relation for higher redshift galaxies. The power-law that they use to describe the redshift evolution of galaxy sizes is of the form

$$\frac{r_e}{\mathrm{kpc}} = B(1+z)^{\beta}, \tag{4.1}$$

where B is the intercept and β is the power-law slope. Equation 4.1 is used as standard in the literature to describe the redshift evolution of r_e, typically for some characteristic stellar mass (Stott et al. 2013a; Shibuya et al. 2015; Paulino-Afonso et al. 2017; Cutler et al. 2022; Sun et al. 2024; van der Wel et al. 2024). Specifically, van der Wel et al. (2014) find that for a fixed stellar mass of $10^{10.75}\,\mathrm{M}_\odot$, the sizes of LTGs and ETGs evolve as $r_e \propto (1+z)^{-0.72}$ and $r_e \propto (1+z)^{-1.24}$ respectively. These results reflect an $\approx 3.7\,\mathrm{kpc}$ ($\approx 55\%$) and $\approx 3.2\,\mathrm{kpc}$ ($\approx 74\%$) decrease in r_e, respectively, between $z < 0.5$ and $2.5 < z < 3$.

Using *JWST* data from The Cosmic Evolution Early Release Survey (CEERS; Finkelstein et al. 2023; Bagley et al. 2023) and *HST* data from CANDELS, Ward et al. (2024) found that the average r_e decreased further out to $z = 5.5$. Their power law slope of $\beta = -0.67 \pm 0.07$ for a characteristic mass of $\approx 10^{10.7}\,\mathrm{M}_\odot$ is also consistent with that of van der Wel et al. (2014). It is crucial to extend analysis of galaxy sizes to even higher redshifts, and for homogeneously-selected populations, in order to constrain this power-law further and to shed new light on the first era of galaxy formation.

In order to disentangle the contributions of active star formation from the longer-term, in-situ SFH on the size evolution discussed above, one must use SFR indicators that are distinct to both, as well as high spatial resolution images to resolve active SF regions. The Hα (6563 Å) emission line is one of the most frequently used SFR indicators for recent star formation in a galaxy (Kennicutt 1998; Erb et al. 2006b; Sobral et al. 2013; Terao et al. 2022; Covelo-Paz et al. 2025). This is because it traces the ionised gas emission resulting from the recombination of hydrogen surrounding the most massive stars (Hao et al. 2011b; Murphy et al. 2011), which typically only live for $\lesssim 10\,\mathrm{Myr}$ (Ekström et al. 2012). The rest-frame UV or near-UV (NUV) continuum of a galaxy can also be used to trace star formation, but on longer timescales ($\sim$ 10–200 Myr) as it traces the photons emitted directly from the photospheres of stars upwards of several solar masses. For a comprehensive review of SFR indicators and the populations they trace, see Kennicutt & Evans (2012; also Madau & Dickinson 2014; Sánchez 2020; Schinnerer & Leroy 2024). Typically, the UV continuum has been used to infer the SFR of galaxies at $z \gtrsim 2$ as its wavelength gets redshifted into optical bands (Wyder et al. 2005; Bouwens et al. 2012a,b, 2015; Oesch et al. 2018; Harikane et al. 2023), whereas Hα is shifted further into IR bands which are more difficult to observe with ground-based instruments. However, UV measurements are extremely sensitive to dust attenuation (e.g. Calzetti et al. 1994; Dunlop et al. 2017; Bouwens et al. 2020; Traina et al. 2024), and there is evidence that the effects of dust continue to impact observations out to the EoR (Gruppioni et al. 2020; Bowler et al. 2022; Algera et al. 2023; Zavala et al. 2023). Moreover, while there exist dust attenuation calibrations that aim to correct for these issues (e.g. Calzetti et al. 2000; Salim et al. 2007), these depend heavily on assumptions of

the UV continuum slope, intrinsic colours and the choice of dust extinction curve which may impact the measured properties of these selected objects (Walcher et al. 2011; Arrabal Haro et al. 2023).

The benefit of the Hα emission line is that it is less affected by dust attenuation, which relieves these issues (though we note that the extinction in the nebular regions is more uncertain at high-z; Reddy et al. 2020, 2026). With *JWST* able to access Hα at $z \gtrsim 2.5$, combined with its high resolution imaging, we are now able to probe the physical properties of samples of SF galaxies at earlier times than before. Some studies are already showcasing the ability to probe star formation using Hα out to $3.7 \lesssim z \lesssim 6.5$ using grism spectroscopy to select on Hα (Matharu et al. 2023; Nelson et al. 2024; Covelo-Paz et al. 2025). Another approach is to use narrow-band (NB) imaging selection on Hα to look for SF galaxies, as this also provides a selection based on the strength of the emission line. A key advantage of NB imaging is that it mitigates some of the selection effects that can arise from slitless spectroscopy, such as source blending, morphology-dependent line sensitivity, and difficulties in assigning emission lines to sources (particularly in crowded regions). When combined with BB photometry, NB imaging also provides a much narrower redshift range for selected sources and it provides a direct image of the ionised gas without needing to reconstruct one from the slitless spectroscopy. This method was notably used by the Hi-Z Emission Line Survey (HiZELS; Geach et al. 2008; Sobral et al. 2009, 2013) which utilised the Wide Field Camera (WFCAM; Casali et al. 2007) on the United Kingdom Infrared Telescope (UKIRT) to significantly expand the volume of previous NB imaging surveys (e.g. Thompson et al. 1996; Moorwood et al. 2000). As a result of the NB imaging selection of HiZELS, many studies were able to measure the properties of homogeneously-selected Hα emitters (HAEs) out to $z = 2.23$ (Sobral et al. 2010; Garn et al. 2010; Swinbank et al. 2012a,b; Sobral et al. 2012, 2013; Stott et al. 2013b; Oteo et al. 2015; Sobral et al. 2016; Cochrane et al. 2017, 2018; Cheng et al. 2020; Cochrane et al. 2021), including r_e measurements (Stott et al. 2013a; Paulino-Afonso et al. 2017; Naufal et al. 2023).

In this chapter, we use data from the *JWST* Emission Line Survey (JELS; GO #2321; PI: Philip Best; see Duncan et al. 2025; Pirie et al. 2025) to probe the r_e properties of 23 $z = 6.1$ SF galaxies in the first Hα-selected sample of

HAEs from NB imaging at the EoR. We combine the JELS observations with ancillary multi-wavelength data from the *JWST* Cycle 1 Observer Treasury Program "Public Release IMaging for Extragalactic Research survey" (PRIMER; PI Dunlop, GO #1837)[1]. We primarily use *JWST*/NIRCam long-wavelength (LW) channel observations in JELS F466N, JELS F470N NB and PRIMER F444W BB filters to study the rest-R-band Sérsic light profiles (Sérsic 1963, 1968) of HAEs at the EoR, taking advantage of the image resolution *JWST* provides at $\lambda \approx 3.8$–$5\,\mu$m. This allows us to probe both active star formation and older stellar populations at $z = 6.1$. In addition to rest-R-band sizes, we also measure the light profiles in PRIMER F277W (rest-NUV) and PRIMER F356W (rest-V-band). Our measured r_e values are then compared to both observations and simulations. We also measure the size ratio of the SF component (traced by the ionised gas from the Hα emission) and the stellar continuum to infer how EoR HAEs have evolved over the preceding 1 Gyr.

This chapter is arranged as follows. In Chapter 4.2, we summarise the JELS survey and photometric catalogue. We explain how we determine our final sample of HAEs in Chapter 4.2.1. In Chapter 4.3, we describe the methods used to fit galaxy sizes in different wavebands. We outline key results in Chapter 4.4, and discuss their implications in Chapter 4.5. We summarise our conclusions in Chapter 4.6.

A standard ΛCDM cosmology model is assumed with values $\Omega_\Lambda = 0.7$, $\Omega_m = 0.3$ and $H_0 = 70\,\mathrm{km\,s^{-1}\,Mpc^{-1}}$. Any magnitudes stated are presented using the AB system (Oke & Gunn 1983). All results and comparisons to the literature in this chapter assume a Chabrier (2003) IMF.

4.2 JELS Data

The JELS survey is described in full by Duncan et al. (2025) and Pirie et al. (2025). Here, we will summarise the key details that are relevant for our work.

The primary goal of JELS is to provide a homogeneously-selected catalogue of Hα-selected galaxies at the EoR from the Cosmic Evolution Survey Deep Field

[1]https://primer-jwst.github.io

(COSMOS; Scoville et al. 2007a,b). In this context, "homogeneously-selected" refers to the fact that galaxies are identified solely based on their Hα emission-line strength, providing a uniform tracer of star formation and avoiding biases introduced by continuum- or colour-based selection methods. This is, in effect, a selection on SFR, though we note here the catalogue described in this chapter is complete in stellar mass to $\approx 10^{8.2}\,\mathrm{M}_{\odot}$. This selection is achieved by employing the F466N and F470N NB filters in the *JWST*/NIRCam LW channels, with pivot wavelengths of $\lambda_{\mathrm{pivot}} = 4.654\,\mu\mathrm{m}$ (effective width $W_{\mathrm{eff}} = 0.0535\,\mu\mathrm{m}$) and $\lambda_{\mathrm{pivot}} = 4.707\,\mu\mathrm{m}$ ($W_{\mathrm{eff}} = 0.0510\,\mu\mathrm{m}$) respectively. These two filters centre on $z \approx 6.09$ and $z \approx 6.17$ for the Hα emission line, which allows for line emitters to be selected through difference imaging in a selection volume of $\sim 2.4 \times 10^4\,\mathrm{Mpc}^3$. In addition, the NB observations from JELS are designed to overlap with multi-wavelength observations from CANDELS (Grogin et al. 2011; Koekemoer et al. 2011; Brammer et al. 2012; Teplitz 2018) and, more crucially, with the *JWST* Cycle 1 Observer Treasury Program PRIMER survey (PI Dunlop, GO #1837)[1]. Specifically, LW BB observations in the F444W filter ($\lambda_{\mathrm{pivot}} = 4.4043\,\mu\mathrm{m}$; $W_{\mathrm{eff}} = 1.0676\,\mu\mathrm{m}$) from PRIMER — with a wavelength range that covers F466N and F470N — allow for this NB excess selection at $\sim 4.7\,\mu\mathrm{m}$. In this work, we also make use of PRIMER observations in F277W ($\lambda_{\mathrm{pivot}} = 2.7617\,\mu\mathrm{m}$; $W_{\mathrm{eff}} = 0.6615\,\mu\mathrm{m}$) and F356W ($\lambda_{\mathrm{pivot}} = 3.5684\,\mu\mathrm{m}$; $W_{\mathrm{eff}} = 0.7239\,\mu\mathrm{m}$) for rest-NUV and rest-$V$-band measurements respectively. The resulting deep, multi-wavelength coverage has enabled robust photometry for SED fitting to constrain the SFH of the HAEs. The SED fitting for our HAEs was performed by Pirie et al. (2025) using the `BAGPIPES` spectral fitting code (Carnall et al. 2018). They use `BPASS` (Eldridge et al. 2017; Stanway & Eldridge 2018) for their stellar population synthesis model, and the `CLOUDY` photoionisation code (Ferland et al. 2017) for nebular emission line computation. They assume a Salim et al. (2018) dust attenuation model and the continuity non-parametric SFH model from Leja et al. (2019). We refer the reader to Table 8 of Pirie et al. (2025) for details on the models and priors.

Overall, the JELS survey has continuous coverage over a $\sim 63\,\mathrm{arcmin}^2$ area of the COSMOS field (see Figure 3 of Duncan et al. 2025) with the final images

homogenised to a common point-spread function (PSF) with a resolution of $0.03 \times 0.03\,\mathrm{arcsec}^2$ per pixel.

We note here that the science conducted in this chapter is based on the initial versions of the JELS imaging products, referred to as v0.8 images, also used in Pirie et al. (2025). The newer v1.0 images incorporate re-observations taken in November 2024 to better mitigate scattered light issues and use an updated version of the *JWST* pipeline for image reduction. We refer the reader to Appendix A of Duncan et al. (2025) for details on the differences between the v0.8 images used here and the updated v1.0 images. Throughout this chapter, all references to source IDs refer to their JELS v0.8 catalogue value and may not correspond to subsequent revisions of the catalogue.

4.2.1 Sample Selection

To analyse the structural properties of SF galaxies at the EoR, we derive our own sample from the multi-wavelength JELS v0.8 catalogues that are described in detail by Pirie et al. (2025), specifically their Sections 3 and 4 where the method for identifying NB excess emitters from multi-wavelength detections is outlined. Briefly, their selection is based on significant NB excess relative to either the overlapping PRIMER F444W BB or neighbouring NB filter, combined with photo-z cuts around $z \sim 6.1$, with additional visual inspection to remove residual contamination. Following this, they finalise a catalogue of 35 HAEs (30 F466N sources; 5 F470N sources). We refer to the Pirie et al. (2025) catalogue as the 'parent' catalogue in this chapter, and it is from this that we determine the sample used for the analysis in this work.

In order to accurately measure r_e, we need a sample of galaxies from which we are able to reliably measure Sérsic profiles. Therefore, we removed sources from the parent catalogue of Pirie et al. (2025) that had some additional complications which made them difficult or impossible to reliably model. Here, we will outline which sources were removed, reiterating that the IDs refer to the JELS v0.8 catalogue. Sources 2768 and 7810 (both F466N selected) were removed because light profile fits in both NB and F444W images strongly preferred a PSF model over a Sérsic model (based on the χ^2 outputs of the `GALFIT` model; see Chapter 4.3.1),

indicative of a point source dominating the galactic emission; 12164 (F466N) was removed because a PSF model was strongly preferred in the F444W image (see Chapter 4.3.1) meaning point source emission is likely dominating; 4453 and 4457 (both F466N) were removed as they appear to be a merging system (see Chapter 4.4.4) that is too faint to individually model in the F444W image; 10983 (F466N) was removed because, despite being an isolated source in the NB image, it appears to be part of a three-way merging system in F444W which made it difficult to isolate when modelling. Finally, a number of HAEs were too faint in F444W to accurately model. From F466N detections, 5629 (≈ 28.7 mag), 6501 (≈ 28.8 mag), 7147 (≈ 29.3 mag) and 9123 (≈ 28.7 mag) were removed, as well as 8033 (≈ 30.1 mag) and 15619 (≈ 28.8 mag) from F470N detections. See Figure A1 of Pirie et al. (2025) for multi-wavelength imaging of all excess sources, including those we do not include in our final HAEs sample.

Following these removals, we obtain a sample of 23 Hα-emitting SF galaxies at $z = 6.1$ (20 detected in F466N; 3 detected in F470N). These galaxies have a stellar mass range of $M_* = 10^{8.06}$–$10^{9.28}\,\mathrm{M}_\odot$ ($M_{*,\mathrm{median}} = 10^{8.30}\,\mathrm{M}_\odot$), and SFR range of $\mathrm{SFR}_{\mathrm{H}\alpha} = 1.03$–$14.22\,\mathrm{M}_\odot\,\mathrm{yr}^{-1}$ (median $\mathrm{SFR}_{\mathrm{H}\alpha,\mathrm{median}} = 2.73\,\mathrm{M}_\odot\,\mathrm{yr}^{-1}$). Stellar masses and SFRs are derived in Pirie et al. (2025), where the latter is determined using the Hα SFR relation in Theios et al. (2019). We note SFR values derived from Hα are consistent with the 10 Myr SFR output from SED fitting. All stellar mass and SFR values in Pirie et al. (2025) are converted here to a Chabrier (2003) IMF.

The parent catalogue is representative of HAEs at $z = 6.1$ in terms of Hα equivalent width (EW; see Figure 11 of Pirie et al. 2025), with an EW limit well below the SF galaxy population at this redshift (see Endsley et al. 2024). Our final sample of 23 HAEs is similarly representative in EW, and note that Hα contributes a median 91% of the total NB flux of these sources. We note that our final sample is also complete in stellar mass down to $\approx 10^{8.2}\,\mathrm{M}_\odot$. For detailed analysis on the SFR properties of these galaxies, we refer the reader to Pirie et al. (2025) who compare to the SF main sequence measured by Cole et al. (2025) for galaxies in CEERS. However, we note that the median offset of our 23 HAEs from the Cole et al. (2025) SFR_{10} SF main sequence is $\Delta_{\mathrm{MS}} \approx +0.56$ dex when using their $5 < z < 6$ relation, and $\Delta_{\mathrm{MS}} \approx +0.39$ dex when using their

$6 < z < 7$ relation. In contrast, relative to the Cole et al. (2025) SFR_{100} main sequence, we find median offsets of $\Delta_{\mathrm{MS}} \approx -0.19\,\mathrm{dex}$ and $\Delta_{\mathrm{MS}} \approx -0.28\,\mathrm{dex}$ for the $5 < z < 6$ and $6 < z < 7$ relations, respectively, suggesting these galaxies are currently undergoing, or have just gone through, a burst of star formation (Pirie et al. 2025).

4.3 Sérsic Modelling

To measure the Sérsic light profiles (Sérsic 1963, 1968) of our sources, we use `GALFIT`[1] version 3.0.7d4 (Peng et al. 2002, 2010a) — a non-linear least-squares fitting algorithm designed for 2D parametric galaxy fitting. `GALFIT` finds the optimum solution using a Levenberg–Marquardt algorithm when modelling the light profile of a source for a given input image. This best-fitting solution is determined via a reduced chi-squared (χ^2_ν) method, whereby `GALFIT` iterates over a large number of possible models by adjusting the input parameters until χ^2 is minimised. χ^2_ν describes the goodness-of-fit of the output model and is determined by

$$\chi^2_\nu = \frac{1}{N_{\mathrm{DOF}}} \sum_{x=1}^{nx} \sum_{y=1}^{ny} \frac{\left(f_{\mathrm{data}}(x,y) - f_{\mathrm{model}}(x,y)\right)^2}{\sigma(x,y)^2}, \tag{4.2}$$

where N_{DOF} is the number of degrees of freedom (DOF), $f_{\mathrm{data}}(x,y)$ represents the data image supplied to `GALFIT`, $f_{\mathrm{model}}(x,y)$ represents the model image that `GALFIT` outputs following the least-squares fitting, and $\sigma(x,y)$ represents the sigma image fed to `GALFIT`. For the Sérsic fits in this work, $f_{\mathrm{model}}(x,y)$ is generated by convolving the intrinsic parametric Sérsic light profile with the input PSF. The sigma image is the relative error of the flux at each position (x,y) within the data image. This is summed over all x and y pixels, where nx and ny are the x and y dimensions, respectively, of the data and model images.

We fit a Sérsic model of the form

[1] https://users.obs.carnegiescience.edu/peng/work/galfit/galfit.html

$$\Sigma(r) = \Sigma_e \exp\left\{-b_n\left[\left(\frac{r}{r_e}\right)^{1/n} - 1\right]\right\}, \tag{4.3}$$

where $\Sigma(r)$ is the pixel surface brightness at radius r from the centre of a source, r_e is the half-light radius of the source and Σ_e is the pixel surface brightness at r_e. The Sérsic index of the model, n, determines the overall shape of the light profile and b_n is a dimensionless scale factor that is dependent on n (see Ciotti & Bertin 1999 for a full explanation and asymptotic expansion). In general, LTGs follow a Sérsic light profile with $n \lesssim 2.5$ (shallow inner profile which truncates more sharply at large r; Sérsic 1968; Kelvin et al. 2012) and ETGs follow a profile where $n \gtrsim 2.5$ (sharply decreasing inner profile with r but extended wing at large r; Caon et al. 1993). The most commonly used Sérsic indices are $n = 1$ which describes a purely exponential profile suitable for galactic disks (Freeman 1970), and $n = 4$ which gives a de Vaucouleurs profile (de Vaucouleurs 1948) suitable for bright elliptical galaxies.

4.3.1 Fitting with `GALFIT`

For our HAEs, we fit a single-component Sérsic profile in all the images we model. We particularly focus on results from the detected JELS F466N and F470N images and the corresponding PRIMER F444W image (equivalent to rest-R-band). This is to measure r_e of both the Hα-selected SF component and the emission from the stellar population respectively. However, we also follow the procedures in this chapter for the PRIMER F277W and PRIMER F356W images for rest-NUV and rest-V-band sizes respectively. From this, we can then assess how our results at $z = 6.1$ compare to sizes in the literature, including other r_e–M_* relations. We can also directly compare the NB and F444W sizes to draw conclusions about how SF galaxies are evolving at the EoR (see Chapter 4.4.2). The steps we take to model our sources are as follows:

i) First, we create $100\times100\,\mathrm{pixel}^2$ ($3\times3\,\mathrm{arcsec}^2$; $\sim 17\times17\,\mathrm{kpc}^2$) cutouts of each source centred on the corresponding R.A. and Dec. of the SExtractor (Bertin & Arnouts 1996) source coordinates in a given band. We do the same

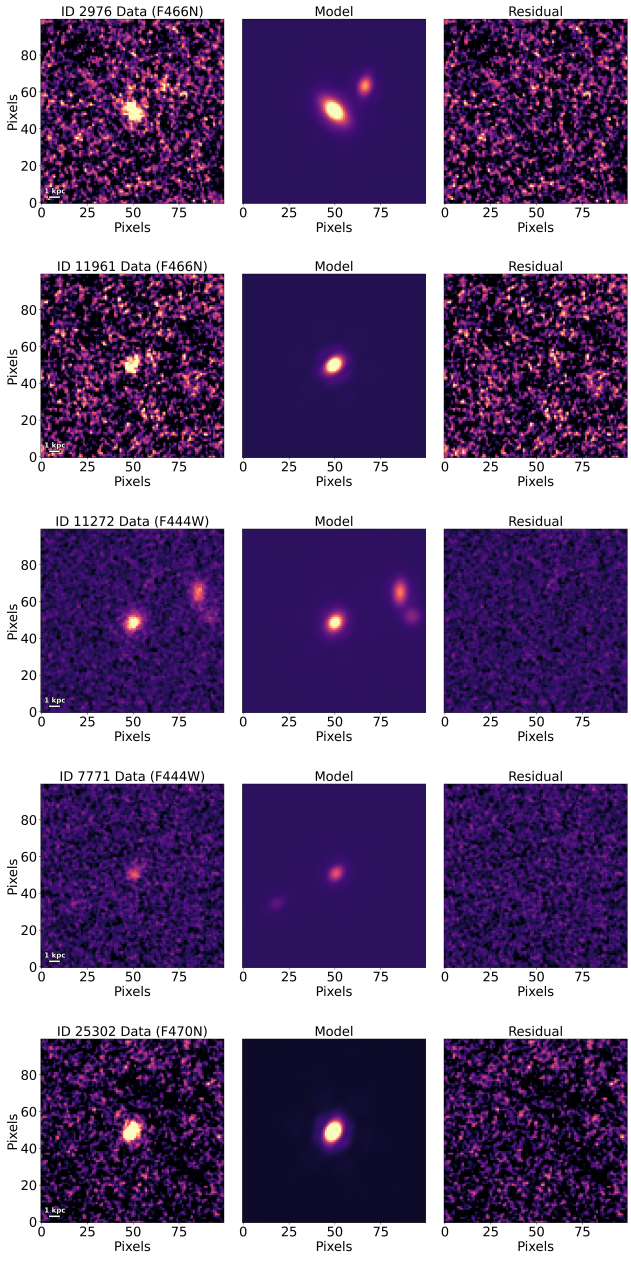

Figure 4.1: Example models for five HAEs in our sample. The left panels are the rest-R-band observations, with the *JWST*/NIRCam filter used for the observation indicated in the title of the panel. The middle panels are the fixed $n = 1$ Sérsic models from `GALFIT` of the selected object. The right panels are the residual emission once the modelled galaxy is removed from the observed image. Each panel is a $3 \times 3\,\mathrm{arcsec}^2$ ($\approx 17 \times 17\,\mathrm{kpc}^2$) cutout centred on the detected galaxy.

for the corresponding "weights" map which is used to create the sigma image to be fed to `GALFIT`. This weights map has pixel values equal to $1/(\sigma(x,y)^2)$ so, accordingly, these values are converted such that the sigma image pixel values are $\sigma(x,y)$. Such a relatively large area for the cutout image was decided in order for `GALFIT` to measure the sky background and confidently capture the wings of the PSF (see below). Any additional sources in the cutout, identified via SExtractor, are modelled separately so that their light is not accounted for in the selected source model.

ii) As with all telescopes, *JWST* images have an intrinsic PSF that must be accounted for (Perrin et al. 2014; Rigby et al. 2023). We chose to use empirical $100 \times 100\,\mathrm{pixel}^2$ PSFs described in detail by Pirie et al. (2025). In summary, these empirical, filter-dependent PSFs were generated by stacking bright and unsaturated stars in a given filter via a bootstrapping method. These PSFs from Pirie et al. (2025) are comparable to simulated PSFs[1] generated by WebbPSF[2] (Perrin et al. 2014). The choice of PSF makes no significant difference to our results.

iii) `GALFIT` requires a set of initial estimates to be provided for each of the fitted parameters. These are the centroid x and y coordinates of the source in pixel units; the integrated apparent magnitude in the chosen filter; r_e in pixel units; the Sérsic index n; the semi-minor axis over semi-major axis radius ratio (axis ratio $b/a = q$, where $q = 1$ for a circle and $q < 1$ for an ellipse); and the position angle (θ_{pa}) of the major axis on the sky in degrees measured anti-clockwise from North. Similar to previous studies, we use the SExtractor outputs for each of these parameters as our initial guess (e.g. van der Wel et al. 2012; Mowla et al. 2019b; Kartaltepe et al. 2023; Ormerod et al. 2023; Westcott et al. 2025), with the exception of the integrated magnitude as we used magnitudes derived from flux inside a 0.6 arcsecond-diameter aperture centred on each source to be consistent with Pirie et al. (2025).

[1] https://jwst-docs.stsci.edu/jwst-near-infrared-camera/nircam-performance/nircam-point-spread-functions

[2] https://www.stsci.edu/jwst/science-planning/proposal-planning-toolbox/psf-simulation-tool

iv) The nature of these observations means that these distant galaxies tend to be very small on the image, causing `GALFIT` to often get stuck in local minima that produce unrealistic output parameters. Additionally, `GALFIT` will fail if it cannot produce a physical solution (Peng et al. 2010a). To avoid these outcomes, we apply constraints to bound each parameter to be between certain values. These constraints are as follows: the centroid coordinates are allowed to vary ± 5 pixels from the input values in both x and y; the integrated magnitude is allowed to vary ± 2 mag from the input value; r_e is constrained to $0.1 \leq r_e \leq 100$ pixels; the axis ratio is constrained to $0.2 \leq q \leq 1$; and $\theta_{\rm pa}$ is allowed to vary $\pm 20°$ from the input values. Each of these constraints is applied to all images. For the Sérsic index n, we initially took two approaches. When modelling in the NB images (F466N and F470N), n is fixed at $n = 1$ since the light profile of any ionised gas emission is expected to be disk-like (e.g. Nelson et al. 2013), and our size measurements are consistent regardless of a fixed or free Sérsic index fit (Figure 4.3). SF galaxies at high-z that appear more prolate or oblate in shape have also been shown to have Sérsic indices of $n \sim 1$ (e.g. Pandya et al. 2024). For the BB images (F277W, F356W and F444W), we produced two sets of results. One in which n is again fixed at $n = 1$, and another set where we allowed n to take values $0.2 \leq n \leq 8$. The measurements of r_e in the BB images using both methods are in agreement (see Figure 4.2 for results in F444W), and so we chose to fix $n = 1$ for all of our models for ease of interpretation. When the Sérsic index was left as a free parameter, we find $n_{\rm F444W,median} \sim 1.5$.

v) It is well documented that `GALFIT` underestimates the uncertainties of each output parameter (Häußler et al. 2007, 2013). Recently, Ward et al. (2024) addressed this by following steps from van der Wel et al. (2012) to recalculate the uncertainty on r_e compared to the reported value from `GALFIT`. They found that their new relative r_e errors for their *JWST* images were $\lesssim 15\%$, similar to those reported in other studies (van der Wel et al. 2012; Nedkova et al. 2021). In light of their findings, we set our uncertainties in r_e to be at least 25% of the `GALFIT` output to be conservative. This is an average

factor increase in uncertainty of ~ 3.6 from the GALFIT output. We refer the reader to Chapter 4.3.1.1 for detailed analysis of r_e recovery in GALFIT from known values.

We show six examples of our GALFIT models in Figure 4.1. The sensitivity of GALFIT is alleviated by the constraints described above but following visual inspection, the input centroid coordinates had to be manually adjusted for a small number of models to be closer to the observed centre of the galaxy. None of the adjustments left the SExtractor source coordinates outside of the range of estimates GALFIT could take (i.e. manual input was never more than 5 pixels from the initial input) but were necessary adjustments for GALFIT to avoid unphysical local minima in its solution, which we define as being any solution that has an output $r_e = 0.1$ pixels or $r_e = 100$ pixels.

We note that there are potential degeneracies with modelling Sérsic light profiles with GALFIT, particularly that r_e and the Sérsic index n may not be independent (see Graham & Driver 2005 for a detailed discussion). This could be a particularly pressing issue for our fixed $n = 1$ sizes, though the lack of posterior distribution outputs from GALFIT makes this difficult to quantify directly (Peng et al. 2010a; Häußler et al. 2007, 2013). However, we show in Figures 4.2 and 4.3 that our sizes are consistent when using either a free Sérsic or fixed $n = 1$, suggesting that the possible limitations of GALFIT do not significantly impact our results.

4.3.1.1 Recovering Known Sizes with GALFIT

In Chapter 4.3.1, we discussed the uncertainty estimations of GALFIT and how it typically underestimates them (see Häußler et al. 2007, 2013; also van der Wel et al. 2012). There is also evidence that for faint, compact objects, GALFIT begins to overestimate the sizes of galaxies. For example, Davari et al. (2014) found that GALFIT can overestimate the sizes by as much as 20% when fitting a single Sérsic profile to multi-component, ETGs (see also Mosleh et al. 2013; Meert et al. 2013; Wang et al. 2024a), though they note galaxies at high-z like those we study in this chapter are not as prone to those specific issues. Moreover, our HAEs are likely LTGs given their selection criteria and SFR (Pirie et al. 2025).

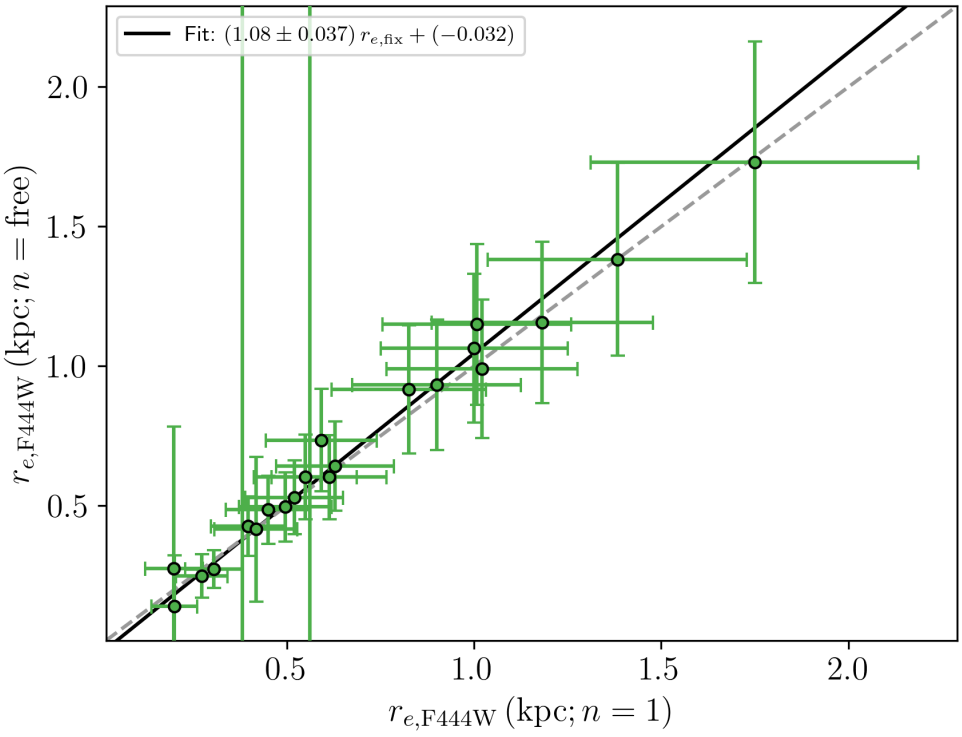

Figure 4.2: The measured free Sérsic r_e against fixed $n = 1$ Sérsic r_e in the F444W observations for each of the HAEs in our sample at $z = 6.1$. The grey dashed line indicates where the r_e would be equal. The solid black lines show the best fit to the data.

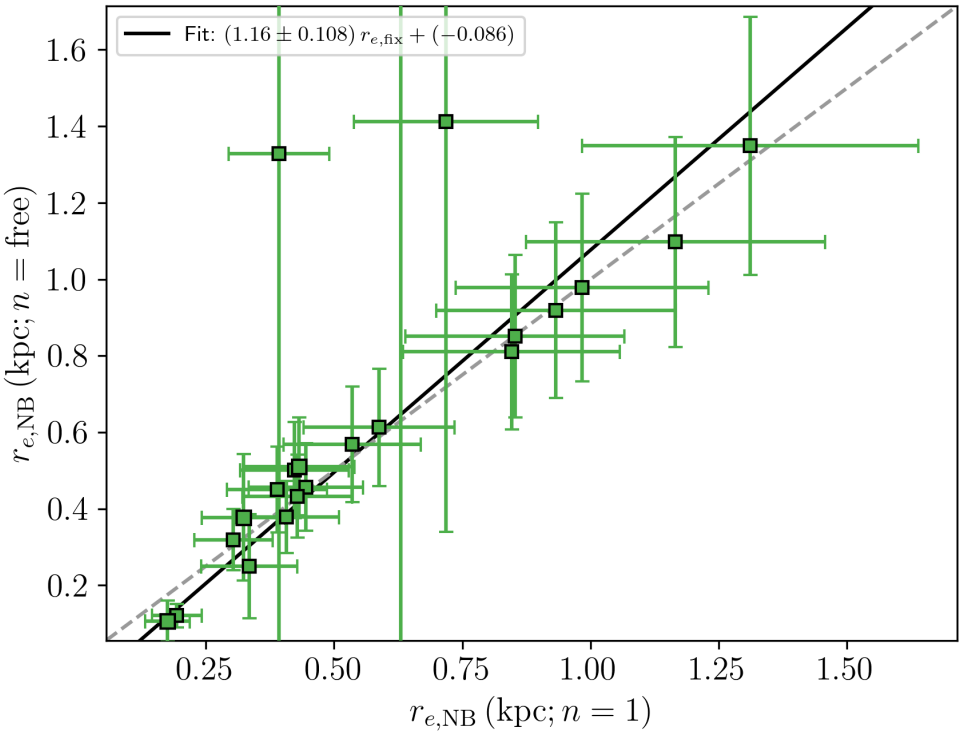

Figure 4.3: As in Figure 4.2, but for observations in F466N/F470N.

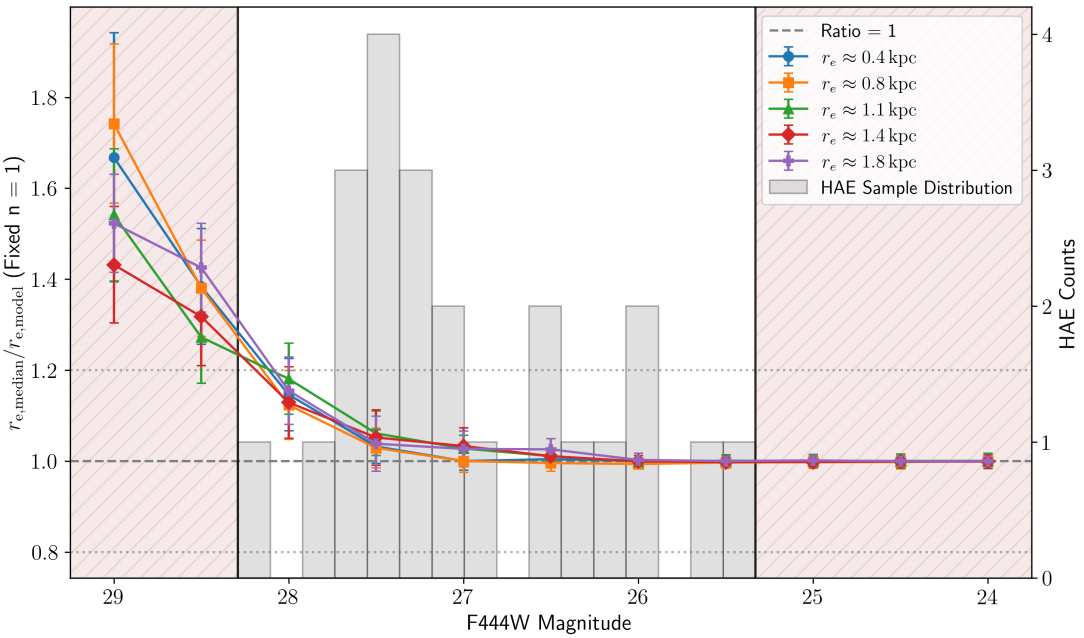

Figure 4.4: The ratio of median extracted $r_{e,\mathrm{F444W}}$ to model values of mock galaxies (left axis) as a function of model F444W magnitude. For each magnitude, recovered $r_{e,\mathrm{median}}$ are determined for mock galaxies with model radii of $\approx 0.4\,\mathrm{kpc}$ (blue dots), $\approx 0.8\,\mathrm{kpc}$ (orange squares), $\approx 1.1\,\mathrm{kpc}$ (green triangles), $\approx 1.4\,\mathrm{kpc}$ (red diamonds) and $\approx 1.8\,\mathrm{kpc}$ (purple pluses) at $z = 6.1$. The grey dashed line represents $r_{e,\mathrm{median}}/r_{e,\mathrm{expected}} = 1$, with the grey dotted lines representing ± 0.2. We represent the F444W magnitude range our actual sample of HAEs with a grey histogram (right axis). The vertical black lines are the upper and lower bounds of the F444W magnitude range of our HAEs, with the shaded brown regions indicating regions outside of that range.

Despite this, we decided to probe GALFIT's ability to recover accurate r_e measurements by measuring the Sérsic light profiles of model galaxies in 33 000 mock images in F444W with similar properties to those of our sample of HAEs. In total, we created 330 $n = 1$ model galaxies using GALFIT with properties in the range $m_{\mathrm{F444W}} = 24$–29 mag, $r_{e,\mathrm{model}} \approx 0.4$–$1.8$ kpc and $b/a = 0.2$–1.0. Each mock galaxy was then placed in 100 random sky cutouts of the full PRIMER F444W image. These sky cutouts were created by ensuring that no SExtractor-detected sources were within $\sqrt{100^2 + 100^2} \approx 141$ pixels of the centre of the cutout. We then ran GALFIT on these model galaxies with sky backgrounds following the steps in Chapter 4.3.1 with n kept fixed at $n = 1$, as well as fits where it is left as a free parameter, for a total of 66 000 fits. We then bin the results on the model F444W magnitude and $r_{e,\mathrm{model}}$, with each bin containing 600 outputs. We then remove any catastrophic fitting errors which we define here as those that run up against the r_e constraint boundaries (or n boundaries for when n is a free parameter). In other words, we remove any fit that produces a fit with $r_e = 0.1$ pixels or $r_e = 100$ pixels ($n = 0.2$ or $n = 8$ for the free Sérsic index fits). The number of catastrophic errors varied depending on model values, reaching as high as 67% (402/600) for models with an apparent F444W magnitude of 29 mag and $r_e \approx 1.4$ kpc. From the remaining fits, we then determine the median recovered r_e ($r_{e,\mathrm{median}}$) in each bin and the standard error.

Figure 4.4 shows the $r_{e,\mathrm{median}}/r_{e,\mathrm{model}}$ ratio (left axis) of fixed $n = 1$ mock galaxies in 0.5-wide magnitude bins. The different coloured points represent different $r_{e,\mathrm{model}}$ values ranging from ≈ 0.4 kpc to ≈ 1.8 kpc. Overlaid is a histogram of the F444W magnitude counts (right axis) of our sample of 23 HAEs, with vertical black lines indicating the upper and lower bounds of our sample. The shaded regions highlight magnitudes outside the range of our sample. From Figure 4.4, we see that for $n = 1$ galaxies at F444W magnitudes $\lesssim 26.5$ mag, the recovered $r_{e,\mathrm{median}}$ are consistent with $r_{e,\mathrm{model}}$ within uncertainties regardless of $r_{e,\mathrm{model}}$. However, at fainter magnitudes, particularly at $\gtrsim 28$ mag, GALFIT consistently overestimates the sizes, reaching as high as $\sim 74\%$ larger for $r_{e,\mathrm{model}} \approx 0.8$ kpc at 29 mag. This extreme is beyond the range of our sample, however, and all of the ratios for any $r_{e,\mathrm{model}}$ within our magnitude range are $\lesssim 20\%$ overestimation. This further justifies our floor uncertainty value of 25% for our HAEs in Chapter 4.3.1

as a conservative estimate. The general trend from Figure 4.4 is that the fainter the magnitude, the more `GALFIT` overestimates the sizes of known models. We believe this is a result of the sky background becoming more indistinguishable from the faint edges of these objects causing `GALFIT` to calculate the r_e of an object that extends further into the sky background than it does in the injected model. This overestimation may introduce some scatter of galaxy sizes at faint magnitudes (see Chapter 4.5.1).

4.4 Results

In this chapter, we detail the key results from our analysis. We do this first by determining whether we observe a r_e–M_* relationship at $z = 6.1$ and then comparing NB and F444W sizes. The latter allows us to compare the size of the Hα-selected SF component of our HAEs to the spatial extent of the established stellar component, inferred from the F444W photometry. Additionally, since both NB filters overlap with F444W, we also fit light profiles to our HAEs with the modelled NB emission removed from the F444W image in order to account for Hα contributions to the BB (see Chapter 4.4.2.1). In Chapter 4.4.3, we will compare our measured $r_{e,\mathrm{F444W}}$ to studies at a range of redshifts.

4.4.1 Size–Mass Relationship

Figures 4.5–4.8 show the r_e–M_* relationship for our HAEs in the PRIMER F277W, PRIMER F356W, PRIMER F444W and JELS F466N/F470N images. In each figure, the red dashed line indicates the best fit power-law of the form $\log_{10}\left(\frac{r_e}{\mathrm{kpc}}\right) = \alpha \log_{10}\left(\frac{M_*}{M_\odot}\right) + A$ to the individual r_e points, determined using the `curve_fit` function from the `scipy.optimize` module in Python (Virtanen et al. 2020). The shaded region indicates the 1σ scatter at fixed stellar mass. The parameters for these fits can be found in Table 4.1. We compare to the $z = 0.4$ r_e–M_* relationship of Stott et al. (2013a) who analysed the structural properties of a sample of HAEs, though we note that their r_e measurements are determined from ground-based observations (Geach et al. 2008; Sobral et al. 2013). We also

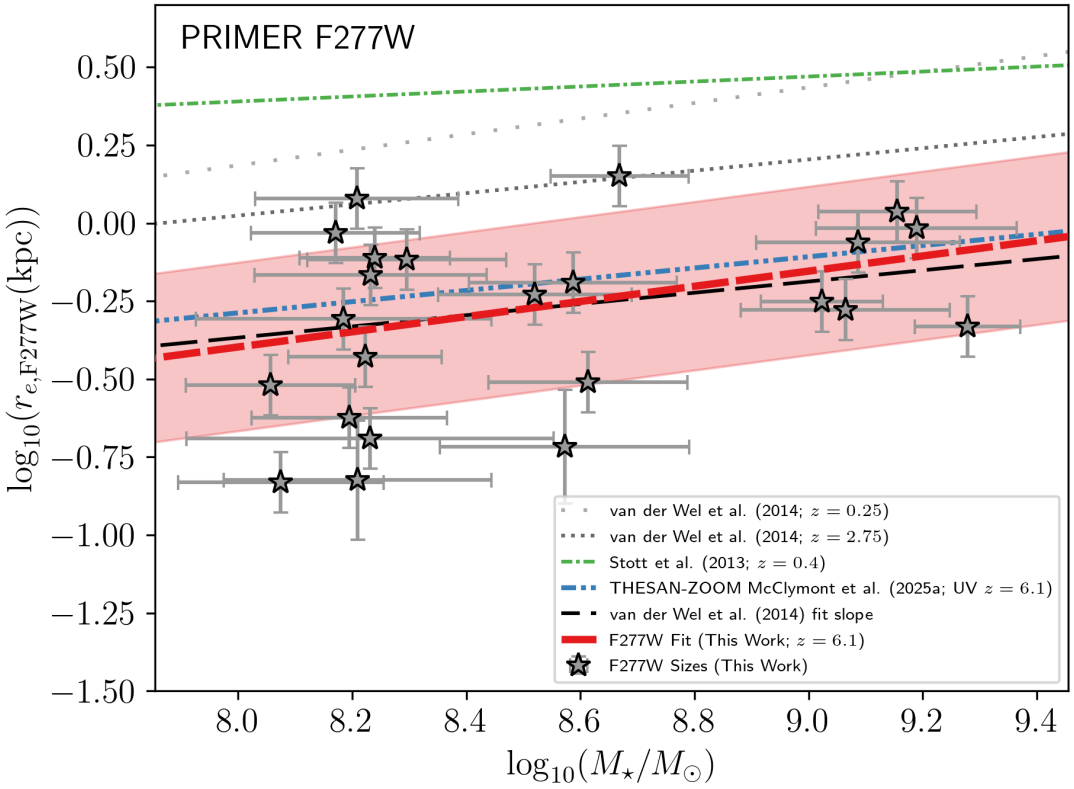

Figure 4.5: The r_e–M_* relationship for our HAEs at $z = 6.1$ from PRIMER F277W (rest-NUV) observations. The grey symbols represent the individual sizes of each galaxy. The red dashed line shows the fitted relationship to the individual points, with the red shaded region indicating the 1σ scatter. We compare to the observed r_e–M_* relationship from Stott et al. (2013a) at $z = 0.4$ (green dash-dotted line), as well as those from van der Wel et al. (2014) at $z = 0.25$ (loosely dotted grey line) and $z = 2.75$ (densely dotted grey line). Also shown is the simulated rest-UV (0.1475–0.1525 µm) r_e–M_* relationship from McClymont et al. (2025b; blue dash-dotted) who employ the THESAN-ZOOM radiation-hydrodynamics zoom-in simulations (Kannan et al. 2025). The black long-dashed line shows the fixed slope of the van der Wel et al. (2014) r_e–M_* relationship at $z = 2.75$ with the offset fitted to our data points.

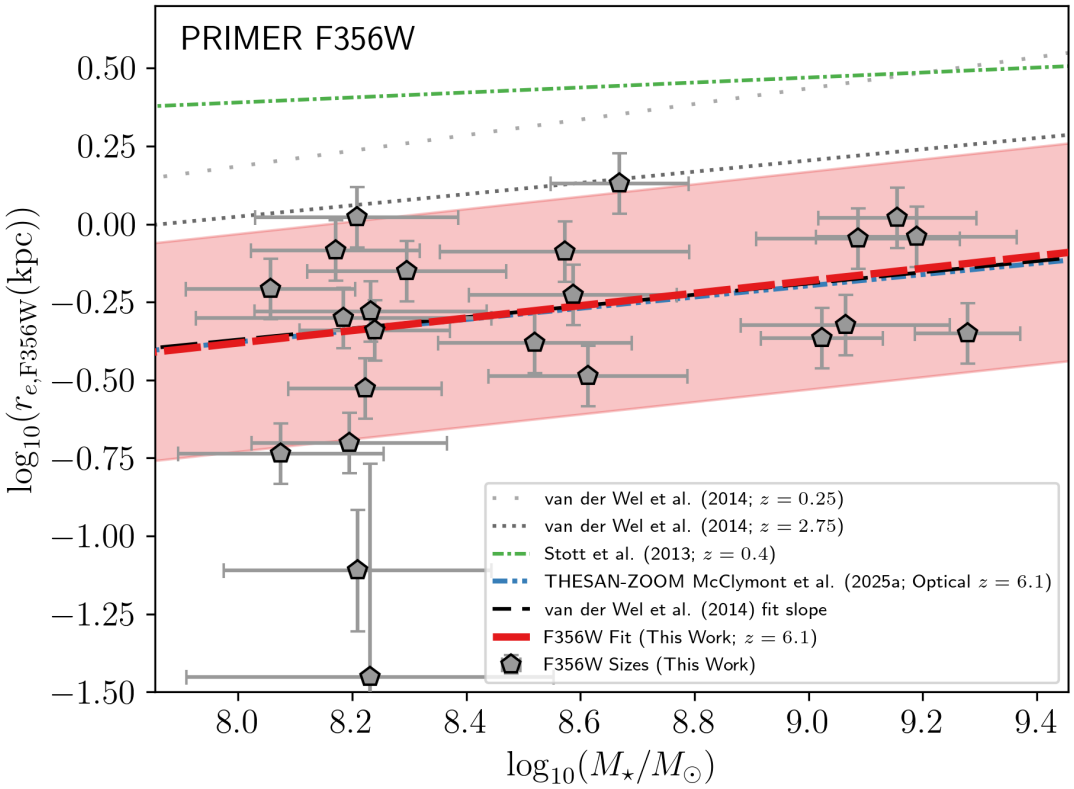

Figure 4.6: As in Figure 4.5 but for our measured r_e–M_* relationship from PRIMER F356W observations (rest-V-band). The blue dash-dotted line shows the McClymont et al. (2025b) rest-optical (0.5–0.6 µm) r_e–M_* relationship from THESAN-ZOOM.

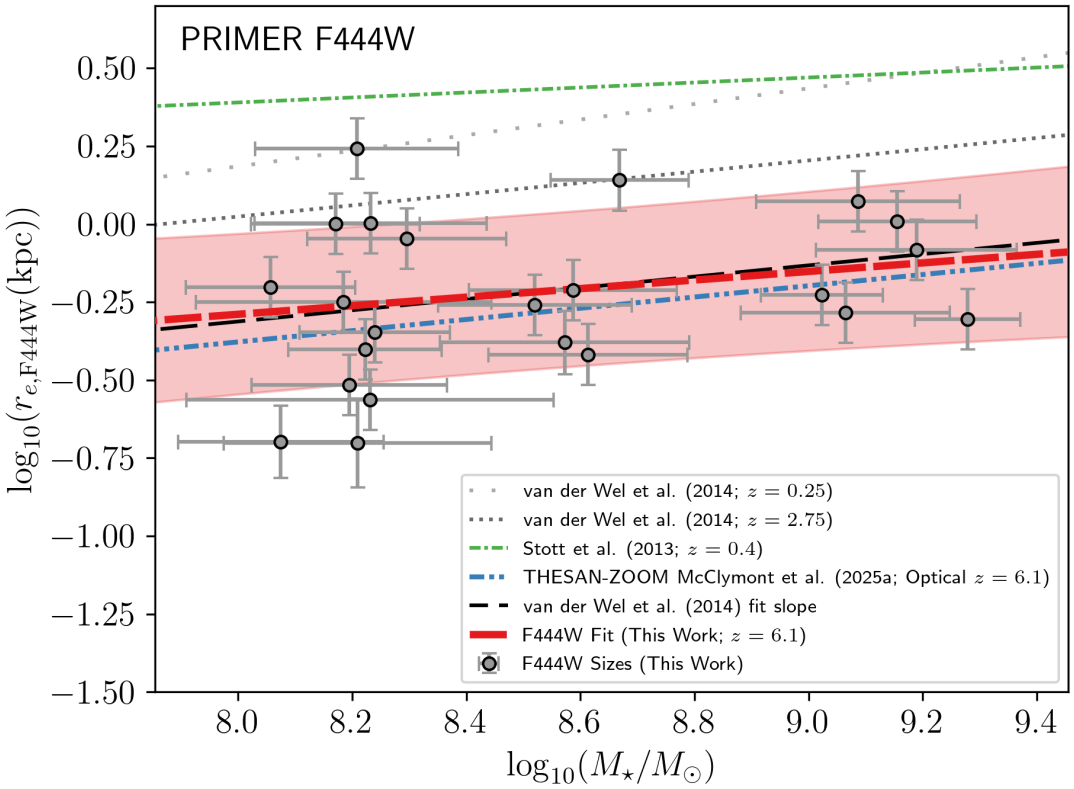

Figure 4.7: As in Figure 4.5 but for our measured r_e–M_* relationship from PRIMER F444W observations (rest-R-band). The blue dash-dotted line shows the McClymont et al. (2025b) rest-optical (0.5–0.6 µm) r_e–M_* relationship from THESAN-ZOOM.

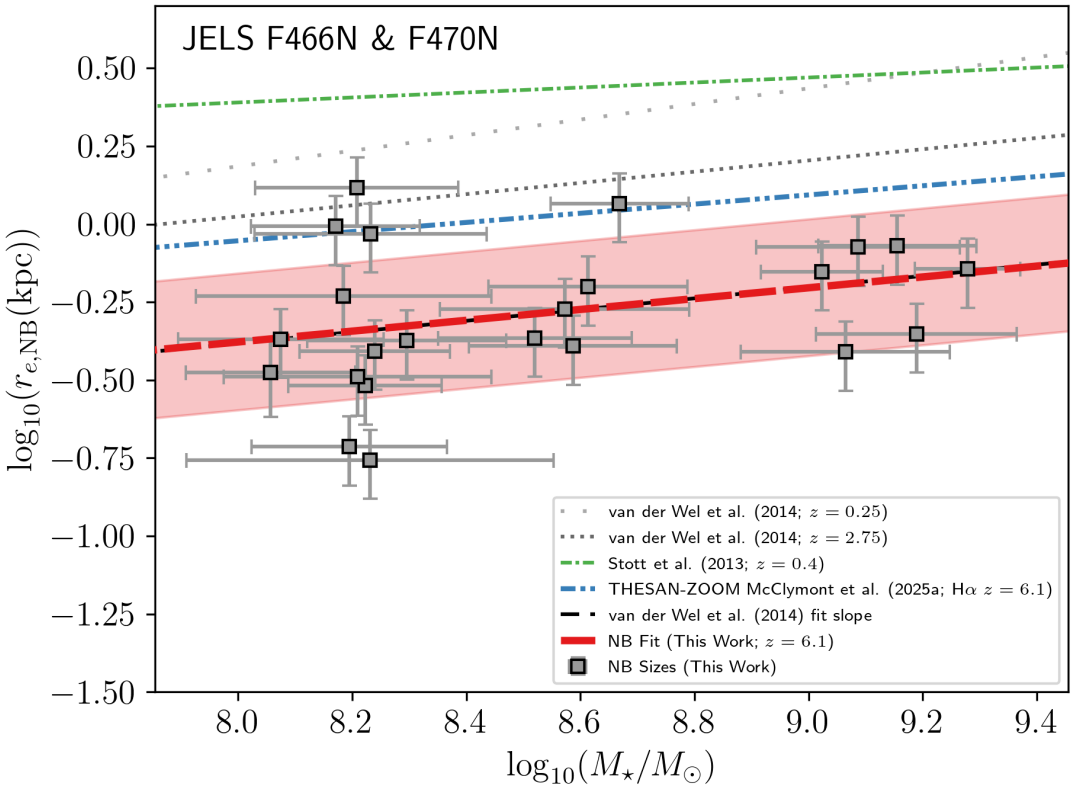

Figure 4.8: As in Figure 4.5 but for our measured r_e–M_* relationship from JELS F466N/F470N observations (rest-Hα). The blue dash-dotted line shows the McClymont et al. (2025b) rest-Hα r_e–M_* relationship from THESAN-ZOOM.

compare to van der Wel et al. (2014) for SF galaxies at $z \sim 0.25$ (rest-Y-band; light-grey dotted line) and $z \sim 2.75$ (rest-B-band; dark-grey dotted line). Despite being at different rest-frame wavelengths, the observed r_e–M_* relationships we compare to in Figures 4.5–4.8 are also measured at wavelengths redward of the rest-4000 Å break so are less affected by ongoing star formation, thus making them reasonable comparisons. We note that these comparisons only apply to BB sizes but we include them on the NB plot for reference. Additionally, we look at how our r_e–M_* relationship compares to those in simulations from McClymont et al. (2025b). They measure the 2D half-light radii of galaxies in the THESAN-ZOOM radiation-hydrodynamics zoom-in simulations (Kannan et al. 2025), a high-resolution successor to the large-volume THESAN simulations (Kannan et al. 2022). After accounting for biases to better match observations, McClymont et al. (2025b) measure the r_e–M_* relationship in three different bands: UV (rest-frame 0.1475–0.1525 µm), optical (rest-frame 0.5–0.6 µm) and Hα emission. We compare each of our measured relationships to those from McClymont et al. (2025b), making sure to use the appropriate observed filter for our sizes. We will focus on the r_e–M_* relationship in F444W (rest-R-band) for the rest of this study as it overlaps with the JELS F466N/F470N NB observations and gives a better reflection of the underlying stellar population than bluer BB or the NB data.

From Figure 4.7, we observe a r_e–M_* relationship for HAEs at $z = 6.1$ with a slope of $\alpha_{\mathrm{F444W}} = 0.14 \pm 0.12$ in F444W and $\alpha_{\mathrm{NB}} = 0.17 \pm 0.12$ in the NB data. The F444W r_e–M_* relationship is significantly offset from those in both Stott et al. (2013a) and van der Wel et al. (2014), reflecting the accepted trend in the literature that, for fixed stellar mass, galaxies at higher redshifts have smaller r_e (e.g. Shibuya et al. 2015; Mowla et al. 2019b; Sun et al. 2024; van der Wel et al. 2024; see Chapter 4.4.3). For a fixed stellar mass of $10^{9.25}\,\mathrm{M}_\odot$, we find an offset in $\log_{10}\left(\frac{r_e}{\mathrm{kpc}}\right)$ from the van der Wel et al. (2014) $z = 2.75$ relationship of -0.37 ± 0.10 dex (-0.41 ± 0.10 dex) for our F444W (NB) derived relationship. We choose to use a fixed stellar mass of $10^{9.25}\,\mathrm{M}_\odot$ despite being near the upper end of our sample because comparisons in the literature are difficult at lower stellar masses (see Chapter 4.4.3). The offset from van der Wel et al. (2014) reflects an increase in average r_e of ≈ 1 kpc from $z = 6.1$ to $z = 2.75$, or a

Table 4.1: Fits for our measured r_e–M_* relationships as seen in as seen in Figures 4.5–4.8 and Figure 4.11. These fits are of the form $\log_{10}\left(\frac{r_e}{\mathrm{kpc}}\right) = \alpha \log_{10}\left(\frac{M_*}{M_\odot}\right) + A$.

Image	α	A
F277W	0.24 ± 0.13	-2.34 ± 1.11
F356W	0.20 ± 0.12	-1.98 ± 1.07
F444W	0.14 ± 0.12	-1.39 ± 1.06
NB	0.17 ± 0.12	-1.77 ± 1.01
$\mathrm{F444W_{sub}}$	0.08 ± 0.12	-0.82 ± 1.04

factor of ~ 2.3–2.5 increase in just $\sim 1.4\,\mathrm{Gyr}$. According to van der Wel et al. (2014), from $z = 2.75$ to $z = 0.25$, the r_e of a $10^{9.25}\,\mathrm{M}_\odot$ SF galaxy increases by a factor of ≈ 1.8 in $\sim 8.2\,\mathrm{Gyr}$, suggesting significantly more rapid galaxy growth before Cosmic Noon than after. This is also indicated by the near-identical value of the $z = 0.4$ relationship found by Stott et al. (2013a) at this stellar mass. Similar offsets and slopes to these observational relationships are seen in all our measured r_e–M_* relationships. Indeed, from Table 4.1, all of our fitted outputs are consistent within errors, with weak evidence that the slope may get shallower with increasing rest-frame wavelength, a trend that has been seen in the literature (Nedkova et al. 2024; Allen et al. 2025; Jia et al. 2024; Yang et al. 2025).

We find good agreement between our BB r_e–M_* relations and the simulated $z = 6.1$ results of McClymont et al. (2025b), with all trends occupying the 1σ scatter about the relationships. This agreement is particularly strong for our PRIMER F356W measurements, where the mean offset is only $\approx -0.01\,\mathrm{dex}$ in half-light radius across our stellar mass range. In contrast, our $z = 6.1$ Hα r_e–M_* relation disagrees with the McClymont et al. (2025b) prediction, with their r_e values $\approx 0.3\,\mathrm{dex}$ larger. They interpret their large Hα sizes as being due to nebular emission beyond the stellar and UV continuum as extreme Lyman-continuum emission from a central starburst region ionises gas reservoirs surrounding the galaxy. However, our observations do not support this scenario.

The slope of our F444W r_e–M_* relationship ($\alpha_{\mathrm{F444W}} = 0.14 \pm 0.12$) is consistent with those for LTGs in van der Wel et al. (2014) who find $\alpha = 0.18 \pm 0.02$ at $z = 2.75$ and $\alpha = 0.25 \pm 0.02$ at $z = 0.25$. We illustrate the consistency with van der Wel et al. (2014) by fitting a line with a fixed slope equal to their $z = 2.75$

relationship to our sample (black dashed line) and finding that it is within the 1σ scatter of our fit for our full stellar mass range. The large errors on our relationship are likely explained by the much-reduced sample size compared to van der Wel et al. (2014; 23 vs ~ 2000) and the large scatter $\sigma_{\rm scatter} = 0.30\,{\rm dex}$ of our individual sizes at low stellar mass ($M_* < 10^{8.4}\,{\rm M}_\odot$; compared to $\sigma_{\rm scatter} = 0.16\,{\rm dex}$ at $M_* \geq 10^{8.4}\,{\rm M}_\odot$). We discuss the possible causes of this increased scatter in Chapter 4.5.1. We also find that the slope of our r_e–M_* relationship is consistent within errors with the HAEs relationship of Stott et al. (2013a) at $z = 0.4$ of $\alpha = 0.03 \pm 0.02$. These consistencies, although caveated by large relative errors, suggest the trend in the literature that the late-type r_e–M_* slope remains generally unchanged with redshift may continue out to $z = 6.1$ (see also Shen et al. 2023; Ito et al. 2023; Ward et al. 2024; Allen et al. 2025), though there is evidence of steeper slopes at $z \lesssim 0.1$ (e.g. Shen et al. 2003; Guo et al. 2009; Paulino-Afonso et al. 2017). When combined with our Hα to stellar continuum size ratios (see Chapter 4.4.2), we believe that the lack of significant evolution in the r_e–M_* slope is a consequence of SF galaxies primarily building their mass through secular star formation across cosmic time. We explore this further in Chapter 4.5.2.

4.4.2 Stellar Component to Star-Forming Region Size Ratio

Figure 4.9 shows the ratio of $r_{e,\rm F444W}$ to r_e measured in NB ($r_{e,\rm NB}$) for each of our HAEs. This ratio reflects the size of any stellar component compared to the SF region traced by Hα emission from H II regions surrounding young, massive stars. We find a median size ratio of $\frac{r_{e,\rm F444W}}{r_{e,\rm NB}} = 1.20 \pm 0.09$, indicating that the stellar emission is marginally larger than the Hα-emitting SF component at the EoR, suggestive of more centrally concentrated SF regions in HAEs at $z = 6.1$. However, the uncertainty on the measurement of $\frac{r_{e,\rm F444W}}{r_{e,\rm NB}}$ for many of the individual galaxies is such that the ratio is consistent with 1. Therefore, we can say more broadly that the ratios in Figure 4.9 indicate that there are already-established stellar components in SF galaxies at $z = 6.1$ that are at

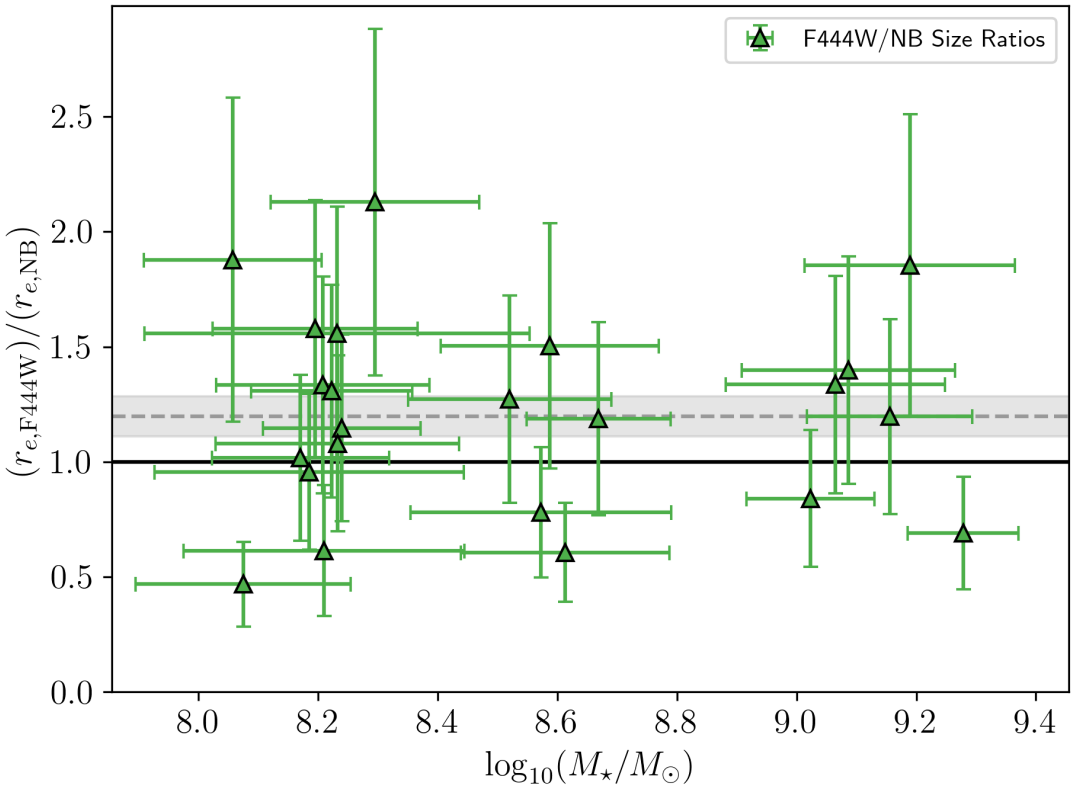

Figure 4.9: The ratio of the measured r_e in F444W (rest-R-band; $r_{e,\mathrm{F444W}}$) to the measured r_e in NB ($r_{e,\mathrm{NB}}$) for each of our HAEs (green triangles) against stellar mass. The error on each size ratio represents the combined error on the respective r_e measurements. The solid black line represents $r_{e,\mathrm{F444W}}/r_{e,\mathrm{NB}} = 1$. The dashed grey line represents the median $r_{e,\mathrm{F444W}}/r_{e,\mathrm{NB}} = 1.20$, with the shaded region indicating the standard error (± 0.09).

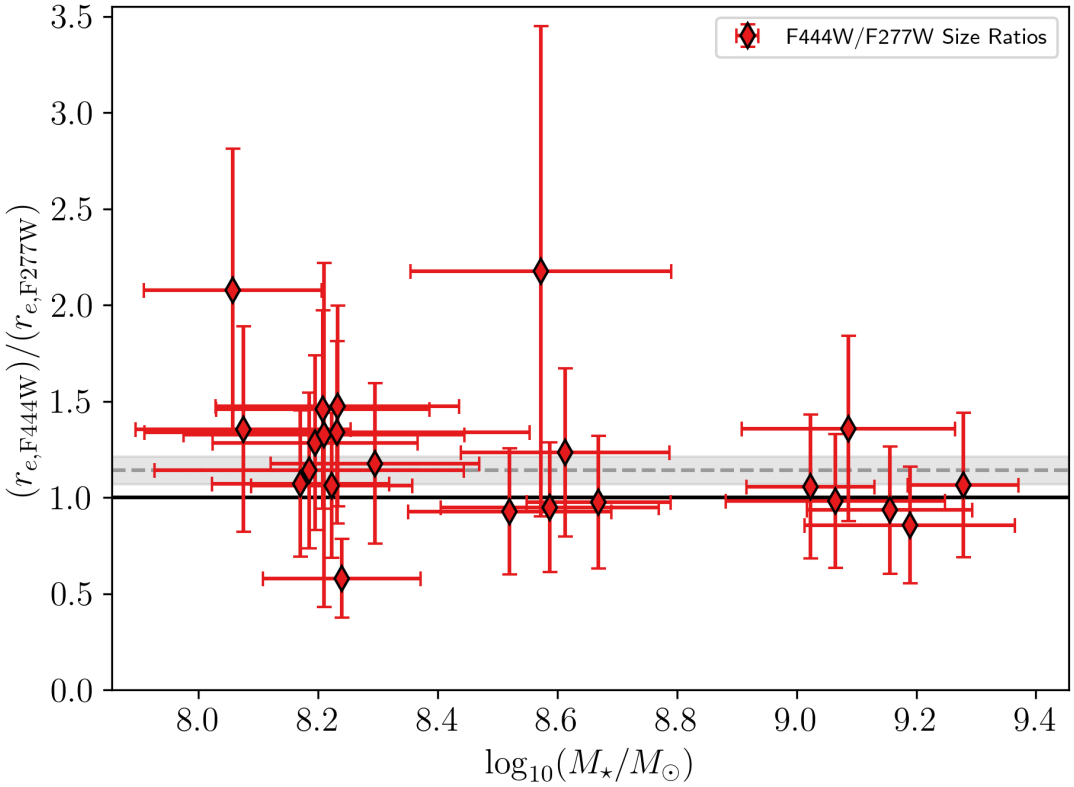

Figure 4.10: As in Figure 4.9, but for our $r_{e,\mathrm{F444W}}$ to r_e measured in F277W (rest-NUV; $r_{e,\mathrm{F277W}}$) ratios (thin red diamonds). The dashed grey line and shaded region represent the median $r_{e,\mathrm{F444W}}/r_{e,\mathrm{F277W}} = 1.14 \pm 0.07$.

least comparable in size to, if not larger than, the expected SF regions. This contrasts with the results of Nelson et al. (2016) who find that the active star formation traced by Hα at $0.7 < z < 1.5$ extends further than the existing stellar continuum. They conclude that their results show SF galaxies at their redshift range are growing in size primarily from star formation (see also Nelson et al. 2012; Matharu et al. 2022; Shen et al. 2024a). Wilman et al. (2020) see a similar result, finding the median (mean) Hα size to be a factor of 1.18 (1.26) larger than the stellar continuum from their sample of $0.7 < z < 2.7$ observations in the KMOS^{3D} survey (Wisnioski et al. 2015, 2019).

As briefly discussed in Chapter 4.1, the UV- or NUV-continuum are other frequently used indicators of star formation. Therefore, another method of measuring the extent of any established stellar component to SF regions is to measure

the ratio of $r_{e,\mathrm{F444W}}$ to r_e measured in F277W (rest-NUV; $r_{e,\mathrm{F277W}}$). We show this in Figure 4.10 where we find a median $\frac{r_{e,\mathrm{F444W}}}{r_{e,\mathrm{F277W}}}$ ratio of 1.14 ± 0.07. This agrees with our median $\frac{r_{e,\mathrm{F444W}}}{r_{e,\mathrm{NB}}}$ from Figure 4.9 and further suggests that the SF region of our HAEs is more centrally concentrated with an established stellar component that may extend beyond this. This reduced value could also be partly caused by UV light being more affected by dust than Hα emission.

Our results imply that, prior to the current period of star formation traced by the Hα emission in the NB data, there must have been a significant enough episode of star formation to form a stellar component with a larger associated r_e. We discuss the implications and the possible causes of this in Chapter 4.5.

4.4.2.1 Hα Contribution to F444W

The nature of NB imaging selection for detecting HAEs means that there could be a significant contribution from the Hα emission line in the overlapping BB emission (in our case contributions to F444W from F466N or F470N). The median observed Hα EW for our sample is $\mathrm{EW}_{\mathrm{H}\alpha} = 748 \pm 89$ Å so we decided to run an analysis where the Hα emission is removed from the F444W image to leave a NB flux-subtracted F444W ($\mathrm{F444W}_{\mathrm{sub}}$) image. To do this, we used the `GALFIT` output models from the NB fitting and subtracted them from the corresponding F444W image cutouts. This subtraction was done by scaling the NB flux density based on the relative effective widths of the F444W, F466N and F470N filters. The full subtraction is described by

$$f_{\lambda,\mathrm{F444W}_{\mathrm{sub}}} = \frac{f_{\lambda,\mathrm{F444W}} - f_{\lambda,\mathrm{NB}} \left(\frac{W_{\mathrm{eff,NB}}}{W_{\mathrm{eff,F444W}}}\right)}{1 - \frac{W_{\mathrm{eff,NB}}}{W_{\mathrm{eff,F444W}}}}, \tag{4.4}$$

where f_λ and W_{eff} are the flux density and effective width of a given filter respectively (Waller 1990). In our case, $f_{\lambda,\mathrm{F444W}}$ is the flux density of the F444W cutout of our HAEs, and $f_{\lambda,\mathrm{NB}}$ is the flux density of the `GALFIT` model output in NB, where NB is either F466N or F470N depending on which image the HAE was detected in (see middle panels of Figure 4.1 for example outputs). This method of model subtraction ensures that we are only removing the Hα emission from the source without increasing the noise in the sky background, which `GALFIT`

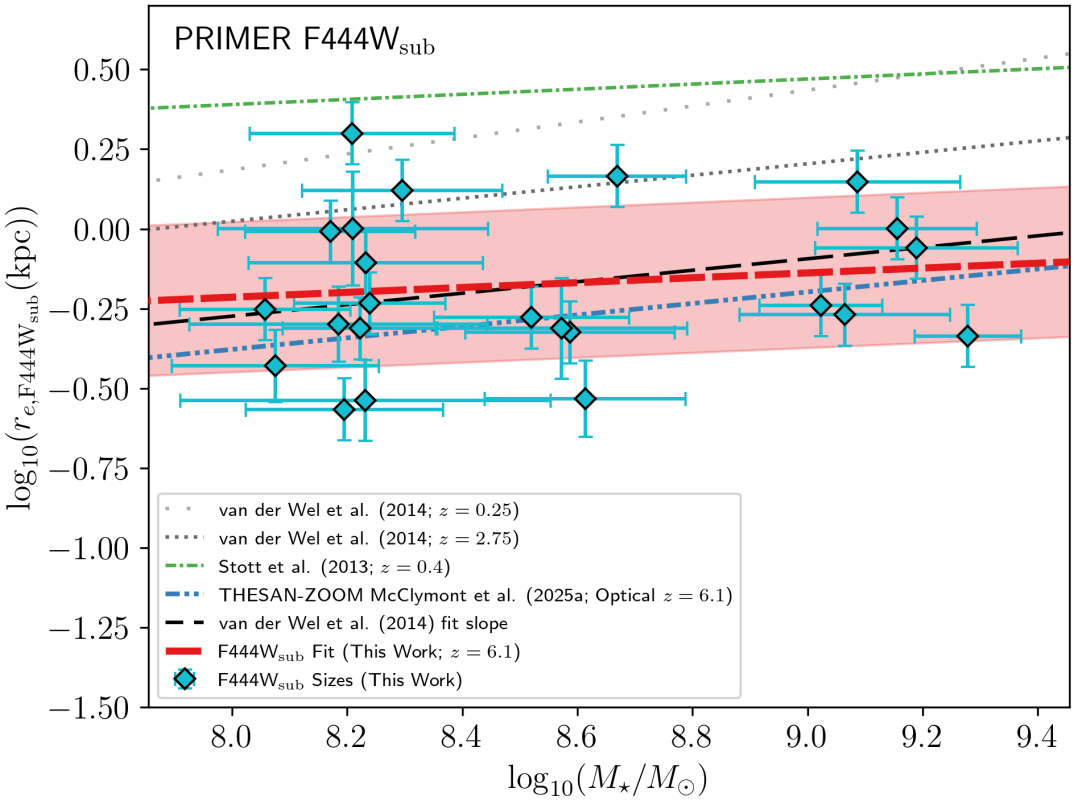

Figure 4.11: The r_e–M_* relationship as in Figure 4.7 for NB flux-subtracted F444W sizes ($r_{e,\rm F444W_{sub}}$; cyan diamonds). The slope here is measured as $\alpha_{\rm F444W_{sub}} = 0.08 \pm 0.12$ which is shallower than the slope seen measured in the F444W r_e–M_* relationship (see Figure 4.7) driven by an increase in $r_{e,\rm F444W_{sub}}$ at $M_* < 10^{8.4}\,\rm M_\odot$.

needs for accurate light profiles (Peng et al. 2010a). Once the NB models have been subtracted from the F444W cutouts, we ran `GALFIT` on the resulting images following the same steps as Chapter 4.3.1.

Figure 4.11 shows the r_e–M_* relationship for our HAEs in the same format as Figure 4.7, but using NB flux-subtracted r_e ($r_{e,\rm F444W_{sub}}$). We find that the slope of this relationship is shallower than those found in Figure 4.7 (see Table 4.1) with $\alpha_{\rm F444W_{sub}} = 0.08 \pm 0.12$. However, this is well within 1σ of the previous relationships, as well as those from Stott et al. (2013a) and van der Wel et al. (2014).

We measure the ratio of $r_{e,\rm F444W_{sub}}$ to $r_{e,\rm NB}$ in Figure 4.12. This gives us

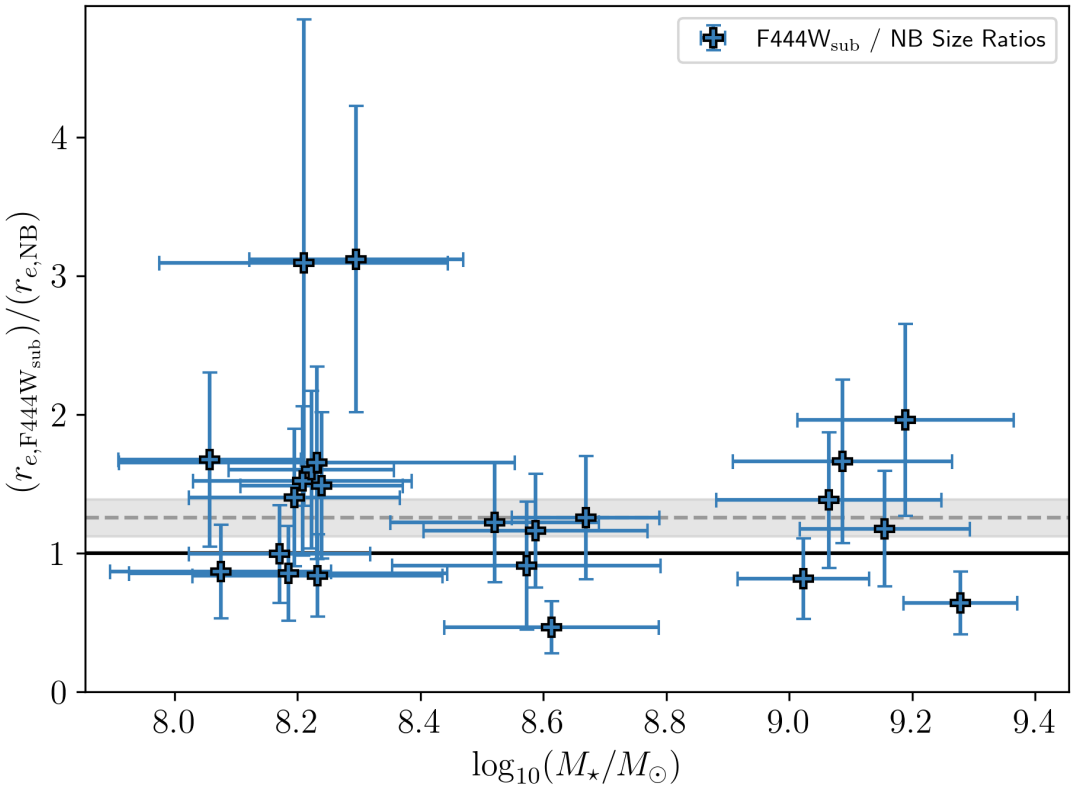

Figure 4.12: As in Figure 4.9, but for our NB flux-subtracted F444W r_e ($r_{e,\rm F444W_{sub}}$) to $r_{e,\rm NB}$ ratios (blue pluses). The dashed grey line and shaded region represent the median $r_{e,\rm F444W_{sub}}/r_{e,\rm NB} = 1.26 \pm 0.14$, which is marginally larger than the $r_{e,\rm F444W}/r_{e,\rm NB} = 1.20 \pm 0.09$ seen in Figure 4.9, though consistent within error.

a cleaner comparison between the size of any stellar components and the SF regions because we have removed contributions from the latter to the BB continuum. We find that the median size ratio when subtracting Hα emission increases marginally to $\frac{r_{e,\mathrm{F444W_{sub}}}}{r_{e,\mathrm{NB}}} = 1.26 \pm 0.14$ (grey dashed line in Figure 4.12), compared to $\frac{r_{e,\mathrm{F444W}}}{r_{e,\mathrm{NB}}} = 1.20 \pm 0.09$ without any subtraction, although the change is not significant. While this is a weak increase within the respective uncertainties, this marginal increase is in line with the SF region traced by Hα emission being more centrally concentrated.

This average increase in r_e may contribute to the flattening of our r_e–M_* slope in Figure 4.11 compared to the F444W r_e–M_* relationship seen in Figure 4.7, particularly if the increase is predominantly in low-mass HAEs. After subtracting Hα emission, our $< 10^{8.4}\,\mathrm{M}_\odot$ HAEs have a ratio of $\frac{r_{e,\mathrm{F444W_{sub}}}}{r_{e,\mathrm{F444W}}} = 1.10 \pm 0.32$ compared to $\frac{r_{e,\mathrm{F444W_{sub}}}}{r_{e,\mathrm{F444W}}} = 0.98 \pm 0.04$ for $\geq 10^{8.4}\,\mathrm{M}_\odot$. The larger errors at $< 10^{8.4}\,\mathrm{M}_\odot$ mean it is difficult to draw any definitive conclusions, and the ratios of both $r_{e,\mathrm{F444W}}$ and $r_{e,\mathrm{F444W_{sub}}}$ to $r_{e,\mathrm{NB}}$ are consistent with one another, which suggests the overall sizes are not significantly affected by Hα emission. This is not surprising, since our median observed $\mathrm{EW}_{\mathrm{H}\alpha} \sim 750\,\text{Å}$ is $\approx 7\%$ the width of the F444W filter ($W_{\mathrm{eff}} = 10676\,\text{Å}$).

4.4.3 Redshift Evolution of Galaxy Sizes

The narrow wavelength range probed by the F466N and F470N filters dictates that the redshift range we can probe for our HAEs is similarly narrow ($6 \lesssim z \lesssim 6.2$, or $\approx 0.04\,\mathrm{Gyr}$ of cosmic time). As a result, we cannot model the redshift evolution of galaxy sizes across the EoR ($6 \lesssim z \lesssim 15$; Fan et al. 2006a; Robertson et al. 2013). Instead, we can see how the results from our unbiased, rest-optical HAEs compare to observations in the literature (Stott et al. 2013a; van der Wel et al. 2014; Paulino-Afonso et al. 2017; van der Wel et al. 2024; Suess et al. 2022; Ormerod et al. 2023; Allen et al. 2025; Martorano et al. 2024; Sun et al. 2024; Ward et al. 2024), as well as predictions from simulations (Wu et al. 2020; Roper et al. 2022; Marshall et al. 2022; Costantin et al. 2023). These studies measure r_e of SF galaxies in different ways and we will briefly outline the data of each individual study, all of which are plotted in Figure 4.13. We note here that all

the observations in the referenced literature measure r_e in rest-optical bands that are redward of the 4000 Å break.

As discussed in Chapter 4.1, van der Wel et al. (2014) analysed the r_e–M_* relation of galaxies between $0 \lesssim z \lesssim 3$ from 3D–HST and CANDELS. Here, we look at the r_e–z relation they find for SF galaxies from their results, as well as individual r_e values for $10^{9.25}\,\mathrm{M}_\odot$ SF galaxies at $z = 0.25$ and $z = 2.75$ derived from their r_e–M_* relationships. Note that the derived r_e values are extrapolations, as van der Wel et al. (2014) only fit their LTG relation for $\gtrsim 10^{9.48}\,\mathrm{M}_\odot$. We also compare to the SF r_e–M_* relation in van der Wel et al. (2024), who combine observations from *JWST*/NIRCam in CEERS combined with CANDELS *HST* imaging. We compare to their median r_e for $10^{9.2}\,\mathrm{M}_\odot$ galaxies at $1.0 < z < 1.5$ in rest-frame 0.5 µm. Suess et al. (2022) used data from CEERS and 3D–HST to measure r_e in the F444W and F150W BB *JWST*/NIRCam filters, with stellar masses measured by Skelton et al. (2014). For our comparison, we use the median rest-R-band size of their 10^9–$10^{9.5}\,\mathrm{M}_\odot$ SF galaxies at $1.3 < z < 1.7$ (median stellar mass $\approx 10^{9.22}\,\mathrm{M}_\odot$). We define a SF galaxy from their sample using a $U - V < 1.0$ colour cut (to distinguish them from passive galaxies) for galaxies that satisfy the Skelton et al. (2014) "use" flag = 1, which they define as a galaxy with photometry of reasonably uniform quality. For comparison to Ormerod et al. (2023), we used the median size of $z = 5$ disk-like galaxies derived from their r_e–z relationship. Ormerod et al. (2023) develop their relationship based on CEERS observations in an overlapping region in the CANDELS field, with the median r_e at $z = 5$ being measured in F356W of *JWST*/NIRCam (rest-R-band). Allen et al. (2025) measures galaxy sizes from public data from CEERS, PRIMER–UDS and PRIMER–COSMOS, accessible via the DAWN *JWST* Archive (DJA[1]; see Valentino et al. 2023). We look at the median r_e they measure in F444W at the four median redshifts they list in Table A.1 of their paper (rest-frame 0.59–1.04 µm). From Martorano et al. (2024), we compare to both the r_e–z relation and the derived r_e of $\log_{10}(M_{*,\mathrm{median}}/M_\odot) \approx 9.27$ SF galaxies from their r_e–M_* relationship at $2 < z < 2.5$. They measured the rest-frame 1.5 µm r_e for galaxies in COSMOS–WEB (Casey et al. 2023) and PRIMER–COSMOS.

[1]https://dawn-cph.github.io/dja/index.html

Sun et al. (2024) used data from CEERS to measure the r_e of SF galaxies, fitting two-dimensional parametric models in seven *JWST*/NIRCam filters in both short-wavelength (SW) and LW channels. We compare to the r_e–z relationship that they derive from their combined rest-frame optical (≈ 0.41–$0.66\,\mu$m) measurements at $4 < z < 9.5$. The final observational result we compare to comes from Ward et al. (2024) who also used imaging from CEERS and CANDELS to measure r_e of galaxies at rest-frame $0.5\,\mu$m. We extrapolated their r_e–M_* relation to derive the r_e of a typical $10^{9.25}\,\mathrm{M}_\odot$ SF galaxy at $3 < z < 5.5$.

As with the observations above, we also looked at predictions from various simulations. Firstly, we compared to the rest-frame optical r_e estimates from the SIMBA cosmological hydrodynamical simulations (Davé et al. 2019) as reported by Wu et al. (2020). We derived the r_e of a typical $10^{9.5}\,\mathrm{M}_\odot$ SF galaxy from their size–luminosity relations in SIMBA-25 assuming a Calzetti et al. (2000) dust-law and their Sérsic fit method (see their Section 3.4). We note that the sizes reported by Wu et al. (2020) assume that dust tracks metals and does not account for radiative transfer. We compare to the r_e–z relation from Roper et al. (2022) as measured in the First Light And Reionisation Epoch Simulations (FLARES; Lovell et al. 2020; Vijayan et al. 2021) — a suite of zoom simulations based on the cosmological hydrodynamical simulations from the EAGLE project (Crain et al. 2015). Roper et al. (2022) constrain the r_e–z relationship at $5 < z < 10$ using rest-UV size measurements. Their r_e–z relation is based on sizes derived from their non-parametric pixel-based method, which they conclude is robust at high-z ($z \gtrsim 5$; see their Section 4.2.2). Despite being primarily based on UV sizes, we note that we find the ratio of $r_{e,\mathrm{F444W}}/r_{e,\mathrm{UV}} = 1.14 \pm 0.07$, suggesting that the rest-V-band emission is slightly larger than the size inferred from the UV continuum, so comparisons to Roper et al. (2022) should be noted with caution. We also compare to the r_e–z relationship modelled by Costantin et al. (2023) at $3 < z < 6$ in the Illustris TNG50 cosmological hydrodynamical simulation (Torrey et al. 2019; Nelson et al. 2019) based on rest-frame optical measurements at ≈ 0.51–$0.89\,\mu$m. Finally, we look at the BlueTides cosmological hydrodynamical simulations in Marshall et al. (2022). The r_e–z model we use from them is constrained at $7 < z < 11$ based on rest-frame far-ultraviolet (FUV), though

they find that their FUV and optical sizes are similar so we decided to keep the comparison.

In Figure 4.13, we show how the $r_{e,\mathrm{F444W}}$ of a $10^{9.25}\,\mathrm{M}_{\odot}$ SF galaxy from our F444W r_e–M_* relationship (see Figure 4.7) compares to the studies mentioned above. We chose to use a stellar mass of $10^{9.25}\,\mathrm{M}_{\odot}$ for these comparisons rather than our median stellar mass of $M_{*,\mathrm{median}} = 10^{8.30}\,\mathrm{M}_{\odot}$ because the majority of the observational studies derive their r_e–z evolution models based on much higher characteristic masses. This value is still within our sample's mass range and is above the mass range where we see the largest scatter in sizes (see Chapter 4.5.1). We show the r_e–z relations as a function of both redshift and lookback time as it is helpful to illustrate to the reader how galaxies grow as a function of linear cosmic time. Details of the studies that compose the individual points in Figure 4.13 can be found in Table 4.2.

From Figure 4.13, for a $10^{9.25}\,\mathrm{M}_{\odot}$ SF galaxy, we predict $r_{e,\mathrm{F444W}} = 0.76 \pm 0.46\,\mathrm{kpc}$ from our F444W r_e–M_* relationship (red point). The error associated with this size is the scatter about the relationship at this stellar mass. This $r_{e,\mathrm{F444W}}$ agrees with a wide range of individual measurements in the literature at $z > 4$, as well as with the r_e–z relationship from Sun et al. (2024) at $z \sim 6$. There is also agreement with the lower-z relationship from Martorano et al. (2024) extrapolated out to $z = 6.1$. The exception to this is the relationship from van der Wel et al. (2014; grey dashed line), constrained between $0 < z < 1.5$. Extrapolating their r_e–z relationship, SF galaxy sizes are $\approx 0.6\,\mathrm{kpc}$ (factor ≈ 1.8) larger at $z = 6.1$ than the other relationships we compare to. On the other hand, the relationship determined from the observations in Sun et al. (2024) agrees with our $r_{e,\mathrm{F444W}}$ at $z = 6.1$, although that relation over-predicts sizes at much lower redshifts (see also the relations in simulations from Roper et al. 2022; Costantin et al. 2023). The discrepancies between these studies can be explained by the fact that their relationships are only measured at certain redshift ranges resulting in them failing to capture galaxy evolution at extrapolated redshifts that are not probed. All the simulated r_e–z relationships that we compare to agree with our r_e at $z = 6.1$.

We fit a power-law of the form $\log_{10}\left(\frac{r_e}{\mathrm{kpc}}\right) = \beta \log_{10}(1+z) + B$ to all the individual points we compare to (solid black line; see Table 4.2), including our

Table 4.2: The studies that make up the individual points in Figure 4.13.

Reference	z	Rest-frame Wavelength (μm)	Stellar Mass ($\log_{10}(M_*/M_\odot)$)
Stott et al. (2013a)	0.4–2.23	0.47–1.57	9.25
Paulino-Afonso et al. (2017)	0.4–2.23	0.25–0.57	9.74–9.96
van der Wel et al. (2024)	0.5–2.3	0.46–0.57	9.2
Suess et al. (2022)	1.3–1.7	0.55–0.65	9.22
Martorano et al. (2024)	2.0–2.5	1.24–1.45	9.27
Allen et al. (2025)	3.0–9.0	0.39–0.62	9.25
Ward et al. (2024)	3.0–5.5	0.42–0.58	9.25
Ormerod et al. (2023)	5.0	0.48–0.76	9.3–11.1
Wu et al. (2020)	6.0	0.62	9.25

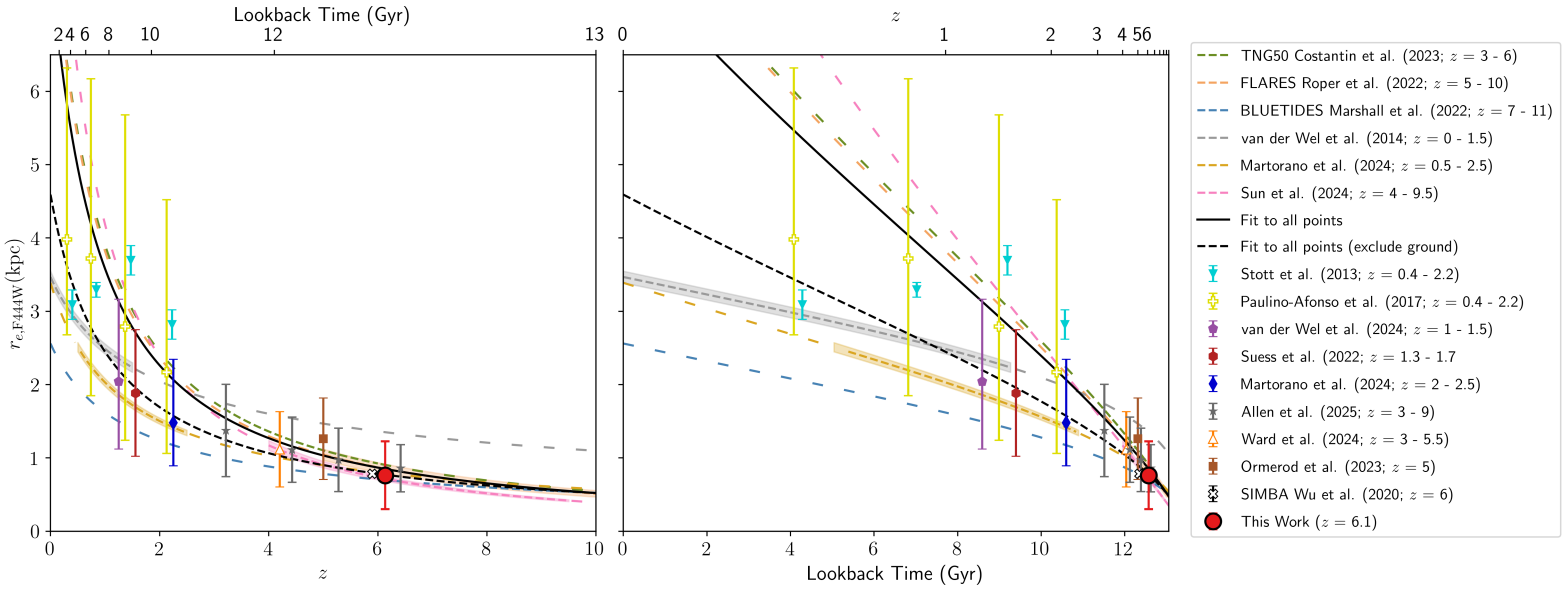

Figure 4.13: *Left* - r_e–z relationship of studies in the literature compared to our work. *Right* - The same as in the left panel, but all points and relations are as a function of lookback time. The large red circle indicates the size of a $10^{9.25}\,\mathrm{M}_\odot$ SF galaxy for our sample derived from our F444W r_e–M_* relationship in Figure 4.7. The error associated with this size is the scatter about the relationship at this stellar mass. For the individual points, filled faces indicate that the inferred size is derived from a study with a stellar mass (or stellar mass range) that is within the range of this work. White faces indicate that the inferred mass has been extrapolated outside the mass range of that study to match the $10^{9.25}\,\mathrm{M}_\odot$ we use for our own estimate. We refer the reader to Table 4.2 for information on these studies. From observations, we compare to the r_e–z relationships of van der Wel et al. (2014; grey; $0 < z < 1.5$), Martorano et al. (2024; yellow; $0.5 < z < 2.5$) and Sun et al. (2024; pink; $4 < z < 9.5$). From simulations, we compare to the r_e–z relationship from the TNG50 cosmological hydrodynamical simulation (Nelson et al. 2019) in Costantin et al. (2023; green; $3 < z < 6$), the FLARES zoom-in simulations (Vijayan et al. 2021) in Roper et al. (2022; orange; $5 < z < 10$) and the BlueTides cosmological hydrodynamical simulations (Feng et al. 2016) analysed in Marshall et al. (2022; blue; $7 < z < 11$). The shaded regions of the literature relationships are the 1σ scatter in their relationships within their z range (if applicable). Where the dashed lines become more spaced is an extrapolation beyond the redshift of the respective study. The solid black line is a fit to each of the individual points, weighted by their errors. We also include a fit that does not include the ground-based observations from Stott et al. (2013a) and Paulino-Afonso et al. (2017; dashed black line). The points from Paulino-Afonso et al. (2017) and Wu et al. (2020) have been shifted in both redshift (-0.1; *left*) and lookback time ($-0.2\,\mathrm{Gyr}$; *right*) for clarity.

Table 4.3: $f_{\rm merger}$ from Equation 4.5 for PRIMER F356W-detected sources within fixed distances, d, from systems in the parent catalogue of HAEs in Pirie et al. (2025).

d (kpc)	$f_{\rm merger}$	$f_{\rm maj.merger}$
17 (HAEs only) ‡	0.09 ± 0.05	...
17	0.29 ± 0.09	0.33 ± 0.19
25	0.43 ± 0.11	0.44 ± 0.22
50	0.71 ± 0.14	0.67 ± 0.27

‡ - only considering other HAEs within the `GALFIT` cutouts.

own $r_{e,\rm F444W}$. The parameters of this fit are $\beta = -1.13 \pm 0.1$ and $B = 0.89 \pm 0.05$, which predict $r_e \approx 7.8\,$kpc at $z = 0$. However, this fit and subsequently inferred $r_{e,\rm F444W}$ may be biased by the ground-based observations of HAEs by Stott et al. (2013a) and Paulino-Afonso et al. (2017) from HiZELS, which are less reliable than space-based measurements and result in a significantly larger size estimate at $z = 0$. Therefore, we also fit a power-law in the same form which excludes these points (dashed black line) with $\beta = -0.91 \pm 0.09$ and $B = 0.66 \pm 0.07$, predicting $r_e \approx 4.6\,$kpc at $z = 0$.

4.4.4 Merger Fraction at $z = 6.1$

As previously discussed, our final sample of 23 HAEs at $z = 6.1$ is drawn from the parent catalogue of 35 derived by Pirie et al. (2025). Present in their catalogue of sources — twelve of which we discarded from our sample for reasons detailed in Chapter 4.2.1 — are some systems with multiple HAEs. Whilst we cannot accurately model the light profiles of those discarded galaxies, we can use them to approximate a merger fraction ($f_{\rm merger}$). This is important to analyse because mergers are one of the primary mechanisms that contribute to galaxy growth (Toomre & Toomre 1972), including at the EoR (e.g. Dalmasso et al. 2024; Duan et al. 2025; Puskás et al. 2025; Westcott et al. 2025; see Chapter 4.5.3). To do this, we estimate a projected pair fraction, which we use as an approximation of the merger fraction. This method is commonly referred to as "pair counting" (Barnes 1988; see also Patton et al. 1997; Le Fevre et al. 2000; Bell et al. 2006a,b). We

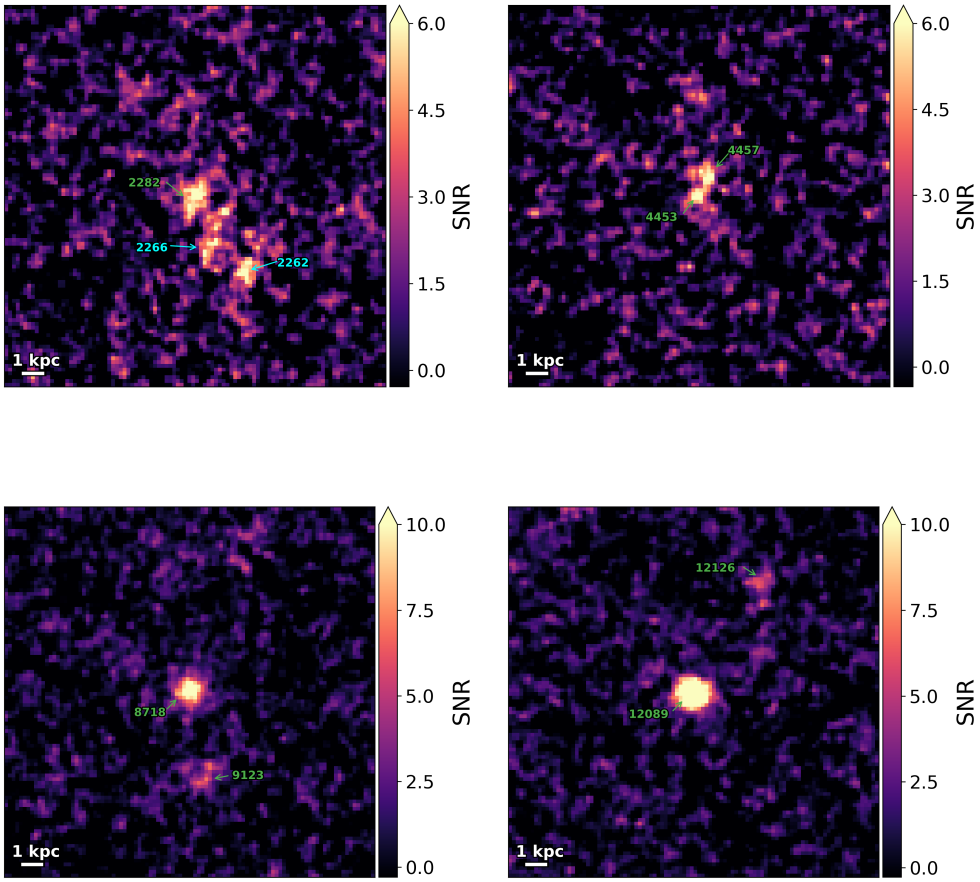

Figure 4.14: $3 \times 3\,\mathrm{arcsec}^2$ ($\sim 17 \times 17\,\mathrm{kpc}^2$) cutouts of four merging systems in JELS F466N, smoothed with a Gaussian kernel with FWHM = 1.5 pixels. The colour bar indicates the SNR per pixel. These cutouts are centred on four different Hα-emitting galaxies at $z = 6.1$ and are defined as merging systems by having at least one other NB-selected source within the cutout. Galaxies labelled in green are in the parent catalogue of HAEs from Pirie et al. (2025). The cutout centred on galaxy 2282 (detected in F466N) has 2 other candidate sources within the cutout; galaxy 2266 has a similar photo-z to galaxy 2282 ($z_{\mathrm{phot}} = 6.29$), but it has an excess significance parameter in F466N compared to F470N of $< 2.5\sigma$ and $< 3\sigma$ compared to F444W, values which are below the required threshold for a significant detection in F466N compared to either filter; galaxy 2262 has $> 3\sigma$ excess compared to F444W, but its $z_{\mathrm{phot}} = 6.51$ is beyond the range required by Pirie et al. (2025) to be in the catalogue of $5.5 < z_{\mathrm{phot}} < 6.5$. These galaxies are therefore highlighted in blue to be clear that these are not in the parent catalogue of HAEs.

define a potential pair as a primary HAE that has a neighbouring source from the PRIMER F356W-detected catalogue of Pirie et al. (2025) that satisfies the photo-z selection for galaxies at $z \sim 6$. Specifically, these sources are required to have $5.5 < z_{\rm phot} < 6.5$ and an integrated redshift posterior probability of $\mathrm{P}(z) > 0.7$ over this same interval. Here, $\mathrm{P}(z)$ refers to the integral of the normalised photo-z posterior within $5.5 < z < 6.5$, rather than the value of the posterior at a single redshift. For the primary galaxy sample, we use the parent catalogue of 35 HAEs. We count the number of unique projected pairs between galaxies in the primary sample and sources in the F356W-detected sample within separations of $d \lesssim 17\,\mathrm{kpc}$ (corresponding to the width of our `GALFIT` cutouts), $d \lesssim 25\,\mathrm{kpc}$, and $d \lesssim 50\,\mathrm{kpc}$, with each unique pair counted once. This pair-counting approach is defined as

$$f_{\rm merger} = \frac{N_{\rm pair}}{N_{\rm primary}}, \tag{4.5}$$

where $N_{\rm pair}$ is the number of unique pairs satisfying the separation and photo-z criteria, and $N_{\rm primary}$ is the number of galaxies in the primary sample. We note that $f_{\rm merger}$ is not necessarily identical to the fraction of primary galaxies with at least one companion, because a single primary system may contribute more than one pair. Consequently, $f_{\rm merger}$ can in principle exceed unity.

We find four systems that have multiple HAEs with $z_{\rm phot} \sim 6.1$ detected within a $3 \times 3\,\mathrm{arcsec}^2$ cutout, equivalent to $\sim 17 \times 17\,\mathrm{kpc}^2$. We show these systems in Figure 4.14. We smoothed these cutouts with a Gaussian kernel with a full width at half maximum (FWHM) of 1.5 pixels to reduce some of the noise. We note that in the upper left panel of Figure 4.14, galaxy 2266 has a $z_{\rm phot} = 6.29$ which is within the range required by Pirie et al. (2025) of $5.5 < z_{\rm phot} < 6.5$, but does not satisfy the other criteria to be in the parent catalogue. Specifically, it has an excess significance parameter in F466N compared to F470N of $< 2.5\sigma$ and $< 3\sigma$ compared to F444W which are both below the required threshold for a significant detection in F466N compared to either filter. Moreover, while galaxy 2262 has $> 3\sigma$ excess compared to F444W, its $z_{\rm phot} = 6.51$ is beyond the range required by Pirie et al. (2025) to be in the catalogue. We therefore highlight the text for these galaxies in blue to be clear that these are not in the parent catalogue of HAEs,

and therefore not the primary sample for our pair-counting approach. However, given that 2266 is a PRIMER F356W detection within the required redshift range, this is considered a pair with galaxy 2282. This potential three-way merger could be an excellent candidate for follow-up with the *JWST*/NIRSpec integral field unit (IFU; Böker et al. 2022) or the Atacama Large Millimeter Array (ALMA; Wootten & Thompson 2009).

Pair fractions in the literature are often selected based on the stellar mass ratio, μ, of the pair. For *major* mergers, this is typically defined as $\mu > 1/4$. Both the JELS parent catalogue of HAEs and the PRIMER F356W-detected catalogue are complete down to $\approx 10^{8.2}\,\mathrm{M}_{\odot}$. To calculate a major close-pair fraction, $f_{\mathrm{maj.merger}}$, we therefore set this as a lower mass limit for secondary galaxies, and $4 \times 10^{8.2} \approx 10^{8.8}\,\mathrm{M}_{\odot}$ as the corresponding lower limit for primary galaxies. For calculating $f_{\mathrm{maj.merger}}$, we also remove any object that exhibits point-source activity, since the stellar mass values from SED fitting are biased to significantly higher masses. This mass cut, and the removal of point sources, reduces our primary galaxy sample to just 9 primary HAEs. As a result, major-pair fractions can be marginally larger than the total pair fraction in some projected-separation bins, because $f_{\mathrm{maj.merger}}$ is calculated over a restricted subset of the full parent catalogue for which the mass-ratio selection is complete, and is therefore not required to be smaller than the total pair fraction.

We list our calculated close-pair fractions in Table 4.3. The uncertainty on each pair fraction is estimated assuming Poisson counting uncertainty on the number of identified pairs, defined as $\sigma_{f_{\mathrm{merger}}} = \frac{\sqrt{N_{\mathrm{pair}}}}{N_{\mathrm{primary}}}$. Within $d \lesssim 17\,\mathrm{kpc}$, we find a $f_{\mathrm{merger}} = 0.29 \pm 0.09$, which rises to $f_{\mathrm{merger}} = 0.43 \pm 0.11$ ($f_{\mathrm{merger}} = 0.71 \pm 0.14$) for detections within $d \lesssim 25\,\mathrm{kpc}$ ($d \lesssim 50\,\mathrm{kpc}$). The systems in Figure 4.14 give us a merger fraction $f_{\mathrm{merger}} \sim 0.09$ if we only consider NB-detected sources within our cutouts. For $f_{\mathrm{maj.merger}}$, our values are consistent with f_{merger}, though we find no examples of major mergers involving multiple HAEs within 17 kpc. We also note that our $f_{\mathrm{maj.merger}}$ value is dominated by system 2282, which accounts for all pairs within $d \lesssim 25\,\mathrm{kpc}$ across the restricted primary sample. We compare our merger fractions to values in the literature in Chapter 4.5.3.

4.5 Discussion

4.5.1 Scatter of HAE Sizes at Low Stellar Mass

From Figures 4.5–4.8, we see that at low stellar mass ($M_* < 10^{8.4}\,\mathrm{M}_\odot$), there is a larger scatter in $\log_{10}(r_e)$ than at high mass for all filters. For example, the scatter of $\log_{10}(r_{e,\mathrm{F444W}})$ in our F444W r_e–M_* relationship (see Figure 4.7) is $\sigma_{\mathrm{scatter}} = 0.30\,\mathrm{dex}$, compared to $\sigma_{\mathrm{scatter}} = 0.16\,\mathrm{dex}$ at $M_* \geq 10^{8.4}\,\mathrm{M}_\odot$. This increased scatter at low stellar mass may be a result of the "bursty" SFH of SF galaxies at the EoR which has been shown to have a greater impact on the evolution of less massive galaxies. Using the Feedback in Realistic Environments (FIRE; Hopkins et al. 2014) cosmological zoom-in hydrodynamical simulations, El-Badry et al. (2016) find that short-term stellar migration ($\sim 100\,\mathrm{Myr}$) can lead to significant fluctuations in r_e by factors of 2–3 during starbursts, and that this effect is strongest in low-mass galaxies (10^7–$10^{9.6}\,\mathrm{M}_\odot$; see also Graus et al. 2019; Mercado et al. 2021). Using the THESAN-ZOOM simulations, McClymont et al. (2025a) showed that star formation in the early Universe is highly bursty on short ($\lesssim 50\,\mathrm{Myr}$) timescales. Similarly, McClymont et al. (2025b) found that the size evolution of SF galaxies is strongly linked to starbursts, with galaxies alternating between phases of compaction and expansion which cause them to "oscillate" about the r_e–M_* relationship. This rapid compaction arises because starbursts are typically centrally concentrated, before inside-out quenching subsequently increases their size once the burst subsides. Together, the results of McClymont et al. (2025b,a) suggest that EoR galaxies undergo dramatic, short-term morphological transformations driven by bursty SFHs, potentially contributing to the scatter we observe in our r_e–M_* relations. The SFH of our HAEs, determined from SED fitting by Pirie et al. (2025), is explored in greater detail in Chapter 4.5.2.

Given the assumption that the large scatter at low stellar masses may be caused by diverse SFHs, as well as the evidence in the literature from simulations, we looked for a connection between $r_{e,\mathrm{F444W}}$ and the SF properties of these $\lesssim 10^{8.4}\,\mathrm{M}_\odot$ HAEs. We did not find any correlation between $r_{e,\mathrm{F444W}}$ and current SFR measured from Hα, UV continuum or SFR derived from SED

fitting. Only a weak correlation is found between $r_{e,\mathrm{F444W}}$ and the ratio of SED-fitted SFR averaged over canonical timescales of 10 Myr to SFR averaged over 100 Myr ($\mathrm{SFR}_{10}/\mathrm{SFR}_{100}$), with a relationship in the form $\mathrm{SFR}_{10}/\mathrm{SFR}_{100} = (0.58 \pm 0.65)\, r_{e,\mathrm{F444W}} + (3.24 \pm 0.51)$, though we note the sample size for this fit is only 12 HAEs. $\mathrm{SFR}_{10}/\mathrm{SFR}_{100}$ is a proxy for the burstiness of star formation (e.g. Broussard et al. 2019) and, as such, gives a good indication of the recent SFH of these galaxies, with Pirie et al. (2025) showing that the HAEs in the parent catalogue, particularly those at low stellar mass, are undergoing a recent upturn in star formation (see Chapter 4.5.2 for further details). However, this analysis is only able to get an estimate of the time averaged SFR over ≤ 100 Myr, which is the SFH from $z \approx 6.7$. It is entirely possible that these galaxies may have undergone previous starbursts at $z \gtrsim 6.7$ (see Chapter 4.4.2) which have contributed to the scatter we observe in the r_e–M_* relationship at $z = 6.1$.

Our analysis in Chapter 4.3.1.1 shows that mock galaxies with magnitudes $\gtrsim 27.5$ mag and $r_e \lesssim 0.8$ kpc have overestimated $r_{e,\mathrm{median}}$ recovered by `GALFIT` compared to $r_{e,\mathrm{model}}$ (see Figure 4.4). While $r_{e,\mathrm{median}}/r_{e,\mathrm{model}}$ does not exceed a factor of 1.2 within the magnitude range of our sample, it is plausible that some of the less massive HAEs (which tend to be fainter) are contributing to this scatter because they have elevated r_e compared to their real size.

Additionally, as explored in Chapter 4.4.2.1, we found some evidence that the F444W sizes of HAEs at $< 10^{8.4}\,\mathrm{M}_\odot$ are more impacted by the removal of Hα contribution to the overlapping F444W, with $r_{e,\mathrm{F444W_{sub}}}$ being larger than $r_{e,\mathrm{F444W}}$ by a factor of 1.10 ± 0.32 (Figure 4.12). We also find that the scatter in $\log_{10}(r_{e,\mathrm{F444W_{sub}}})$ reduces to $\sigma_{\mathrm{scatter}} = 0.25$ dex. This suggests that the scatter in F444W at low stellar mass is being contributed to by Hα emission in the BB, though this does not explain the scatter observed in other filters which are also $\gtrsim 0.3$ dex. Ultimately, it is likely that a combination of all the reasons discussed above are contributing to the scatter of HAE sizes.

4.5.2 Implications for Inside-Out Growth of Galaxies

From Figure 4.9, we find that the physical sizes of the stellar continuum of $z = 6.1$ SF galaxies are marginally bigger than the sizes inferred from their Hα emission.

Given that the ratio for many of the individual objects is consistent with $\frac{r_{e,\mathrm{F444W}}}{r_{e,\mathrm{NB}}} = 1$, we can say that, at the very least, our results show that significant stellar populations have been built up by the end of the EoR that are comparable to the sizes of the SF components and that this SF region may be more centrally concentrated. It should be noted that using the Hα emission as a direct proxy for the extent of the SF component of galaxies can have its complications as a result of potential dust obscuration of the rest-frame optical light (e.g. Wuyts et al. 2011; Nelson et al. 2012; Tacchella et al. 2015). However, from their BAGPIPES[1] (Carnall et al. 2018) SED fitting, Pirie et al. (2025) have demonstrated that our sample of HAEs are relatively dust-poor with a median $A_V = 0.23$. Indeed, rest-R-band light is less susceptible to dust attenuation compared to rest-UV emission (Calzetti et al. 2000; Salim et al. 2018), which is often used in the literature to identify SF regions (e.g. Murphy et al. 2011; Mosleh et al. 2012; Ono et al. 2023; Morishita et al. 2024) so any impacts on our overall sizes will not be as great as those studies. Additionally, we are observing the ratio of the stellar component to the SF region at approximately the same wavelength between the NB and F444W filters ($\lambda \approx 4.4$–$4.7\,\mu$m rest-R-band). Therefore, should there be any significant impact from dust, it would affect the sizes in both the NB and F444W images approximately the same. A caveat to this is the possibility there may be a difference in the dust extinction for the stellar continuum and nebular components, but this remains uncertain at high-z (Sanders et al. 2025).

Evidence in the literature suggests that galaxies experience what is known as "inside-out" growth (van Dokkum et al. 2010). In this paradigm, galaxies predominantly grow their mass and sizes from centrally concentrated SF regions first before expanding out into, and indeed forming, extended stellar disks towards lower redshifts. This transition of primary mass/size build-up from central regions to extended disks has been shown to come from either elevated SFRs in the disk compared to the central bulge (e.g. Dekel & Burkert 2014; Zolotov et al. 2015; Ellison et al. 2018; Shen et al. 2024b) or from wet mergers (e.g. Mihos & Hernquist 1994a; Lin et al. 2008; Lapiner et al. 2023). Whilst this is a reasonably well-known evolutionary track from Cosmic Noon, when the global SFR peaks ($1 \lesssim z \lesssim 3$; Madau & Dickinson 2014), only recently has *JWST* allowed inside-out growth to

[1] https://bagpipes.readthedocs.io

be observed directly, and in greater detail, out to the EoR. For example, Baker et al. (2025) discovered a mature SF galaxy at $z = 7.43$ in the Great Observatories Origins Deep Survey–South (GOODS–S) field (Giavalisco et al. 2004) from the *JWST* Advanced Deep Extragalactic Survey (JADES; Eisenstein et al. 2026). From this, they were able to ascertain the recent and extended SFH of the galaxy which shows that the time-averaged SFR over the prior 100 Myr was highest in the central core of the galaxy, but over the most recent 10 Myr, the SFR is significantly higher in the disk, consistent with inside-out growth. Other studies have shown similar consistency with inside-out growth at $z \gtrsim 6$ (e.g. Morishita et al. 2024; Matharu et al. 2024; Kocevski et al. 2025). More generally, prior to the launch of *JWST*, observations found that rest-frame optical emission lines in galaxies at $z \gtrsim 6$ had high rest-frame EWs ($\gtrsim 500$ Å; e.g. Labbé et al. 2013; Smit et al. 2015; Roberts-Borsani et al. 2016; Endsley et al. 2020; Stefanon et al. 2022), indicating strong sSFRs at these redshifts which could imply rapid growth that aligns with the inside-out paradigm.

However, whilst evidence exists that galaxies evolve inside-out during the EoR, it is becoming apparent that the SFHs of galaxies at this epoch are complex and diverse. Galaxies have been shown to go through bursts of star formation (often referred to as bursty SFHs; Dressler et al. 2023, 2024; Ciesla et al. 2024; Harshan et al. 2024; Wang et al. 2024b; Looser et al. 2025), which were predicted by simulations prior to *JWST* (Kimm & Cen 2014; Ceverino et al. 2018; Furlanetto & Mirocha 2022). Recently, Endsley et al. (2025) analysed 368 $z \sim 6$ Lyman-break galaxies in the GOODS fields and lensed fields surrounding the Abell2744 cluster and found a dramatic range of SFHs. They analyse the Hα to UV luminosity ratio ($L_{\mathrm{H}\alpha}/L_{\mathrm{UV}}$) to infer the recent SFH of their galaxies and find their sample has properties consistent with extremely bursty SFHs, as well as finding that many of their galaxies have experienced strong recent SFR upturns *and* downturns. This followed a similar result from Endsley et al. (2024) who similarly concluded that $z \gtrsim 6$ galaxies experienced bursty SFHs with evidence of strong recent downturns, this time using [O III], Hβ and Hα EWs.

For our sample of HAEs, Pirie et al. (2025) demonstrated that they are going through a recent burst of star formation from their SED fitting, particularly those with stellar masses $M_* \lesssim 10^9\,\mathrm{M}_\odot$. As they point out, this was to be expected

as Hα emission is a good tracer of recent star formation ($\approx$ 10 Myr; Murphy et al. 2011) compared to the UV-continuum, for example, which can be used to probe longer timescales ($\gtrsim$ 100 Myr; Hao et al. 2011a), though we caveat that UV emission is produced by a combination of different stellar populations that range in lifespans ($\sim$ 10–200 Myr), meaning it can only be confidently used to trace stellar populations older than $\gtrsim$ 100 Myr in galaxies with steady-state star formation. However, in line with the studies we mention above, Pirie et al. (2025) find that their results indicate that these HAEs at $z = 6.1$ have bursty SFHs.

In this context, given our results in this chapter show that a significant stellar component has already been built up, and that the results of Pirie et al. (2025) show that these same galaxies are currently undergoing a burst of star formation (especially those at $M_* \lesssim 10^9\,\mathrm{M}_\odot$), we conclude that the stellar component must have been built by previous episodes of star formation and that these were likely bursts themselves. Moreover, we also believe that these episodes of star formation may have occurred at $z \gtrsim 6.7$ ($\approx$ 100 Myr prior to $z = 6.1$) since the median $\mathrm{SFR}_{10}/\mathrm{SFR}_{100} \approx 2.9$ for our sample of 23 HAEs, suggesting the recent burst is significantly elevated compared to the averaged 100 Myr SFR. These bursts of star formation may then be regulated by stellar feedback (i.e. Ma et al. 2018; Katz et al. 2023; Shen et al. 2024a) and/or mergers (see Chapter 4.5.3). This is not necessarily in contradiction to inside-out growth evolution, as Pirie et al. (2025) have shown that higher mass sources ($M_* \gtrsim 10^9\,\mathrm{M}_\odot$) show evidence of a more consistent SFH. Additionally, the stochastic SFH exhibited by these sources may consistently be centrally concentrated given we are observing the current SF region as being marginally smaller than the stellar component on average. This is best illustrated when we compare $r_{e,\mathrm{F444W_{sub}}}$ to $r_{e,\mathrm{NB}}$ and find that NB flux-subtracted F444W sizes are a factor of 1.26 ± 0.14 larger, which suggests a centrally concentrated SF region. Stars formed during these bursts may then "fan" out with time as a result of stellar migration (Schönrich & Binney 2009; El-Badry et al. 2016) in a manner consistent with inside-out growth. Given the evidence of bursty star formation in the literature combined with our results, we suggest that a more complex approach to galaxy evolution is needed at the EoR.

4.5.3 Merger Fraction Comparisons

Here, we compare our measured $f_{\rm merger}$ and $f_{\rm maj.merger}$ to values in the literature, from both observations and simulations. For the purposes of all comparisons, we use our estimates at $5.5 < z_{\rm phot} < 6.5$ within $d \lesssim 25\,{\rm kpc}$ (see Table 4.3) as this is the most comparable value to the comparison studies in Figure 4.15.

Figure 4.15 shows how our close-pair fractions at $z = 6.1$ compare to measurements in the literature for a range of redshifts. Most of these measurements use a similar close-pair fraction methodology to this work, with the exception of Dalmasso et al. (2024; green pentagons) who use a combination of morphological statistical parameters, and we refer the reader to their paper for details on their methods. We highlight here that direct comparisons to their work should be treated with caution due to potential systematic effects that arise from the differences between our methods. We also note that the $z = 0$ $f_{\rm merger}$ from Casteels et al. (2014; purple triangle) is used by Duan et al. (2025) as a supplementary zero-point for their $f_{\rm merger}$–z relationship (brown dashed line). All of the merger fractions at $z \gtrsim 3$ in Figure 4.15, as well as the Casteels et al. (2014) value, are based on galaxy samples with a comparable stellar mass range to our own. The merger fractions of Duncan et al. (2019; black stars; typical stellar mass $M_* \sim 10^{10}\,{\rm M}_\odot$), and the relation from Lin et al. (2008; grey dashed line and shaded region; $M_* \sim 10^{10.7}\,{\rm M}_\odot$) are based on stellar mass ranges that exceed our sample.

From Figure 4.15, we can see that our measured close-pair fractions of $f_{\rm merger} = 0.43 \pm 0.11$ and $f_{\rm maj.merger} = 0.44 \pm 0.22$ broadly agree with literature values at $z = 6.1$ within uncertainties, though we find they are higher than the relationship of Duan et al. (2025) and the values from Dalmasso et al. (2024). We particularly find excellent agreement with the $f_{\rm merger}$ from Puskás et al. (2025). Their results are derived from JADES observations of the GOODS–North (GOODS–N) and GOODS–S fields at $3 \lesssim z \lesssim 9$ for separations of $5 < d < 30\,{\rm kpc}$. As a result of their large sample size ($\sim 300\,000$), they split their $f_{\rm merger}$ into different stellar mass ranges, and we find the best agreement with their 10^8–$10^{8.5}\,{\rm M}_\odot$ values. This range also best matches the stellar mass of the parent catalogue of JELS HAEs ($M_{*,\rm median} = 10^{8.36}\,{\rm M}_\odot$). Specifically, in this mass range, they find

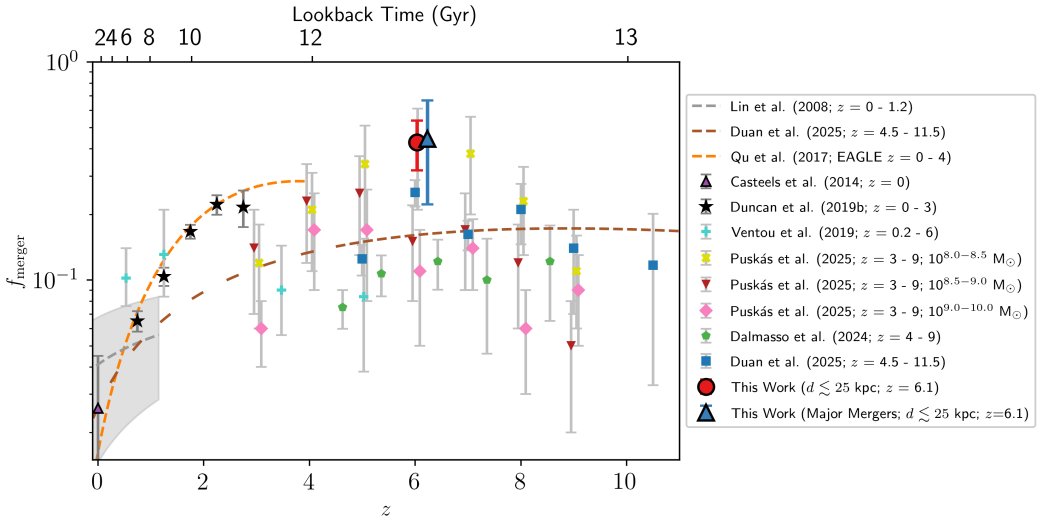

Figure 4.15: Our measured close-pair merger fraction, $f_{\rm merger}$, based on PRIMER F356W detections at $z_{\rm phot} \sim 6$ within $d \lesssim 25$ kpc of HAEs in the parent catalogue of Pirie et al. (2025; large red circle). The large blue triangle represents our pair fraction for major mergers, $f_{\rm maj.merger}$, with a stellar mass ratio of $\mu > 1/4$. Our $f_{\rm merger}$ ($f_{\rm maj.merger}$) value is offset by +0.1 (−0.1) in redshift for clarity. The error on all individual points represents the standard error of the measured fraction at that redshift. Most comparisons in the literature use a similar close-pair fraction method to the one in this study, with the exception of Dalmasso et al. (2024) who use morphological statistical parameters for their fraction. The dashed lines from Qu et al. (2017) and Duan et al. (2025) show the redshift evolution of merger fractions as a power law with an additional exponential component of the form $f_{\rm merger} = f_0 \cdot (1+z)^m \cdot e^{\tau(a+z)}$. The grey dashed line indicates the power law evolution measured by Lin et al. (2008) at $0 < z < 1.2$ based on analysis of close-pair fractions. Their relationship is of the form $f_{\rm merger} = f_0 \cdot (1+z)^m$, with the grey shaded region indicating the 1σ error of their relationship. The brown dashed line is the observed evolution measured by Duan et al. (2025) between $4.5 < z < 11.5$, who use Casteels et al. (2014) as their $z = 0$ point. Where the Duan et al. (2025) relationship becomes more spaced is where it is extrapolate beyond their redshift range. The orange dashed line indicates the redshift evolution from the EAGLE cosmological hydrodynamical simulations (Crain et al. 2015) as measured by Qu et al. (2017) from $0 < z < 4$.

$f_{\rm merger} = 0.41 \pm 0.20$ at $5.5 < z < 6.5$ which is consistent with all of our $f_{\rm merger}$ and $f_{\rm maj.merger}$ values in Table 4.3.

Compared to the $z = 0$ $f_{\rm merger}$ from Casteels et al. (2014), we find that close-pair fractions at $z = 6.1$ are a factor of ~ 12 higher than in the local Universe for $d \lesssim 25\,{\rm kpc}$. Comparing instead to the $z = 0$ value inferred from the Lin et al. (2008) relationship, our close-pair fractions are a factor of ≈ 8 higher. Both of these comparisons demonstrate that the merger fraction of galaxies during the EoR is significantly higher than in the local Universe, as also indicated by the other studies in Figure 4.15. However, there is evidence in the literature that galaxy merger fractions rise from $z = 0$ before flattening and remaining consistent at $z \gtrsim 3$, which is seen in both the observed $f_{\rm merger}$–z relationship in Duan et al. (2025) and results from the EAGLE simulations in Qu et al. (2017; see Figure 4.15; see also Conselice 2014; Mundy et al. 2017; O'Leary et al. 2021; Huško et al. 2022; Westcott et al. 2025). Our results in Table 4.3 for all separations, combined with results in the literature, suggest that galaxy mergers play an important role in galaxy evolution at the EoR.

4.6 Conclusions

We utilised data from JELS to study the sizes of 23 HAEs at $z = 6.1$. Our sample is drawn from a parent catalogue of 35 HAEs described in Pirie et al. (2025). We measured the size of both the ionised Hα emission from $\lambda \sim 4.7\,\mu{\rm m}$ NB data taken by JELS, and the stellar emission from $\lambda \sim 4.4\,\mu{\rm m}$ PRIMER F444W images (both rest-R-band). In addition, sizes were also measured in PRIMER F277W (rest-NUV) and PRIMER F356W (rest-V-band) to allow us to compare the light profiles of different stellar populations at the EoR. We measured r_e using $n = 1$ Sérsic light profiles from `GALFIT`. We used these values to determine the size–mass (r_e–M_*) relationship of SF galaxies at this epoch and compare to studies at lower redshift. We compared the average $r_{e,{\rm F444W}}$ of our sample to a range of observational and simulated results in the literature from $0 < z < 11$. Using robust photo-z detections in F356W at $z = 6.1$, we were also

able to determine an estimate of the merger fraction ($f_{\rm merger}$) of galaxies during the EoR. Our key results are summarised as follows:

i) We observe a r_e–M_* relationship in our sample of HAEs in all observed *JWST*/NIRCam filters (Figures 4.5–4.7 and Table 4.1). Our r_e–M_* relationships are offset from those found at lower redshift. We find an offset of -0.37 ± 0.10 dex in $\log_{10}(r_{e,\rm F444W}/\rm kpc)$ relative to the van der Wel et al. (2014) relationship at $z = 2.75$ for a fixed stellar mass of $10^{9.25}\,\rm M_\odot$. This offset reflects a $\sim$ 2.3–2.5 factor increase in the sizes of the stellar component between $z = 6.1$ and $z = 2.75$ (≈ 1.4 Gyr), suggesting SF galaxies grow rapidly from the EoR to Cosmic Noon.

ii) We measure the slope of the F444W r_e–M_* relationship to be $\alpha_{\rm F444W} = 0.14 \pm 0.12$ (see Figure 4.7). This slope is consistent with those found by van der Wel et al. (2014) at both $z = 0.25$ and $z = 2.75$ as well as the r_e–M_* slope of HAEs at $z = 0.4$ found by Stott et al. (2013a). These results suggest that there is no significant redshift evolution in the slope of the r_e–M_* relationship between $0.3 \lesssim z \lesssim 6.1$.

iii) The average $r_{e,\rm F444W}$ of a $10^{9.25}\,\rm M_\odot$ SF galaxy at $z = 6.1$, inferred from our r_e–M_* relationship, is 0.76 ± 0.46 kpc. This value is in excellent agreement with a wide range of literature values at $z = 6.1$, both from observations and simulations (Figure 4.13).

iv) We measured the ratio of the F444W sizes to NB sizes for each of the galaxies in our sample (Figure 4.9). This traces the size ratio of any established stellar component to the SF region traced by ionised gas. We find that the median ratio of these sizes is $\frac{r_{e,\rm F444W}}{r_{e,\rm NB}} = 1.20 \pm 0.09$. Using rest-NUV as a tracer of active star formation, we find $\frac{r_{e,\rm F444W}}{r_{e,\rm F277W}} = 1.14 \pm 0.07$ (Figure 4.10). These measured ratios imply that SF galaxies at $z = 6.1$ have an already-established stellar component that is at least comparable to the size of the SF region when the Universe was ~ 900 Myr old. This also agrees with SF galaxies exhibiting more centrally concentrated star formation at the EoR.

v) Previous analysis from Pirie et al. (2025) indicates that these galaxies are undergoing a strong, recent starburst, with our sample of 23 HAEs showing a median $\mathrm{SFR}_{10}/\mathrm{SFR}_{100} \approx 2.9$. Given the evidence in the literature that galaxies at the EoR have bursty SFH, we suggest that the established stellar component we observe in our sample may have resulted from episodes of star formation at $z \gtrsim 6.7$ ($\gtrsim 100\,\mathrm{Myr}$ prior to $z = 6.1$). Additionally, we believe the large scatter ($\sigma_{\mathrm{scatter}} \sim 0.30\,\mathrm{dex}$) in the r_e–M_* relationship at $M_* < 10^{8.4}\,\mathrm{M}_\odot$ is being significantly contributed to by low-mass galaxies, which are more strongly affected by bursts of star formation giving them more diverse SFH. This could also be affected by `GALFIT` overestimating r_e at faint magnitudes (Figure 4.4).

vi) We determine a close-pair fraction using pair counting based on PRIMER F356W $z_{\mathrm{phot}} \sim 6$ detections from Pirie et al. (2025) and their parent HAE catalogue. We find $f_{\mathrm{merger}} = 0.43 \pm 0.11$ at $z = 6.1$ using a galaxy separation of $d \lesssim 25\,\mathrm{kpc}$. Using a stellar mass ratio of $\mu \geq 1/4$, we determine a close-pair fraction for major mergers of $f_{\mathrm{maj.merger}} = 0.44 \pm 0.22$. These values agree with merger fractions in the literature at the EoR (Figure 4.15). This shows mergers play an important role in galaxy growth from the EoR to Cosmic Noon.

Chapter 5

Conclusion

In this thesis, we have presented a series of observational studies of SF galaxy populations, aimed at probing the evolution of key scaling relations in the high-redshift Universe and assessing the impact of LSS on galaxy properties in clusters. This research makes use of a range of selection techniques and instrumentation, including *HST* grism spectroscopy, wide-field imaging from Subaru, and *JWST* NB observations.

Through these studies, we have examined how galaxies at the EoR and during Cosmic Noon significantly differ in their physical properties relative to analogous populations in the local Universe, with these differences reflecting distinct evolutionary pathways operating at different cosmic epochs. We further show that, within massive galaxy clusters, variations in the spatial distribution of galaxy populations and in their SF properties arise from the relative location of cosmic filaments with respect to the BCG, as well as from environmental quenching processes acting within these filamentary structures. In this chapter, we summarise the key research projects that yielded these results, before outlining future work building on this thesis in Chapter 5.4.

5.1 Cosmic Noon Metallicities in QSAGE

In Chapter 2, we investigated the chemical evolution of SF galaxies at Cosmic Noon ($1.99 < z < 2.32$; $z_{\rm median} = 2.16$) in QSAGE, a NIR grism spectroscopic *HST* Large Programme. We analysed the relationship between gas-phase metallicity and stellar mass (MZR), and the extended relation which includes a dependence on SFR (FMR). Utilising the grism spectroscopic data, gas-phase metallicities were determined using strong emission-line calibrations.

Using both low- (Maiolino et al. 2008) and high-z (Bian et al. 2018) calibrations, we observed an MZR at $z \approx 2.2$. The relations we find agree with other studies in the literature at a similar redshift when using consistent metallicity calibrations (Erb et al. 2006a; Cullen et al. 2014). We find a negative metallicity offset relative to local studies, reflecting an increase in cosmic metallicity values as SFRs decrease toward lower redshifts. The MZR we measure also agree with those seen in various cosmological hydrodynamical simulations and semi-analytic models, with particularly strong agreement at high stellar masses ($\approx 10^{10.25}$–$10^{10.75}\,{\rm M}_{\odot}$). When assessing the FMR, we projected into 2D by combining stellar mass and SFR into a single variable following the method of Mannucci et al. (2010). We observe an FMR in the QSAGE sample such that SF galaxies with higher SFRs have lower gas-phase metallicities at fixed stellar mass. Comparisons with the literature require a shift into their respective FMR planes for consistency as a result of different SFR scaling factors in the two-dimensional projection. When shifting to locally measured FMR planes, we find similar slopes to those observed at all redshifts, but again a negative metallicity offset with redshift.

We interpret the observed anti-correlation between SFR and gas-phase metallicity at fixed stellar mass as a consequence of metal-poor gas accretion regulating star formation at Cosmic Noon. In this context, the inflow of low-metallicity gas both dilutes the ISM and fuels elevated star formation on short timescales, resulting in the observed FMR in the QSAGE sample. This interpretation is supported by both observational evidence for centrally driven star formation and metallicity dilution, and by cosmological simulations in which gas accretion and feedback jointly govern the chemical evolution of SF galaxies.

5.2 Anisotropic Quenching in CLASH

In Chapter 3, we presented an analysis of the anisotropic distribution of SF and passive galaxies in massive clusters, commonly referred to as anisotropic quenching. We used Subaru Suprime-Cam imaging of galaxies in 11 CLASH clusters at $z \approx 0.2$–0.5 ($z_{\rm median} = 0.36$) to measure galaxy colours, $(B-R)_{\rm corr.}$, and passive galaxy fractions, $f_{\rm pass.}$, as a function of orientation angle with respect to the BCG.

We found a significant anisotropic distribution in both $(B-R)_{\rm corr.}$ and $f_{\rm pass.}$, such that galaxies residing along the major axis of the BCG are more likely to be quenched (redder in colour) than those along the minor axis (bluer). This signal is consistent with previous observational studies (Martín-Navarro et al. 2021; Stott 2022; Ando et al. 2023), and is the strongest anisotropic quenching signal reported in the literature to date.

X-ray cavities created by feedback from BCG AGN were ruled out as a driving mechanism for the observed anisotropy, contrary to suggestions by Martín-Navarro et al. (2021), because examples of cavities in the literature are neither common enough, consistently aligned with the BCG minor axis, nor extended to the cluster-centric radii over which we detect the signal. Following a similar method to Ando et al. (2023), we also dismiss variations in local number density as the dominant cause, as passive galaxy fractions remain systematically higher along the BCG major axis even at fixed local densities.

We therefore attribute anisotropic quenching to the preferential accretion of pre-processed galaxies along filaments of the cosmic web, which are typically aligned with the BCG major axis. In this scenario, galaxies infall into clusters as part of groups that have experienced environmental quenching over longer timescales than satellites along the minor axis. There is evidence for this in our observations, as we find elevated $f_{\rm pass.}$ and local surface density values along the major axis compared to the minor axis, with both quantities declining more rapidly along the minor axis with increasing cluster-centric radius. This interpretation is independently supported for lower-mass haloes by cosmological hydrodynamical simulations presented by Zakharova et al. (2025), published at a similar time as our work.

5.3 Galaxy Sizes and Merger Fractions in JELS

In Chapter 4, we investigated the structural properties of SF galaxies at the EoR using data from JELS, the first survey to perform NB rest-optical emission-line selection at the EoR and with *JWST*. JELS targets HAEs in the COSMOS field, allowing us to directly compare the sizes of actively SF regions to established stellar populations. By combining NB rest-frame Hα imaging with BB data from PRIMER, we measured galaxy sizes across multiple rest-frame wavelengths. Structural sizes were inferred from Sérsic light-profile modelling using `GALFIT`.

We find a clear r_e–M_* relationship for SF galaxies at $z = 6.1$ across all observed rest-frame wavelengths, with little observed redshift evolution in the slope compared to studies in the literature between $0.3 \lesssim z \lesssim 6.1$. Our r_e–M_* relationship is significantly offset relative to lower-redshift measurements, indicating rapid physical growth of galaxies over the $\sim 1.4\,\mathrm{Gyr}$ between the EoR and Cosmic Noon. From the rest-R-band relation, we infer an average half-light radius of $r_{e,\mathrm{F444W}} \approx 0.8\,\mathrm{kpc}$ for a $10^{9.25}\,\mathrm{M}_\odot$ SF galaxy at $z = 6.1$, in excellent agreement with both observational and theoretical studies.

By comparing galaxy sizes measured from NB rest-frame Hα emission and rest-optical BB emission, we find that SF galaxies at $z = 6.1$ already host an established stellar component that is comparable in extent to their actively SF regions. The larger BB sizes relative to NB and rest-frame NUV sizes imply that ongoing star formation is more centrally concentrated than the underlying stellar distribution at the EoR. When combined with evidence for bursty SFHs, this suggests that a significant fraction of the stellar mass in these galaxies was assembled during earlier bursts of star formation at $z \gtrsim 6.7$. The increased scatter observed in the r_e–M_* relationship at low stellar masses is consistent with this picture, as this reflects the greater susceptibility of low-mass systems to intense bursts of star formation during the first billion years of the Universe.

We also measure a close-pair fraction for SF galaxies at $z = 6.1$. Our measured major merger fraction indicates that mergers are a common feature of galaxy assembly during the EoR, and are consistent with previous studies at similar redshifts and stellar mass ranges. This result suggests that interactions

play a significant role in driving early galaxy growth. Combined with our structural analysis, these results imply that both mergers and in-situ star formation contribute to the rapid structural evolution of galaxies from the EoR to Cosmic Noon.

Taken together, the results presented in this thesis point to a broader picture in which galaxy evolution is governed by the evolving interplay between gas accretion, feedback, internal structural growth, and environment across cosmic time. During the EoR, star formation is bursty and compact, and strong associated feedback effects, combined with frequent interactions, likely drive the rapid early assembly of stellar mass while inhibiting the widespread emergence of stable, rotationally supported disks. These early episodes of star formation raise questions about whether the paradigm of inside-out growth is applicable to galaxy evolution *during* the EoR, or whether it more accurately describes subsequent galaxy growth when star formation becomes less bursty and more spatially extended. By the peak of the cosmic SFR density at Cosmic Noon, metal-poor gas inflows, feedback-driven outflows and star formation are much more balanced, reflected in the chemical scaling relations of SF galaxies. Around this time, and certainly at later times, environmental effects associated with LSS become increasingly important, as protoclusters grow in number and eventually evolve into massive, virialised clusters with thousands of satellites. The increasing influence of these environmental processes appear to alter this balance, driving the quenching of galaxies while shaping their colours, spatial distributions, and chemical abundances. These connections motivate future work aimed at linking the earliest phases of galaxy evolution to the later formation of stable SF disks and the paradigm of inside-out growth, as well as determining how internal and environmental processes jointly regulate galaxy growth, with a particular focus on *when* these environmental mechanisms begin to dominate.

5.4 Future Works

5.4.1 Gas-phase Metallicities with WEAVE/LOFAR

We used *HST* grism spectroscopy to determine the gas-phase metallicity relations of SF galaxies in Chapter 2. These galaxies were selected based on their [O III] emission and, due to the limited rest-frame wavelength coverage at Cosmic Noon, source classification relied on MEx diagrams instead of the traditional BPT diagnostics. From this analysis, we concluded that the slopes of both the MZR and FMR remain largely unchanged out to Cosmic Noon. A crucial future science case is therefore to determine whether these results are impacted by the selection criteria and source classification methods, or whether they are instead driven by physical processes within the galaxy populations being studied. One way to address this is through the use of a dust-independent SFR indicator, such as radio emission (Condon 1992; Yun et al. 2001; Bell 2003; Murphy et al. 2011).

The William Herschel Telescope (WHT; Boksenberg 1985) Enhanced Area Velocity Explorer (WEAVE; Dalton et al. 2012, 2014, 2016; Jin et al. 2024) is a rest-optical multi-object (MOS) and multi-IFU spectroscopy facility principally designed to provide spectroscopic follow-up for LOFAR and Gaia surveys. WEAVE is mounted at the prime focus of the 4.2 m WHT, delivering spectra at $R \sim 5000$ over 365–960 nm (in low-resolution mode) for up to 1000 robotically positioned fibres across a 2-degree FOV. First light observations of NGC 7318a and NGC 7318b in the Stephan's Quintet galaxy group (Stephan 1877) were presented in December 2022[1] (see Arnaudova et al. 2024), with science verification (SV) data from the MOS being made available in October 2025.

The WEAVE/LOFAR survey (Smith et al. 2016) is designed to provide the primary spectroscopic follow-up for the LOFAR Surveys Key Science Project (KSP; Röttgering et al. 2011) and is expected to generate $\sim 10^6$ spectra of radio-selected sources. As a member of the WEAVE/LOFAR Quality Assessment Group, we are in the process of performing SV on ≈ 700 MOS spectra, including redshift determination, validation of spectral stacking pipelines, and optimisa-

[1] https://www.ing.iac.es/PR/press/weave_LIFU_first_light.html

tion of sky-line masking, in preparation for survey science currently scheduled to commence in April 2026.

With this survey, we will be able to investigate the gas-phase metallicity relations of radio-selected SF galaxies at $z \lesssim 0.44$ (beyond which the [N II]6548, 6583 and Hα emission lines shift beyond the spectral coverage of WEAVE). The primary motivation for such a study is to test whether the scaling relations and physical interpretations inferred at Cosmic Noon remain valid when star formation is selected in a dust-insensitive way. Furthermore, the spectral coverage provided by WEAVE at these redshifts will enable BPT source classification based directly on ionisation physics, rather than proxy-based MEx diagrams.

5.4.2 Impact of Backsplash Galaxies on Anisotropic Quenching

For the analysis in Chapter 3, we probed the impact of AGN feedback (and associated cavities), surface densities, and LSS on the anisotropic quenching signal observed in clusters. We also noted the results of Zakharova et al. (2025), who investigated this signal in simulations and came to the same conclusion as our work. What neither study investigates directly is the contribution of backsplash galaxies to the signal, particularly within annuli at cluster-centric radii where the signal peaks.

As part of continued research into anisotropic quenching, particularly in the most massive clusters where the signal is strongest (see Chapter 3), future studies should utilise simulations that are able to track the orbits of backsplash galaxies and measure anisotropic quenching both with and without these satellites included. As briefly noted in Chapter 3, it may be that the peak of the signal coincides with the turnaround radius of these galaxies following their first pass through the cluster, during which they will have experienced significantly enhanced environmental quenching mechanisms from the hot ICL. Such simulations will also be able to track infalling groups from filaments to probe whether the signal peaks at the point where nodes connect to the cluster, at which point galaxies may have experienced sufficient quenching to maximise the difference

between the major and minor axis of the BCG, or indeed the cluster DM halo itself.

TheThreeHundred simulations (Cui et al. 2018) provide the ideal requirements for such a project. They are a suite of full-physics hydrodynamical re-simulations of 324 massive galaxy clusters with masses $M_{200} > 6 \times 10^{14}\, h^{-1}\, \mathrm{M}_{\odot}$. In order to determine the influence of backsplash galaxies and further probe the impact of LSS, analysis could be performed in TheThreeHundred simulations with a closely-matched sample of clusters to those in CLASH. The primary objective should be to see if the signal can be recreated and to quantify any differences relative to observations, before investigating how backsplash galaxies influence the signal at various cluster-centric distances. It would also be possible to probe the redshift evolution of the signal within such a cluster sample.

5.4.3 Clumpy Star Formation in the High-redshift Universe

The unprecedented spatial resolution of *JWST* made the analysis of galaxy light profiles at $z = 6.1$ in Chapter 4 possible. Owing to the novel NB imaging of JELS, we determined the sizes of HAEs at this epoch for the first time. We were able to link this analysis to the results of Pirie et al. (2025), who found that the SF galaxies in the JELS sample at the EoR are undergoing a current burst of star formation and exhibit bursty SFHs. This paradigm of bursty star formation at the EoR is becoming increasingly well established in the literature (e.g. Dressler et al. 2023, 2024; Looser et al. 2025), and it is imperative to understand how such highly variable SFHs give rise to stable, rotating disks by Cosmic Noon, where the cosmic SFR density peaks. Stochastic SFHs may also have profound consequences for the paradigm of inside-out growth (see Chapter 4.5.2) and for cosmic reionisation.

The key to this transition may lie in the physical properties and evolution of "clumps" of star formation. These are compact regions of intense SF activity that are typically short-lived but are associated with significant feedback effects (Hopkins et al. 2012; Iani et al. 2021; Ceverino et al. 2023), and are a common

feature of SF galaxies at $1 < z < 4$ (Guo et al. 2015; Shibuya et al. 2016; Vanzella et al. 2021), including in Hα emission maps (Livermore et al. 2012, 2015; Whitmore et al. 2020). If the bursts of star formation that are seemingly ubiquitous during the EoR are consistently centrally concentrated (e.g. Chapter 4), then stable disks of gas may be partially shielded from the effects of stellar feedback. However, if clumps of star formation appear in the outer regions of galaxies at this epoch, they may increase the velocity dispersion of early systems and inhibit the formation of stable disks. There is emerging evidence supporting this scenario in the literature, with Danhaive et al. (2025b) finding that disks do not dominate their sample of HAEs at $z \gtrsim 5.5$. However, Danhaive et al. (2025a) find Hα sizes that are larger than the BB rest-optical emission for a similar, though differently selected, sample of galaxies, in contrast to the results presented in Chapter 4. These larger Hα sizes imply intense star formation that extends beyond the central regions of galaxies, which may act to disturb any stably rotating gas. The reasons for this discrepancy are not presently known. Further dedicated studies in this area are therefore required to clarify the role of SF clumps, and their location within galaxies, in the formation of disks in the early Universe.

JELS has also observed the COSMOS field using *JWST* F212N NB imaging, which targets Hα at $z \sim 2.23$, alongside F200W BB imaging to facilitate NB excess selection. These observations probe SFRs more than $\sim 5\times$ fainter than previous ground-based NB imaging selection surveys (Duncan et al. 2025) and add to the wealth of multi-wavelength imaging data in the PRIMER/COSMOS field. These observations enable a similar analysis to Chapter 4 to be performed on the Cosmic Noon JELS sample. A key focus should be to quantify the clumpy fraction, and the individual "clumpiness", of galaxies at both epochs in order to observe directly how spatially resolved star formation evolves. To assess the impact of clumps on these respective populations, future *JWST*/NIRSpec IFU observations should aim to measure the gas kinematics of JELS HAEs at $z \sim 2.23$ and $z \sim 6.1$ to probe the paradigm of inside-out growth in the *JWST* era. Ideally, these observational results would then be matched to high-resolution hydrodynamical simulations of galaxy formation in order to better constrain the physical mechanisms driving clump formation, such as violent disk instabilities (Noguchi

1998; Nelson et al. 2013; Mandelker et al. 2017) and mergers that efficiently compress cold gas (Matteo et al. 2008; Renaud et al. 2015; Nakazato et al. 2024).

References

Abazajian K. N., et al., 2009, The Astrophysical Journal Supplement Series, 182, 543

Adelman-McCarthy J. K., et al., 2006, The Astrophysical Journal Supplement Series, 162, 38

Ahn C. P., et al., 2014, The Astrophysical Journal Supplement Series, 211, 17

Aihara H., et al., 2018, Publications of the Astronomical Society of Japan, 70, S4

Aihara H., et al., 2022, Publications of the Astronomical Society of Japan, 74, 247

Akins H. B., et al., 2021, The Astrophysical Journal, 909, 139

Algera H. S. B., et al., 2023, Monthly Notices of the Royal Astronomical Society, 518, 6142

Allen N., et al., 2025, Astronomy & Astrophysics, 698, A30

Altay G., Colberg J. M., Croft R. A. C., 2006, Monthly Notices of the Royal Astronomical Society, 370, 1422

Ando M., Shimasaku K., Ito K., 2023, Monthly Notices of the Royal Astronomical Society, 519, 13

Andrews B. H., Martini P., 2013, The Astrophysical Journal, 765, 140

Annunziatella M., et al., 2016, Astronomy & Astrophysics, 585, A160

Applegate D. E., et al., 2014, Monthly Notices of the Royal Astronomical Society, 439, 48

Aravena M., et al., 2016, Monthly Notices of the Royal Astronomical Society, 457, 4406

Argyres P. C., et al., 1986, The Astronomical Journal, 91, 471

Arnaudova M. I., et al., 2024, Monthly Notices of the Royal Astronomical Society, 535, 2269

Arrabal Haro P., et al., 2023, Nature, 622, 707

Asplund M., et al., 2009, Annual Review of Astronomy and Astrophysics, 47, 481

Aver E., Olive K. A., Skillman E. D., 2015, Journal of Cosmology and Astroparticle Physics, 2015, 011

Azzaro M., et al., 2007, Monthly Notices of the Royal Astronomical Society: Letters, 376, L43

Baade D., et al., 1999, The Messenger, 95, 15

Bagley M. B., et al., 2023, The Astrophysical Journal Letters, 946, L12

Bakels L., Ludlow A. D., Power C., 2021, Monthly Notices of the Royal Astronomical Society, 501, 5948

Baker W. M., Maiolino R., 2023, Monthly Notices of the Royal Astronomical Society, 521, 4173

Baker W. M., et al., 2022, Monthly Notices of the Royal Astronomical Society, 519, 1149

Baker W. M., et al., 2025, Nature Astronomy, 9, 141

Baldry I. K., et al., 2004, The Astrophysical Journal, 600, 681

Baldry I. K., et al., 2006, Monthly Notices of the Royal Astronomical Society, 373, 469

Baldwin J. A., Phillips M. M., Terlevich R., 1981, Publications of the Astronomical Society of the Pacific, 93, 5

Balogh M. L., Navarro J. F., Morris S. L., 2000, The Astrophysical Journal, 540, 113

Bamford S. P., et al., 2009, Monthly Notices of the Royal Astronomical Society, 393, 1324

Bardeen J. M., Steinhardt P. J., Turner M. S., 1983, Physical Review D, 28, 679

Barkana R., Loeb A., 2001, Physics Reports, 349, 125

Barnes J. E., 1988, The Astrophysical Journal, 331, 699

Barnes J. E., 2004, Monthly Notices of the Royal Astronomical Society, 350, 798

Barnes J. E., Hernquist L., 1996, The Astrophysical Journal, 471, 115

Barrera-Ballesteros J. K., et al., 2017, The Astrophysical Journal, 844, 80

Barro G., et al., 2019, The Astrophysical Journal Supplement Series, 243, 22

Beckwith S. V. W., et al., 2006, The Astronomical Journal, 132, 1729

Behroozi P., et al., 2019, Monthly Notices of the Royal Astronomical Society, 488, 3143

Bell E. F., 2003, The Astrophysical Journal, 586, 794

Bell E. F., et al., 2004, The Astrophysical Journal, 608, 752

Bell E. F., et al., 2006a, The Astrophysical Journal, 640, 241

Bell E. F., et al., 2006b, The Astrophysical Journal, 652, 270

Bell E. F., et al., 2007, The Astrophysical Journal, 663, 834

Benítez N., 2000, The Astrophysical Journal, 536, 571

Bennett C. L., et al., 1996, The Astrophysical Journal, 464, L1

Bertin E., Arnouts S., 1996, Astronomy and Astrophysics Supplement Series, 117, 393

Bian F., Kewley L. J., Dopita M. A., 2018, The Astrophysical Journal, 859, 175

Bianconi M., et al., 2018, Monthly Notices of the Royal Astronomical Society: Letters, 473, L79

Bielby R., et al., 2017, Monthly Notices of the Royal Astronomical Society, 468, 1373

Bielby R. M., et al., 2019, Monthly Notices of the Royal Astronomical Society, 486, 21

Binggeli B., 1982, Astronomy and Astrophysics, 107, 338

Bîrzan L., et al., 2020, Monthly Notices of the Royal Astronomical Society, 496, 2613

Biviano A., et al., 2013, Astronomy & Astrophysics, 558, A1

Blumenthal G. R., et al., 1984, Nature, 311, 517

Boehringer H., et al., 1993, Monthly Notices of the Royal Astronomical Society, 264, L25

Böker T., et al., 2022, Astronomy & Astrophysics, 661, A82

Boksenberg A., 1985, Vistas in Astronomy, 28, 531

Bond J. R., Kofman L., Pogosyan D., 1996, Nature, 380, 603

Boselli A., et al., 2014, Astronomy & Astrophysics, 570, A69

Bosma A., 1978, PhD thesis

Bothwell M. S., et al., 2013, Monthly Notices of the Royal Astronomical Society, 433, 1425

Bouwens R. J., et al., 2012a, The Astrophysical Journal Letters, 752, L5

Bouwens R. J., et al., 2012b, The Astrophysical Journal, 754, 83

Bouwens R. J., et al., 2015, The Astrophysical Journal, 803, 34

Bouwens R., et al., 2020, The Astrophysical Journal, 902, 112

Bowler R. A. A., et al., 2022, Monthly Notices of the Royal Astronomical Society, 510, 5088

Brainerd T. G., 2005, The Astrophysical Journal, 628, L101

Brammer G., 2023, grizli, Zenodo, doi:10.5281/zenodo.6672538

Brammer G. B., et al., 2009, The Astrophysical Journal, 706, L173

Brammer G. B., et al., 2012, The Astrophysical Journal Supplement Series, 200, 13

Brammer G. B., et al., 2016, The Astrophysical Journal Supplement Series, 226, 6

Bresolin F., 2007, The Astrophysical Journal, 656, 186

Brinchmann J., et al., 2004, Monthly Notices of the Royal Astronomical Society, 351, 1151

Bromm V., 2013, Reports on Progress in Physics, 76, 112901

Bromm V., Coppi P. S., Larson R. B., 2002, The Astrophysical Journal, 564, 23

Broussard A., et al., 2019, The Astrophysical Journal, 873, 74

Brown T., et al., 2018, Monthly Notices of the Royal Astronomical Society, 473, 1868

Bruzual G., Charlot S., 2003, Monthly Notices of the Royal Astronomical Society, 344, 1000

Bullock J. S., et al., 2001, The Astrophysical Journal, 555, 240

Bundy K., et al., 2015, The Astrophysical Journal, 798, 7

Butcher H., Oemler Jr. A., 1978, The Astrophysical Journal, 226, 559

Butcher H., Oemler Jr. A., 1984, The Astrophysical Journal, 285, 426

Byrd G., Valtonen M., 1990, The Astrophysical Journal, 350, 89

Calzetti D., Kinney A. L., Storchi-Bergmann T., 1994, The Astrophysical Journal, 429, 582

Calzetti D., et al., 2000, The Astrophysical Journal, 533, 682

Cano-Díaz M., et al., 2019, Monthly Notices of the Royal Astronomical Society, 488, 3929

Caon N., Capaccioli M., D'Onofrio M., 1993, Monthly Notices of the Royal Astronomical Society, 265, 1013

Cappellari M., et al., 2011, Monthly Notices of the Royal Astronomical Society, 416, 1680

Carnall A. C., et al., 2018, Monthly Notices of the Royal Astronomical Society, 480, 4379

Carter D., Metcalfe N., 1980, Monthly Notices of the Royal Astronomical Society, 191, 325

Casali M., et al., 2007, Astronomy & Astrophysics, 467, 777

Casey C. M., et al., 2023, The Astrophysical Journal, 954, 31

Casteels K. R. V., et al., 2014, Monthly Notices of the Royal Astronomical Society, 445, 1157

Catelan P., Theuns T., 1996, Monthly Notices of the Royal Astronomical Society, 282, 455

Ceverino D., Klessen R. S., Glover S. C. O., 2018, Monthly Notices of the Royal Astronomical Society, 480, 4842

Ceverino D., et al., 2023, Monthly Notices of the Royal Astronomical Society, 522, 3912

Chabrier G., 2003, Publications of the Astronomical Society of the Pacific, 115, 763

Chandrasekhar S., 1931, The Astrophysical Journal, 74, 81

Charlot S., Longhetti M., 2001, Monthly Notices of the Royal Astronomical Society, 323, 887

Chartab N., et al., 2020, The Astrophysical Journal, 890, 7

Cheng C., et al., 2020, Monthly Notices of the Royal Astronomical Society, 499, 5241

Cielo S., et al., 2018, Astronomy & Astrophysics, 617, A58

Ciesla L., et al., 2024, Astronomy & Astrophysics, 686, A128

Ciotti L., Bertin G., 1999, Astronomy and Astrophysics, 352, 447

Cochrane R. K., et al., 2017, Monthly Notices of the Royal Astronomical Society, 469, 2913

Cochrane R. K., et al., 2018, Monthly Notices of the Royal Astronomical Society, 475, 3730

Cochrane R. K., et al., 2021, Monthly Notices of the Royal Astronomical Society, 503, 2622

Coe D., et al., 2019, The Astrophysical Journal, 884, 85

Coil A. L., et al., 2015, The Astrophysical Journal, 801, 35

Colbert J. W., et al., 2013, The Astrophysical Journal, 779, 34

Cole J. W., et al., 2025, The Astrophysical Journal, 979, 193

Collacchioni F., et al., 2018, Monthly Notices of the Royal Astronomical Society, 481, 954

Condon J. J., 1992, Annual Review of Astronomy and Astrophysics, 30, 575

Conselice C. J., 2003, The Astrophysical Journal Supplement Series, 147, 1

Conselice C. J., 2014, Annual Review of Astronomy and Astrophysics, 52, 291

Cooper M. C., et al., 2005, The Astrophysical Journal, 634, 833

Cortese L., et al., 2004, Astronomy & Astrophysics, 425, 429

Cortese L., et al., 2006, Astronomy & Astrophysics, 453, 847

Costantin L., et al., 2023, The Astrophysical Journal, 946, 71

Cousins A. W. J., 1978, Monthly Notes of the Astronomical Society of South Africa, 37, 8

Covelo-Paz A., et al., 2025, Astronomy & Astrophysics, 694, A178

Crain R. A., et al., 2015, Monthly Notices of the Royal Astronomical Society, 450, 1937

Cresci G., Mannucci F., Curti M., 2019, Astronomy & Astrophysics, 627, A42

Crossett J. P., et al., 2017, Monthly Notices of the Royal Astronomical Society, 464, 480

Cui Y., et al., 2014, in IEEE Winter Conference on Applications of Computer Vision. pp 213–219, doi:10.1109/WACV.2014.6836098

Cui W., et al., 2018, Monthly Notices of the Royal Astronomical Society, 480, 2898

Cui W., et al., 2021, Nature Astronomy, 5, 1069

Cullen F., et al., 2014, Monthly Notices of the Royal Astronomical Society, 440, 2300

Cullen F., et al., 2019, Monthly Notices of the Royal Astronomical Society, 487, 2038

Cullen F., et al., 2021, Monthly Notices of the Royal Astronomical Society, 505, 903

Curti M., et al., 2020a, Monthly Notices of the Royal Astronomical Society, 491, 944

Curti M., et al., 2020b, Monthly Notices of the Royal Astronomical Society, 492, 821

Curti M., et al., 2022, Monthly Notices of the Royal Astronomical Society, 518, 425

Curti M., et al., 2024, Astronomy & Astrophysics, 684, A75

Cutler S. E., et al., 2022, The Astrophysical Journal, 925, 34

Daddi E., et al., 2005, The Astrophysical Journal, 626, 680

Daddi E., et al., 2007, The Astrophysical Journal, 670, 156

Daddi E., et al., 2010, The Astrophysical Journal, 713, 686

Dalmasso N., et al., 2024, Monthly Notices of the Royal Astronomical Society, 533, 4472

Dalton G., et al., 2012, in McLean I. S., Ramsay S. K., Takami H., eds, Vol. 8446, Ground-based and Airborne Instrumentation for Astronomy IV. SPIE, pp 220–231, doi:10.1117/12.925950

Dalton G., et al., 2014, in Ramsay S. K., McLean I. S., Takami H., eds, Vol. 9147, Ground-based and Airborne Instrumentation for Astronomy V. SPIE, pp 177–187, doi:10.1117/12.2055132

Dalton G., et al., 2016, in Evans C. J., Simard L., Takami H., eds, Vol. 9908, Ground-based and Airborne Instrumentation for Astronomy VI. SPIE, pp 394–403, doi:10.1117/12.2231078

Danhaive A. L., et al., 2025a, Beyond the Stars: Linking Hα Sizes, Kinematics, and Star Formation in Galaxies at z $\approx$ 4–6 with JWST Grism Surveys and geko (`arXiv:2510.06315`), doi:10.48550/arXiv.2510.06315

Danhaive A. L., et al., 2025b, Monthly Notices of the Royal Astronomical Society, 543, 3249

Darvish B., et al., 2016, The Astrophysical Journal, 825, 113

Davari R., et al., 2014, The Astrophysical Journal, 787, 69

Davé R., et al., 2010, Monthly Notices of the Royal Astronomical Society, 404, 1355

Davé R., et al., 2019, Monthly Notices of the Royal Astronomical Society, 486, 2827

De Lucia G., et al., 2006, Monthly Notices of the Royal Astronomical Society, 366, 499

De Lucia G., et al., 2020, Monthly Notices of the Royal Astronomical Society, 498, 3215

De Rossi M. E., et al., 2017, Monthly Notices of the Royal Astronomical Society, 472, 3354

Dekel A., Birnboim Y., 2006, Monthly Notices of the Royal Astronomical Society, 368, 2

Dekel A., Burkert A., 2014, Monthly Notices of the Royal Astronomical Society, 438, 1870

Dekel A., Silk J., 1986, The Astrophysical Journal, 303, 39

Dekel A., Sari R., Ceverino D., 2009, The Astrophysical Journal, 703, 785

Despali G., et al., 2017, Monthly Notices of the Royal Astronomical Society, 466, 181

Dicke R. H., et al., 1965, The Astrophysical Journal, 142, 414

Dong X. C., et al., 2014, The Astrophysical Journal, 791, L33

Donnan C. T., Tojeiro R., Kraljic K., 2022, Nature Astronomy, 6, 599

Dopita M. A., et al., 2006, The Astrophysical Journal Supplement Series, 167, 177

Dopita M. A., et al., 2016, Astrophysics and Space Science, 361, 61

Dors Jr O. L., et al., 2011, Monthly Notices of the Royal Astronomical Society, 415, 3616

Dressler A., 1980, The Astrophysical Journal, 236, 351

Dressler A., Shectman S. A., 1987, The Astronomical Journal, 94, 899

Dressler A., et al., 2011, Publications of the Astronomical Society of the Pacific, 123, 288

Dressler A., et al., 2013, The Astrophysical Journal, 770, 62

Dressler A., et al., 2023, The Astrophysical Journal Letters, 947, L27

Dressler A., et al., 2024, The Astrophysical Journal, 964, 150

Duan Q., et al., 2025, Monthly Notices of the Royal Astronomical Society, 540, 774

Dullo B. T., Graham A. W., Knapen J. H., 2017, Monthly Notices of the Royal Astronomical Society, 471, 2321

Duncan K., et al., 2019, The Astrophysical Journal, 876, 110

Duncan K. J., et al., 2025, Monthly Notices of the Royal Astronomical Society, 541, 1329

Dunkley J., et al., 2009, The Astrophysical Journal Supplement Series, 180, 306

Dunlop J. S., et al., 2017, Monthly Notices of the Royal Astronomical Society, 466, 861

Dutta R., et al., 2021, Monthly Notices of the Royal Astronomical Society, 508, 4573

Dutton A. A., 2009, Monthly Notices of the Royal Astronomical Society, 396, 121

Dutton A. A., et al., 2007, The Astrophysical Journal, 654, 27

Džudžar R., et al., 2019, Monthly Notices of the Royal Astronomical Society: Letters, 490, L6

Ebeling H., Edge A. C., Henry J. P., 2001, The Astrophysical Journal, 553, 668

Ebeling H., Barrett E., Donovan D., 2004, The Astrophysical Journal, 609, L49

Edmunds M. G., 1990, Monthly Notices of the Royal Astronomical Society, 246, 678

Einasto M., et al., 2020, Astronomy & Astrophysics, 641, A172

Eisenstein D. J., et al., 2026, The Astrophysical Journal Supplement Series, 283, 6

Eke V. R., et al., 2004, Monthly Notices of the Royal Astronomical Society, 348, 866

Ekström S., et al., 2012, Astronomy & Astrophysics, 537, A146

El-Badry K., et al., 2016, The Astrophysical Journal, 820, 131

Eldridge J. J., et al., 2017, Publications of the Astronomical Society of Australia, 34, e058

Ellison S. L., et al., 2008, The Astrophysical Journal, 672, L107

Ellison S. L., et al., 2010, Monthly Notices of the Royal Astronomical Society, 407, 1514

Ellison S. L., et al., 2018, Monthly Notices of the Royal Astronomical Society, 474, 2039

Endsley R., et al., 2020, Monthly Notices of the Royal Astronomical Society, 500, 5229

Endsley R., et al., 2024, Monthly Notices of the Royal Astronomical Society, 533, 1111

Endsley R., et al., 2025, The Astrophysical Journal, 987, 189

Erb D. K., et al., 2006a, The Astrophysical Journal, 644, 813

Erb D. K., et al., 2006b, The Astrophysical Journal, 647, 128

Estrada N., et al., 2023, Astronomy & Astrophysics, 671, A146

Etherington J., Thomas D., 2015, Monthly Notices of the Royal Astronomical Society, 451, 660

Fabian A., 2012, Annual Review of Astronomy and Astrophysics, 50, 455

Faisst A. L., et al., 2017, The Astrophysical Journal, 839, 71

Fall S. M., Efstathiou G., 1980, Monthly Notices of the Royal Astronomical Society, 193, 189

Fan X., Carilli C. L., Keating B., 2006a, Annual Review of Astronomy and Astrophysics, 44, 415

Fan X., et al., 2006b, The Astronomical Journal, 132, 117

Farouki R., Shapiro S. L., 1981, The Astrophysical Journal, 243, 32

Feng Y., et al., 2016, Monthly Notices of the Royal Astronomical Society, 455, 2778

Ferland G. J., et al., 2017, Revista Mexicana de Astronomía y Astrofísica, 58, 385

Finkelstein S. L., et al., 2023, The Astrophysical Journal Letters, 946, L13

Finlator K., Davé R., 2008, Monthly Notices of the Royal Astronomical Society, 385, 2181

Fontanot F., et al., 2021, Monthly Notices of the Royal Astronomical Society, 504, 4481

Freeman K. C., 1970, The Astrophysical Journal, 160, 811

Frenk C. S., et al., 1988, The Astrophysical Journal, 327, 507

Frieman J. A., Turner M. S., Huterer D., 2008, Annual Review of Astronomy and Astrophysics, 46, 385

Fu J., et al., 2010, Monthly Notices of the Royal Astronomical Society, 409, 515

Fujita Y., 2004, Publications of the Astronomical Society of Japan, 56, 29

Fujita Y., Nagashima M., 1999, The Astrophysical Journal, 516, 619

Fukugita M., et al., 1996, The Astronomical Journal, 111, 1748

Furlanetto S. R., Mirocha J., 2022, Monthly Notices of the Royal Astronomical Society, 511, 3895

Gardner J. P., et al., 2006, Space Science Reviews, 123, 485

Garg P., et al., 2022, The Astrophysical Journal, 926, 80

Garg P., et al., 2024, The Astrophysical Journal, 972, 113

Garn T., Best P. N., 2010, Monthly Notices of the Royal Astronomical Society, 409, 421

Garn T., et al., 2010, Monthly Notices of the Royal Astronomical Society, 402, 2017

Garnett D. R., Shields G. A., 1987, The Astrophysical Journal, 317, 82

Gaskell C. M., Ferland G. J., 1984, Publications of the Astronomical Society of the Pacific, 96, 393

Gavazzi G., et al., 2015, Astronomy & Astrophysics, 580, A116

Geach J. E., et al., 2008, Monthly Notices of the Royal Astronomical Society, 388, 1473

Gebhardt K., et al., 2001, The Astronomical Journal, 122, 2469

Géron T., et al., 2021, Monthly Notices of the Royal Astronomical Society, 507, 4389

Giavalisco M., et al., 2004, The Astrophysical Journal, 600, L93

Gill S. P. D., Knebe A., Gibson B. K., 2005, Monthly Notices of the Royal Astronomical Society, 356, 1327

Gillman S., et al., 2020, Monthly Notices of the Royal Astronomical Society, 500, 4229

Gillman S., et al., 2022, Monthly Notices of the Royal Astronomical Society, 512, 3480

Goldsmith P. F., Langer W. D., 1978, The Astrophysical Journal, 222, 881

Gonzalez E. J., et al., 2021, Monthly Notices of the Royal Astronomical Society, 501, 5239

Gouin C., et al., 2020, Astronomy & Astrophysics, 635, A195

Govoni F., et al., 2019, Science, 364, 981

Graham A. W., 2013, Elliptical and Disk Galaxy Structure and Modern Scaling Laws, in Oswalt T. D., Keel W. C., eds, Planets, Stars and Stellar Systems, Vol. 6, Extragalactic Astronomy and Cosmology, 1 edn, Springer, Dordrecht, pp 91–139, doi:10.1007/978-94-007-5609-0_2

Graham A. W., Driver S. P., 2005, Publications of the Astronomical Society of Australia, 22, 118

Graus A. S., et al., 2019, Monthly Notices of the Royal Astronomical Society, 490, 1186

Gregory S. A., Thompson L. A., 1978, The Astrophysical Journal, 222, 784

Grillo C., et al., 2016, The Astrophysical Journal, 822, 78

Grogin N. A., et al., 2011, The Astrophysical Journal Supplement Series, 197, 35

Gruppioni C., et al., 2020, Astronomy & Astrophysics, 643, A8

Gu Q., et al., 2022, Monthly Notices of the Royal Astronomical Society, 514, 390

Gunn J. E., Gott III J. R., 1972, The Astrophysical Journal, 176, 1

Guo Y., et al., 2009, Monthly Notices of the Royal Astronomical Society, 398, 1129

Guo Y., et al., 2015, The Astrophysical Journal, 800, 39

Guo Y., et al., 2016, The Astrophysical Journal, 822, 103

Guth A. H., 1981, Physical Review D, 23, 347

Han S., et al., 2018, The Astrophysical Journal, 866, 78

Hao J., et al., 2011a, The Astrophysical Journal, 740, 39

Hao C.-N., et al., 2011b, The Astrophysical Journal, 741, 124

Harikane Y., et al., 2023, The Astrophysical Journal, 960, 56

Harrison C. M., 2017, Nature Astronomy, 1, 0165

Harshan A., et al., 2024, Monthly Notices of the Royal Astronomical Society, 532, 1112

Häußler B., et al., 2007, The Astrophysical Journal Supplement Series, 172, 615

Häußler B., et al., 2013, Monthly Notices of the Royal Astronomical Society, 430, 330

Hayashi M., et al., 2020, Publications of the Astronomical Society of Japan, 72, 86

Heckman T. M., Best P. N., 2014, Annual Review of Astronomy and Astrophysics, 52, 589

Heintz K. E., et al., 2023, Nature Astronomy, 7, 1517

Henriques B. M. B., et al., 2020, Monthly Notices of the Royal Astronomical Society, 491, 5795

Henry A., et al., 2013, The Astrophysical Journal, 776, L27

Hirschmann M., De Lucia G., Fontanot F., 2016, Monthly Notices of the Royal Astronomical Society, 461, 1760

Hlavacek-Larrondo J., et al., 2012, Monthly Notices of the Royal Astronomical Society, 421, 1360

Hlavacek-Larrondo J., et al., 2013, The Astrophysical Journal, 777, 163

Hoosain M., et al., 2024, Monthly Notices of the Royal Astronomical Society, 528, 4139

Hopkins P. F., 2013, Monthly Notices of the Royal Astronomical Society, 428, 2840

Hopkins P. F., et al., 2008, The Astrophysical Journal Supplement Series, 175, 356

Hopkins P. F., et al., 2012, Monthly Notices of the Royal Astronomical Society, 427, 968

Hopkins P. F., et al., 2014, Monthly Notices of the Royal Astronomical Society, 445, 581

Huang H.-J., et al., 2016, Monthly Notices of the Royal Astronomical Society, 463, 222

Huang H.-J., et al., 2018, Monthly Notices of the Royal Astronomical Society, 474, 4772

Hubble E. P., 1925, Popular Astronomy, 33, 252

Hubble E. P., 1926, The Astrophysical Journal, 64, 321

Hubble E., 1929, Proceedings of the National Academy of Sciences, 15, 168

Hubble E. P., 1930, The Astrophysical Journal, 71, 231

Hubble E. P., 1936, Realm of the Nebulae. Yale University Press, New Haven, CT

Hubble E., Humason M. L., 1931, The Astrophysical Journal, 74, 43

Hunter D. A., Elmegreen B. G., Madden S. C., 2024, Annual Review of Astronomy and Astrophysics, 62, 113

Huško F., Lacey C. G., Baugh C. M., 2022, Monthly Notices of the Royal Astronomical Society, 509, 5918

Iani E., et al., 2021, Monthly Notices of the Royal Astronomical Society, 507, 3830

Iglesias-Páramo J., et al., 2002, Astronomy & Astrophysics, 384, 383

Ilbert O., et al., 2010, The Astrophysical Journal, 709, 644

Ilbert O., et al., 2013, Astronomy & Astrophysics, 556, A55

Ilbert O., et al., 2015, Astronomy & Astrophysics, 579, A2

Ito K., et al., 2023, The Astrophysical Journal Letters, 945, L9

Ito K., et al., 2024, The Astrophysical Journal, 964, 192

Ivezić Ž., et al., 2019, The Astrophysical Journal, 873, 111

Jarosik N., et al., 2011, The Astrophysical Journal Supplement Series, 192, 14

Ji Z., et al., 2024, The Astrophysical Journal, 974, 135

Ji Z., et al., 2026, The Astrophysical Journal, 998, 239

Jia C., et al., 2024, The Astrophysical Journal, 977, 165

Jian H.-Y., et al., 2023, The Astrophysical Journal, 957, 85

Jimmy et al., 2015, The Astrophysical Journal, 812, 98

Jin S., et al., 2024, Monthly Notices of the Royal Astronomical Society, 530, 2688

Jôeveer M., Einasto J., Tago E., 1978, Monthly Notices of the Royal Astronomical Society, 185, 357

Johnson H. L., Morgan W. W., 1953, The Astrophysical Journal, 117, 313

Joshi G. D., Wadsley J., Parker L. C., 2017, Monthly Notices of the Royal Astronomical Society, 468, 4625

Juneau S., et al., 2011, The Astrophysical Journal, 736, 104

Juneau S., et al., 2013, The Astrophysical Journal, 764, 176

Juneau S., et al., 2014, The Astrophysical Journal, 788, 88

Kang X., et al., 2007, Monthly Notices of the Royal Astronomical Society, 378, 1531

Kannan R., et al., 2022, Monthly Notices of the Royal Astronomical Society, 511, 4005

Kannan R., et al., 2025, The Open Journal of Astrophysics, 8, 153

Karp J. S. M., Lange J. U., Wechsler R. H., 2023, The Astrophysical Journal Letters, 949, L13

Kartaltepe J. S., et al., 2023, The Astrophysical Journal Letters, 946, L15

Kashibadze O. G., Karachentsev I. D., Karachentseva V. E., 2020, Astronomy & Astrophysics, 635, A135

Kashino D., et al., 2017, The Astrophysical Journal, 835, 88

Kashino D., et al., 2022, The Astrophysical Journal, 925, 82

Kashlinsky A., Rees M. J., 1983, Monthly Notices of the Royal Astronomical Society, 205, 955

Katz N., 1992, The Astrophysical Journal, 391, 502

Katz N., Gunn J. E., 1991, The Astrophysical Journal, 377, 365

Katz H., et al., 2023, The Open Journal of Astrophysics, 6, 44

Kauffmann G., et al., 2003, Monthly Notices of the Royal Astronomical Society, 341, 33

Kawamata R., et al., 2015, The Astrophysical Journal, 804, 103

Kawinwanichakij L., et al., 2017, The Astrophysical Journal, 847, 134

Kelly P. L., et al., 2014, Monthly Notices of the Royal Astronomical Society, 439, 28

Kelvin L. S., et al., 2012, Monthly Notices of the Royal Astronomical Society, 421, 1007

Kennicutt R. C., 1998, Annual Review of Astronomy and Astrophysics, 36, 189

Kennicutt R. C., Evans N. J., 2012, Annual Review of Astronomy and Astrophysics, 50, 531

Kereš D., et al., 2005, Monthly Notices of the Royal Astronomical Society, 363, 2

Kewley L. J., Dopita M. A., 2002, The Astrophysical Journal Supplement Series, 142, 35

Kewley L. J., Ellison S. L., 2008, The Astrophysical Journal, 681, 1183

Kewley L. J., et al., 2006, Monthly Notices of the Royal Astronomical Society, 372, 961

Kewley L. J., et al., 2013, The Astrophysical Journal, 774, 100

Kewley L. J., Nicholls D. C., Sutherland R. S., 2019, Annual Review of Astronomy and Astrophysics, 57, 511

Khoperskov S., et al., 2018, Astronomy & Astrophysics, 609, A60

Khostovan A. A., et al., 2015, Monthly Notices of the Royal Astronomical Society, 452, 3948

Kiessling A., et al., 2015, Space Science Reviews, 193, 67

Kimm T., Cen R., 2014, The Astrophysical Journal, 788, 121

Kirk D., et al., 2015, Space Science Reviews, 193, 139

Klessen R. S., Glover S. C. O., 2023, Annual Review of Astronomy and Astrophysics, 61, 65

Klypin A., et al., 2016, Monthly Notices of the Royal Astronomical Society, 457, 4340

Knebe A., et al., 2011, Monthly Notices of the Royal Astronomical Society, 412, 529

Kocevski D. D., et al., 2025, The Astrophysical Journal, 986, 126

Koekemoer A. M., et al., 2011, The Astrophysical Journal Supplement Series, 197, 36

Kraljic K., et al., 2020, Monthly Notices of the Royal Astronomical Society, 491, 4294

Kravtsov A. V., Borgani S., 2012, Annual Review of Astronomy and Astrophysics, 50, 353

Kriek M., et al., 2011, The Astrophysical Journal, 743, 168

Kriek M., et al., 2015, The Astrophysical Journal Supplement Series, 218, 15

Kroupa P., 2001, Monthly Notices of the Royal Astronomical Society, 322, 231

Kuchner U., et al., 2021, Monthly Notices of the Royal Astronomical Society, 510, 581

Labbé I., et al., 2013, The Astrophysical Journal Letters, 777, L19

Lagos P., et al., 2016, Monthly Notices of the Royal Astronomical Society, 456, 1549

Lambas D. G., Groth E. J., Peebles P. J. E., 1988, The Astronomical Journal, 95, 996

Langan I., et al., 2023, Monthly Notices of the Royal Astronomical Society, 521, 546

Lange R., et al., 2015, Monthly Notices of the Royal Astronomical Society, 447, 2603

Lapiner S., et al., 2023, Monthly Notices of the Royal Astronomical Society, 522, 4515

Lara-López M. A., et al., 2010, Astronomy and Astrophysics, 521, L53

Larson R. B., 1974, Monthly Notices of the Royal Astronomical Society, 169, 229

Larson R. B., 1998, Monthly Notices of the Royal Astronomical Society, 301, 569

Larson R. B., Tinsley B. M., Caldwell C. N., 1980, The Astrophysical Journal, 237, 692

Le Fevre O., et al., 2000, Monthly Notices of the Royal Astronomical Society, 311, 565

Lee N., et al., 2015, The Astrophysical Journal, 801, 80

Leja J., et al., 2019, The Astrophysical Journal, 876, 3

Leja J., et al., 2022, The Astrophysical Journal, 936, 165

Lemaître G., 1927, Annales de la Société Scientifique de Bruxelles, 47, 49

Lemaître A. G., 1931, Monthly Notices of the Royal Astronomical Society, 91, 483

Lequeux J., et al., 1979, Astronomy and Astrophysics, 80, 155

Li M., et al., 2023, The Astrophysical Journal Letters, 955, L18

Li J., et al., 2024, The Astrophysical Journal, 976, 70

Libeskind N. I., et al., 2011, Monthly Notices of the Royal Astronomical Society, 411, 1525

Libeskind N. I., et al., 2013, Monthly Notices of the Royal Astronomical Society, 428, 2489

Lin L., et al., 2008, The Astrophysical Journal, 681, 232

Livermore R. C., et al., 2012, Monthly Notices of the Royal Astronomical Society, 427, 688

Livermore R. C., et al., 2015, Monthly Notices of the Royal Astronomical Society, 450, 1812

Looser T. J., et al., 2025, Astronomy & Astrophysics, 697, A88

Lovell C. C., et al., 2020, Monthly Notices of the Royal Astronomical Society, 500, 2127

Ly C., et al., 2016, The Astrophysical Journal, 828, 67

Ma X., et al., 2018, Monthly Notices of the Royal Astronomical Society, 477, 219

MacKenty J. W., et al., 2008, in Oschmann Jr. J. M., de Graauw M. W. M., MacEwan H. A., eds, Vol. 7010, Space Telescopes and Instrumentation 2008: Optical, Infrared, and Millimeter. SPIE, pp 443–451, doi:10.1117/12.790039

MacKenty J. W., et al., 2010, in Oschmann Jr. J. M., Clampin M. C., MacEwan

H. A., eds, Vol. 7731, Space Telescopes and Instrumentation 2010: Optical, Infrared, and Millimeter Wave. SPIE, pp 310–321, doi:10.1117/12.857533

Macconi D., et al., 2022, Astronomy & Astrophysics, 660, A32

Madau P., Dickinson M., 2014, Annual Review of Astronomy and Astrophysics, 52, 415

Madau P., et al., 1996, Monthly Notices of the Royal Astronomical Society, 283, 1388

Maiolino R., Mannucci F., 2019, The Astronomy and Astrophysics Review, 27, 3

Maiolino R., et al., 2008, Astronomy & Astrophysics, 488, 463

Mamon G. A., et al., 2004, Astronomy & Astrophysics, 414, 445

Mandelker N., et al., 2017, Monthly Notices of the Royal Astronomical Society, 464, 635

Mannucci F., et al., 2009, Monthly Notices of the Royal Astronomical Society, 398, 1915

Mannucci F., et al., 2010, Monthly Notices of the Royal Astronomical Society, 408, 2115

Mannucci F., Salvaterra R., Campisi M. A., 2011, Monthly Notices of the Royal Astronomical Society, 414, 1263

Mantz A. B., et al., 2015, Monthly Notices of the Royal Astronomical Society, 446, 2205

Mantz A. B., et al., 2016, Monthly Notices of the Royal Astronomical Society, 463, 3582

Marinacci F., et al., 2018, Monthly Notices of the Royal Astronomical Society, 480, 5113

Marks M., et al., 2012, Monthly Notices of the Royal Astronomical Society, 422, 2246

Marshall M. A., et al., 2022, Monthly Notices of the Royal Astronomical Society, 511, 5475

Martig M., et al., 2009, The Astrophysical Journal, 707, 250

Martig M., et al., 2013, Monthly Notices of the Royal Astronomical Society, 432, 1914

Martín-Navarro I., Burchett J. N., Mezcua M., 2019, The Astrophysical Journal Letters, 884, L45

Martín-Navarro I., et al., 2021, Nature, 594, 187

Martínez H. J., Muriel H., Coenda V., 2016, Monthly Notices of the Royal Astronomical Society, 455, 127

Martorano M., et al., 2024, The Astrophysical Journal, 972, 134

Matharu J., et al., 2022, The Astrophysical Journal, 937, 16

Matharu J., et al., 2023, The Astrophysical Journal Letters, 949, L11

Matharu J., et al., 2024, Astronomy & Astrophysics, 690, A64

Matteo P. D., et al., 2008, Astronomy & Astrophysics, 492, 31

McClymont W., et al., 2025a, Monthly Notices of the Royal Astronomical Society, 544, 513

McClymont W., et al., 2025b, Monthly Notices of the Royal Astronomical Society, 544, 1732

McConnachie A. W., 2012, The Astronomical Journal, 144, 4

McDowell J. C., 1986, Monthly Notices of the Royal Astronomical Society, 223, 763

McGee S. L., et al., 2009, Monthly Notices of the Royal Astronomical Society, 400, 937

McKee C. F., Ostriker E. C., 2007, Annual Review of Astronomy and Astrophysics, 45, 565

McNamara B., Nulsen P., 2007, Annual Review of Astronomy and Astrophysics, 45, 117

McNamara B. R., et al., 2005, Nature, 433, 45

McQuinn M., et al., 2007, Monthly Notices of the Royal Astronomical Society, 377, 1043

Meert A., Vikram V., Bernardi M., 2013, Monthly Notices of the Royal Astronomical Society, 433, 1344

Mercado F. J., et al., 2021, Monthly Notices of the Royal Astronomical Society, 501, 5121

Mercurio A., et al., 2003, Astronomy & Astrophysics, 408, 57

Mercurio A., et al., 2008, Monthly Notices of the Royal Astronomical Society, 387, 1374

Merten J., et al., 2015, The Astrophysical Journal, 806, 4

Messier C., 1781, Connoissance des Temps ou des Mouvements Célestes, pp 227–267

Mihos J. C., Hernquist L., 1994a, The Astrophysical Journal, 425, L13

Mihos J. C., Hernquist L., 1994b, The Astrophysical Journal, 431, L9

Mihos J. C., Hernquist L., 1996, The Astrophysical Journal, 464, 641

Miller T. B., et al., 2025, The Astrophysical Journal, 988, 196

Miyazaki S., et al., 2002, Publications of the Astronomical Society of Japan, 54, 833

Miyazaki S., et al., 2012, in McLean I. S., Ramsay S. K., Takami H., eds, Vol. 8446, Ground-based and Airborne Instrumentation for Astronomy IV. SPIE, pp 327–335, doi:10.1117/12.926844

Mo H. J., Mao S., White S. D. M., 1998, Monthly Notices of the Royal Astronomical Society, 295, 319

Molino A., et al., 2017, Monthly Notices of the Royal Astronomical Society, 470, 95

Monna A., et al., 2017, Monthly Notices of the Royal Astronomical Society, 466, 4094

Moore B., et al., 1996, Nature, 379, 613

Moore B., et al., 1999, The Astrophysical Journal, 524, L19

Moorwood A. F. M., et al., 2000, Astronomy and Astrophysics, 362, 9

Morishita T., et al., 2024, The Astrophysical Journal, 963, 9

Mosleh M., et al., 2012, The Astrophysical Journal, 756, L12

Mosleh M., Williams R. J., Franx M., 2013, The Astrophysical Journal, 777, 117

Moustakas J., et al., 2013, The Astrophysical Journal, 767, 50

Mowla L., et al., 2019a, The Astrophysical Journal Letters, 872, L13

Mowla L. A., et al., 2019b, The Astrophysical Journal, 880, 57

Muldrew S. I., et al., 2012, Monthly Notices of the Royal Astronomical Society, 419, 2670

Mundy C. J., et al., 2017, Monthly Notices of the Royal Astronomical Society, 470, 3507

Murphy E. J., et al., 2011, The Astrophysical Journal, 737, 67

Naab T., Johansson P. H., Ostriker J. P., 2009, The Astrophysical Journal, 699, L178

Nagao T., Maiolino R., Marconi A., 2006, Astronomy & Astrophysics, 459, 85

Nakazato Y., Ceverino D., Yoshida N., 2024, The Astrophysical Journal, 975, 238

Naufal A., et al., 2023, The Astrophysical Journal, 958, 170

Navarro J. F., Benz W., 1991, The Astrophysical Journal, 380, 320

Navarro J. F., White S. D. M., 1994, Monthly Notices of the Royal Astronomical Society, 267, 401

Navarro J. F., Frenk C. S., White S. D. M., 1996, The Astrophysical Journal, 462, 563

Nedkova K. V., et al., 2021, Monthly Notices of the Royal Astronomical Society, 506, 928

Nedkova K. V., et al., 2024, The Astrophysical Journal, 970, 188

Nelson E. J., et al., 2012, The Astrophysical Journal, 747, L28

Nelson E. J., et al., 2013, The Astrophysical Journal Letters, 763, L16

Nelson E. J., et al., 2016, The Astrophysical Journal, 828, 27

Nelson D., et al., 2018, Monthly Notices of the Royal Astronomical Society, 475, 624

Nelson D., et al., 2019, Monthly Notices of the Royal Astronomical Society, 490, 3234

Nelson E., et al., 2024, The Astrophysical Journal Letters, 976, L27

Newman S. F., et al., 2013, The Astrophysical Journal, 781, 21

Noguchi M., 1998, Nature, 392, 253

Nomoto K., Kobayashi C., Tominaga N., 2013, Annual Review of Astronomy and Astrophysics, 51, 457

Nulsen P. E. J., et al., 2005, The Astrophysical Journal, 628, 629

O'Leary J. A., et al., 2021, Monthly Notices of the Royal Astronomical Society, 501, 3215

Oesch P. A., et al., 2018, The Astrophysical Journal, 855, 105

Oguri M., 2014, Monthly Notices of the Royal Astronomical Society, 444, 147

Oguri M., et al., 2018, Publications of the Astronomical Society of Japan, 70, S20

Okabe T., et al., 2020, Monthly Notices of the Royal Astronomical Society, 491, 2268

Oke J. B., Gunn J. E., 1983, The Astrophysical Journal, 266, 713

Olave-Rojas D., et al., 2018, Monthly Notices of the Royal Astronomical Society, 479, 2328

Olivares V., et al., 2023, The Astrophysical Journal, 954, 56

Ono Y., et al., 2023, The Astrophysical Journal, 951, 72

Ono Y., et al., 2024, Publications of the Astronomical Society of Japan, 76, 219

Ono Y., et al., 2025, The Astrophysical Journal, 991, 222

Ormerod K., et al., 2023, Monthly Notices of the Royal Astronomical Society, 527, 6110

Osterbrock D. E., Ferland G. J., 2006, Astrophysics of Gaseous Nebulae and Active Galactic Nuclei, 2 edn. University Science Books, Sausalito, CA

Oteo I., et al., 2015, Monthly Notices of the Royal Astronomical Society, 452, 2018

Overzier R. A., 2016, The Astronomy and Astrophysics Review, 24, 14

Ownsworth J. R., et al., 2014, Monthly Notices of the Royal Astronomical Society, 445, 2198

Pan D. C., et al., 2012, Monthly Notices of the Royal Astronomical Society, 421, 926

Panagoulia E. K., et al., 2014, Monthly Notices of the Royal Astronomical Society, 444, 1236

Pandya V., et al., 2024, The Astrophysical Journal, 963, 54

Patterson F. S., 1940, Harvard College Observatory Bulletin, 914, 9

Patton D. R., et al., 1997, The Astrophysical Journal, 475, 29

Paulino-Afonso A., et al., 2017, Monthly Notices of the Royal Astronomical Society, 465, 2717

Paz D. J., et al., 2006, Monthly Notices of the Royal Astronomical Society, 366, 1503

Paz D. J., et al., 2011, Monthly Notices of the Royal Astronomical Society, 414, 2029

Peimbert A., Peimbert M., Luridiana V., 2016, Revista Mexicana de Astronomía y Astrofísica, 52, 419

Peng C. Y., et al., 2002, The Astronomical Journal, 124, 266

Peng C. Y., et al., 2010a, The Astronomical Journal, 139, 2097

Peng Y.-j., et al., 2010b, The Astrophysical Journal, 721, 193

Peng Y.-j., et al., 2012, The Astrophysical Journal, 757, 4

Peng Y.-j., et al., 2014, The Astrophysical Journal, 790, 95

Peng Y., Maiolino R., Cochrane R., 2015, Nature, 521, 192

Penzias A. A., Wilson R. W., 1965, The Astrophysical Journal, 142, 419

Perlmutter S., et al., 1998, Nature, 391, 51

Perlmutter S., et al., 1999, The Astrophysical Journal, 517, 565

Perrin M. D., et al., 2014, in Oschmann Jr. J. M., et al., eds, Vol. 9143, Space Telescopes and Instrumentation 2014: Optical, Infrared, and Millimeter Wave. SPIE, pp 1174–1184, doi:10.1117/12.2056689

Pettini M., Pagel B. E. J., 2004, Monthly Notices of the Royal Astronomical Society, 348, L59

Pirie C. A., et al., 2025, Monthly Notices of the Royal Astronomical Society, 541, 1348

Planck Collaboration et al., 2020a, Astronomy and Astrophysics, 641, A6

Planck Collaboration et al., 2020b, Astronomy and Astrophysics, 641, A10

Poggianti B. M., et al., 2017, Nature, 548, 304

Popesso P., et al., 2023, Monthly Notices of the Royal Astronomical Society, 519, 1526

Postman M., et al., 2005, The Astrophysical Journal, 623, 721

Postman M., et al., 2012, The Astrophysical Journal Supplement Series, 199, 25

Price S. H., et al., 2014, The Astrophysical Journal, 788, 86

Puskás D., et al., 2025, Monthly Notices of the Royal Astronomical Society, 540, 2146

Putman M., Peek J., Joung M., 2012, Annual Review of Astronomy and Astrophysics, 50, 491

Qu Y., et al., 2017, Monthly Notices of the Royal Astronomical Society, 464, 1659

Quilis V., Moore B., Bower R., 2000, Science, 288, 1617

Rafferty D. A., et al., 2006, The Astrophysical Journal, 652, 216

Ragone-Figueroa C., et al., 2020, Monthly Notices of the Royal Astronomical Society, 495, 2436

Reddy N. A., et al., 2020, The Astrophysical Journal, 902, 123

Reddy N. A., et al., 2026, The Astrophysical Journal, 999, 15

Renaud F., Bournaud F., Duc P.-A., 2015, Monthly Notices of the Royal Astronomical Society, 446, 2038

Repp A., Ebeling H., 2018, Monthly Notices of the Royal Astronomical Society, 479, 844

Reynolds J. H., 1913, Monthly Notices of the Royal Astronomical Society, 74, 132

Richstone D. O., 1975, The Astrophysical Journal, 200, 535

Richstone D. O., 1976, The Astrophysical Journal, 204, 642

Riess A. G., et al., 1998, The Astronomical Journal, 116, 1009

Rigby J., et al., 2023, Publications of the Astronomical Society of the Pacific, 135, 048001

Roberts-Borsani G. W., et al., 2016, The Astrophysical Journal, 823, 143

Roberts I. D., et al., 2019, The Astrophysical Journal, 873, 42

Robertson B. E., et al., 2013, The Astrophysical Journal, 768, 71

Rodriguez-Gomez V., et al., 2019, Monthly Notices of the Royal Astronomical Society, 483, 4140

Rodríguez-Puebla A., et al., 2016, Monthly Notices of the Royal Astronomical Society, 462, 893

Romeo A. D., et al., 2008, Monthly Notices of the Royal Astronomical Society, 389, 13

Roper W. J., et al., 2022, Monthly Notices of the Royal Astronomical Society, 514, 1921

Rosati P., et al., 2014, The Messenger, 158, 48

Röttgering H., et al., 2011, Journal of Astrophysics and Astronomy, 32, 557

Rubin V. C., Ford Jr. W. K., 1970, The Astrophysical Journal, 159, 379

Rubin V. C., Ford Jr. W. K., Thonnard N., 1980, The Astrophysical Journal, 238, 471

Rupke D. S. N., Kewley L. J., Barnes J. E., 2010, The Astrophysical Journal, 710, L156

Rykoff E. S., et al., 2014, The Astrophysical Journal, 785, 104

Sakai S., et al., 2002, The Astrophysical Journal, 578, 842

Sakstein J., et al., 2011, Monthly Notices of the Royal Astronomical Society, 410, 2203

Salerno J. M., Martínez H. J., Muriel H., 2019, Monthly Notices of the Royal Astronomical Society, 484, 2

Salim S., et al., 2007, The Astrophysical Journal Supplement Series, 173, 267

Salim S., et al., 2014, The Astrophysical Journal, 797, 126

Salim S., et al., 2015, The Astrophysical Journal, 808, 25

Salim S., Boquien M., Lee J. C., 2018, The Astrophysical Journal, 859, 11

Salpeter E. E., 1955, The Astrophysical Journal, 121, 161

Sánchez S. F., 2020, Annual Review of Astronomy and Astrophysics, 58, 99

Sánchez S. F., et al., 2012, Astronomy & Astrophysics, 538, A8

Sánchez S. F., et al., 2013, Astronomy and Astrophysics, 554, A58

Sánchez S. F., et al., 2017, Monthly Notices of the Royal Astronomical Society, 469, 2121

Sanders R. L., et al., 2020, Monthly Notices of the Royal Astronomical Society, 491, 1427

Sanders R. L., et al., 2021, The Astrophysical Journal, 914, 19

Sanders R. L., et al., 2024, The Astrophysical Journal, 962, 24

Sanders R. L., et al., 2025, The Astrophysical Journal, 989, 209

Santucci G., et al., 2023, Monthly Notices of the Royal Astronomical Society, 521, 2671

Saracco P., et al., 2023, Monthly Notices of the Royal Astronomical Society, 520, 3027

Sarron F., et al., 2019, Astronomy & Astrophysics, 632, A49

Sastry G. N., 1968, Publications of the Astronomical Society of the Pacific, 80, 252

Savaglio S., et al., 2005, The Astrophysical Journal, 635, 260

Scannapieco E., Schneider R., Ferrara A., 2003, The Astrophysical Journal, 589, 35

Schaefer A. L., et al., 2019, Monthly Notices of the Royal Astronomical Society, 483, 2851

Schaefer A. L., et al., 2022, The Astrophysical Journal, 930, 160

Schinnerer E., Leroy A., 2024, Annual Review of Astronomy and Astrophysics, 62, 369

Schlegel D. J., Finkbeiner D. P., Davis M., 1998, The Astrophysical Journal, 500, 525

Schmidt K. B., et al., 2014, The Astrophysical Journal, 782, L36

Scholte D., Saintonge A., 2022, Monthly Notices of the Royal Astronomical Society, 518, 353

Schönrich R., Binney J., 2009, Monthly Notices of the Royal Astronomical Society, 396, 203

Schreiber N. M. F., Wuyts S., 2020, Annual Review of Astronomy and Astrophysics, 58, 661

Schreiber C., et al., 2015, Astronomy & Astrophysics, 575, A74

Schreiber C., et al., 2016, Astronomy & Astrophysics, 589, A35

Scoville N., et al., 2007a, The Astrophysical Journal Supplement Series, 172, 1

Scoville N., et al., 2007b, The Astrophysical Journal Supplement Series, 172, 38

Seldner M., et al., 1977, The Astronomical Journal, 82, 249

Sereno M., et al., 2013, Monthly Notices of the Royal Astronomical Society, 428, 2241

Sérsic J. L., 1963, Boletin de la Asociacion Argentina de Astronomia La Plata Argentina, 6, 41

Sérsic J. L., 1968, Atlas de Galaxias Australes. Observatorio Astronómico, Córdoba, Argentina

Sextl E., et al., 2023, The Astrophysical Journal, 949, 60

Shapley H., Ames Adelaide., 1926, Harvard College Observatory Circular, 294, 1

Shapley A. E., et al., 2015, The Astrophysical Journal, 801, 88

Sharda P., et al., 2021, Monthly Notices of the Royal Astronomical Society, 502, 5935

Shen S., et al., 2003, Monthly Notices of the Royal Astronomical Society, 343, 978

Shen L., et al., 2023, The Astrophysical Journal, 950, 7

Shen X., et al., 2024a, Monthly Notices of the Royal Astronomical Society, 534, 1433

Shen L., et al., 2024b, The Astrophysical Journal Letters, 963, L49

Shibuya T., Ouchi M., Harikane Y., 2015, The Astrophysical Journal Supplement Series, 219, 15

Shibuya T., et al., 2016, The Astrophysical Journal, 821, 72

Shimwell T. W., et al., 2017, Astronomy & Astrophysics, 598, A104

Shimwell T. W., et al., 2019, Astronomy & Astrophysics, 622, A1

Shin J., Woo J.-H., Mulchaey J. S., 2016, The Astrophysical Journal Supplement Series, 227, 31

Simons R. C., et al., 2021, The Astrophysical Journal, 923, 203

Skelton R. E., et al., 2014, The Astrophysical Journal Supplement Series, 214, 24

Slipher V. M., 1917, Proceedings of the American Philosophical Society, 56, 403

Smargon A., et al., 2012, Monthly Notices of the Royal Astronomical Society, 423, 856

Smit R., et al., 2015, The Astrophysical Journal, 801, 122

Smith S., 1936, The Astrophysical Journal, 83, 23

Smith D. J. B., et al., 2016, in Reylé, Corinne et al., eds, SF2A-2016: Proceedings of the Annual Meeting of the French Society of Astronomy and Astrophysics. arXiv, eprint: arXiv:1611.02706, pp 271–280, doi:10.48550/arXiv.1611.02706

Smith R., et al., 2023, Monthly Notices of the Royal Astronomical Society, 525, 4685

Sobral D., et al., 2009, Monthly Notices of the Royal Astronomical Society, 398, 75

Sobral D., et al., 2010, Monthly Notices of the Royal Astronomical Society, 404, 1551

Sobral D., et al., 2012, Monthly Notices of the Royal Astronomical Society, 420, 1926

Sobral D., et al., 2013, Monthly Notices of the Royal Astronomical Society, 428, 1128

Sobral D., et al., 2016, Monthly Notices of the Royal Astronomical Society, 457, 1739

Speagle J. S., et al., 2014, The Astrophysical Journal Supplement Series, 214, 15

Spitoni E., et al., 2010, Astronomy and Astrophysics, 514, A73

Spitoni E., Vincenzo F., Matteucci F., 2017, Astronomy & Astrophysics, 599, A6

Springel V., Di Matteo T., Hernquist L., 2005, The Astrophysical Journal, 620, L79

Stanway E. R., Eldridge J. J., 2018, Monthly Notices of the Royal Astronomical Society, 479, 75

Stasińska G., 2005, Astronomy & Astrophysics, 434, 507

Stefanon M., et al., 2022, The Astrophysical Journal, 927, 48

Steidel C. C., et al., 2014, The Astrophysical Journal, 795, 165

Stephan P. M. E., 1877, Monthly Notices of the Royal Astronomical Society, 37, 334

Steyrleithner P., Hensler G., Boselli A., 2020, Monthly Notices of the Royal Astronomical Society, 494, 1114

Stinson G., et al., 2006, Monthly Notices of the Royal Astronomical Society, 373, 1074

Storey P. J., Zeippen C. J., 2000, Monthly Notices of the Royal Astronomical Society, 312, 813

Stott J. P., 2022, Monthly Notices of the Royal Astronomical Society, 511, 2659

Stott J. P., et al., 2011, Monthly Notices of the Royal Astronomical Society, 414, 445

Stott J. P., et al., 2013a, Monthly Notices of the Royal Astronomical Society, 430, 1158

Stott J. P., et al., 2013b, Monthly Notices of the Royal Astronomical Society, 436, 1130

Stott J. P., et al., 2014, Monthly Notices of the Royal Astronomical Society, 443, 2695

Stott J. P., et al., 2020, Monthly Notices of the Royal Astronomical Society, 497, 3083

Strateva I., et al., 2001, The Astronomical Journal, 122, 1861

Struble M. F., Rood H. J., 1999, The Astrophysical Journal Supplement Series, 125, 35

Suess K. A., et al., 2022, The Astrophysical Journal Letters, 937, L33

Sun W., et al., 2024, The Astrophysical Journal, 960, 104

Suzuki T. L., et al., 2021, The Astrophysical Journal, 908, 15

Swinbank A. M., et al., 2012a, Monthly Notices of the Royal Astronomical Society, 426, 935

Swinbank A. M., et al., 2012b, The Astrophysical Journal, 760, 130

Tacchella S., et al., 2015, The Astrophysical Journal, 802, 101

Tacconi L. J., et al., 2013, The Astrophysical Journal, 768, 74

Tacconi L. J., et al., 2018, The Astrophysical Journal, 853, 179

Taylor E. N., et al., 2015, Monthly Notices of the Royal Astronomical Society, 446, 2144

Teklu B. B., et al., 2020, The Astrophysical Journal, 897, 61

Tempel E., et al., 2014, Astronomy & Astrophysics, 566, A1

Teplitz H., 2018, HST Proposal, p. 15647

Terao Y., et al., 2022, The Astrophysical Journal, 941, 70

Theios R. L., et al., 2019, The Astrophysical Journal, 871, 128

Thompson D., Mannucci F., Beckwith S. V. W., 1996, The Astronomical Journal, 112, 1794

Timmerman R., et al., 2022, Astronomy & Astrophysics, 668, A65

Tinsley B. M., 1979, The Astrophysical Journal, 229, 1046

Toomre A., Toomre J., 1972, The Astrophysical Journal, 178, 623

Tornatore L., Ferrara A., Schneider R., 2007, Monthly Notices of the Royal Astronomical Society, 382, 945

Torrey P., et al., 2019, Monthly Notices of the Royal Astronomical Society, 484, 5587

Traina A., et al., 2024, Astronomy & Astrophysics, 681, A118

Tremonti C. A., et al., 2004, The Astrophysical Journal, 613, 898

Trenti M., Stiavelli M., Shull J. M., 2009, The Astrophysical Journal, 700, 1672

Treu T., et al., 2015, The Astrophysical Journal, 812, 114

Treu T., et al., 2016, The Astrophysical Journal, 817, 60

Troncoso P., et al., 2014, Astronomy & Astrophysics, 563, A58

Trujillo I., et al., 2006, The Astrophysical Journal, 650, 18

Trujillo I., et al., 2007, Monthly Notices of the Royal Astronomical Society, 382, 109

Trump J. R., et al., 2013, The Astrophysical Journal, 763, L6

Tully R. B., 2015, The Astronomical Journal, 149, 171

Tully R. B., Courtois H. M., Sorce J. G., 2016, The Astronomical Journal, 152, 50

Umetsu K., et al., 2012, The Astrophysical Journal, 755, 56

Umetsu K., et al., 2014, The Astrophysical Journal, 795, 163

Valentino F., et al., 2023, The Astrophysical Journal, 947, 20

Vanzella E., et al., 2021, Astronomy & Astrophysics, 646, A57

Varadaraj R. G., et al., 2024, Monthly Notices of the Royal Astronomical Society, 533, 3724

Vaughan S. P., et al., 2020, Monthly Notices of the Royal Astronomical Society, 496, 3841

Vega-Ferrero J., Yepes G., Gottlöber S., 2017, Monthly Notices of the Royal Astronomical Society, 467, 3226

Vega-Ferrero J., et al., 2024, The Astrophysical Journal, 961, 51

Vijayan A. P., et al., 2021, Monthly Notices of the Royal Astronomical Society, 501, 3289

Virtanen P., et al., 2020, Nature Methods, 17, 261

Von Der Linden A., et al., 2014, Monthly Notices of the Royal Astronomical Society, 439, 2

Wake D. A., et al., 2017, The Astronomical Journal, 154, 86

Walcher J., et al., 2011, Astrophysics and Space Science, 331, 1

Waller W. H., 1990, Publications of the Astronomical Society of the Pacific, 102, 1217

Wang Y., et al., 2008, Monthly Notices of the Royal Astronomical Society, 385, 1511

Wang X., et al., 2017, The Astrophysical Journal, 837, 89

Wang X., et al., 2019, The Astrophysical Journal, 882, 94

Wang X., et al., 2022, The Astrophysical Journal, 926, 70

Wang K., Peng Y., Chen Y., 2023, Monthly Notices of the Royal Astronomical Society, 523, 1268

Wang J.-H., et al., 2024a, Astronomy & Astrophysics, 686, A100

Wang B., et al., 2024b, The Astrophysical Journal Letters, 969, L13

Ward E., et al., 2024, The Astrophysical Journal, 962, 176

Weinberger R., et al., 2017, Monthly Notices of the Royal Astronomical Society, 465, 3291

Weisskopf M. C., et al., 2002, Publications of the Astronomical Society of the Pacific, 114, 1

Welker C., et al., 2018, Astronomy & Astrophysics, 613, A4

Werner S. V., et al., 2021, Monthly Notices of the Royal Astronomical Society, 510, 674

West M. J., 1994, Monthly Notices of the Royal Astronomical Society, 268, 79

Westcott L., et al., 2025, The Astrophysical Journal, 983, 121

Wetzel A. R., Tinker J. L., Conroy C., 2012, Monthly Notices of the Royal Astronomical Society, 424, 232

Whitaker K. E., et al., 2012, The Astrophysical Journal Letters, 754, L29

White S. D. M., Frenk C. S., 1991, The Astrophysical Journal, 379, 52

White S. D. M., Rees M. J., 1978, Monthly Notices of the Royal Astronomical Society, 183, 341

Whitmore B. C., et al., 2020, The Astrophysical Journal, 889, 154

Williams R. E., et al., 1996, The Astronomical Journal, 112, 1335

Wilman D. J., et al., 2020, The Astrophysical Journal, 892, 1

Wise M. W., et al., 2007, The Astrophysical Journal, 659, 1153

Wisnioski E., et al., 2015, The Astrophysical Journal, 799, 209

Wisnioski E., et al., 2019, The Astrophysical Journal, 886, 124

Wootten A., Thompson A. R., 2009, Proceedings of the IEEE, 97, 1463

Wu X., et al., 2020, Monthly Notices of the Royal Astronomical Society, 494, 5636

Wuyts S., et al., 2011, The Astrophysical Journal, 742, 96

Wuyts E., et al., 2016, The Astrophysical Journal, 827, 74

Wyder T. K., et al., 2005, The Astrophysical Journal, 619, L15

Yang X., et al., 2006, Monthly Notices of the Royal Astronomical Society, 369, 1293

Yang X., et al., 2007, The Astrophysical Journal, 671, 153

Yang L., et al., 2022, The Astrophysical Journal Letters, 938, L17

Yang L., et al., 2025, The Astrophysical Journal Supplement Series, 281, 68

Yates R. M., Kauffmann G., Guo Q., 2012, Monthly Notices of the Royal Astronomical Society, 422, 215

Yates R. M., et al., 2023, Monthly Notices of the Royal Astronomical Society, 527, 6292

Yi S. K., et al., 2013, Astronomy & Astrophysics, 554, A122

York D. G., et al., 2000, The Astronomical Journal, 120, 1579

Yun M. S., Reddy N. A., Condon J. J., 2001, The Astrophysical Journal, 554, 803

Zabludoff A. I., Mulchaey J. S., 1998, The Astrophysical Journal, 498, L5

Zahid H. J., et al., 2013, The Astrophysical Journal, 763, 92

Zahid H. J., et al., 2014, The Astrophysical Journal, 791, 130

Zakharova D., et al., 2025, Astronomy & Astrophysics, 693, A113

Zavala J. A., et al., 2023, The Astrophysical Journal Letters, 943, L9

Zhang H., Zaritsky D., 2022, The Astrophysical Journal, 941, 18

Zhang C., et al., 2021, The Astrophysical Journal, 911, 57

Zolotov A., et al., 2015, Monthly Notices of the Royal Astronomical Society, 450, 2327

Zwicky F., 1933, Helvetica Physica Acta, 6, 110

Zwicky F., 1937, The Astrophysical Journal, 86, 217

de Vaucouleurs G., 1948, Annales d'Astrophysique, 11, 247

de Vos K., Merrifield M. R., Hatch N. A., 2024, Monthly Notices of the Royal Astronomical Society, 531, 4383

van Dokkum P. G., et al., 2010, The Astrophysical Journal, 709, 1018

van Haarlem M. P., et al., 2013, Astronomy & Astrophysics, 556, A2

van Loon M. L., Mitchell P. D., Schaye J., 2021, Monthly Notices of the Royal Astronomical Society, 504, 4817

van Uitert E., Joachimi B., 2017, Monthly Notices of the Royal Astronomical Society, 468, 4502

van der Wel A., et al., 2012, The Astrophysical Journal Supplement Series, 203, 24

van der Wel A., et al., 2014, The Astrophysical Journal, 788, 28

van der Wel A., et al., 2024, The Astrophysical Journal, 960, 53